21 March 2008 | S10

Science

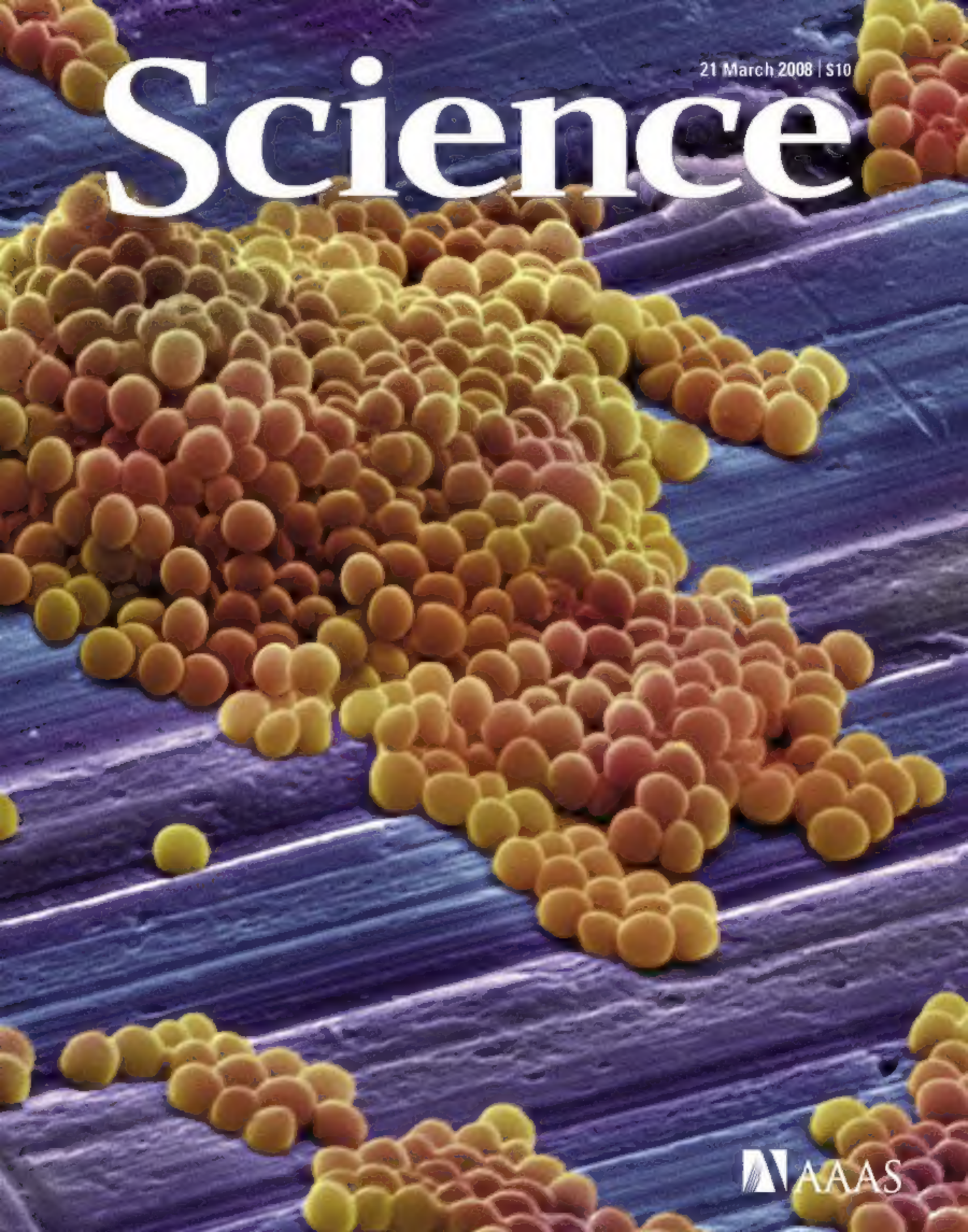

AAAS

Volume 319, Issue 5870

COVER

Clusters of the pathogenic bacterium *Staphylococcus aureus* visualized by scanning electron microscopy. *Staphylococcus aureus* has been called a "superbug" because of its ability to resist numerous antibiotics and evade host antimicrobial mediators, including nitric oxide. See page 1672.

Image: Annie Cavanagh/Wellcome Images

DEPARTMENTS

EDITORIAL

NEWS OF THE WEEK

NEWS FOCUS

LETTERS

BOOKS *ET AL.*

1618

EDUCATION FORUM

PERSPECTIVES

CONTENTS continued >>

Science

SCIENCE EXPRESS

www.sciencexpress.org

GENETICS

Mechanism of Self-Sterility in a Hermaphroditic Chordate
Y. Harada et al.
The sea squirt prevents self-fertilization by using a tightly linked genetic locus to encode a sperm-egg receptor-ligand pair, a system similar to that used by flowering plants.
10.1126/science.1152488

MATERIALS SCIENCE

High-Thermoelectric Performance of Nanostructured Bismuth Antimony Telluride Bulk Alloys
B. Poudel et al.
Milling a thermoelectric alloy, which produces electricity from a thermal gradient, into a nanopowder, then pressing it into a bulk form, greatly improves its performance.
10.1126/science.1156446

PLANETARY SCIENCE

Ancient Asteroids Enriched in Refractory Inclusions
J. M. Sunshine, H. C. Connolly Jr., T. J. McCoy, S. J. Bus, L. M. La Croix
Spectral data imply that some asteroids contain higher concentrations of early solar system grains and materials than are found in any sampled meteorite.
10.1126/science.1154340

EVOLUTION

Metabolic Diversification—Independent Assembly of Operon-Like Gene Clusters in Plants
B. Field and A. E. Osbourn
Through strong selection, similar clusters of genes for triterpene biosynthesis have arisen independently through gene duplication and neofunctionalization in several plant lines.
10.1126/science.1154990

TECHNICAL COMMENT ABSTRACTS

OCEAN SCIENCE

REVIEWS

GEOCHEMISTRY

GEOCHEMISTRY

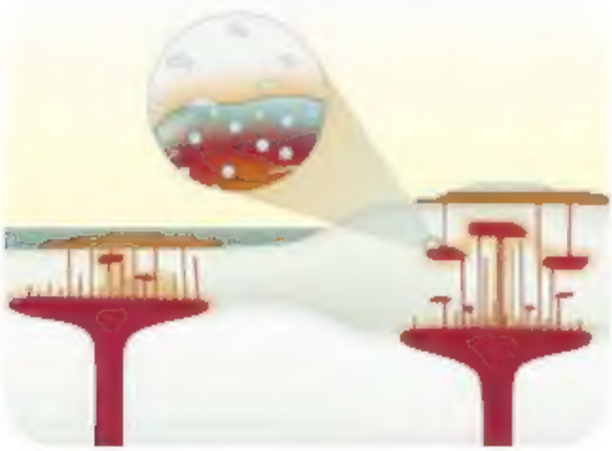

BREVIA

PSYCHOLOGY

RESEARCH ARTICLE

NEUROSCIENCE

REPORTS

APPLIED PHYSICS

MATERIALS SCIENCE

PLANETARY SCIENCE

CONTENTS continued >>

REPORTS *CONTINUED...*

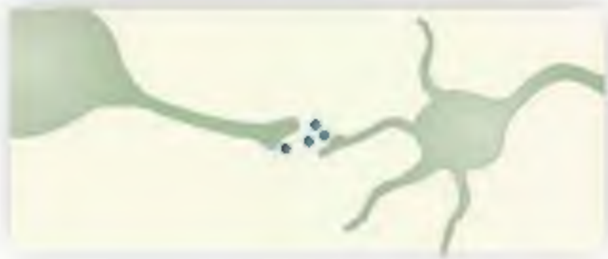

AAAS
ADVANCING SCIENCE, SERVING SOCIETY

SCIENCE (ISSN 0036-8075) is published weekly on Friday, except the last week in December, by the American Association for the Advancement of Science, 1200 New York Avenue, NW, Washington, DC 20005. Periodicals Mail postage (publication No. 484460) paid at Washington, DC, and additional mailing offices. Copyright © 2008 by the American Association for the Advancement of Science. The title SCIENCE is a registered trademark of the AAAS. Domestic individual membership and subscription (51 issues): $144 ($74 allocated to subscription). Domestic institutional subscription (51 issues): $770; Foreign postage extra: Mexico, Caribbean (surface mail) $55; other countries (air assist delivery) $85. First class, airmail, student, and canadian rates on request. Canadian rates with GST available upon request, GST #1254 88122. Publications Mail Agreement Number 1069624. SCIENCE is printed on 30 percent post-consumer recycled paper. Printed in the U.S.A.

Change of address: Allow 4 weeks, giving old and new addresses and 8-digit account number. Postmaster: Send change of address to AAAS, P.O. Box 96178, Washington, DC 20090-6178. Single-copy sales: $10.00 current issue, $15.00 back issue prepaid (includes surface postage; bulk rates on request). Authorization to photocopy material for internal or personal use under circumstances not falling within the fair use provisions of the Copyright Act is granted by AAAS to libraries and other users registered with the Copyright Clearance Center (CCC) Transactional Reporting Service, provided that $20.00 per article is paid directly to CCC, 222 Rosewood Drive, Danvers, MA 01923. The identification code for Science is 0036-8075. Science is indexed in the Reader's Guide to Periodical Literature and in several specialized indexes.

CONTENTS continued >>

Signaling researchers met in Weimar, Germany.

SCIENCE SIGNALING

www.stke.org THE SIGNAL TRANSDUCTION KNOWLEDGE ENVIRONMENT

EDITORIAL GUIDE: Hear It, Watch It, Read It
N. R. Gough
Four new sections of *Science Signaling* bring new resources to the cell signaling community.

MEETING REPORT: Watching Molecules Talking to Each Other
K. Friedrich, O. Janssen, R. Hass
The 2007 meeting of the Signal Transduction Society focused on results obtained using state-of-the-art imaging methodologies.

PRESENTATION: Matrix Metalloproteinase-7 and the 20S Proteasome Contribute to Cellular Senescence
C. Bertram and R. Hass
Two cultured cell systems provide insight into intracellular and extracellular events involved in cellular differentiation and senescence.

PRESENTATION: In Vivo Imaging of T Cell Priming
S. E. Henrickson et al.
History of prior antigenic experience controls T cell activation.

PRESENTATION: Geranylgeranylation but Not GTP-Loading of Rho GTPases Determines T Cell Function
S. Wolczies, I. Bendix, F. Zipp
Posttranslational lipid modification of RhoA is necessary for T cell migration into the central nervous system during neuroinflammation.

SCIENCE ONLINE FEATURE

THE GONZO SCIENTIST: Play It Again, Robot
The fifth installment in this series, with accompanying video, investigates the state of the art of robot music.

www.sciencemag.org/sciext/gonzoscientist/

SCIENCENOW

www.sciencenow.org DAILY NEWS COVERAGE

One Tail, Many Feats
Fifth appendage keeps geckos upright and agile and even helps them glide.

Hobbit Skull Suggests a Separate Species
Diminutive hominid may have ties to human ancestors.

Gators Dive With Flexible Air Tanks
A special muscle may give alligators a deadly edge in the water.

Opportunities for scientists in public health.

SCIENCE CAREERS

www.sciencecareers.org CAREER RESOURCES FOR SCIENTISTS

Public Health Goes Global
S. Webb
Scientists are needed with experience and expertise to address global health challenges.

Tooling Up: Breaking Free of Academia
D. Jensen
The cultural shift from academia to nonacademic workplaces requires careful self-assessment.

Ahead of Her Time
E. Pain
At age 24, Katerina Ailantis received a grant from the European Research Council to start an independent lab.

From the Archives: Thanks for the Great Postdoc Bargain
R. Freeman
The Harvard economist thanks postdocs for their skilled and diligent servitude.

SCIENCEPODCAST

Download the 14 March *Science* Podcast to hear about the evolution of human bipedalism, subliminal influence on behavior, and for farewell thoughts from senior news correspondent Jean Marx.

www.sciencemag.org/about/podcast.dtl

CREDITS: (SCIENCE CAREERS) SANOVA; (SCIENCE LAB; SCIENCE ONLINE FEATURE) KATHRIN KOLDEWEG

Separate individual or institutional subscriptions to these products may be required for full-text access.

EDITED BY STELLA HURTLEY AND PHIL SZUROMI

CREDITS (LEFT TO RIGHT): RICHMOND AND JUNGERS; ISHIWATA ET AL.

Secrets of an Ancient Thigh Bone

The functional and phylogenetic significance the 6-million-year-old femora of *Orrorin tugenensis*, one of the earliest fossils from the human lineage has been debated since their discovery in Kenya in 2000. Richmond and Jungers (p. 1662; see the news story by Gibbons) present a comparative morphometric analysis of these remains with femora from modern humans, living apes, and other fossil hominins to reveal and confirm bipedal adaptations in the femora of *Orrorin*. The *Orrorin* femora closely resemble those of *Australopithecus* and *Paranthropus*, which are 2 to 3 million years old, which contradict the hypothesis that *Orrorin* is more closely related to *Homo* than to *Australopithecus*. The morphology of the *Orrorin* femora strongly suggests that the australopithecine pattern of hip biomechanics evolved very early in human evolution and persisted as a stable locomotor strategy for as long as 4 million years, the majority of human evolutionary history.

Small Minerals, Big Implications

Many geologic processes involve reactions between minerals and between minerals and surface water, groundwater, or air. Increasingly, it has been recognized that many important reactions involve minerals that are less than about 1 micrometer in size (or nanominerals), and two Reviews discuss how minerals properties can depend on crystal size. **Hochella *et al.*** (p. 1631) summarizes our understanding of these nanominerals, their occurrence, and their potential implications in geologic processes. **Navrotsky *et al.*** (p. 1635) focus on the thermodynamics and stability of one of the most important and ubiquitous classes of nanominerals, the iron oxides.

Diffusion in Overdrive

The motion of impurity atoms within a crystal is a thermally driven process, and for a perfect crystal, this process should be fairly slow. However, there are numerous examples where faster diffusion has been observed that generally have been attributed to the presence of dislocations and grain boundaries. **Legros *et al.*** (p. 1646) measure the motion of silicon precipitates inside a thin film of aluminum and directly observed "pipe diffusion," in which the dislocations in the aluminum act as a channel for more rapid travel of the silicon. Diffusion can be accelerated by three orders of magnitude compared with bulk diffusion, in support of the theories on pipe diffusion.

How Titan Turns

Titan, Saturn's largest moon, is covered with an icy crust and dense atmosphere. **Lorenz *et al.*** (p. 1649; see the Perspective **Sotin and Tobie**) used several years of Cassini radar observations to show that Titan's rotational period differs from its orbital period, which implies that there is an exchange of angular momentum seasonally between the planet and its atmosphere. Modeling of this exchange requires an internal model of Titan that includes a crust and core separated by a liquid ocean, as on Jupiter's moon Europa.

Ancient Volcanic Gas in Glass

The influence on climate of massive volcanic eruptions that have formed flood basalts, such as the Deccan traps at the end of the Cretaceous, has been difficult to assess, in part because of the lack of data on the gas contents of most of the magmas (much of the erupted basalt degassed as crystals formed or during later alteration). **Self *et al.*** (p. 1654; see the Perspective by **Scaillet**) screened many samples of the Deccan basalts and found a few samples preserving glass inclusions in crystals or glassy rims that could preserve information on the original sulfur and chlorine contents of the Deccan magma. The results imply that the Deccan basalts released huge amounts of sulfur, perhaps nearly an order of magnitude or more than recent global anthropogenic emissions, for decades or centuries.

Low-Field Multiferroics

The ability to electrically manipulate the magnetic properties of a solid offers great potential for device functionality. Materials of particular interest are those in which the magneto-electric (ME) response, which couples electric and magnetic dipole moments, is an intrinsic property of the crystalline symmetry. So far, however, the ME effect in such materials has only been seen at large magnetic fields and low temperature. **Ishiwata *et al.*** (p. 1643) present results on the hexaferrite $Ba_2Mg_2Fe_{12}O_{22}$, which has a chiral spin structure, and show that the electric polarization can be manipulated with a very low magnetic field of 30 millitesla.

Insights into Early Multicellular Life

Multicellular life first appeared in the Late Precambrian, but the affinity and habits of many of the fossils remain enigmatic. **Droser and Gehling** (p. 1660; see the Book Review by **Xiao**) reveal a newly described tubular organism that is particularly abundant in one area where many fossils have been found, the Ediacara of the Flinders Range of South Australia. The tubular fossils are as long as 30 centimeters and 12 millimeters in diameter and are composed of smaller units. A few exhibit branching, and multiple modes of growth are represented. The fossils reveal attachment structures to the sediment substrate, and probably represent a stem-group Cnidarian or Poriferan.

Continued on page 1587

Continued from page 1585

Functional Differentiation Within the Human Hippocampus

Structures in the temporal lobe of the human brain support declarative (fact and event) memory. How these structures operate and interact is unclear. Recent studies in rodents observed pattern separation processes in the CA3 field and dentate gyrus. Using high-resolution brain imaging, **Bakker *et al.*** (p. 1640; see the Perspective by **Leutgeb**) have now analyzed these operations in humans. A technique was developed to infer changes in the pattern of activity across neurons in the medial temporal lobe with respect to pattern separation and pattern completion processes. In striking similarity to the rodent data, strong pattern separation was observed in the CA3 and dentate gyrus, whereas a tendency toward pattern completion was observed in hippocampal CA1, the subiculum, the entorhinal, and parahippocampal cortices.

CREDIT: BAKKER ET AL.

Radical Avoidance Strategy

Staphylococcus aureus is responsible for severe infections that, in the wake of widespread antibiotic resistance, are a growing threat. Unlike very closely related commensal species, *S. aureus* can both inhibit and avoid the damaging effects of NO released during host defensive responses. **Richardson *et al.*** (p. 1672, see the cover) show that in addition to free-radical scavenging mechanisms, *S. aureus* possesses an inducible L-lactate dehydrogenase through which it can divert glucose metabolism exclusively to L-lactate during NO exposure when other more sensitive enzymes shut down. This strategy allows the organism to maintain redox balance, retain virulence, grow, and replicate despite the host assault.

Faulty Scaffolding and Cancer

Differentiation, survival, and growth of B cells requires proper functioning of the nuclear factor–κB (NF-κB) signaling pathway, including CARD11, a cytoplasmic scaffolding protein that serves as a docking site for signaling molecules. **Lenz *et al.*** (p. 1676, published online 6 March) have discovered that a certain subtype of diffuse large B cell lymphoma, the most common form of non-Hodgkin's lymphoma in humans, is caused by mutations in the *CARD11* gene. In cell culture experiments, these mutant forms of CARD11 caused inappropriate activation of the NF-κB pathway.

Individual Egg, Individual Attention

Female flies are selective in choosing suitable sites to lay their eggs, presumably to promote survival of their progeny. However, **Yang *et al.*** (p. 1679) found that even at sites suitable for egg-laying, for every single egg to be deposited, *Drosophila melanogaster* went through a stereotyped behavior sequence: A searchlike program, egg-laying, cleaning of ovipositor, and rest. Females selected plain or bitter-tasting substrates over sucrose-containing media when given a chance to explore available options. However, when only sucrose was available, they laid eggs on it, and in approximately equal numbers, which suggests that while sucrose is not their preferred choice, it is not absolutely repulsive.

'Tis Better to Give

Now that the holiday shopping season is over, many people can ask whether, as in the adage, it truly was better to give than to receive. **Dunn *et al.*** (p. 1687) address this question, by using the results from a survey of Americans, by analyzing the actual spending patterns of bonuses meted out at a Boston area firm and by conducting an experimental manipulation on a stereotypical subject pool (psychology undergraduates). All three studies suggest that spending money on other people produces more happiness than spending on oneself, in contrast to the expectations of the undergraduates.

Bruce Alberts is Editor-in-Chief of *Science*.

Considering Science Education

I CONSIDER SCIENCE EDUCATION TO BE CRITICALLY IMPORTANT TO BOTH SCIENCE AND THE world, and I shall frequently address this topic on this page. Let's start with a big-picture view. The scientific enterprise has greatly advanced our understanding of the natural world and has thereby enabled the creation of countless medicines and useful devices. It has also led to behaviors that have improved lives. The public appreciates these practical benefits of science, and science and scientists are generally respected, even by those who are not familiar with how science works or what exactly it has discovered.

But society may less appreciate the advantage of having everyone aquire, as part of their formal education, the ways of thinking and behaving that are central to the practice of successful science: scientific habits of mind. These habits include a skeptical attitude toward dogmatic claims and a strong desire for logic and evidence. As famed astronomer Carl Sagan put it, science is our best "bunk" detector. Individuals and societies clearly need a means to logically test the onslaught of constant clever attempts to manipulate our purchasing and political decisions. They also need to challenge what is irrational, including the intolerance that fuels so many regional and global conflicts.

So how does this relate to science education? Might it be possible to encourage, across the world, scientific habits of mind, so as to create more rational societies everywhere? In principle, a vigorous expansion of science education could provide the world with such an opportunity, but only if scientists, educators, and policy-makers redefine the goals of science education, beginning with college-level teaching. Rather than only conveying what science has discovered about the natural world, as is done now in most countries, a top priority should be to empower all students with the knowledge and practice of how to think like a scientist.

Scientists share a common way of reaching conclusions that is based not only on evidence and logic, but also requires honesty, creativity, and openness to new ideas. The scientific community can thus often work together across cultures, bridging political divides. Such collaborations have mostly focused on the discovery of new knowledge about the natural world. But scientists can also collaborate effectively on developing and promulgating a form of science education for all students that builds scientific habits of mind.

Inquiry-based science curricula for children ages 5 to 13 have been undergoing development and refinement in the United States for more than 50 years. These curricula require that students engage in active investigations, while a teacher serves as a coach to guide them to an understanding of one of many topics. This approach takes advantage of the natural curiosity of young people, and in the hands of a prepared teacher, it can be highly effective in increasing a student's reasoning and problem-solving skills. In addition, because communication is emphasized, inquiry-based science teaching has been shown to increase reading and writing abilities. This approach to science education has been slowly spreading throughout the United States in the past decade, but it requires resources and energy on the part of school districts that are often not available. With strong support from scientists and science academies, a similar type of science education is also being increasingly implemented in France, Sweden, Chile, China, and other countries. In these efforts, catalyzed for the past 8 years by the InterAcademy Panel in Trieste, scientists are sharing resources and helping to form new bridges between nations.

With appropriate modifications, could such an education also help make students more rational and tolerant human beings, thereby reducing the dogmatism that threatens the world today with deadly conflict? In future editorials, I will explore the many potential advantages of inquiry-based science education. I will also discuss the barriers that must be overcome for its widespread implementation across the globe, because we may face no more urgent task if future generations are to inherit a peaceful world.

– Bruce Alberts

10.1126/science.1157518

EDITED BY GILBERT CHIN AND JAKE YESTON

PLANT SCIENCE

At Root of the Matter

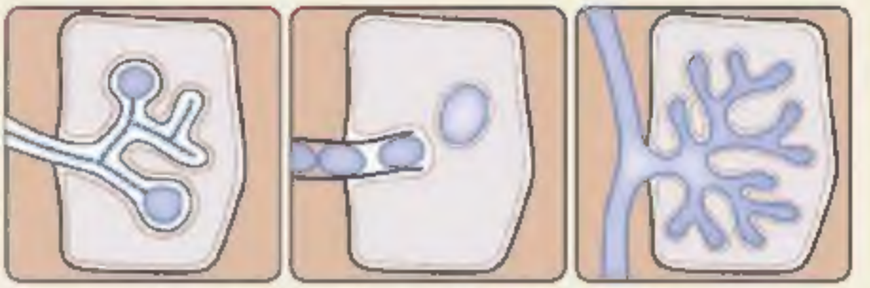

Intimate associations between plants and bacteria and fungi.

Many plant roots establish a symbiotic relationship with either bacteria or fungi in order to gain access to nutrients, such as fixed nitrogen or phosphate, respectively. Markmann *et al.* and Gherbi *et al.* have investigated the evolution of symbiotic relationships between plants and their symbionts and suggest that, on the basis of its nearly universal presence, a single signal transduction component, the leucine-rich-repeat, receptor-like kinase SYMRK, is essential for a host of angiosperms. Genetic knockdown in a member of the cucumber family (*Datisca glomerata*, a close legume relative) and in the tree *Casuarina glauca* showed that this protein was essential for bacterial nodulation; furthermore, it also affected fungal symbiosis. Additional investigation revealed that the protein is highly conserved in its ability to mediate these interactions and that this protein does not mediate the exclusive host/symbiont interactions found among species. In addition, three structural SYMRK versions exist among plants with different functional capabilities in the development of root/symbiont interactions, providing an evolutionary hypothesis for the origin of the highly derived nodules in legumes and their close relatives. — LMZ

PLoS Biol. **6**, e68; *Proc. Natl. Acad. Sci. U.S.A.* **105**, 10.1073/pnas.0710618105 (2008).

MOLECULAR BIOLOGY

SINEs of Repression

Mammalian genomes are packed to overflowing with a menagerie of repetitive DNA elements, many of which are derived from defunct transposons. Short interspersed elements (SINEs)—relic retrotransposons—are maintained in both mouse and human genomes. A clue to the basis for the persistence of these apparently "parasitic" DNA regions in the mouse comes from the observation that the noncoding (nc) RNA transcribed from B2 SINEs in response to heat shock can act to repress specific protein-coding genes by binding to and repressing RNA polymerase II (pol II).

The predominant SINEs in humans are Alu elements, similar in part to mouse B1 SINEs but evolutionarily unrelated to the other predominant mouse SINE, B2. Mariner *et al.* show that human Alu ncRNA, like mouse B2 ncRNA, can repress specific genes in response to heat shock, and that, like B2 RNA, it achieves this by binding to the RNA pol II pre-initiation complex, probably preventing appropriate interaction with promoter DNA. Human Alu RNA has a similar effect in mouse cells, and conversely, mouse B2 RNA in human cells. The mouse B1 SINE RNA is related to a processed short cytoplasmic RNA fragment of Alu (corresponding to the 5′ half of Alu ncRNA) and both can bind RNA pol II. Although neither can repress transcription in vitro, it is quite possible they also have related regulatory functions. Thus it would seem that humans do not have either of the B1 or B2 SINE family of repeats because the Alu repeats can by themselves carry out the function of both of the mouse SINE RNAs, and possibly supplanted them during evolution. — GR

Mol. Cell **29**, 499 (2008).

OCEAN SCIENCE

Phosphate Clues from Coral

Phosphorus is an essential macronutrient for marine organisms, and its availability probably exerts a major control on climate, due to its potential to affect the intensity of marine productivity and thereby contribute to regulation of the concentration of carbon dioxide in the atmosphere. Unfortunately, no direct method to determine the abundance of marine phosphorus in the productive surface ocean in the geological past has been found, so the relationship between phosphorus availability and paleoclimate remains uncertain. La Vigne *et al.* report that the phosphorus-to-calcium ratio of a scleractinian coral, *Pavona gigantea*, tracks variations in seawater phosphate concentration, thereby offering a possible solution to the dilemma of not being able to reconstruct the history of that nutrient in the past. If their method proves robust, coral skeleton P/Ca might be a reliable proxy record of nutrient availability on time scales of decades to millennia. — HJS

Geophys. Res. Lett. **35**, L05604 (2008).

PHYSICS

A Matter of Extended Coherence

The splitting and subsequent re-overlapping of a coherent light beam provides the basis for exquisitely sensitive detection of path-length differences; this technique of optical interferometry finds applications ranging from stellar observations to holographic imaging and characterization of optical components. Analogously, the cooling of a cloud of bosonic atoms into a Bose-Einstein condensate, a state in which all the atoms share the same quantum state, is described in terms of a coherent matter wave. Because atoms sense gravity, the interference of matter waves can then be used to provide a sensitive gravity detector, with a comparably diverse set of applications ranging from testing relativity to detecting underground bunkers. Unlike photons, however, which do not interact much with each other, the atoms in the

CREDITS (TOP TO BOTTOM): MARKMANN *ET AL.*, *PLOS BIOL.* 6, E68; LA VIGNE *ET AL.*, *GEOPHYS. RES. LETT.* 35, L05604 (2008)

trapped cloud do interact by way of collisions. These collisions then give rise to losses and induce shifts in the phase of the matter wave, thereby limiting the sensitivity of any atom interferometer. Gustavsson *et al.* and Fattori *et al.* present setups in which the interaction strength between the atoms in the condensate (cesium and potassium, respectively) is tuned via magnetic field so that the scattering between the atoms is significantly reduced. The resulting extension of the matter-wave coherence time leads to improved sensitivity of the atom interferometers. — ISO

Phys. Rev. Lett. **100**, 080404; 080405 (2008).

CELL BIOLOGY

Resection and Repair

When the outer membrane of a eukaryotic cell is damaged (for instance, by ripping), a calcium-dependent repair process involving the fusion of lysosomal membrane with the plasma membrane is set in motion. Bacterial toxins can also perforate the plasma membrane, but do so by forming protein-delimited holes. How does a cell repair this kind of puncture? Idone *et al.* show that, in addition to patching the portion of damaged membrane using exocytosis, the cell arranges for the removal of the perforated areas from the cell surface via a process of calcium-stimulated endocytosis. Treating cells with the bacterial toxin streptolysin, which forms stable membrane-embedded pores, induced a calcium- and sterol-dependent form of endocytosis that cleared the pores from the plasma membrane, leading to the rapid (in less than a minute) resealing of the cell; independently stimulating endocytosis also promoted membrane repair. Thus, cells use two mechanistically linked pathways, which are both stimulated by high levels of extracellular calcium, to activate membrane repair after physical injury. — SMH

J. Cell Biol. **180**, 905 (2008).

CHEMISTRY

O Flow Dims Glow

In a polymer electrolyte membrane (PEM) fuel cell, hydrogen is oxidized at the anode to form protons that migrate through a membrane and then react with the oxygen being reduced at the cathode. Efficient operation relies in part on optimizing interactions of the respective isolated electrodes with flowing hydrogen and oxygen gas. Toward this end, Inukai *et al.* have devised a technique for visualizing oxygen flow as PEM fuel cells operate. They disperse a phosphorescent chromophore in a polymer matrix and apply the resulting oxygen-permeable film to specially constructed transparent fuel-cell elements. Because oxygen quenches the phosphorescence, the authors can track oxygen flow by monitoring emission intensity after excitation of the dye-impregnated film with 407-nm light. The scheme offers 300-μm spatial resolution and 500-ms temporal resolution. — JSY

Angew. Chem. Int. Ed. **47**, 10.1002/anie.200705516 (2008).

NEUROSCIENCE

Time Is on Our Side

The cerebellum is a highly ordered brain structure, with the axons of small numerous granule cells projecting to the dendritic tree of large Purkinje cells in a stereotyped way. All of the daughters of individual granule cell precursors connect to the same horizontal layer within the Purkinje cell dendrites, although their cell bodies are not grouped together. How does this structure assemble so precisely?

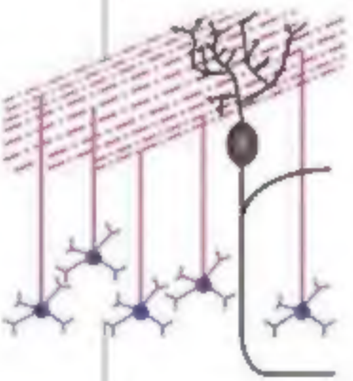

The axons (fuchsia) of granule cells (blue) innervate the Purkinje cell dendrites (black).

By tracing the lineal descent and migration of granule cells with a method that visualizes their axonal and dendritic projections, Espinosa and Luo have revealed that it occurs by application of a straightforward principle. All of the offspring of each precursor granule cell exit the cell cycle within a narrow time window and synchronously connect their axons to the top surface of the layer containing the Purkinje cell dendrites. Each clonally related family of granule cells takes its turn to differentiate and connect to the Purkinje cell dendrites, resulting in their axons stacking in the dendrites in chronological order from deep to superficial. This sequential maturation of granule cells coincides with the ordered arrival of their mossy fiber inputs, which arrive from other brain areas at different times. Inputs from each brain region would therefore target a different region of the Purkinje cell dendritic tree and so have a distinct influence on computation. Thus, the developing brain uses the simple principle of temporal sequencing to assemble a precise and complex computational machine. — KK

J. Neurosci. **28**, 2301 (2008).

CREDIT: ESPINOSA AND LUO, J. NEUROSCI. 28, 2301 (2008)

Drifting Hominids

Many researchers assume that differences between the skulls of modern humans and Neandertals—with their jutting faces and thick brow ridges—are due to natural selection. Neandertal crania (see top skull) might be adapted to using teeth as tools, while the moderns (below) were moving toward language proficiency.

But a new study supports the notion that these dramatic contrasts result from "genetic drift," the random changes that occur in any population. Anthropologist Timothy Weaver of the University of California, Davis, and colleagues made 37 measurements on 2524 modern human skulls and 20 Neandertal skulls. They plugged the numbers into a model based on a well-established example of human genetic drift. They came up with a "divergence time estimator" that put the Neandertal-*Homo sapiens* evolutionary split at between 311,000 and 435,000 years ago. That range agrees with recent estimates from Neandertal DNA (*Science*, 17 November 2006, p. 1113). Eric Delson, a paleoanthropologist at Lehman College in New York City, says the study, in this week's issue of the *Proceedings of the National Academy of Sciences*, adds to "the growing body of evidence in support of a genetic-drift explanation for a major portion of human cranial evolution." But he cautions that these findings apply only to features of the skull, not to the brain inside.

Verbs Across the Bering Strait

When Edward Vajda first encountered descriptions of an isolated Siberian language, Ket, in the early 1990s, its verbal structure reminded him of Navajo.

Now Vajda, a linguist at Western Washington University in Bellingham, has demonstrated the first solid connection between Native American languages and those spoken by north Asians who came across the Bering Strait some 12,000 years ago.

At a meeting of the Alaska Anthropological Association in Anchorage last month, Vajda showed how Yeniseic, a language family containing Ket, is linguistically related to Na-Dene, a North American language group including Navajo. Vajda compared verbs in Ket and Na-Dene tonal languages, and showed how tones in Ket words arose from consonant shifts in similar Na-Dene words. He also identified shared vocabulary. The modern Ket word for "mosquito," for example, is pronounced "soo-ee"; the ancestral Athabaskan is "tsoo-ee."

Although a linguistic tie between the two language families has long been supposed, scholars have been skeptical of previous attempts to link them that far back. Vajda's work, says linguist Johanna Nichols of the University of California, Berkeley, is a "successful demonstration of a long-distance, temporally deep connection."

Ket man relaxes by Siberia's Yelogui River

CREDITS (TOP TO BOTTOM): PALLAVA BAGLA; WEAVER ET AL., JOURNAL OF HUMAN EVOLUTION, VOL. 53, AUGUST 2007; EDWARD VAJDA

India's Floating Lab

India has established a state-of-the-art marine research presence with its new $58 million ship, the *Sagar Nidhi* ("ocean wealth"). The 103-meter-long Italian-built ship, India's largest research vessel to date, will survey marine resources along the country's 7500-km coastline, conduct underwater archaeology and deploy deep-sea sensors for early warning against tsunamis. Launched on 3 March in Chennai, the ship will house 30 scientists.

Genes and Humor

If you use humor to lighten your life, you can thank your genes. But sarcasm is more likely a reaction to your environment, according to a twin study on "humor styles."

Psychologist Philip Vernon and colleagues at the University of Western Ontario in London, Canada, gave a questionnaire to 456 pairs of adult, same-sex twins in Britain; 300 pairs were identical and 156 pairs were fraternal. The questions measure two positive humor styles: "affiliative" and "self-enhancing" (with items such as, "I'm often amused by the absurdities of life"). There are also two negative styles, "aggressive" and "self-defeating" (as in, "I will often tease people" about their mistakes).

The researchers reported in last month's issue of *Twin Research and Human Genetics* that for positive humor, correlations were far higher in the identical than the fraternal twins, in line with their genetic relatedness. Negative humor, in contrast, showed little genetic influence.

But Brits and Americans diverge a bit in their propensity for nasty jokes. The British study revealed some genetic influence for negative humor, whereas a study of U.S. twins, also headed by Vernon (in press in *Personality and Individual Differences*), found almost none.

Vernon theorizes that the difference reflects a "larger tolerance" for "diverse" types of humor in the U.K. Americans "might be less likely to enjoy" negative humor, he says. The contrasting results, says psychologist Nancy Segal of California State University, Fullerton, make for "a fascinating intermixing of biology and culture."

EDITED BY YUDHIJIT BHATTACHARJEE

CELEBRITIES

WAITING FOR BILL. Inside a packed room in Washington, D.C., last week, members of the House Science and Technology Committee begged Bill Gates, retiring Microsoft chair and billionaire philanthropist, to tell them how to get more U.S. students interested in science and engineering. "What's our next Sputnik moment?" asked Representative Gabrielle Giffords (D–AZ), whose husband, Mark Kelly, is an astronaut.

Gates, who called for more spending on research and education, himself may be part of the answer. His presence last week at the committee's 50th anniversary hearing generated enough buzz that the queue for the 10:00 a.m. hearing began forming shortly after sunrise. There was a preponderance of 20-somethings in one. "I just thought it would be neat to hear him," said Sean Connolly, a University of Mississippi student visiting Washington, D.C.

AWARDS

IN ABSENTIA. A decade ago, Middle East politics derailed plans to honor Israeli physicist Daniel Amit of Hebrew University in Jerusalem for fostering scientific cooperation in the region. This month, the European group that administers the Rammal Award chose to give it to Amit—4 months after he committed suicide in his Jerusalem home at the age of 69.

The award is named for the late Lebanese physicist Rammal Rammal. In 1998, a jury chose Amit for helping to incorporate physics into neuroscience and for working toward peace in the region. But the French Physical Society, which administered the prize at the time, chose not to give an award that year after some Lebanese scientists protested, arguing that no Israeli should receive the prize until there was peace between Israel and Lebanon (*Science*, 5 March 1999, p. 1422).

Yet Gérard Toulouse, a physicist at the Ecole Normale Supérieure in Paris who established the award in the early 1990s, never abandoned his campaign to honor Amit. And this year, Euroscience, the organization that now administers the award, chose to honor Amit posthumously.

Toulouse, who is still mourning his friend's death, says the prize gives him a "huge sense of relief" as well as a deep feeling of regret. Honoring Amit in 1998 would have made him "a grand symbolic figure," he says. "That might have changed Amit's fate."

INTEL SCHOLARS. Shivani Sud has won the top, $100,000 prize in the Intel Science Talent Search for finding a genomic signature that predicts colon cancer relapse and identifying drugs that could help prevent it. A senior at Charles E. Jordan High School in Durham, North Carolina, Sud worked with Duke University oncologist Anil Potti. "There were days she would bring her homework to the lab and stay till 2 in the morning," Potti says.

In the News >>

LAST-MINUTE SWITCH. A violation of training rules has cost a South Korean researcher his chance to become the country's first space hero.

Last September, the South Korean government announced that Ko San, 30, a researcher at the Samsung Advanced Institute of Technology, would fly to the international space station next month aboard the Russian spacecraft Soyuz (*Science*, 21 September 2007, p. 1659). But during his training, Ko violated mission protocols by taking home a training manual and later borrowing a space flight manual he was not authorized to examine.

For these infractions, South Korean officials last week decided to give his seat to his backup, Yi So-yeon (right), who last month received a Ph.D. in bioengineering at the Korea Advanced Institute of Science and Technology in Daejeon. Yi, 29, will become the 50th woman, and first Korean, to fly in space.

Three Q's

Michael Heller, a Polish cosmologist and Catholic priest who advocates a convergence of scientific and theological inquiry, has won the $1.6 million Templeton Prize from the John Templeton Foundation. The 72-year-old professor at the Pontifical Academy of Theology in Krakow will use the prize to create an institute named for Copernicus, for research on science, philosophy, and theology.

Q: You talk about a theology of science. Can there be such a thing?

I don't think it exists. But I hope it could be created. If you are investigating the world using the standard scientific method, there are some aspects of the world that are automatically switched off. A theology of science would accept that the limits of rationality do not coincide with the limits of the scientific method, allowing for questions such as the ultimate cause of the universe.

Q: You say science is the discovery of the mind of God. Can a complete scientific understanding of the universe supplant the idea of God?

I don't think so. I believe God is immanent, and so every law of physics is a manifestation of God. But God is also transcendent and extends beyond the universe. I don't think one day we could solve an equation that will prove that God exists.

Q: You suggest that God may be too complex for humans to understand. Why should that be?

Our brains evolved over millions of years through our interaction with the environment. Evolution required us to develop certain mental faculties to survive. We are fortunate that we somehow developed the surplus brainpower to understand things like quantum mechanics, but I doubt whether that is sufficient to comprehend the full nature of reality.

CREDITS: (TOP TO BOTTOM) LANDOV; NANCY BECHTOL; TEMPLETON FOUNDATION

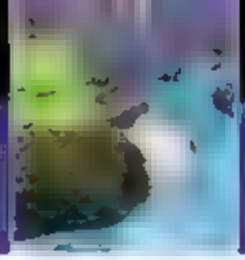

1604

1605

DNA DATA

Proposal to 'Wikify' GenBank Meets Stiff Resistance

When Thomas Bruns turns to GenBank, the U.S. public archive of sequence data, to identify a fungus based on its DNA sequence, he does so with some trepidation. As many as 20% of his queries return incorrect or incomplete information, says Bruns, a mycologist at the University of California, Berkeley. In a letter on page 1615, Bruns, Martin Bidartondo of Imperial College London, and 250 colleagues who work on fungi urge GenBank to allow researchers who discover inaccuracies in the database to append corrections. GenBank, however, says such a fix would cause more problems than it solves.

The letter comes from a relatively small research community concerned primarily with making sure that the species from which a sequence came is correctly identified. But "the problem extends far beyond fungi, to much bigger—and [more] recognizable—creatures," says James Hanken, director of the Museum of Comparative Zoology at Harvard University. Other sorts of errors—such as inaccurate information on a gene's structure or on what its proteins do—also plague the database.

Incorrect data are more than just an inconvenience. Analyses of new data depend in a large part on comparisons with what's already in GenBank—be it right or wrong. Computers predict gene function, for example, based in part on similarities with known genes. And

Up and up. Critics fear that GenBank's rapid growth is leading to error propagation.

Bruns and others ferret out species' identities—often of organisms otherwise indistinguishable—by looking for matches to named GenBank entries. Under the current setup, "error propagation is all too likely," says Thomas Kuyper, a mycologist at Wageningen University in the Netherlands.

What the mycologists are asking for is a scheme like those used in herbaria and museums, where specimens often have multiple annotations listing original and new entries side by side. It would be a community operation, like Wikipedia, in which the users themselves update and add information, but not anonymously.

GenBank's managers are dead set against letting users into GenBank's files, however. They say there already are procedures to deal with errors in the database, and researchers themselves have created secondary databases that improve on what GenBank has to offer. "That we would wholesale start changing people's records goes against our idea of an archive," says David Lipman, director of the National Center for Biotechnology Information (NCBI), GenBank's home in Bethesda, Maryland. "It would be chaos."

The standoff over the quality of GenBank's data is in part a product of the database's success—and the issues are only going to get more intense. Researchers have been contributing genes, gene fragments, even whole genomes to GenBank since 1982, making it an incredibly valuable resource for many thousands of investigators worldwide. Today GenBank provides 194 + publicly accessible gigabases—a number that will double in 18 months, thanks in part to cheaper, faster sequencing technologies and a rise in "environmental" sequencing: mass sequencing of all the DNA in soil, skin, or other samples.

From early on, researchers recognized that errors would be inevitable (*Science*, 15 October 1999, p. 447), and although GenBank runs some quality-control checks on incoming sequences, it cannot catch many mistakes. GenBank has just one mycologist on staff, for example, but 150,000 fungal sequences were deposited this past year. "That's not something that a single person can curate," says Lipman.

GenBank's creators consider the database a "library" of sequence records that, like books or journal articles, belong to the authors and therefore can be changed only by the submitters of that data. A note indicates when a record has been updated and points to the archived original. Stephen O'Brien, who does comparative genomics at the National Cancer Institute in Frederick, Maryland, argues that author privilege is necessary. "One of the reasons GenBank is so doggone useful and comprehensive is that nobody edits or micromanages it except the authors," he says. "This makes for downstream errors but almost universal buy-in."

Lipman says authors do take the time to make corrections. GenBank gets about 30 such messages a day, he points out. But others disagree, citing case after case in which problems were not fixed. Often the submitters have moved on to other projects and never get around to making the changes, says Steven Salzberg, a bioinformaticist at the University of Maryland, College Park. And, he adds, the big sequencing centers—which churn out genome after genome with preliminary annotation—are the worst offenders. "They won't let anybody touch their GenBank sequences, and they won't change it, for whatever reason."

Lipman points out that other researchers improve on GenBank's data in a variety ▶

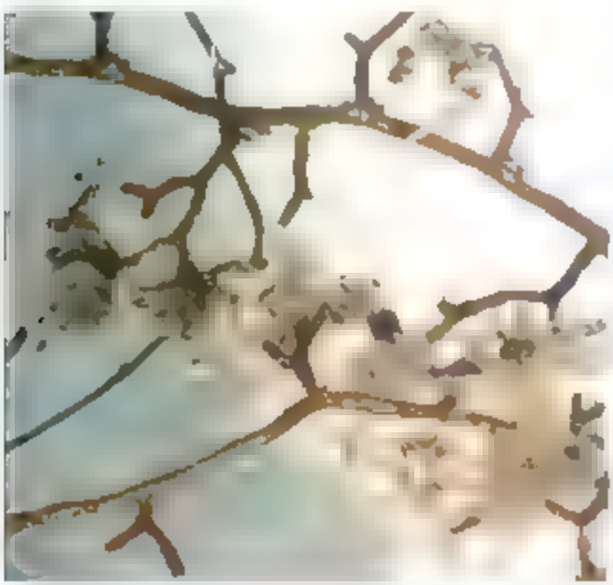

Tangled mess. The fungal threads (white fluff) on these pine roots require GenBank comparisons to identify.

TOP: GENBANK; BOTTOM: THOMAS BRUNS

of ways. NCBI, for example, curates genes along with other interesting DNA and RNA sequences, and puts them in a database called RefSeq that is updated as new information about these sequences comes along. And researchers focused on particular groups of organisms have set up their own secondary databases, such as FlyBase for the fruit fly genomes and TAIR for *Arabidopsis* that offer cleaned-up GenBank data, along with other genomic information and tools for analyzing them. And, Lipman notes, NCBI even offers a way for researchers to do third-party annotation. But it's not the third-party annotation scheme the mycologists want.

For starters, GenBank has set a high bar for accepting changes. Entries must be backed by a publication. Annotations concerning a gene's function, for example, require published experimental data about that gene's protein or a related one. This discourages legitimate improvements, says Carol Bult, a geneticist at the Jackson Laboratory in Bar Harbor, Maine, because often a proposed correction doesn't justify an entire publication. Furthermore, an indication that additional annotation exists is deeply buried in the original sequence record.

Although he's adamant that NCBI is not going to "wikify" GenBank, Lipman says he's eager to work with mycologists to come up with a solution, possibly through RefSeq. Salzberg thinks NCBI will eventually come up with a way to maintain GenBank as an archive while allowing greater community involvement in annotation. "I think it will be solved eventually," he says. "But it's not clear how it will be solved."

–ELIZABETH PENNISI

ANTHROPOLOGY

Millennium Ancestor Gets Its Walking Papers

Ever since its discovery in 2000, the 6-million-year-old fossil known as the Millennium Ancestor has been in a sort of scientific purgatory, with researchers disagreeing about its identity as one of the earliest ancestors of humans or other apes. Now, an independent team's analysis of this primate's thighbones on page 1662 concludes that its species, *Orrorin tugenensis*, was indeed an early ancestor of humans. But it challenges a controversial proposal that *Orrorin* gave rise to our genus, *Homo*, directly.

The new study confirms that *Orrorin* walked upright—a defining characteristic of being a hominin, the primate group that includes humans and our ancestors but not other apes. "The data provide really strong confirming evidence that it was bipedal about 6 million years ago, which reinforces its status as a hominin," says author Brian Richmond, a paleoanthropologist at George Washington University in Washington, DC.

Richmond got permission to measure *O. tugenensis* in 2003, 3 years after the fossils were discovered in the Tugen Hills of Kenya by Martin Pickford of the College de France and Brigitte Senut of the Museum National d'Histoire Naturelle in Paris and their co-workers. The pair proposed that it was a hominid based on features in the teeth and the upper thighbone, or femur. But that bone is incomplete, and many researchers had reservations about Pickford and Senut's analysis (*Science*, 24 September 2004, p. 1885) and about controversy surrounding the pair's permits to work in the Tugen Hills.

Walking the walk. A new study says the primate *Orrorin* really did walk upright in Kenya 6 million years ago.

CREDITS: (ARTWORK AND COMPOSITE) JOHN GURCHE (PHOTOGRAPH) BRIAN RICHMOND

(*Science*, 13 April 2001, p. 198).

Richmond took eight measurements of the femur, which has been stored in a bank vault in Nairobi, using calipers while a burly bodyguard watched. He plugged these measurements into standard statistical analyses that calculated the size and shape of the bone and compared them with those from about 300 thighbones from great apes and fossil and modern humans.

The analysis suggests that *Orrorin* is most closely related to australopithecines, a diverse group of hominids that arose about 4 million years ago in Africa. That's in contrast to Pickford and Senut's proposal that it was a direct ancestor of our genus, which would have pushed australopithecines off the line to modern humans. "Frankly, I was surprised to see how similar it was to australopithecines, since it was twice as old," says Richmond. The new analysis "goes a long way toward resolving the mystery of *Orrorin*," says paleoanthropologist Henry McHenry of the University of California, Davis. "Few of us agreed that *Orrorin* gave rise to *Homo* [directly]. … This study helps lay that hypothesis to rest."

Richmond's analysis shows that the femur was adapted for upright walking, and he proposes that this set of adaptations persisted from *Orrorin*'s time with only minor changes through all the australopithecines, until early *Homo* evolved a new hip and thigh configuration. "The overall mechanics of walking appear to be pretty darn similar from 6 million years to 2 million years ago," says William Jungers of Stony Brook University in New York. ▶

Richmond's former thesis adviser.

Pickford and Senut say they are glad to see confirmation of their proposal that *Orrorin* walked upright. But they still argue that other features not included in Richmond's analysis, such as the tilt of the bony head of the femur and a bump called the lesser trochanter, link it more closely to *Homo* than australopithecines.

Many researchers say the new analysis is the "most convincing evidence" so far that *Orrorin* walked upright, but they are more skeptical that early hominins had a single type of upright walking. "The situation was much more complex," says anatomist Christopher Ruff of Johns Hopkins University in Baltimore, Maryland. To resolve this debate, says anatomist Owen Lovejoy of Kent State University in Ohio, researchers should also look at the pelvis, back, foot, and ankle of other early hominins, still under analysis.

–ANN GIBBONS

PEER REVIEW

Pfizer Denied Access to Journals' Files

A federal judge in Chicago last week denied a company's efforts to obtain confidential peer-review documents about arthritis drugs it manufactured. The company, Pfizer, sued for files from three major medical journals. It lost against two in Illinois and is waiting for a decision in Massachusetts on the third.

Pfizer's actions stem from a lawsuit in which the company was sued by patients who took the drugs Bextra and Celebrex, which have been linked to serious side effects. In January, Pfizer filed a motion in Massachusetts to force the *New England Journal of Medicine* (*NEJM*) to comply with subpoenas for peer-review documents from 11 studies the journal had published on the drugs. Pfizer also sued in Illinois to get peer reviews from the *Journal of the American Medical Association* (*JAMA*) and the *Archives of Internal Medicine*, which together had also published 11 studies on the drugs. Pfizer said data from accepted and rejected studies could be useful for its defense.

Gatekeeper. *JAMA* Editor-in-Chief Catherine DeAngelis convinced a U.S. judge that peer review must remain confidential.

Attorneys for the three journals argued that releasing confidential reviews would compromise the anonymity of peer review. [The outgoing editor-in-chief of *Science*, Donald Kennedy, filed an affidavit supporting *NEJM*'s position (*Science*, 22 February, p. 1009).] In an affidavit, *JAMA* Editor-in-Chief Catherine DeAngelis argued that if the courts routinely allowed such subpoenas, it could result in a "severe decline" in the number of peer reviewers and affect the journals' ability to "properly discharge their mission to advance the betterment of public health."

The U.S. court in Chicago agreed with DeAngelis. "Although her statements are quite dramatic, it is not unreasonable to believe that compelling production of peer review documents would compromise the process," wrote Judge Arlander Keys. The court also found that Pfizer had not adequately explained how unpublished information could help it defend itself. Keys's conclusion: "Whatever probative value the subpoenaed documents and information may have is outweighed by the burden and harm" to the journals.

"We're delighted," says DeAngelis. "If you interfere with the process and the confidentiality, you might as well pack it up and go home."

A handful of such cases have come up before, such as a 1994 subpoena of *NEJM* seeking peer-review comments as part of breast-implant litigation. Journals have usually prevailed, but the judge in each case must weigh the arguments anew, notes Debra Parrish, an attorney in Pittsburgh, Pennsylvania, who specializes in science law. The *JAMA* decision "is important," she says.

The *NEJM* case appears to be winding down as well. At a hearing last week, Pfizer narrowed its request to the peer-review comments returned to authors, according to *NEJM*'s Boston attorney, Paul Shaw. He expects a decision within days.

–JOCELYN KAISER

Budget Blueprint Boosts Science

They aren't binding, but the 2009 budget resolutions passed last week by each house of Congress would provide sizable increases for U.S. research agencies. The Senate's version would add $3 billion, or 10.3%, to President George W. Bush's request for a flat budget at the National Institutes of Health (NIH). That amount includes a $2.1 billion boost added during floor debate by the chair and ranking member of the spending panel that sets NIH's budget. "We still have a long way to go on this, but they're positive signs of support," says Dave Moore of the Association of American Medical Colleges in Washington, D.C. The House version added no additional funding for NIH. Both House and Senate budget resolutions endorsed the president's request for big hikes at the National Science Foundation and the Department of Energy's Office of Science. But getting the additional money will be difficult, because the White House has said Bush would veto any bill that exceeds his request. –JOCELYN KAISER

Paging Dr. Planck

Germany's famed Max Planck Society will for the first time lend its name to doctoral degrees. In an agreement announced last week, the society and Johannes Gutenberg University in Mainz will form a cooperation that oversees the granting of degrees for students at the International Max Planck Research School for Polymer Materials in Mainz. This arrangement breaks with tradition in Germany, where only universities are allowed to grant doctorate degrees, the 4000 students who work at Max Planck Institutes have had to receive their degrees from cooperating schools. In Mainz, a new Max Planck Graduate Center will select students, set degree requirements, and allow Max Planck researchers to join dissertation panels. Officials hope the arrangement will be a model for other Max Planck Research Schools.

–GRETCHEN VOGEL

Taxonomy Sinking Down Under

Australia's taxonomists are going extinct, says a report released this week by the Federation of Australian Scientific and Technological Societies. For every taxonomist joining the 150-person workforce in universities, museums, and herbaria, four are leaving the profession, and many aren't being replaced, according to the report, which urges the government to fund new positions. Andrew Austin, director of Adelaide University's Australian Centre for Evolutionary Biology and Biodiversity, says the trend is bad news for conservation, biosecurity, and agriculture. –CHERYL JONES

CREDIT: MYRANDA ZABLENDO VARGAS

Smog. EPA tightened its health standard but less than its science advisers urged

AIR QUALITY STANDARDS

EPA Adjusts a Smog Standard to White House Preference

In December 2005, Stephen Johnson dunked himself in hot water. Johnson, the administrator of the U.S. Environmental Protection Agency (EPA), decided to discard advice from a scientific advisory committee when he set a major air-quality standard for soot. Scientists and environmental groups were outraged (*Science*, 6 January 2006, p. 27). Last week, Johnson did it again with ozone, the main component of smog. And this time, the hand of the White House was plain to see. The Administration is "flouting the law" by not protecting public health adequately, says epidemiologist Lynn Goldman of Johns Hopkins University Bloomberg School of Public Health in Baltimore, Maryland, who was assistant administrator for the EPA's Office of Prevention, Pesticides, and Toxic Substances during the Clinton Administration. "It's tragic."

The Clean Air Act requires EPA to review the standards for six major pollutants, including soot, also known as particulate matter, and ozone, every 5 years. The agency last did this for ozone in 1997, so the American Lung Association (ALA) and other groups sued and won a deadline of 12 March for the agency to issue a new standard. These standards influence the regulation of power plants, vehicles, and other sources of the chemicals that react with sunlight to become ozone.

The lobbying leading up to the decision was heavy. Industry groups told Johnson to leave the primary ozone standard, which is designed to protect public health with a margin of safety for sensitive groups such as asthmatics and children, at 80 parts per billion (ppb). ALA and other groups, including EPA's Children's Health Protection Advisory Committee, pushed for a standard of 60 ppb. And EPA's Clean Air Scientific Advisory Committee (CASAC) unanimously recommended that the standard not exceed 70 ppb, citing "overwhelming scientific evidence."

On 12 March, Johnson announced that he had "carefully considered" the scientific advice but was tightening the primary standard to just 75 ppb. "I followed my obligations, [I] adhered to the law, [and] I adhered to the science," he said during a telephone press conference. After comparing models of exposure and analysis of uncertainty by EPA staff scientists, Johnson notes in the final rule that "there is not an appreciable difference, from a public health perspective," between 70 and 75 ppb. Public health advocates disagree, citing an analysis in which EPA concluded that 70 ppb would mean 780 fewer deaths a year, 280 fewer heart attacks, and 720 fewer visits to emergency rooms for asthma attacks.

Johnson veered from his scientific advisers again when he tightened the secondary standard. This standard is intended to protect "human welfare," a broadly defined phrase in the Clean Air Act that includes effects on soil, vegetation, visibility, and property. The secondary and primary standard for ozone have been measured in the same way—a daily 8-hour average—and set at the same levels, but CASAC recommended that EPA change the

BIOMEDICAL PATENTS

Wisconsin Stem Cell Patents Upheld

Scientists are still grumbling about the Wisconsin Alumni Research Foundation's grip on stem cell patents—a hold strengthened by rulings this and last month affirming WARF's patents on primate and human embryonic stem (ES) cells. But there is a widespread feeling that challenges to WARF's patents and continuing public pressure have had a desirable effect. "I think [WARF has] been moving toward what I would consider to be a more reasonable policy" with regard to giving scientists access to the cells, says bioethicist LeRoy Walters of Georgetown University in Washington, D.C.

WARF, affiliated with the University of Wisconsin, Madison, holds three patents arising from work done in the 1990s by Wisconsin researcher James Thomson. On 25 February, the U.S. Patent and Trademark Office (PTO) upheld a 2006 patent that describes a method for cultivating pluripotent cells. Then on 10 March, it upheld patents, granted in 1998 and 2001, on nonhuman primate and human ES cells, which apply to all such cells regardless of how they are derived.

Two citizens' groups first challenged WARF's patents in October 2006, claiming that the method for deriving the cells was "obvious" and could have been successfully applied by anyone equipped with the necessary resources. Last April, PTO agreed to reexamine them (*Science*, 13 April 2007, p. 182). In its final decision, PTO rejected the challengers' arguments, saying that "[I]n view of the unpredictability" associated with both the isolation and long-term sustainability of primate ES cells, "the present claims are not obvious. . ."

WARF Managing Director Carl Gulbrandsen, who had predicted a "tough fight," proclaimed WARF to be "heartened that . . . the patent office reached the correct conclusion."

During the course of the patent examination, WARF eased up on proprietary claims. It no longer demands licensing fees from companies that do university-based research with its cells, and it narrowed its claims to apply only to ES cells derived from fertilized embryos and not pluripotent cells from other sources, such as clones or the newly developed induced pluripotent stem (iPS) cells.

CREDIT: JON HICKS/CORBIS

method of measurement to better protect trees, crops, and other vegetation from the cumulative damage of exposure to ozone throughout the growing season. In EPA's preliminary rule, released for public comment last year, the agency agreed, although it preferred a standard of 21 parts-per-million hours (hourly concentrations summed over 3 consecutive months) rather than the 15 ppm-hours that CASAC recommended.

Less than a week before the final rule was due, EPA received a memo from the White House, which is now part of the public record, of the regulation. Susan Dudley, who heads regulatory affairs at the White House's Office of Management and Budget, objected to changing the method of measurement for the secondary standard. She argued that EPA had focused exclusively on vegetation and ignored other impacts, such as those on "economic values." EPA apparently interpreted this as Dudley asking EPA to consider the economic costs of changing the standard, which by law it cannot do. In a memo the next day, EPA Deputy Administrator Marcus Peacock defended the agency's position.

Exposed. Critics say EPA's standard won't adequately protect plants, such as this maple, from ozone.

Shortly before the press conference announcing the final ruling, however, EPA received another memo from Dudley saying that President George W. Bush had sided with her. This memo had not yet been placed in the public docket by press time, but *Science* obtained a copy from a public advocacy group in Washington, D.C. EPA officials postponed the press conference for 5 hours while they rewrote the rule, keeping the measurement method and level of the secondary standard equivalent to the new primary standard. CASAC member Richard Poirot of the Vermont Department of Environmental Conservation's Air Pollution Control Division in Waterbury suggests that "the White House was concerned about the dangerous precedent of having any environmentally focused secondary standard at all."

During the press conference, Johnson also announced that he plans to ask Congress to amend the Clean Air Act. Among the changes he sketched briefly, Johnson would like EPA to be able to consider costs and feasibility of implementation when it sets air standards. In a statement, ALA called those ideas "completely unacceptable." It's unlikely that the Democrat-controlled Congress would make such changes. Meanwhile, Henry Waxman (D-CA), chair of the House Oversight and Government Reform Committee, plans to hold a hearing on the ozone standard on 10 April. I expect more hot water.

–ERIK STOKSTAD

These actions mean that despite the PTO ruling, "we think we've already won a major victory with these patent challenges," says John Simpson of the Foundation for Taxpayer and Consumer Rights in Santa Monica, California, the "requestor" in the dispute.

Nonetheless, the groups plan to appeal the decision on the one patent that can be appealed under PTO rules. "Frankly, I don't trust them to behave well unless we keep up the pressure," says stem cell researcher Jeanne Loring of the Scripps Research Institute in San Diego, California, who supports the patent challenge.

Harvard University stem cell researcher Chad Cowan agrees with others that the case has "caused WARF to finally wake up to the fact that they needed to be a lot more engaging with academic scientists." But Cowan still thinks the patents are a drag on the field. The recent early successes with iPS cells, which can be grown without the use of eggs or embryos (*Science*, 1 February, p. 560), will only intensify the interest in T S research, he says. ES cells are still needed to validate iPS cells, and even if iPS cells prove viable substitutes for ES cells in research, some scientists believe they will never be suitable for cell therapy.

Alan Trounson, president of the California Institute for Regenerative Medicine in San Francisco, says his biggest concern is down the road, because "the patents could delay developments" of therapies with ES cells. He says it would be bad for everyone if a biotech company got a monopoly on certain therapies.

Meanwhile, as iPS patent applications flood into PTO, future patent issues will no doubt become even more complicated.

–[illegible]

CREDIT: ROBERT L. ANDERSON, USDA FOREST SERVICE, BUGWOOD.ORG

EPA Panels Under Scrutiny

A congressional oversight committee is investigating how the U.S. Environmental Protection Agency (EPA) manages potential conflicts of interest among scientists who review its health assessments.

The inquiry stems from the August 2007 dismissal of Deborah Rice, a toxicologist with the state of Maine, as chair of a panel reviewing an EPA health assessment of decabromodiphenyl ether, a flame retardant used in computers, upholstery, and other products. The American Chemistry Council, an industry group, had complained of an "appearance of a lack of impartiality" because Rice had testified to Maine lawmakers in February 2007 that they should restrict use of the chemical, which has been found in breast milk. The agency removed her comments and plans to release the assessment 28 March. Last week, the House Energy and Commerce Committee asked EPA for documents relating to Rice's dismissal. In a statement, Representative Bart Stupak (D-MI), who chairs the oversight subcommittee, said the matter "raises serious concerns about EPA's scientific integrity."

Democrats also worry about direct corporate influence in the agency's review panels. The committee asked EPA for records on nine scientists on current or past review panels who either work for companies or have received money from them.

–ERIK STOKSTAD

New Ag Fund

In a country famous for having more sheep than people, New Zealand's agricultural researchers are celebrating an unprecedented budget boost. Last week, the country's prime minister promised to create an $875 million fund for agricultural research that would grow to $2.5 billion by 2023, paying for science with the interest from the fund, which could double ag research's $100 million annual budget.

The government has not decided how to divide the new pie, which will be the focus of heated debate. Industry researchers note that fish and farm products are the country's major exports, but some scientists argue that New Zealand should start weaning itself off farm exports. "Converting most of our forest into greenhouse gas has given us an abundance of grass and a thriving dairy industry," says physicist Paul Callaghan of the MacDiarmid Institute for Advanced Materials and Nanotechnology in Wellington, but climate change and higher energy costs darken that sector's economic outlook. "Until we expand our high-technology businesses, we will continue to drift down the [international] rankings of prosperity."

–JOHN BOHANNON

ECOLOGY

Showdown Looms Over a Biological Treasure Trove

BEIJING—Can rubber plantations and tropical rainforest coexist? How about hydropower dams and a mountain-ringed refuge for golden monkeys, gibbons, and half of the rhododendron species on Earth? In impoverished Yunnan Province in southwestern China, a confrontation is brewing between economic growth and habitat preservation and authorities are sending mixed signals about their intentions.

Conservation got a boost at a conference in Kunming last month and on the sidelines of a major political gathering in Beijing last week, when Yunnan Governor Qin Guangrong unveiled a $986 million, 3-year initiative to protect biodiversity in the province's northwest. But also last month, according to news accounts, work quietly commenced on a controversial series of hydroelectric dams on the Nu River.

The ecological situation may be even more precarious in southern Yunnan's Xishuangbanna region. There, two-thirds of a unique rainforest has been lost over the past 30 years, largely to rubber plantations, two new studies report. Yet last week, Xishuangbanna's top official vowed to expand his region's rubber industry.

To ecologists, the northwest initiative may be the bright spot in an otherwise grim picture. It would protect biodiversity in an 80,000-square-kilometer area fed by three rivers—Nu (Salween), Lancang (Mekong), and Jinsha—that wend through deep gorges, creating a patchwork of ecosystems. The Three Parallel Rivers area amounts to 1% of China's territory but has a third of the country's native species, including three kinds of gibbons found nowhere else in the world. Although the region boasts three national nature reserves, logging on unprotected land is rampant. "The destruction of forest even on the edges of the nature reserves has been going on for a long time," says Sun Wei-Bang, executive director of Kunming Botanical Garden.

Although details are sketchy, the biodiversity initiative plans to expand nature reserves in northwestern Yunnan, reforest degraded land, and fund research on energy and environmental protection. It will also provide unspecified compensation to villagers and businesses affected by natural-resource extraction. The two main industries in northwestern Yunnan are mining and hydropower.

"We must strike a balance between environmental protection and the need for development," Qin told *China Daily* last week. "Restricting development is not a solution."

Some observers speculate that the Yunnan initiative is designed to appease critics of the Nu River hydropower project. In 2003, a consortium led by China Huadian Corp., a holding company that manages several regional utilities, proposed erecting 13 dams on the Nu with a combined capacity of 20,000 megawatts; the current plan is not publicly available. A chief argument of critics is that as reservoirs behind the dams fill up, flooding and landslides would imperil habitats. Tens of thousands of people would be relocated.

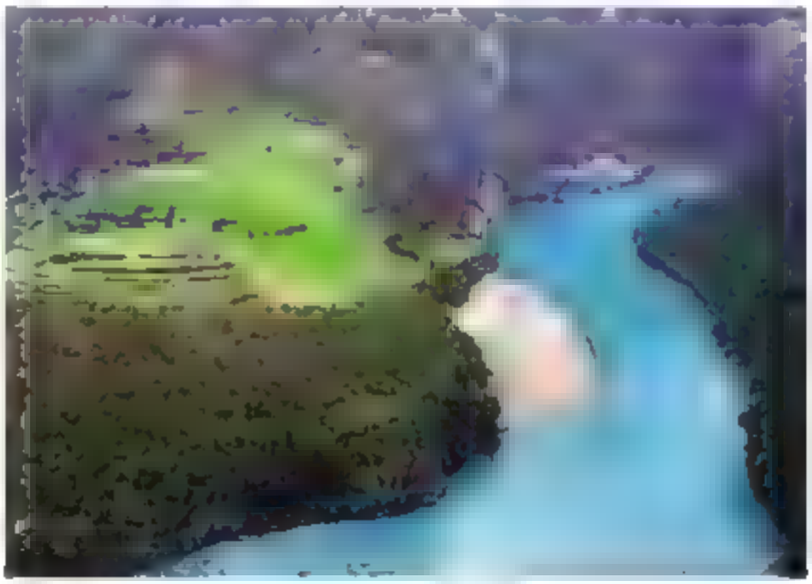

Awaiting its fate. The Nu River, which winds through diverse ecosystems in southern China, is being considered for a massive dam-building program.

Four years ago, in a decree that delighted conservationists, Premier Wen Jiabao suspended the dam project pending an environmental review. The review was carried out by a research arm of China Guodian Corp., another power holding company. But the report is classified as a state secret. It's unclear whether the central government has given a green light to recent resettlement and earthmoving at the site for the planned Luku dam, described in local news accounts last month.

In southern Yunnan, meanwhile, a unique tropical seasonal rainforest is under siege. The Xishuangbanna region—three counties that border Myanmar and Laos—is a few degrees cooler and has less rainfall, on average, than Southeast Asia. A dense fog during the dry season keeps vulnerable dipterocarps and other trees on life support. Tropical seasonal rainforest covered 10.9% of Xishuangbanna in 1976. By 2003, according to satellite imagery, coverage had eroded to 3.6%, representing a loss of nearly 140,000 hectares, ecologist Ma Youxin of Xishuangbanna Tropical Botanical Garden (XTBG) in Kunming and colleagues report in the 20 February issue of *Forest Ecology and Management*. XTBG ecologist Zhu Hua, in an article last week in the debut issue of the online journal *Tropical Conservation Science*, lays the blame squarely on the rubber industry. It's not just a matter of plantations razing acreage. Rubber trees are also invading intact forest. "In Xishuangbanna, the area suitable for rubber to grow is exactly the area that's suitable for tropical forest," says Zhu.

The only way to save the rainforest is to limit new rubber plantations to land now used for other crops, says Ma. "We've recommended to the local government not to allow farmers to convert rainforest to plantations," he says. That may be a hard sell. Last week, the Communist Party secretary of Xishuangbanna, Jiang Pusheng, told *Yunnan Info Daily* that rubber plantations on his turf covered 23.9 million hectares by the end of 2007. "Xishuangbanna will continue to spare no effort to develop its rubber industry," he said. Nevertheless, local authorities have asked XTBG to draft a plan that would help rein in rubber-plantation expansion, Ma says.

Four decades ago, the central government began pushing rubber as a way to help pull Yunnan's ethnic melting pot out of poverty. That strategy has largely backfired, as many plantations are now run by people from outside Yunnan, says Zhu: "Most of the money just leaves the province." An alternative cash crop touted by scientists—teak and other expensive hardwoods—has flopped. "The teak just gets cut down and replaced by rubber," Zhu says.

For a region that prides itself on its biological riches, the losses are mounting.

—RICHARD STONE

With reporting by Hao Xin.

CREDIT: RYAN PYLE/CORBIS

U.S. MATH EDUCATION

Expert Panel Lays Out the Path to Algebra—and Why It Matters

The voyage spanned 2 years, 12 public meetings, and 14,000 e-mails. But Larry Faulkner, a chemist and former president of the University of Texas, Austin, has successfully steered the National Mathematics Advisory Panel through some of the roughest waters in U.S. education. The result, out last week, is a 120-page report on the importance of preparing students for algebra, normally taught in the eighth and ninth grades, and its role as a gateway course for later success in high school, college, and the workplace (*Science*, 7 December 2007, p. 1534).

The report (www.ed.gov/mathpanel) urges educators to keep it simple: Define a few key topics and teach them until students master them. Along the way, it says, students should memorize basic arithmetic facts and spend more time on fractions and their meaning. How teachers achieve those goals is up to them. Faulkner says, advice that allowed the panel to avoid taking sides in a debilitating 2-decade-long debate about the appropriate balance between drilling students on the material and making sure they understand what they are doing.

The 19-member panel was supposed to rely on sound science in its advice to U.S. Secretary of Education Margaret Spellings, but only a relative handful of the 16,000 studies it examined turned out to be useful. The vast majority, says Faulkner, were of insufficient quality, too narrow in scope, or lacked conclusive findings. The literature is especially thin on how to train teachers and how good teachers help students learn.

Spellings has promised to hold a national summit this year on implementing the panel's 45 recommendations. But the primacy of local control over education could make the federal government more of a cheerleader than a participant.

Faulkner, whose day job is president of the Houston Endowment, a Texas philanthropy, spoke with *Science* on 13 March, the day the report was released.

—JEFFREY MERVIS

Q: The report notes that U.S. elementary students do okay on international math tests and that the falloff begins at the end of middle school and accelerates into high school. So why focus on K-8 math?

L.F.: You can also argue that the falloff reflects the inability of students to handle algebra. If you look at success rates in algebra or proficiency in algebraic concepts, there's ample evidence that students are not succeeding, and our charge is to increase the likelihood that they will succeed.

Q: Why do so many students have trouble with fractions?

L.F.: Fractions have been downplayed. There's been a tendency in recent decades to regard fractions to be operationally less important than numbers because you can express everything in decimals or in spreadsheets. But it's important to have an instinctual sense of what a third of a pie is, or what 20% of something is, to understand the ratio of numbers involved and what happens as you manipulate it.

Q: How could schools lose sight of that?

L.F.: Well, they did.

CREDIT: MARSHA MILLER/UT AUSTIN

Q: Was the panel disappointed by the overall quality of the existing research?

L.F.: I think quality is an issue, but that's not all there is. Some of what we examined was topically irrelevant, or the studies were not very generalizable. Some high-quality studies were so narrowly defined that they don't tell you much about what goes on in the classroom.

It may have to do with what the researchers could do with the money available. So we want to be careful about throwing rocks at people. ... We go to great lengths to point out that we think the nation requires a balanced program that includes what I would call smaller scale pilot-oriented research as well as larger scale investigations that are more analogous to clinical trials in medicine. We found a serious lack of studies with adequate scale and design for us to reach conclusions about their applicability for implementation.

Q: Should the government be spending more money on this research?

L.F.: Education research covers a lot of territory, so we don't really know. ... When I briefed the science adviser, Jack Marburger, yesterday, I said maybe his office should be thinking about it. He just nodded. We think this is an item that deserves the attention of the federal government. It probably means bigger grants. If you want to get the value, you probably need to pay for it.

Q: Were you surprised by the dearth of good data on professional development programs?

L.F.: There's tremendous variation in in-service programs. And the evidence is that many are not very effective. ... I think districts should be very careful. Large amounts of money are being spent in this area, and serious questions should be raised.

Q: What's the panel's view on calculators?

L.F.: We feel strongly that they should not get in the way of acquiring automaticity [memorization of basic facts]. But the larger issue is the effectiveness of pedagogical software. At this stage, there's no evidence of substantial benefit or damage, but we wouldn't rule out products that could show a benefit. If a product could be demonstrated to be effective on a sizable scale under various conditions, the panel would be interested.

Q: What message should the next president take from this report?

L.F.: The most important thing is that success in math is not just about a school subject. It's about the real opportunities it creates for people and for the well-being and safety of society. It's important that we succeed to a better level than we do now.

CREDIT: JOERG BOETHLING/PETER ARNOLD INC

Driven to Extinction

Rinderpest, an animal disease that devastated cattle and other animals—and their human keepers—across Eurasia and Africa for millennia, may join smallpox as the only viral diseases to have been eradicated

For just the second time in history, scientists are on the cusp of declaring that a devastating infectious viral disease has been wiped off the face of the planet. The first was smallpox, officially vanquished in 1979. This time it is rinderpest, an animal disease that has plagued cattle and related animals—and their human keepers—for millennia.

"There is growing confidence that rinderpest has been eradicated," declares Peter Roeder, a veterinarian associated with a global rinderpest-eradication program from its inception in 1993 until he retired last year. A disease once endemic throughout Eurasia and Africa has almost certainly been eradicated save for the Somali pastoral ecosystem that straddles the borders of Kenya, Somalia, and Ethiopia. And the latest field-surveillance results, now being reviewed by experts, suggest the virus is gone from there as well.

If the absence of rinderpest can be confirmed, "it would be a remarkable achievement for the veterinary profession, probably the most significant achievement in its history," says Roeder. "Rinderpest is such a nasty disease, its eradication would be a huge step forward, particularly for the underdeveloped world," seconds Tim Leyland, a vet now with the United Kingdom's Department for International Development.

But nobody is yet declaring victory. An earlier rinderpest-eradication effort was ended prematurely, and the disease came roaring back. This time Roeder would like to see governments take the extra steps necessary to ensure that the disease is gone for good.

A natural calamity

Rinderpest can be devastating. The rinderpest paramyxovirus is one of a family of single-stranded RNA viruses. (The family includes the viruses causing canine distemper and human measles.) It attacks the lymph nodes and the epithelium of the alimentary, respiratory, and urogenital tracts and spreads through the infected droplets of the breath and excretions of a sick animal.

Symptoms start with a fever often missed by herders and vets. Days later, animals stop feeding but become thirsty and restless and labor to breathe. Oozing sores appear in the mouths, nasal passages, and urogenital tracts. Diarrhea sets in, followed by dehydration and wasting and then death 6 to 12 days after symptoms appear. Like human measles, it is a disease primarily of the young; animals that survive an infection are immune for life.

Rinderpest epidemics have washed across Eurasia since antiquity, typically killing 30% of affected herds. Its catastrophic

CREDIT: HENRIETTA ROEDER

effect on naive herds and wildlife was horrifically illustrated when cattle shipped from India to feed an Italian army carried the virus to the horn of Africa in 1889. By 1897, the virus had reached Cape Town, South Africa, killing about 90% of the cattle as well as large proportions of domestic sheep and goats in sub-Saharan Africa. Domesticated oxen died, leaving farmers unable to plow fields.

The virus also decimated wild populations of buffalo, giraffe, and wildebeest. With herding, farming, and hunting all but gone, mass starvation set in. An estimated one-third of the population of Ethiopia and two-thirds of the Maasai people of Tanzania died of starvation. The rinderpest epizootic also altered the continent's ecological balance by reducing the number of grazing animals, which had kept grasslands from turning into the thickets that provide breeding grounds for the tsetse fly. Human sleeping sickness mortality surged. The rinderpest epizootic was "the greatest natural calamity ever to befall the African continent, a calamity which has no natural parallel elsewhere," author John Reader wrote in his 1999 book *Africa: A Biography of the Continent*.

The virus never became established in the Americas. In the 1920s, Europe managed to eradicate rinderpest by controlling animal movements and slaughtering infected animals. But periodic outbreaks continued to afflict much of Asia and sub-Saharan Africa. Wars, which create demand for livestock brought in from afar to feed troops, and droughts, which bring herders to scarce sources of water, often triggered rinderpest outbreaks. After rinderpest wreaked havoc with food production in Asia and Africa following World War II, the disease became a priority of the fledgling United Nations' agricultural efforts and then the U.N. Food and Agriculture Organization (FAO), which was created in 1945. A vaccine grown in goats became available in the 1950s. And in the 1960s, a British virologist named Walter Plowright developed a live attenuated vaccine that became widely used in rinderpest-eradication efforts.

Try, try again

There have been almost as many rinderpest-eradication campaigns as rinderpest pandemics. One effort came close to freeing Africa of the virus. With international funding, the Organization of African Unity (OAU) launched Joint Project 15 (JP15) in 1962. Operating in 22 countries, the strategy was to vaccinate all cattle each year for three successive years and thereafter all calves annually. At first, JP15 seemed like a dramatic success. By the mid-1970s, rinderpest had disappeared from many countries, and outbreaks were local and sporadic. But success led to complacency. Many countries terminated or scaled back expensive vaccination and surveillance programs, and in the late 1970s, the disease resurged, fanning out from two lingering foci of infection, an area on the Mali-Mauritania border in west Africa and from southern Sudan in the east.

Vanquishing rinderpest "would be a remarkable achievement for the veterinary profession, probably the most significant achievement in its history."

—PETER ROEDER, GREP

In Asia as well, inadequate vaccination and poor surveillance allowed the virus to spread from several pockets of persistence. By the early 1980s, rinderpest had recolonized a swath of Asia stretching from Turkey to Bangladesh, virtually all of the Middle East, and Africa from Senegal to Somalia and Egypt to Tanzania. Losses from the second African rinderpest pandemic rivaled those of the first a century before. One study estimated 100 million cattle died, the economic loss in Nigeria alone ran to nearly $2 billion. "JP15 showed what you could do with mass vaccination campaigns, but without an endgame, pockets were left and it slipped back" into broad circulation, says William Taylor, a retired veterinary virologist who battled rinderpest in several countries in Africa and Asia. "There was a huge lesson in that," he adds.

OAU decided to try to again with the Pan-African Rinderpest Campaign, which started in 1987 in 34 African nations with the goal of ridding the continent of the virus. Similar regional campaigns were launched in south and west Asia. Yoshihiro Ozawa, then chief of veterinary services for FAO, says that at about that time, it became clear that cattle exported from India and Pakistan were continually reseeding the rinderpest virus on the Arabian Peninsula, indicating "that a global campaign should be organized." To stitch together regional and national efforts and share expertise, FAO initiated the Global Rinderpest Eradication Programme (GREP) in 1993. Roeder, then FAO's chief of veterinary services, helped establish the program and was named secretary of GREP in 2000. The program set the ambitious goal of eradicating rinderpest by 2004, this would be followed by a period of intensive surveillance to confirm that the virus was gone by 2010.

Once again, the program started with mass vaccinations. But to finish the job, "we knew we needed to understand the epidemiological situation," Roeder says. Traditional epidemiological investigations were augmented by new molecular and serological tools unavailable for previous campaigns. Molecular analyses revealed that there were three lineages of rinderpest—two in Africa and one in Asia—and enabled scientists to track outbreak viruses to their source reservoir. Tests to detect antibodies to the virus helped monitor the

effectiveness of vaccination campaigns and—more important for the later stages of the program—look for evidence of the virus when vaccination was stopped.

Remaining reservoirs

Evidence soon pointed to a limited number of endemic rinderpest reservoirs, primarily in the herds of often-isolated communities in Ethiopia, Sudan, Yemen, Pakistan, and India. From time to time, the virus would spread from these reservoirs into normally free areas. Roeder notes that the virus has a complicating quirk. It can persist in a mild form, producing symptoms missed even by experienced vets, but it can quickly turn virulent when introduced into a new herd. As mass vaccination campaigns drove the virus back to these reservoirs, GREP decided to intensify vaccination in those foci of infection while stopping it in peripheral areas. With proper surveillance, unvaccinated animals could be the sentinels warning that the virus was expanding its range again.

Unfortunately, many of those reservoirs were hard to reach. Leyland, who was working for the United Nations Children's Fund (UNICEF) in southern Sudan in the early 1990s, explains that traditional vaccination campaigns relied on town-based vets or internationally staffed mobile veterinary clinics to make periodic forays into the countryside. "U.N. agencies put fortunes into buying Land Rovers and Land Cruisers to have mobile clinics touring around," he says. But this didn't work where governmental vet services had broken down or in areas beyond the end of the road. In addition, herders often didn't want to bring their animals to vaccination posts "because it would put them at risk of being raided," says Christine Jost, a vet from Tufts University's Cummings School of Veterinary Medicine in North Grafton, Massachusetts, who worked with a rinderpest-eradication program in Uganda.

As an alternative, Leyland says the program adapted community-based animal health approaches previously tried in Afghanistan and other places where traditional vet services were weak or had been disrupted. This included training government vets in afflicted countries in techniques to get reliable epidemiological information directly from livestock farmers, says Manzoor Hussain, a veterinary virologist who worked for the Pakistani government and is now a consultant to FAO. At first, both government vets and farmers were dubious, says Hussain, but it turned out to be enormously useful in tracking the disease.

GREP also enlisted the help of other international and government agencies. UNICEF's involvement in rinderpest eradication in Sudan, for instance, was born of necessity. That country's long-running civil war had displaced thousands of families. UNICEF wanted to vaccinate Sudanese children against childhood diseases, but many families refused. At the time, Leyland recalls, herders were losing 80% of their calves to rinderpest. Without cattle, there was no milk for the children, and the herders saw no point in vaccinating starving children. "They said, 'Bring us cattle vaccine first and then we'll let you vaccinate our children,'" Leyland says. Because international agencies would not send their workers into conflict zones, UNICEF workers asked each community to select a trustworthy representative for training in vaccination and other animal health basics.

The program then got a boost from a new vaccine. The effective workhorse vaccine of the 1960s and '70s had one drawback for use in remote areas of Africa: It had to be refrigerated up to the point of use. In 1990, Jeffrey Mariner, a vet at Tufts University School of Veterinary Medicine, developed an improved freeze-drying process that produced a live attenuated vaccine that retained efficacy at 30°C for at least a month. "This simplified the logistics and opened up options" for vaccination, says Mariner, now at the International Livestock Research Institute in Nairobi.

By 1992, several labs in Africa were producing the new vaccine. It proved a perfect fit for the community animal health system, which started vaccinating cattle in conflict-ridden south Sudan in 1993. When international organizations pulled their staffs out of the path of advancing troops, community animal health workers continued to operate. Leyland says some would walk 2 or 3 days to reach an operating supply post in a safe area and then walk back, carrying several thousand doses of vaccine in gunnysacks periodically soaked so evaporation would keep it cool. It was a dangerous job. Several workers were killed when caught crossing the territory of a rival tribe, Leyland says. Still, "it was a hugely successful program" that contributed to eventually squeezing rinderpest out of Sudan, he says.

The Last drop. Tom Olaka, a community animal health worker from Uganda's Karamajong community, was among scores who drove rinderpest toward extinction.

CREDIT: CHRISTINE JOST/ SOURCE: FAO

The endgame

As rinderpest became increasingly scarce, eradication experts progressively scaled back vaccination. "Stopping vaccination

Tool of the trade. For many community animal health workers such as this unidentified Sudanese man, an AK-47 was an essential piece of personal protection equipment.

CREDIT: JEFFREY MARINER

was the hardest thing we achieved," says Taylor, then an adviser to the government of India. Livestock farmers and local vets didn't want to run the risk of losing animals again. But Taylor and his colleagues believed vaccination had to cease to determine whether the virus was truly gone, as antibody tests can't distinguish a vaccinated animal from one that has survived infection. There was also a risk that the attenuated virus used in the vaccine might regain its virulence, sparking a new rinderpest outbreak. This happened at least once in the Amur Region of Russian Siberia in 1998. "This outbreak was thousands of kilometers from the nearest known source of rinderpest virus," Roeder says. Investigators traced the outbreak to a vaccine-derived virus used in a buffer zone along the borders with China and Mongolia.

Sri Lanka and Iran reported their last outbreaks in 1994, India in 1995, Iraq in 1996, Saudi Arabia and Yemen in 1997, and Pakistan in 2000. In Africa, Uganda has apparently been free of rinderpest since 1994, Ethiopia and Djibouti since 1995, Tanzania since 1998, and Sudan since at least 2001. The virus was last detected in 2001 in wild buffaloes in Meru National Park in Kenya, which lies on the edge of the Somali ecosystem, the putative last remaining reservoir. For several years, studies in the region have detected antibodies to the rinderpest virus in cattle, but Roeder suspects that this comes from sampling older cattle still carrying antigens from long-ago vaccinations. The most recent serosurveillance results from late 2007 "strongly support the view that rinderpest is no longer there," Roeder says. At this point, says Roeder, no one is vaccinating against rinderpest, and no one is even making a rinderpest vaccine, although several labs are keeping stockpiles, and production could be rapidly resumed if necessary.

One down, others to go?

With the end of rinderpest in sight, experts are pondering the lessons for other animal health issues. Taylor says that in many ways, rinderpest was "a doable target" because the virus was well-understood, good vaccines existed, and herders, animal health experts, and donors alike agreed on the benefits of a concerted eradication effort.

Other animal diseases that conceivably could be eradicated include foot-and-mouth disease and peste des petits ruminants, a highly virulent disease related to rinderpest that is increasingly affecting sheep and goats in Africa and Asia. Some experts, such as Leyland, note that rather than another eradication campaign, money might be better spent upgrading basic veterinary services in developing countries. "There's a huge amount to do just on ordinary diseases," he says.

> *"Bring us cattle vaccine first and then we'll let you vaccinate our children."*
>
> —TIM LEYLAND ON HERDERS' VIEW OF RINDERPEST IN WAR-TORN SUDAN IN THE EARLY 1990S

Before the animal health community moves on, Roeder says that even though he is retired, he is determined to push countries to confirm that the rinderpest virus is gone. For rinderpest-free accreditation by the Paris-based World Organisation for Animal Health, countries must have stopped vaccinating for at least 2 years and during that time had no outbreaks or evidence of infection, as documented by an adequate surveillance program. Some 30 countries with histories of rinderpest outbreaks scattered across central Asia, the Middle East, and Africa still need to be accredited, he says. If the disease does emerge from some obscure pocket of infection, it would be devastating to the now-naive herds of Africa and Asia.

It's impossible to tease out exactly what had been spent in the fight against rinderpest, but Roeder estimates that since 1986, international donors and participating countries spent approximately $610 million on animal health in Africa and Asia, primarily targeting rinderpest but covering other diseases and infrastructure. One FAO estimate puts the benefits of rinderpest eradication at $1 billion annually in Africa alone. The additional $10 million or $12 million needed for the remaining countries to complete the accreditation process "would be a small price to pay for finalizing the eradication of this devastating disease," he says. With just a final push, rinderpest could officially join smallpox as a disease of the past.

—DENNIS NORMILE

STRUCTURAL BIOLOGY

Protein Structure Initiative: Phase 3 or Phase Out

The production-line approach to finding protein structures is rapidly filling up databases. But is it the data researchers want, and is it worth the cost?

In the early 1990s when structural biologist Andrzej Joachimiak was working in the labs of Paul Sigler and Arthur Horwich at Yale University, he and six colleagues worked together for more than 2 years to solve the x-ray crystal structure of a protein known as GroEL. To obtain such structures, researchers must arrange copies of a protein into the regular pattern of a crystal and then ricochet beams of x-rays off it to map out the position of each of the protein's atoms. At the time, the structure was hailed for offering a host of insights into how GroEL carries out its role as a "chaperone" helping other proteins fold into their proper three-dimensional shapes. But GroEL's large size made it a bear to solve.

Today, as head of the Midwest Center for Structural Genomics, a consortium of investigators at eight institutions in the United States and Canada, Joachimiak and his colleagues churn out some 180 such structures a year, an average of one every 2 days. Not all are as difficult as the GroEL structure, but Joachimiak estimates that recent technological advances would allow them to solve something as complex as GroEL within about 2 months. That, Joachimiak says, "is a true revolution."

Speedster. Andrzej Joachimiak and his colleagues at the Midwest Center for Structural Genomics are pushing the pace for solving protein structures.

But some in the field say the revolution has gone far enough. Joachimiak's center is one of four high-throughput structural biology centers participating in the Protein Structure Initiative (PSI), a big science project funded by the U.S. National Institute of General Medical Sciences (NIGMS), part of the National Institutes of Health (NIH) in Bethesda, Maryland. PSI is doing for protein structures what the Human Genome Project did for sequencing, turning it into a mass-production exercise. Already, PSI's four main centers and six smaller ones have turned out nearly 3000 protein structures and over the past 7 years have contributed about 40% of all the novel structures deposited in the Protein Data Bank (PDB), a global repository for protein structures.

But with PSI now halfway through its second 5-year phase, critics say the cost of the program is too high. This year, NIGMS will spend approximately $80 million on PSI. By the end of phase 2 in July 2010, the total tab will be more than three-quarters of a billion dollars. At a time when NIH funding is flat, many critics argue that the money is better spent on traditional small-scale structural biology projects, ones geared toward solving particular questions about the detailed working of proteins highly relevant to biology and medicine. In December that message was underscored by an external review committee of prominent biologists charged with assessing PSI. Among the report's conclusions: "The large PSI structure-determination centers are not cost-effective in terms of benefit to biomedical research." Structural biologist Gregory Petsko of Brandeis University in Waltham, Massachusetts, echoed the sentiment in an editorial last year in *Genome Biology*, in which he labeled PSI "an idea whose time has gone."

PSI proponents have plenty of counterarguments, and the debate shows no signs of waning. "It's a real hot point in the community," says Janet Smith, a structural biologist at the University of Michigan, Ann Arbor, who led the recent PSI review panel. "It's a fairly contentious topic, and opinion tends to run high," she adds. In the midst of this debate, NIGMS officials will have to decide soon on PSI's fate. The current round of PSI funding is scheduled to run through July 2010. If agency officials want to continue uninterrupted funding for the project, they must send out a request for proposals sometime next year, according to NIGMS Director Jeremy Berg. That means they will likely need to decide by the end of this year whether PSI has a future. At this point, Berg says, funding for PSI 3 "is not a given."

A family affair

Whereas genomics can reveal the sequence of amino acids in a protein, structural biology tells us how that sequence folds up into a particular shape, which is key to a protein's function. These structures have long been seen as a treasure trove of information about life's molecular machines. By revealing structures through x-ray crystallography and nuclear magnetic resonance spectroscopy, structural biologists glean insights into how they operate. In some cases, those insights can discover the likely function of an unknown protein, lead to a deep understanding of how misshaped proteins cause disease, and potentially reveal a path to new drug treatments. For example, resolving the structure of the HIV-1 protease led to the creation of the first protease inhibitors used to fight AIDS.

Structural biologists have traditionally taken a hypothesis-driven approach to their science, asking questions about proteins known to be of interest. PSI, by contrast, chose a novel and somewhat controversial strategy: a "discovery-based" approach primarily targeted at proteins from different structural classes, or "families," throughout

CREDITS: (TOP TO BOTTOM) NEW YORK STRUCTURAL GENOMICS RESEARCH CONSORTIUM; PSI-1 ARGONNE NATIONAL LABORATORY

Twister. The catalytic part of a human phosphatase enzyme.

the protein landscape. Members of each family fold up into similar shapes, often adopting similar functions, such as proteases, kinases, and phosphatases. One major goal of PSI has been to obtain structures of representatives of as many of these families as possible, in particular the large families that have the most members. Proponents argue that each structure could be the key to many more; information on how the sequences fold into proteins should enable computational biologists to create "homology models," detailed simulations of closely related family members for which no physical structure exists, and thereby glean insights into their function (see sidebar, p. 1612).

Success was far from certain. When the project started in July 2000, perhaps the biggest question was whether PSI centers would be able to automate all of the many steps involved in mapping proteins. Unlike genomics, which relies on speeding up one technology—reading the sequence of DNA's nucleotide bases—PSI leaders had to speed up numerous technologies including cloning genes into microbes, expressing and purifying proteins, coaxing them to form crystals, testing their quality, collecting x-ray data, and solving the structure. "Early on, we didn't know whether we were going to be able to build these pipelines," says Ian Wilson, a structural biologist at the Scripps Research Institute in San Diego, California, who heads one of PSI's four large centers, the Joint Center for Structural Genomics in San Diego.

But the recent review panel concluded that PSI's technology development had been "highly successful," with advances dramatically speeding all phases of structure determination. In many cases, the panel's report concludes, PSI has fostered technology that can be adopted by more traditional structural biology efforts. The centers not only developed new technology, they've applied it effectively, too: The large centers now crank out an average of 135 protein structures each per year.

PSI proponents argue that this production-line approach has dropped the cost of solving structures from about $250,000 apiece in 2000 to about $66,000 today. But PSI's success is not just about the bottom line, they argue. It's also revealing a diversity in protein structures never seen before. A 2006 analysis in *Science* by Steven Brenner and John Marc Chandonia of Lawrence Berkeley National Laboratory (20 January 2006, p. 347) in California found that PSI centers account for about half of the novel structures submitted to PDB. These are structures for which their immunoacid sequence overlaps with that of any other proteins by less than 30%. Another study in the *Proceedings of the National Academy of Sciences* last year by Michael Levitt at Stanford University in Palo Alto, California, showed this trend continuing, and that PSI centers reversed an earlier steady decline among structural biologists in the number of novel structures being added to PDB. Wilson and several colleagues argued in an editorial in the January issue of *Structure* that the novelty of the PSI structures is a great benefit to the community because it provides data complementary to traditional structural biology rather than simply answering the same sets of questions.

But researchers are still divided over just how useful all this new information is. "I had reservations from the outset," says Petsko, who says he objected because protein structures are only useful when they can answer specific biochemical questions about the detailed workings of a protein. The recent PSI assessment report echoes this criticism, calling PSI's strategy of focusing primarily on novelty "seriously flawed." One problem, Smith and her co-authors argue, is that the number of new protein families identified by gene-sequencing efforts worldwide continues to grow more rapidly than the number of protein structures being produced. A team of researchers reported last March in *PLoS Biology*, for example, that a random sequencing of DNA from the world's oceans showed that more than half of all the protein families they found had never been seen before, suggesting that researchers are nowhere near completing their survey of the diversity of protein families. That makes the challenge of obtaining representative structures from each family "an open-ended problem," say the authors of the assessment report.

What is more, the assessment panel concluded that although having a protein structure can help computer modelers make models of other members of that protein family, those models almost always have a low resolution and lack detail of the precise location of all the protein's different amino acid residues. Such detail is key to nailing down the exact biochemical workings of a protein and often its specific function. "The ability to model structures, particularly complex ones, is very far from being able to connect most PSI structures to function," the report states. Even if an accurate model can be

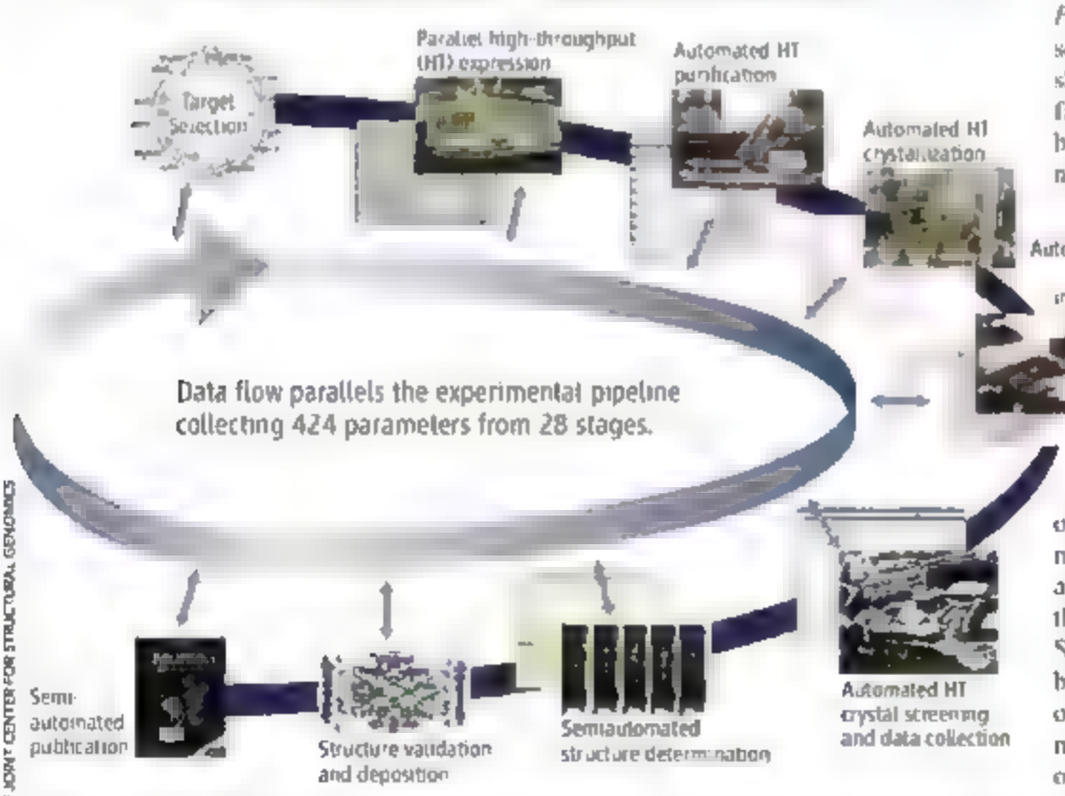

CREDIT: JOINT CENTER FOR STRUCTURAL GENOMICS

Building a bigger pipeline. PSI groups created a series of new technologies to speed up the many steps involved in determining a protein's structure, such as robots to purify and crystallize proteins.

made, using that to discern a protein's function is not a straightforward task. A structure, Smith says, "is a little bit of data" that can be used to discern a protein's function. "But it's not as much as folks had hoped it would be."

On top of these problems, critics say PSI's data are not getting picked up by the broader community of biologists. In part they argue that's because only a relatively small fraction of this broader community knows how to use this type of structural information. The bottom line, Smith says, is that "the number of structures provided [by PSI] is not providing a boon to biology." By contrast, she adds, when the Human Genome Project began to release its data, it was instantly seized upon. "There was no need to ask, 'Was this worthwhile?'"

Function follows form

PSI leaders counter that although it's true that the number of protein families is growing rapidly, most of the newly discovered

Researchers Hone Their Homology Tools

The Protein Structure Initiative (PSI) is churning out new protein structures at a pace never seen before. But even the hundreds of structures the initiative unveils each year don't make much of a dent in the millions of proteins and multiprotein complexes thought to be out there. One hope for PSI, however, is that the proteins it has solved will give researchers insights into the structures and functions of some of those whose shapes are unknown. For such work, computational biologists employ "homology models," which use solved structures as templates for computer models of the three dimensional (3D) shapes of closely related proteins.

Model behavior. Computational biologists use known protein structures to help them model the shape of closely related proteins.

How well do homology models work? Not well enough, according to members of a review panel that issued a mixed report card on PSI in December. Although such models often get the general shape of related proteins correct, they typically lack the atomic scale resolution needed to gain specific insights into how a protein does its job—or even what job it does. "The large numbers of new structures determined by the PSI effort have not led to significant improvements in the accuracy of homology modeling that would allow modeling of more biologically relevant proteins, complexes or conformational states," the report concluded.

But computer modelers say that conclusion misses the mark on several counts. First off, they point out, it was never a stated goal of PSI to improve the accuracy of homology models. "This was a completely new thing," says John Moult, a computational biologist at the University of Maryland Biotechnology Institute in Rockville. Moult says the initial intention was simply to allow computational biologists to apply existing models to a larger number of target proteins. And that, he says, has undoubtedly occurred. Of all the structures submitted to the global Protein Data Bank, PSI now contributes about 40% of all the "novel" protein structures—those significantly different from any solved previously. And according to one recent estimate, those allow for the creation of more than 40,000 homology models that could otherwise not be made.

That said, Moult and others argue that PSI is actually now beginning to contribute to the improvement of homology models themselves. In its second phase, PSI has supported two small centers geared toward improving computer models and has also supported individual computer modeling groups. That bioinformatics support was perhaps "a little slow" in coming, says Andrej Sali, a computational biologist at the University of California, San Francisco. But he and others argue that this support, together with the increased number of structures, has helped spur advances in the basic algorithms to improve the accuracy of models.

Whether due to PSI or not, Moult and others say there's plenty of evidence homology models are improving. For starters, they point to a biennial competition among computational biologists to predict the structure for a series of proteins. The Critical Assessment of Structure Prediction (CASP), which began in 1994, will hold its eighth competition later this year. The first "was embarrassing," says Moult, who heads the CASP competitions. Few of the early models even came close to figuring out the actual structure of their target proteins, which were also simultaneously solved by x-ray crystallography for comparison. But by 2002, 60% of the models got close enough to the final structures to add useful information. By 2006, that number had climbed to 80%. "I don't want to say modeling was improving only because of the PSI," Moult says. But the added structures in the database, he argues, are making a "very significant contribution." Adds David Baker, a computational biologist at the University of Washington, Seattle: "Homology modeling is definitely getting better."

In another key advance, improved computer models are making it easier for x-ray crystallographers to solve their structures. Experimentalists solve these structures by firing powerful beams of x-rays at protein crystals and tracking how those x-rays ricochet off their targets. These data give them much of what they need to nail down the position of all the atoms in the protein. But for a complete 3D picture, researchers typically compare the original data with another set taken from a closely related protein. Combining the two data sets is usually enough to finish the job. Not all proteins have close relatives that have been solved. But in a *Nature* paper last November, Baker's team showed that it was possible to use newer high-resolution homology models as the close relative to help researchers solve the x-ray structures. "It's not an established method yet," Baker says. However, he argues, it shows the synergy that can occur between high-quality experimental data and computational models.

–R.F.S.

CREDIT: NEW YORK STRUCTURAL GENOMIX RESEARCH CONSORTIUM, PSI-1

families have only a few members. The majority of proteins are found in a small number of large families that are the focus of PSI's targeting. Gaetano Montelione, a structural biologist at Rutgers University in Piscataway, New Jersey, argues that as a result of focusing on large families the impact of PSI structures is increasing because each solved structure carries more leverage, or ability to model a greater number of related structures, than those solved along traditional lines. Even with the limitations of current computer models, "the large information leverage provided by determining the first structural representatives from very large sequence families is tremendously enabling to biomedical research," Montelione writes in a February 2008 response to the PSI assessment report. Although homology models may not always reveal a protein's function, Montelione and others argue, in many cases it can offer important clues to guide future biochemical experiments designed to nail down that function.

Many researchers also dispute the claim that many PSI structures lack biological relevance. A fraction of PSI targets are chosen for biological interest. And any of its structures' relevance, as with the value of any basic research, takes time to grow, they argue. "The benefits we will see 2 to 3 years from now will be very great," Wilson says, and will include a growing understanding of how protein families evolved and the evolutionary connections between different families. And as for the dissemination of PSI data, PSI leaders say that a new knowledge base (kb.psi-structuralgenomics.org/KB) that came online earlier this month should improve matters dramatically.

David Baker, a computational biologist at the University of Washington, Seattle, adds that the large number of PSI structures is also making possible an emerging approach to designing new therapeutics. Baker's group uses the full gamut of PDB structures to help them design better protein-based inhibitors to toxins, as well as vaccines for diseases such as HIV. When the group designs their proteins, they start with the shape of the target they are trying to block. Then they conduct a computer scan through all the known protein structures in PDB—including PSI structures—looking for as many proteins shaped to fit into those targets as possible. Then they set their computational program loose to refine those matches and design a novel protein for an optimal fit. And the more close matches they have, the more accurate and effective the designed protein tends to be. As such Baker says, the value of the database will only grow. "These structures are really going to help protein design," Baker says. "I don't think that was anticipated originally."

The messenger. Janet Smith led a recent panel of biologists that criticized PSI for having a limited impact on the broader community of biologists.

A question of value

Smith and others say they readily agree that PSI is producing good science, but they question whether it's worth the cost. "It's how do you get the most bang for your buck," says Philip Cole, a pharmacologist who specializes in signal transduction at the Johns Hopkins School of Medicine in Baltimore, Maryland.

Still, Cole and others worry that even if PSI isn't funded for a third phase, there's no guarantee that money saved will flow to traditional structural biology groups. That's not how science funding works. "If PSI were to be discontinued, the money would go back to the general pool within NIGMS," Berg says. Structural biology funding, he adds, accounts for about 10% of the NIGMS budget, with traditional single-investigator grants taking up about 6.3%. So doing away with PSI would likely increase the share of funding for individual structural biology grants from about 6.3% to perhaps 6.7%, Berg says. What is more, structural biologists currently working on PSI would then be competing for those funds. So the net result could wind up being "a pretty big negative" for the community, Berg says.

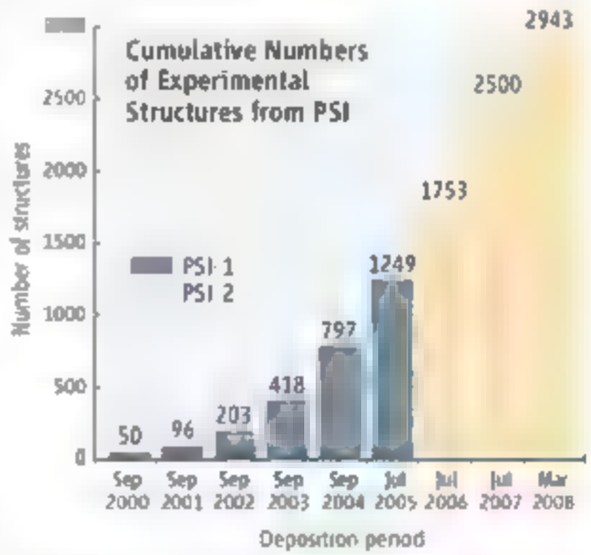

Off the charts. PSI centers are determining structures at a pace never seen before. But critics doubt that the impact has kept pace.

So what's next? Berg says NIGMS is currently evaluating all of its large-scale projects to decide which ones to continue. The PSI assessment panel argued against continuing the project in its present form. Future effort might be focused on smaller projects with much higher experimental coupling to biological function and improving computational methods of analyzing and predicting protein structure," the report concluded. In his response to the report, Montelione agreed that connecting more directly with the priorities of biologists "needs to be a priority" in designing PSI 3.

Others agree that perhaps the best solution is to focus more tightly on protein targets with known biological relevance, such as multiprotein complexes, proteins that are embedded in cell membranes, and proteins from disease-causing microbes. "This can evolve," says Joel Sussman, a structural biologist at the Weizmann Institute of Science in Rehovot, Israel. "Now you can use these enormous platforms [built in the PSI centers] to tackle biological problems." Whether the broader biological community can agree on such a compromise will largely depend on whether NIGMS sees budget increases anytime soon. Says Wilson: "When the money gets tight, the knives come out."

–ROBERT F. SERVICE

CREDITS: (TOP TO BOTTOM) LIFESCIENCES INSTITUTE, THE UNIVERSITY OF MICHIGAN; (SOURCE) PSI

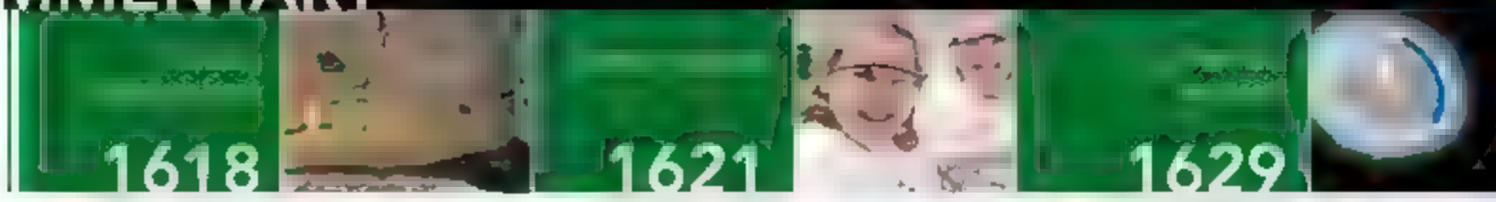

LETTERS

edited by Jennifer Sills

Open Letter to Senator Rita Levi-Montalcini

CREDIT: ANDREW MEDICHINI/AP PHOTO

WE ARE A GROUP OF RESEARCHERS (1). WE WRITE THIS LETTER TO YOU WITH THE UTMOST respect and gratitude for what you have done and still do for research in Italy. We appreciated all the statements of intent of the past governments as well as the current one: more money for research, transparent competitions, and the like. But all this never went beyond mere words.

Professor, in Italy there are 60,000 university researchers with temporary contracts.[1] This is no "marginal phenomenon"—we make up 50% of the university labor force.

Unfortunately, the situation is no better in research agencies. We do research work, lecture, supervise students writing graduation theses, publish articles, attend congresses, and draw up appeals for funds (in which our names do not even appear).

Researchers protest in Rome, 2005. Almost 100,000 participants protested the lack of concrete actions taken by the Senate to improve the conditions of research in Italy and to reduce the use of temporary contracts for researchers.

We work at least as much as long-term employees but we do not have the same rights. In Italy there are only a few open competitions, and, even worse, they often look like farces. The name of the winner is known even before the call for expression of interest is issued.[1] Meritocracy in Italy is an empty word seldom translated into reality. Fast university careers are only for the chosen ones or the descendants of families traditionally connected with the university. Everybody knows that it takes good opportunities to improve one's skills, but opportunities are not for everyone according to their merits. And the situation is even worse for women.

As we strive to defeat cancer, discover new molecules and genes, develop new software, support an ever-changing culture, and identify new ways to teach and learn, remember that achieving these goals is partly due to the work of university researchers with temporary contracts, who have worked for years hoping to finally obtain a job that would give them economic stability and freedom.

University researchers with temporary contracts are not free. They have to make compromises or their contracts won't be renewed; they have to withdraw from open competitions to let a "chosen one" be hired; they have to accept that their data are published without their names among the coauthors. They do all this to survive. We will be a generation of pensioners without a pension. Then, maybe, the state will take care of us. For many years, many people (and governments) forgot all about us. Researchers who are now 30, 40, 45 years old still have temporary contracts and may now be too old for a long-term contract as university researchers. Many among us have had a temporary contract for 10 to 15 years; they have had many different kinds of short-term contracts and their work has been evaluated every year before their contract could be renewed. We wonder what else we have to endure before we are considered suitable for a long-term contract.

Professor, with your usual strength of mind you will certainly be able to pass on the message that the university in Italy can be saved only if this problem is solved.

Thank you in advance for your understanding and support.

RITA CLEMENTI,[2]* LEONARDO BARGIGLI,[2] SILVIA SABBIONI[3]

[2]Via Corridoni 5, 27100 Pavia, Italy. [2]Via della Greve 120, 50018 Scandicci (FI), Italy. [3]Department of Experimental and Diagnostic Medicine, University of Ferrara, Luigi Borsari 46, 44100 Ferrara, Italy.

*To whom correspondence should be addressed. E-mail: rita.clementi@gmail.com

Reference

1. This Letter has been signed by 776 researchers with temporary contracts in Italy or abroad. The complete list is available as Supporting Online Material at www.sciencemag.org/cgi/content/full/319/5868/1615a/DC1.

Response

I AM WELL AWARE OF THE PRECARIOUS SITUation in Italy regarding researchers with temporary employment contracts. During the approval of Italy's 2008 Budget, I supported measures to stabilize employment for those working under temporary contracts. Although the government was not able to invest heavily in this expenditure, the Budget Law did allocate funds to reduce unsteady employment.

I hope the new government will be able to ameliorate this long-standing problem, and I also assure my continued support during the next legislature.

RITA LEVI-MONTALCINI

President, European Brain Research Institute, Via del Fosso di Fiorano 64, 00143 Rome, Italy.

Preserving Accuracy in GenBank

GENBANK, THE PUBLIC REPOSITORY FOR nucleotide and protein sequences, is a critical resource for molecular biology, evolutionary biology, and ecology. While some attention has been drawn to sequence errors (*1*), common annotation errors also reduce the value of this database. In fact, for organisms such as fungi, which are notoriously difficult to identify, up to 20% of DNA sequence records may have erroneous lineage designations in GenBank (*2*). Gene function annotation in protein sequence databases is similarly error-prone (*3*, *4*). Because identity and function of new sequences are often determined by bioinformatic analyses, both types of errors are propagated into new accessions, leading to long-term degradation of the quality of the database.

Currently, primary sequence data are annotated by the authors of those data, and can only be reannotated by the same authors. This is inefficient and unsustainable over the long term as authors eventually leave the field. Although it is possible to link third-party databases to GenBank records, this is a short-term solution that has little guarantee of permanence. Similarly, the current third-party annotation option in GenBank (TPA) complicates rather than solves the problem by creating an identical record with a new annotation, while leaving the original record unflagged and unlinked to the new record.

Since the origin of public zoological and botanical specimen collections, an open system of cumulative annotation has evolved, whereby the original name is retained, but additional opinion is directly appended and used for filing and retrieval. This was needed as new specimens and analyses allowed for reevaluation of older specimens and the original depositors became unavailable. The time has come for the public sequence database to incorporate a community-curated, cumulative annotation process that allows third parties to improve the annotations of sequences when warranted by published peer-reviewed analyses (*5*).

M. I. BIDARTONDO *ET AL.*

Imperial College London and Royal Botanic Gardens, Kew TW9 3DS, UK

References

1. J. D. Harris, *Trends Ecol. Evol.* **18**, 317 (2003).
2. R. H. Nilsson *et al.*, *PLoS ONE* **1**, e59 (2006).
3. W. R. Gilks *et al.*, *Bioinformatics* **18**, 1641 (2002).
4. S. Brenner, *Trends Genet.* **15**, 132 (1999).
5. The names of all 256 authors can be found in the Supporting Online Material (www.sciencemag.org/cgi/content/full/319/5870/1616a/DC1).

TECHNICAL COMMENT ABSTRACTS

COMMENT ON "Physical Model for the Decay and Preservation of Marine Organic Carbon"

Bernard P. Boudreau, Carol Arnosti, Bo Barker Jørgensen, Donald E. Canfield

Rothman and Forney (Reports, 1 June 2007, p. 1325) described a model for the decay of marine organic carbon. However, the enzyme deactivation rates required by their model are too fast compared with available data, and the model fails to explain the similarity in observed decay rate constants from different experiments. Alternative models provide equally good fit to the observed temporal trend in decay rate constants.

Full text at www.sciencemag.org/cgi/content/full/319/5870/1616b

RESPONSE TO COMMENT ON "Physical Model for the Decay and Preservation of Marine Organic Carbon"

Daniel H. Rothman and David C. Forney

Fast enzyme deactivation rates are not required by our physical model of organic matter decay. Instead, low effective diffusivities arising from sorption of enzymes and physical protection by minerals are sufficient. Our model predicts observed temporal trends in organic matter decay rather than specific rate constants. Existing statistical models of intrinsic reactivity explain observed trends empirically but not theoretically.

Full text at www.sciencemag.org/cgi/content/full/319/5870/1616c

Malaria Eradication in India: A Failure?

IN THE 7 DECEMBER 2007 ISSUE, L. ROBERTS and M. Enserink discuss malaria eradication in the News Focus story "Did they really say … eradication?"

In the mid-1950s, I optimistically promoted malaria eradication by promising the Minister of Finance of India that there would be no need to spend money on malaria control in 10 years' time if India matched the USAID grant for malaria eradication. Subsequently, I felt guilty because total eradication had not been achieved. However, comparison of the statements on malaria in the first and 10th 5-year economic plans of India shows the value of investments in malaria eradication.

The first 5-year plan states, "Malaria is the most important public health problem in India and its control should therefore be assigned topmost priority in any national planning. It has been estimated that about a million deaths are caused in India every year by malaria among the 100 million people who suffer from this disease. The economic loss is estimated at several hundred crores (a crore equals 10 million) of rupees every year. Vast fertile areas remain fallow and natural resources remain unexploited, largely due to the ravages of malaria. Aggregation of labor in irrigation, hydroelectric and industrial projects is attended with severe outbreaks of malaria if special steps are not taken for its control. The use of DDT as a residual insecticide has brought about far-reaching changes in the technique of the control of malaria…" (*1*)

Fifty years later, the 10th 5-year plan reports less than a thousand deaths in a population double the size of that in 1950 (*2*). The drop from a million to a thousand deaths underscores the value of the malaria program.

The fact that malaria has been eliminated in the United States and Western Europe and largely controlled in India does not ensure success of eradication programs in Africa. However, there is cause for some optimism, given that the most effective mosquito vector in Africa, *Anopheles gambiae*, has been eradicated in northeast Brazil.

Information from India's 5-year economic plans shows that even if complete eradication cannot be secured, economic gains and reduced suffering may be worth the effort.

TIMOTHY D. BAKER

Department of International Health, and Environmental Health Sciences, Johns Hopkins School of Public Health, Baltimore, MD 21205, USA.

References

1. First 5-Year Plan (Planning Commission, Government of India, New Delhi, 1951), chap. 32, paragraphs 32–33 (http://planningcommission.nic.in/plans/planrel/fiveyr/welcome.html).
2. Tenth 5-Year Plan (Planning Commission, Government of India, New Delhi, 2002), chap. 2.8, p. 104 (http://planningcommission.nic.in/plans/planrel/fiveyr/welcome.html).

PALEONTOLOGY

Rise and Demise of Ghostly Animals

Shuhai Xiao

Between 1908 and 1914, German geologists P. Range and H. Schneiderhohn discovered some enigmatic fossils including *Rangea schneiderhoehni*, later named after them, in southern Namibia. Similar organisms have since been found at more than 30 localities and on most continents. These fossils are collectively known as the Ediacaran biota, after a site in South Australia. The geological age of the Ediacaran fossils is now well established as 575–542 million years ago, an interval immediately before the Cambrian radiation of animals. However, the evolutionary relationship between Ediacaran taxa and Cambrian animals remains ambiguous. Thus, the implications of Ediacara fossils for the Cambrian radiation are intensely debated among a small group of paleontologists. Two recent books authored and edited by Mikhail Fedonkin (Russian Academy of Sciences), Patricia Vickers-Rich (Monash University, Australia), and their colleagues offer new insights into the ongoing debates and unveil the Ediacara controversies to a much wider audience.

In *The Rise of Animals*, veteran researchers, some of whom have spent their entire career unraveling Ediacaran puzzles, lead a guided tour of most of the best-known Ediacaran localities. Telling numerous stories about the fossil hunters, they chronicle decades of Ediacaran research in Newfoundland, Namibia, Australia, Russia, and other often remote parts of the world. Along the way, Fedonkin and his fellow authors discuss the preservation, ecology, and phylogenetic affinity of the Ediacaran fossils.

Most Ediacaran fossils are preserved as casts and molds in clastic rocks; sometimes they are only ghostly impressions on the surface of coarse-grained sandstones. The organisms have been traditionally placed in extant animal phyla, including cnidarians, annelids, and arthropods. As such, they represent forerunners of Cambrian animals and support the idea of a short phylogenetic fuse to the Cambrian explosion.

However, Adolf Seilacher, a University of Tubingen paleontologist, argues that most Ediacaran organisms could not have functioned as free-living animals. He interprets them instead as having had bodies of stuffed tubes (similar to an inflated air mattress) that were organized concentrically, radially, serially, or fractally. This unique construction of the body forms the basis for his recognition of a new kingdom, Vendobionta (*1*). Although Seilacher admits that there were bona fide animals in the Ediacaran biota, he argues that those animals lived in the shadows of vendobionts that are not closely related to extant metazoans. He believes that the vendobionts were giant protists resembling modern xenophyophoran foraminifers (*2*).

Many paleontologists disagree with Seilacher, and Fedonkin and colleagues defend the traditional interpretation. A case for affinity with more-recent animals has been made for such vendobionts as *Dickinsonia* and *Yorgia*, which left resting traces that are taken as evidence for animal-like mobility. But current hypotheses about how such resting traces were made and how these vendobionts fed find few analogues among modern animals. Other examples of possible animals include *Iusia*, which has been suggested as a possible urochordate. The authors also follow the traditional interpretation of many other Ediacara fossils as animals, although such vendobionts as rangeomorphs, with a fractal body construction, have body plans and lifestyles that seem to have been distinct from those of modern animals. Thus, vendobionts remain phylogenetic ghosts whose placement in the tree of life is elusive. Paleontologists continue to debate whether vendobionts are monophyletic and, if they are, whether they fit within the crown of the animal tree, lie along the stem leading to that crown, or rest somewhere else in the eukaryote tree.

The Rise and Fall of the Ediacaran Biota comprises a collection of papers that was developed from two interdisciplinary symposia (2004 and 2006) held for the International Geological Correlation Project 493. The wide range of topics encompasses tectonics, paleomagnetism, and evolutionary developmental biology, but the bulk of the book focuses on Ediacaran fossils and contemporaneous life forms. Like most edited volumes, the individual chapters are of uneven breadth and depth.

I am most impressed by the thorough analysis of *Kimberella* provided by Fedonkin and his co-authors. Fedonkin regards *Kimberella* as the crown jewel of the Ediacaran biota, whereas Seilacher considers it as a promising newcomer that lived during the vendobiont dynasty, although both agree that it was indeed an animal. Fedonkin's careful examination of a large collection of *Kimberella* specimens has revealed many anatomical structures, including a proboscis-like structure at the presumed anterior end, a dorsal shield, and a ventral foot. These structures clearly establish *Kimberella* as a bilaterian animal whose development involved programmed anterior-posterior and dorsal-ventral differentiation.

Equally intriguing is Jerzy Dzik's analysis of trace fossils, which provides a fresh perspective on animal activities prior to the Cambrian. His plausible and provocative take

Contemplating evolutionary relationships? A stumpy-tail lizard (*Tiliqua rugosa*) gazing at an ancient Ediacaran fossil (*Parvancorina minchami*) in Australia.

CREDIT: JAMES O. DEHLING

The reviewer is at the Department of Geosciences, Virginia Polytechnic Institute and State University, Blacksburg, VA 24061, USA. E-mail: xiao@vt.edu

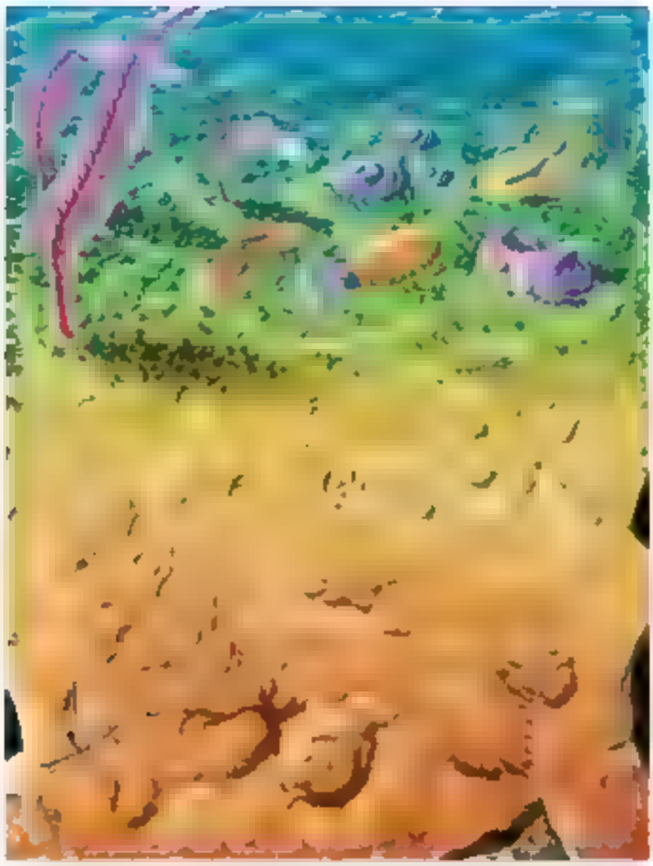

Ghostly animals. For Australia Post's "Creatures of the Slime" stamp issue (2005), Peter Trusler depicted six Ediacaran organisms (clockwise from top left) *Charnodiscus*, *Tribrachidium*, *Dickinsonia*, *Inaria Kimberella*, and *Spriggina*

on early burrows is that they represent refugia from early predators rather than feeding traces (the exploitation of organic carbon in the sediments). Testing this interpretation will require independent evidence for early predators.

Also fascinating are the new observations and innovative morphometric analyses of vendobionts by Marc Laflamme, Richard Jenkins, Jonathan Antcliffe, and their colleagues as well as Erik Sperling *et al.*'s stimulating hypothesis that the early diversification of sponges may have triggered a major disturbance in the global carbon cycle. With regard to the demise of the Ediacaran biota, Breandan MacGabhann's careful examination of purported Ediacaran fossils from Cambrian rocks accentuates the extinction of Ediacaran organisms before the Cambrian explosion, although the cause of this extinction is unresolved.

To solve the puzzle of Ediacaran fossils, paleontologists have to become more receptive to unorthodox thinking. They also need to broaden their field searches to seek fossils in such sediments as black shales, cherts, and bituminous limestones. These unconventional preservational windows may offer novel perspectives on Ediacaran fossils. In addition, future analyses should focus on the evolutionary patterns and processes of the rise and demise of the Ediacaran biota. These two books would have been richer had these aspects of Ediacaran research been explored in greater depth. Nonetheless, the beautifully produced books will serve as valuable references. Particularly useful is the atlas in *The Rise of Animals*, which includes illustrations of many important Ediacaran fossils that previously had been shown only in poor figures published in obscure journals.

The two books by Fedonkin, Vickers-Rich, and colleagues arrive while Ediacaran researchers celebrate the 100th anniversary of Rangea and Schneiderhöhn's discovery. It is perhaps coincidental that their findings in Namibia were made at about the same time as Charles Doolittle Walcott's unearthing of the Middle Cambrian Burgess Shale fauna in the Canadian Rockies. Like the Ediacaran fossils, many Burgess Shale fossils have also been phylogenetic ghosts, variously interpreted as members of extant animal phyla, stems leading to such phyla, or representatives of extinct phyla. Unlike the Ediacaran organisms, however, Burgess Shale animals are known to a much larger audience, largely thanks to Stephen Jay Gould's popular book *Wonderful Life* (*3*). *The Rise of Animals* offers a much-needed avenue to communicate to the general public the past decade's exciting discoveries of Ediacaran fossils. *The Rise and Fall of the Ediacaran Biota* will reward any scientist interested in the topic. I certainly recommend that both books be placed next to Gould's on your bookshelf.

References

1. A. Seilacher, *Lethaia* **22**, 229 (1989).
2. A. Seilacher, D. Grazhdankin, A. Legouta, *Paleontol. Res.* **7**, 43 (2003).
3. S. J. Gould, *Wonderful Life: The Burgess Shale and the Meaning of History* (Norton, New York, 1989).

10.1126/science.1156033

NEUROSCIENCE

The Female Equally with the Male I Sing

Evan Balaban

Differences between men and women have occupied people's thoughts for a very long time. Our creation myths feature them prominently; our religions and governments try to use them to define our potentialities; and our intellectual traditions are rife with rancorous debates about why sex differences exist, what they mean, and what power they should be accorded over our lives. Notions about what is "natural" for, and therefore what is naturally different about, men and women have always played a major part in this discourse.

The first post-Darwinian analysis of human sex differences in mental abilities by an evolutionary scientist—written at a time when higher education for women was a subject of intense debate—argued that brain size was an adaptive, sexually dimorphic characteristic and that women's physically smaller brains doomed them to an inferior mental status (*1*). A contemporary commentary in the *British Medical Journal* (*2*) tepidly disagreed with the conclusion of inferiority and mildly ridiculed as presumed scientific basis, endorsing instead a "separate but equal" distribution of abilities whereby men and women emphasize different specialties. Discussions over the ensuing 120 years have largely replicated such arguments, simultaneously blurring the distinction between biological characteristics that cause sex differences and those that are consequences of them. Should the average wages paid to men and women and the difference in the occurrence of attention deficit hyperactivity disorder (both are higher in males in the United States) be thought of as secondary sexual characteristics? And are these inevitable consequences of our biology?

The current profusion of popular books on

The reviewer is at the Behavioral Neurosciences Program, Stewart Biological Sciences Building N8/15, McGill University, 1205 Avenue Docteur Penfield, Montreal, QC H3A 1B1, Canada, and the Cognitive Neuroscience Sector, SISSA, Via Lionello Stock 2/2, 34135 Trieste, Italy. E-mail: evan.balaban@mcgill.ca

"Of physiology from top to toe I sing. Not physiognomy alone nor brain alone is worthy for the Muse. I say the Form complete is worthier far. The Female equally with the Male I sing." Walt Whitman, "One's Self I Sing"

sex differences by scientifically trained (*3*) and untrained (*4*) authors alike are still mired in the same hackneyed "biology as qualified destiny" arguments. A typical recent example lists "hardwired" sex differences and tries to show "how denial of these differences has led to the sexual revolution, fatherless families and calls for universal day care" (*4*). To be fair, this author feels that certain hand-picked "hardwired" differences are not imperatives. He advocates discouraging "men's desire for irresponsible sex" and further nurturing women's "greater interest and talent in caring for babies." Within the more staid walls of scientific discourse, nine pages in *Science* (*5*) were recently devoted to criticism by over 40 evolutionary scientists responding to a review that questioned the ability of parental investment theory (a component of the theory of sexual selection) to adequately explain all differences in reproductive social behavior between males and females (*6*, *7*). The heated nature of the discussion suggests something more is at stake than which mathematical model provides the best predictions.

Why should people who are not obsessed with the "natural" order of things, with proscribing sex roles, or with the minutiae of scientific theories care about sex differences? One good reason was provided by a 2001 report (*8*), which found that biomedical research has failed to pay adequate attention to sex differences in ways that differentially and negatively impact the health of over half the world's population, women. Yet it has been difficult for an interested person (without a particular axe to grind) to get an accurate, up-to-date understanding of sex differences in the brain and their potential relation to behavioral differences and human health. Good textbooks on behavioral endocrinology exist but cannot provide the kind of multifaceted coverage that a timely specialty volume can.

Sex Differences in the Brain: From Genes to Behavior sets a high standard, although it is not for readers with weak backgrounds in biology, endocrinology, and neuroscience. The edited volume has three major sections. Strategies, Methods, and Background delves deeply and critically into sex dimorphisms in an evolutionary context, new findings that have injected considerable complexity and fascination into research on sex and the brain, and new tools for unraveling causal factors from consequential ones. It also contains a lengthy assessment of methodological issues in human and animal research. Shorter chapters focus on monitoring menstrual cycles, pharmacogenomic techniques, and sex differences in stress. Sex Differences in Neurobiology and Behavior, comprising the bulk of the book, contains chapters on steroid hormone receptors in relation to behavioral differences; differences in affiliative behavior, movement, motivation, neuroplasticity, and cognitive function (mostly animal work); eating behavior, energy metabolism, and obesity (human and animal work); and sex differences in play behavior, language, and visuospatial cognition (human work). The last section, Sex Differences in the Neurobiology of Disease, rounds out the volume with chapters on sex differences in susceptibility to infectious and autoimmune diseases, neuroimmunology, pain, and anxiety, mood, Alzheimer's, and Parkinson's disorders.

The volume curiously lacks any treatment of relevant historical, ethical, and social dimensions to sex difference research. The book's value as a reference and teaching resource would have been substantially increased by the inclusion of at least one concise chapter documenting health issues that have historically been influenced by a lack of knowledge about sex differences and at least one other focused on the ethics of sex-difference research (including the impact of such studies on legal and social issues and the responsibilities that scientists bear). At a time when awareness of the damaging effects of authority figures describing sex differences to young people in particular ways is increasing (*9*, *10*), such issues deserve a prominent place in scientific training and consciousness.

All readers will learn something of value from this book, even if they don't agree with the views of particular authors. Information content is high, references are ample, and the continuity between different chapters has been skillfully coordinated. The chapters in the first section on brain sex differences and methodological issues are especially noteworthy for their concise and critical presentation of material and ideas while generating excitement and interest. These chapters deserve to be widely read, and they will undoubtedly attract bright young minds to the field. The organizers of *Sex Differences in the Brain* would perform an enormous public service if they prepared a version of the material for popular consumption.

References

1. G. J. Romanes, *Nineteenth Century* **21**, 654 (1887).
2. Anonymous, *Br. Med. J.* **96**, 415 (1887).
3. R. M. Young, E. Balaban, *Nature* **443**, 634 (2006).
4. S. E. Rhoades, *Taking Sex Differences Seriously* (Encounter, San Francisco, 2004).
5. A. T. D. Bennett *et al.*, Debating sexual selection and mating strategies, *Science* **312**, 689–697 (2006).
6. J. Roughgarden, M. Dishi, E. Akçay, *Science* **311**, 965 (2006).
7. T. Clutton-Brock, *Science* **318**, 1882 (2007).
8. T. M. Wizemann, M. L. Pardue, Eds. *Exploring the Biological Contributions to Human Health: Does Sex Matter?* (National Academy Press, Washington, DC, [illegible]).
9. I. Bar-Nimrod, S. J. Heine, *Science* **314**, 435 (2006).
10. B. Barres, *Nature* **442**, 133 (2006).

10.1126/science.1154447

THE PIPELINE

Igniting Girls' Interest in Science

A partnership between university and Girl Scouts engaged young girls' interests in chemistry.

Sheryl A. Tucker,[1]* Deborah L. Hanuscin,[2] Constance J. Beames[3]

Girls' interest, participation, and achievement in science decline as they advance in grade levels (*1*). For example, in fourth grade, the number of girls and boys who like math and science is about the same, but by eighth grade, twice as many boys as girls show an interest in these subjects (*2*). As the career expectations of eighth-grade students affect actual career outcomes (*3*), this interest deficit among girls may contribute to the continuing gender gap in science, particularly in terms of labor market outcomes (*4*).

Informal out-of-school programs have been shown to increase girls' interest and participation in science (*5*–*7*). Successful programs incorporate hands-on activities, role models, an emphasis on practical applications, and practices that promote equitable learning environments for girls (*6*, *8*) (table S1). Although the research is mixed, single-sex programs can provide a supportive learning environment for girls (*6*). Unfortunately, girls have fewer out-of-school science experiences than boys (*9*, *10*), a difference that may account for their lowered interest in school science courses (*9*, *11*). Additionally, girls' (and boys') participation in such programs dwindle during the transition from elementary to middle school, just as girls' interest in science wanes (*12*).

Program Overview

"Magic of Chemistry" was created to ignite interest in science among girls during this critical transition period (*13*) (see figure, right). The program is sponsored by the University of Missouri in partnership with the Girl Scouts–Heart of Missouri Council (*8*). The program has served more than 2500 girls over the past 10 years.

Each year, two identical Saturday workshops for 200 Junior Girl Scouts are organized in conjunction with National Chemistry and National Girl Scout weeks. Three different workshops rotate annually: Case of the Unsigned Letter, Fun with Polymers, and Chemistry of Color (*8*). Each utilizes American Chemical Society materials that reflect National Science Education Standards (*14*–*17*), specifically Standard A: "Science as Inquiry." Workshops provide specific questions and data collection protocols to guide investigations. The girls formulate explanations from evidence, connect explanations to scientific knowledge, and communicate and justify their explanations (*18*).

Members of Troop 511 make "incrediblobs" in the Magic of Chemistry program.

During the 6-hour day, small groups rotate through experiments. Each girl is provided materials at an individual station, as well as a scientific notebook with questions and protocols. The notebook facilitates continuity in learning, and demonstrations related to each experiment reinforce scientific concepts. At each experiment's end, the girls discuss results and formulate a conclusion as a group.

Even though the overall program reflects best practices (*6*) (table S1), the story line that weaves each investigation together into a cohesive unit sets Magic of Chemistry apart from other informal science programs that rely on a series of disconnected experiments. The narrative comes to life with the assistance of highly trained volunteers including professional scientists who have the ability to help girls see the relevance of science to everyday life. The presence of prepared and qualified staff with sufficient knowledge of science is also important to the success of informal science programs (*6*).

Program Assessment

Participants from 10 workshops from 1999 to 2006 completed postworkshop evaluations, rating the workshop on four indicators (*19*). Six of the 10 program evaluations included questions about college and science interest. Responses were tabulated and percentages calculated based on the total number of completed evaluations.

Open-ended questions asked participants to identify what they learned and liked about the workshop. Responses were analyzed using N-Vivo qualitative data analysis software (QSR International), and codes assigned using low-inference observation measures. Two separate blind analyses of the data were completed, and a high degree of interrater agreement (92%) was found. Codes were grouped into categories based on frequency, and patterns analyzed for themes.

Outcomes, Benefits, and Follow-Up

Workshops consistently received top ratings on all indicators (see chart, below). The perceived ease of each workshop is consistent with the level of difficulty of each investigation. Case of the Unsigned Letter contains single-step experiments; the other two workshops contain multistep experiments. When surveyed, adults' views mirrored those of the participants.

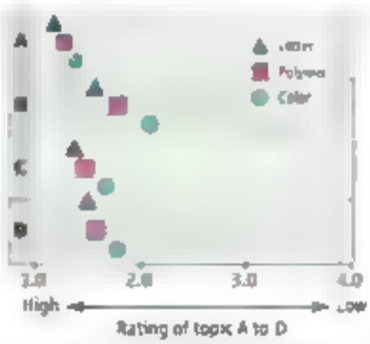

Summary of workshop evaluations. Level of A, quality; B, ease; C, interest; D, necessity. Data points represent the average score received on the evaluations ($n = 1395$ girls and $n = 232$ adults).

On average, 81% (range 66 to 88%) of participants wanted, after the workshops, to learn more about science and science careers (see chart page 1622, top, and table S2). Participant interest levels may be linked to each workshop's perceived difficulty; for example, Chemistry of Color was

[1]Department of Chemistry and Graduate School, University of Missouri (MU), 210 Jesse Hall, Columbia, MO 65211, USA. [2]Department of Learning, Teaching, and Curriculum and Department of Physics and Astronomy, MU Science Education Center, 303 Townsend Hall, Columbia, MO 65211, USA. [3]Girl Scouts–Heart of Missouri Council, 230 Metro Drive, Jefferson City, MO 65109, USA.

*To whom correspondence should be addressed. E-mail: tuckers@missouri.edu

PHOTO CREDIT: REBECCA BERGFELD

evaluated as the most difficult and also generated the lowest amount of interest of the three workshops (table S2).

Learning outcomes reflect the program's goal of teaching girls about science and its relevance to their daily lives. Although the majority of participants gave examples of activities and experiments (e.g., "doing tie-dye") as learning outcomes, they also cited scientific facts and concepts (e.g., "a dye can contain many different colors" and "carbon dioxide is heavier than air"), as well as real-world applications of science (e.g., "With DNA, you can find out if someone's family"). (See table below, and tables S3 and S4.) Beyond these primary outcomes, girls also noted learning laboratory techniques (e.g., "I learned how to do a soil analysis"), and how to use scientific equipment, a need for girls that has been documented (*2*, *6*). Although not an explicit learning objective, laboratory safety was also a notable learning outcome.

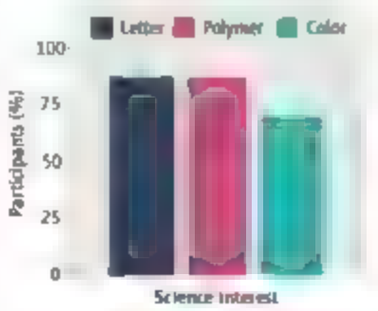

Percentages of girls with interest in learning more about science and science careers (n = 911)

The fun aspects of workshops, the opportunity to learn new things, and social interaction with peers were all cited as things liked about the workshops (see table below, and tables S3 and S5). These responses are frequently cited by youth as reasons for participating in informal learning programs (*2*). As such, we feel successful in having met our objective of creating a positive association with science.

Although important, fun alone is not enough. We also strive to instill in girls a lifelong desire for learning. The number of responses focused on the program's campus location is clear indication that this other primary objective has been met (see table, right, and tables S2 to S5). Besides being able to eat in the campus dining hall, girls liked being able to "see what college is like," "feeling more grown up," and interacting with college students. About 30% of respondents indicated that this was their first visit to a college campus (table S2).

Although encouraging, these results cannot tell us whether girls who participate in Magic of Chemistry maintain an interest in science. Evaluation of long-term effects is a challenge of informal programs (*20*). Because interest levels have been shown to increase the longer students participate in informal programs (*21*), some insight, albeit anecdotal, may be garnered from participation rates in Magic of Chemistry. About 29% of girls participated in more than one workshop; 11% participated in three (table S6). Furthermore, a continuing interest in science has been cited as a reason by former participants who later volunteer to help with the program (table S7). Other anecdotal support comes from parents and teachers who have witnessed girls displaying a more notable interest in science following participation. Of course, a longitudinal study of participants would provide better evidence of the program's effectiveness at inspiring a long-term interest in science.

Portability

Magic of Chemistry has been successfully adopted at three other institutions of higher education in Missouri and Kansas (*22*), and the workshops are being used as a science enrichment activity for a mixed-sex public elementary school audience. Portability is facilitated by the use of program kits (*3*) and the 3-year workshop cycle. The only real restriction caused by adopting the Magic of Chemistry is the age group it addresses.

Conclusions

Magic of Chemistry educates young girls about science and, more important, encourages their interest in scientific discovery at a critical time in their educational development. Informal programs such as this one can help break down the walls between the formal education system and the students' real life, bringing context to one and insights to the other.

Response categories	Percent of responses
Learned	
Activities and experiments	60
Scientific facts and concepts	46
Laboratory techniques	41
Results of experiments	24
Understanding of scientific work	14
Real-world applications of science	10
Safety in the laboratory	5
Liked	
Food	52
Fun	25
Learning	25
Experiencing campus life	19
Social interaction with peers	19
Interacting with college students	10

Responses to open-ended questions. Girls were asked to respond to two questions: "What are two things you learned from the Magic of Chemistry activities?" and "What are three things you liked most about attending a special event at the University of Missouri?" (n = 967)

References and Notes

1. C. Shakeshaft, *Theor. Pract.* **34**, 74 (1995).
2. V. Bae, S. Choy, C. Geddes, J. Sable, T. Snyder, "Trends in educational equity of girls and women" [NCES 2000–030, U.S. Department of Education, National Center for Education Statistics (NCES), Washington, DC, 2000].
3. R. H. Tai, C. Q. Liu, A. V. Maltese, X. Fan, *Science* **312**, 1143 (2006).
4. C. E. Freeman, "Trends in educational equity of girls and women: 2004" (NCES 2005–016, U.S. Department of Education, NCES, Washington, DC, 2004).
5. D. M. Casey, M. N. Ripke, A. C. Huston, in *Organized Activities as Contexts of Development: Extracurricular Activities, After School and Community Programs*, J. L. Mahoney, R. W. Larson, J. S. Eccles, Eds. (Lawrence Erlbaum Associates, Mahwah, NJ, 2005), pp. 65–84.
6. C. Fancsali, *SIGCSE* **32**, 99 (2000).
7. P. Campbell, J. Storo, K. Acerbo, *Math, Science Sports, and Empowerment: Girls Incorporated Replication and Expansion of the EUREKA! Model* (Campbell-Kibler Associates, Groton, MA, 1995).
8. Materials and methods, supporting text, a figure, and tables are available as supporting material on *Science* Online.
9. S. Farenga, thesis, Columbia University (1995).
10. J. Kahle, L. Parker, L. Rennie, D. Riley, *Educ. Psychol.* **28**, 374 (1993).
11. J. Kahle, in *The Equity Equation: Fostering the Advancement of Women in the Sciences, Mathematics, and Engineering*, C. S. Davis *et al.*, Eds. (Jossey-Bass, San Francisco, 1998), pp. 57–95.
12. S. Glauver, P. M. D. Little, H. B. Weiss, "Moving beyond the barriers: Attracting and sustaining youth participation in out-of-school time programs" (Harvard Family Research Project, 2004).
13. Magic of Chemistry, http://magicofchemistry.missouri.edu.
14. *Kids & Chemistry Hands-On Activities and Demonstrations Guide* (Education and International Activities Division, American Chemical Society (ACS), Washington, DC, 1998).
15. *Kids & Chemistry Large Event Guide* (Education and International Activities Division, ACS, Washington, DC, 1995).
16. *Best of WonderScience*, vol. 1 (ACS, Delmar Publishers, Albany, NY, 1997).
17. *Best of WonderScience*, vol. 2 (ACS, Wadsworth/Thomson Learning, Belmont, CA, 2001).
18. National Research Council, *Inquiry and the National Science Education Standards: A Guide for Teaching and Learning*, S. Olson, S. Loucks-Horsley, Eds. (National Academies Press, Washington, DC, 2000).
19. Participants voluntarily and anonymously completed evaluation surveys, administered by the Girl Scouts–Heart of Missouri Council with parental consent.
20. C. Fancsali, "What we know about girls, STEM, and after-school programs: A summary" (Educational Equity Concepts, New York, 2003).
21. P. M. D. Little, E. Harris, "A review of out-of-school time program quasi-experimental and experimental evaluation results" (Harvard Family Research Project, Cambridge, MA, 2003).
22. Truman State University (TSU) and Hannibal-LaGrange College in Missouri and Emporia State University in Kansas.

23. We sincerely thank the reviewers for their constructive and thoughtful comments. They have helped us better demonstrate the significance of the program in a clear and concise manner. We also thank J. L. Atwood and MU's Department of Chemistry without whose support the program would not have been possible; A. E. Moody of TSU, for insightful discussions during program development and serving as the first expansion site; M. M. Kroll for editing various drafts of this manuscript; and B. D. Hostetler for assisting with data analysis. Funding was provided by the Dreyfus Foundation, the American Chemical Society, and the National Science Foundation.

Supporting Online Material
www.sciencemag.org/cgi/content/full/319/5870/1621/DC1

10.1126/science.1153261

NEUROSCIENCE

Detailed Differences

Brain imaging shows that, as in other animals, the human hippocampus has regions that help us keep our memories from becoming jumbled.

Stefan Leutgeb

Our subjective experience might tell us that events are unprecedented, even though many situations that we encounter from day to day have prominent similarities and may only differ in important detail. To form separate memories for each day and for the many events that occur within a day, it is thus necessary to keep them distinct by somewhat ignoring the similarities and emphasizing the differences. Evidence for such a process, called "pattern separation," has been found to occur in the hippocampus—specifically the dentate gyrus and CA3 regions—in the rodent brain (*1*–*5*). On page 1640 of this issue, Bakker *et al.* (*6*) report that the human dentate gyrus and CA3 regions have the same function, evidence that the contribution of the hippocampus to memory processing is common across mammalian species, including humans.

To test whether pattern separation can be found in the human medial temporal lobe, a brain region that is central to memory storage (*7*) (there are two lobes, one each on the left and right hemispheres of the brain, and each contains a hippocampus), Bakker *et al.* used functional magnetic resonance imaging (fMRI) to investigate the incidental encoding of visual images by human subjects. While being scanned, subjects were shown images that were initially new to them and were then repeated after approximately 30 other images had been shown. In this design, greater brain activity was seen within the medial temporal lobe during the first presentation of the images, whereas such activation was lower in these same regions when an earlier stimulus was repeated (neither observation is surprising nor unexpected for this standard procedure).

Bakker *et al.* then varied the approach, using visual stimuli that were very similar, but not absolutely identical, to those previously presented. If the subjects were lured into thinking that an imperfect copy was identical to a previously shown stimulus, they would respond as if it were an exact repetition. If they succeeded in detecting the small difference, they would recognize the slightly altered stimulus as new and would display brain activity of similar amplitude as during the first presentation of a visual stimulus—a so-called novelty signal." The authors found that only two areas embedded in the left and right dentate gyrus and CA3 regions of the hippocampus detected imperfections and responded with a novelty signal to the slightly altered replicas.

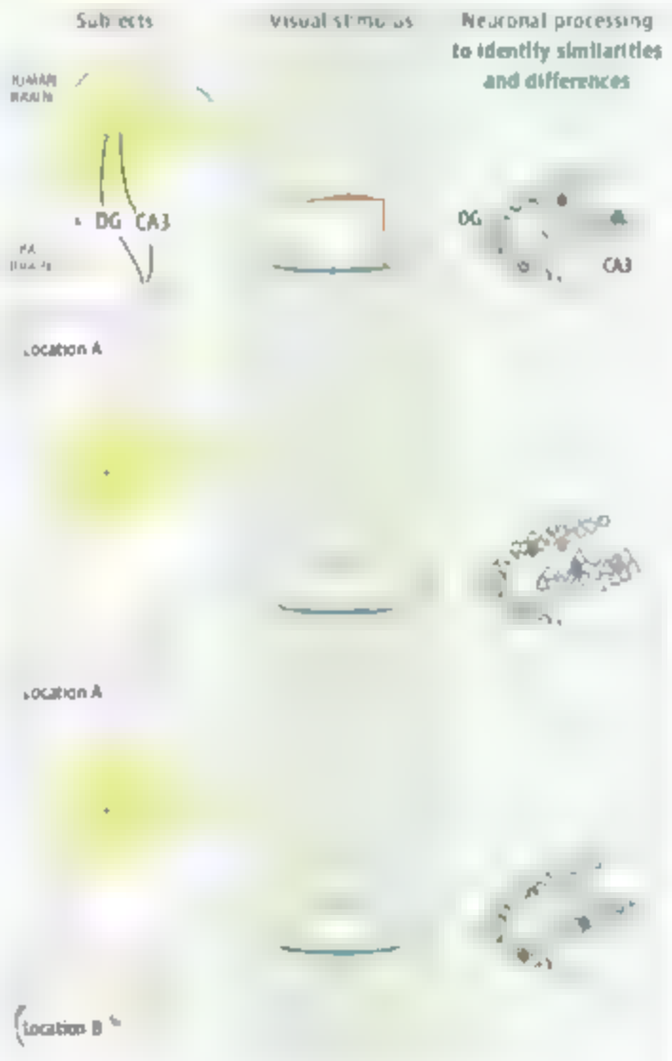

Memory is in the details. The dentate gyrus (DG) and CA3 regions in the human and rodent brain function in distinguishing stimuli (or events) that may otherwise seem similar. In rodents, two distinct processes in the DG and CA3 select different neuron activation patterns for each sensory input and location.

In combination with earlier studies in rodents (*1*–*5*), the current findings show a striking convergence in identifying a common function for the hippocampal dentate gyrus and CA3 regions across mammalian species. All these studies identify pattern separation processes in specific neuronal populations in these regions. However, as a consequence of not being able to resolve neuronal activity between these two subregions with the currently available technology, Bakker *et al.* have actually detected pattern separation in the combined activity signal from both areas. The relative role of either region therefore has not yet been directly observed in humans, as it has in rodents (see the figure). Theoretical studies (applying to all mammals) have pointed to a pronounced influence of the dentate gyrus on CA3 at the time of new learning of a separate pattern (*8*–*10*), which suggests that these areas may be functionally coupled at the time of recording a novelty signal, as in the current fMRI study.

By contrast, recent studies in rodents have shown that pattern separation may not be based on a unitary network mechanism—that is, the one-on-one activation of CA3 neurons by dentate gyrus neurons—but rather might rely on two types of neuronal processing activities in these regions. The rodent dentate gyrus shows a more pronounced encoding of differences between similar sensory input patterns that occur at a single location (*4*). CA3 adds another layer of pattern separation that effectively distinguishes different locations by activating different neuronal subpopulations (*2*, *4*). The latter mechanism suggests that pattern separation is automatically achieved by neuronal networks that can activate a randomly selected set of CA3 neurons at each new location. If such new activation of cells is initially not bound to common sensory features (*11*), it is an efficient process to distinguish stimuli or events that would otherwise share a large number of common sensory features.

Kavli Institute for Systems Neuroscience and Centre for the Biology of Memory, Norwegian University for Science and Technology, 7489 Trondheim, Norway. E-mail: stefan.leutgeb@ntnu.no

CREDIT: ADAPTED FROM STEFAN LEUTGEB

It is not yet clear what the precise cellular mechanisms are, in humans or other animals, that generate novel and separate neuronal firing patterns (the composition of electrical impulses that neurons discharge when excited by a stimulus) for images that share a striking number of common features. However, the mechanisms require that neuronal firing is initially not strongly influenced by the large number of visual features that are shared between similar images (*12*). It also remains to be determined whether neuronal processes that accentuate differences between sensory inputs in humans could be mechanistically related to those that select new, random neuronal firing patterns for spatial locations in rodents.

If such strong pattern separation is not available in other cortical architectures of the brain, it could be one of the defining processes that make the hippocampus and its connected regions in the medial temporal lobe essential for automatically recording detailed memories in humans and other mammals. It will therefore be important to address whether any related separation of sensory inputs also occurs outside of the medial temporal lobe, although such processes might be more difficult to identify if they are not bound to novelty signals in the same way as in the hippocampus. Conversely, it will be important to find how pattern separation and novelty signals might be integrated in the dentate gyrus and CA3 and across the entire medial temporal lobe to give rise to memory for detailed differences but still let us see the big picture. Although these questions are challenging to address even in animal models, the findings of Bakker *et al.* have paved the way for a new category of imaging studies that can investigate neuronal network mechanisms in the human brain.

References

1. P. E. Gilbert, R. P. Kesner, I. Lee, *Hippocampus* **11**, 626 (2001).
2. S. Leutgeb, J. K. Leutgeb, A. Treves, M.-B. Moser, E. I. Moser, *Science* **305**, 1295 (2004); published online 22 July 2004 (10.1126/science.1100265).
3. A. Vazdarjanova, J. F. Guzowski, *J. Neurosci.* **24**, 6489 (2004).
4. J. K. Leutgeb, S. Leutgeb, M.-B. Moser, E. I. Moser, *Science* **315**, 961 (2007).
5. T. J. McHugh *et al.*, *Science* **317**, 94 (2007); published online 7 June 2007 (10.1126/science.1140263).
6. A. Bakker, C. B. Kirwan, M. Miller, C. E. L. Stark, *Science* **319**, 1640 (2008).
7. L. R. Squire, C. E. Stark, R. E. Clark, *Annu. Rev. Neurosci.* **27**, 279 (2004).
8. D. Marr, *Philos. Trans. R. Soc. London Ser. B* **262**, 23 (1971).
9. B. L. McNaughton, R. G. M. Morris, *Trends Neurosci.* **10**, 408 (1987).
10. A. Treves, E. T. Rolls, *Hippocampus* **2**, 189 (1992).
11. B. L. McNaughton *et al.*, *J. Exp. Biol.* **199**, 173 (1996).
12. B. Blumenfeld, S. Preminger, D. Sagi, M. Tsodyks, *Neuron* **52**, 383 (2006).

10.1126/science.1156724

ATMOSPHERIC CHEMISTRY

Rethinking Ozone Production

Laboratory data suggest that atmospheric models are missing a source of hydroxyl, which plays a central role in tropospheric ozone production

Paul O. Wennberg[1] and Donald Dabdub[2]

More than a hundred million people live in cities that fail to meet international standards for air quality. Efforts to improve conditions in these urban areas have usually focused on reducing emissions of reactive hydrocarbons (such as unburned gasoline vapors), nitrogen oxide free radicals (NO and NO_2, together known as NO_x), and primary and secondary sources of particulate matter (such as diesel smoke and sulfur dioxide). Control strategies have changed over time in response to evolving understanding about atmospheric photochemistry and the impact of urban emissions on air quality downwind of cities (*1*, *2*). The results reported by Li *et al.* on page 1657 of this issue (*3*) may require another rethinking of these control strategies.

There are three essential ingredients for producing ozone, O_3, in urban atmospheres: sunlight, NO_x, and hydrocarbons (see the first figure). Ozone production chemistry is initiated when hydroxyl free radicals, OH, are produced from water vapor. Classical theory suggests that the O-H bond in water is broken by excited-state oxygen atoms produced in the photolysis of ozone. In the atmosphere, OH oxidizes hydrocarbons to produce peroxy radicals, RO_2 (where R is a hydrogen atom or carbon-containing fragment). In the presence of NO_x, the RO_2 radicals convert NO to NO_2; subsequent photolysis of NO_2 yields O_3. When sufficient amounts of NO are available, the chemistry is catalytic. For each OH produced from water, many hydrocarbons can be oxidized and large amounts of ozone produced. However, when NO_2 levels become high, the loss of OH to nitric acid, $HONO_2$, slows the reactivity, and the rate of ozone production drops. As a result, in many cities, including Los Angeles, ozone levels are generally higher on weekends, when NO_x levels are lower due to the lack of truck traffic.

Li *et al.* add another level of complexity to the story. In laboratory experiments, they show that excited-state NO_2 (denoted NO_2^*) may also break the O-H bond in water, yielding OH and HONO. NO_2^* is produced in the atmosphere when NO_2 absorbs sunlight between 400 and 650 nm. Li *et al.* find that for typical urban conditions, 1 in 10,000 of the NO_2^* molecules produced reacts with H_2O to produce OH and HONO. Despite this low efficiency, the rate of OH production from NO_2^* in urban atmospheres can be comparable to the classical OH source (ozone photolysis). The amount of OH produced from NO_2^*

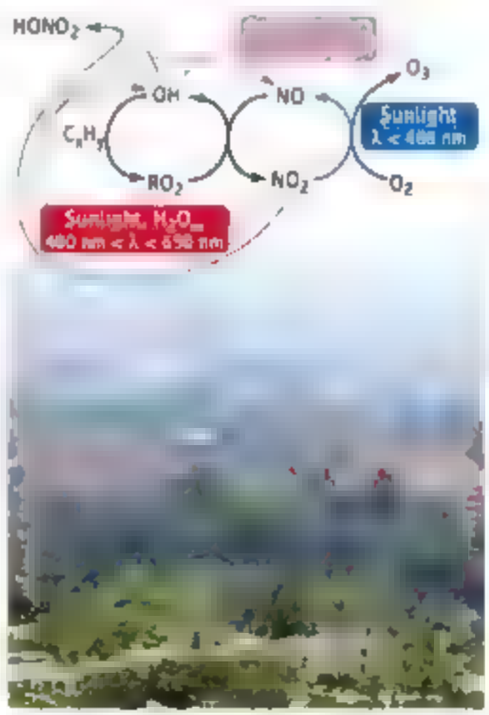

Ozone chemistry. When NO and NO_2 are present, O_3 is produced in the catalytic oxidation of hydrocarbons by the OH radical. Classical theory suggests that the chemistry is initiated when OH is produced after the photolysis of ozone in the presence of water vapor (purple). Li *et al.* find that the O-H bond in water can also be broken by excited-state NO_2 (red). This chemistry increases the amount of OH and thus O_3 production.

PHOTO CREDIT: PDPHOTO.ORG

[1]California Institute of Technology, Pasadena, CA 91125, USA. E-mail: wennberg@caltech.edu [2]Department of Mechanical and Aerospace Engineering, University of California at Irvine, Irvine, CA 92697, USA. E-mail: ddabdub@uci.edu

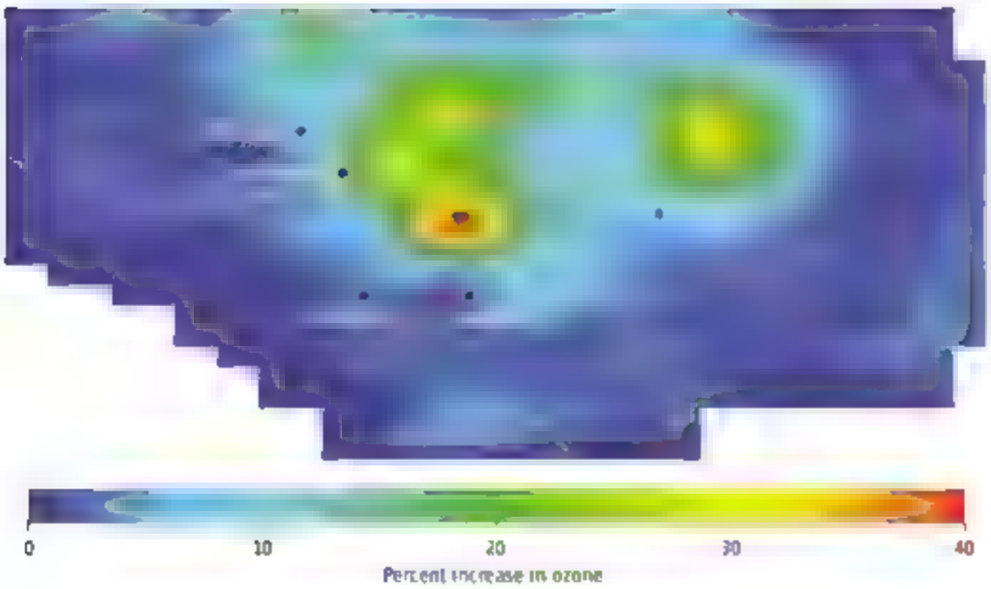

More pollution? Photochemical simulations for 27 to 29 August 1987 in the South Coast Air Basin of California were obtained with and without including the OH source from NO_2^* described by Li *et al*. Shown are the percentage increases in ozone concentrations in the afternoon due to the NO_2^* chemistry

scales linearly with the amount of NO_2 in the atmosphere. The net result is that the calculated ozone production rate is higher. In addition, the maximum ozone production rate occurs at higher NO_x concentrations.

We have performed model simulations of air quality in the Los Angeles basin for a typical summer smog episode (*4*, *5*) both with and without the NO_2^* source of OH. With the NO_2^* source, ozone concentrations are calculated to be much higher throughout the city, with increases of up to 55 parts per billion, percentage increases in ozone concentrations are as high as 30 to 40% (see the second figure). The most affected area is downwind of the city, near Riverside, where NO_x is most abundant. Aerosol levels are also affected, especially near Riverside, where small particle concentrations (diameter <2.5 μm) increase by 20 μg m^3.

Our simulations that include the NO_2^* OH source generally overestimate the observed distribution of O_3 in Los Angeles. Is it possible that the rate constant reported by Li *et al*. is too large? Perhaps. Following a suggestion by Paul Crutzen that the reaction of NO_2^* with H_2O might be important, Crowley and Carl studied this chemistry a decade ago (*6*). They found that the rate of the reaction with H_2O was more than an order of magnitude slower than determined by Li *et al*. When we used this slower reaction rate in our model, we obtained a smaller, but still significant, air quality impact. Ozone concentrations increase by up to 10 parts per billion and the small-particle concentration by up to 10 μg/m^3.

The experimental approach used by Li *et al*. differs slightly from that used by Crowley and Carl, but it seems unlikely that this alone explains the different findings. We find no obvious problem with either study. Given the potential importance of this chemistry and the high sensitivity of atmospheric models to the reaction of NO_2^* with H_2O, further investigation is clearly needed.

References

1. NRC Committee on Tropospheric Ozone Formation and Measurement, *Rethinking the Ozone Problem in Urban and Regional Air Pollution* (National Academy Press, Washington, DC, 1991).
2. NARSTO Synthesis Team, *An Assessment of Tropospheric Ozone Pollution—A North American Perspective* (NARSTO Management Office, Pasco, WA, 2000); available from ftp://narsto.esd.ornl.gov/pub/Ozone_Assessment/Cover/OC&Preface.pdf.
3. S. Li *et al*., *Science* **319**, 1657 (2008).
4. O. Dabdub, J. H. Seinfeld, *Parallel Comput.* **22**, 111 (1996).
5. R. A. Harley, A. G. Russell, G. J. McRae, G. R. Cass, J. H. Seinfeld, *Environ. Sci. Tech.* **27**, 378 (1993).
6. J. N. Crowley, S. A. Carl, *J. Phys. Chem.* **101**, 4178 (1997).

10.1126/science.1155747

MATERIALS SCIENCE

Who Wins the Nonvolatile Memory Race?

New memory concepts may lead to computer systems that do not require a lengthy start-up process when turned on

G. I. Meijer

IBM Research, Zurich Research Laboratory, CH-8803 Rüschlikon, Switzerland. E-mail: imm@zurich.ibm.com

The semiconductor industry has long sought a high-density, high-speed, low-power memory device that retains its data even when the power is interrupted. Therefore a concept called resistance-change memory, in which a change in how easily current can flow through a material is exploited to store a memory bit, has recently sparked scientific and commercial interest. Can this concept surpass the performance of state-of-the-art devices?

DRAM (dynamic random-access memory), which is omnipresent in today's computers, must be powered continuously to keep its memory state. So-called flash memory, on the other hand, is nonvolatile, but this advantage comes at the price of a slow write speed and a limited number of write/erase cycles. Flash memory therefore cannot be used in a computer's main memory, which must frequently be rewritten. Instead, flash technology is restricted to applications that require neither high speed nor unlimited endurance, such as solid-state hard disks and storage media for digital cameras and cellular phones. Nonetheless, flash memory represented about a third of the US$ 60 billion memory market in 2007.

Traditional memory technologies are rapidly approaching miniaturization limits as the industry moves toward memory cells with 22-nm lateral features projected for 2016 (*1*). The reason is that they are based on charge storage—and it becomes increasingly difficult to reliably retain sufficient electrons in these shrinking cells. Magnetic and ferroelectric random-access memories, which are currently used in niche markets, share this struggle with scaling. Or, to adapt the famous quote from

Feynman (2): There isn't plenty of room at the bottom anymore.

Nonvolatile memory concepts aimed at the horizon beyond 2013 are based on resistance change rather than charge storage (see the figure). They include (i) phase-change memory in chalcogenides, (ii) programmable-metallization-cell memory in solid electrolytes, and (iii) resistance-change memory in transition-metal oxides. But which of these three candidates is the most likely to win the race?

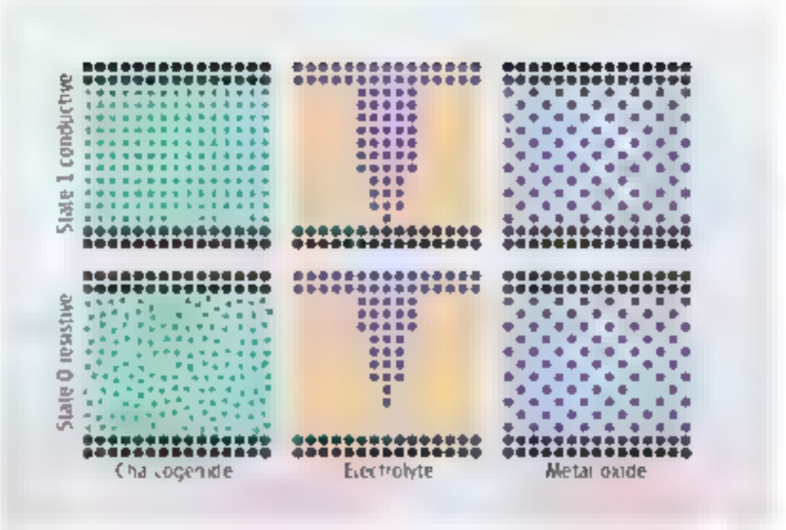

Resistance-change memory concepts. **(Left)** Phase change between a crystalline and an amorphous $Ge_2Sb_2Te_5$ chalcogenide. **(Middle)** Creation and annihilation of a metallic Ag protrusion in a GeSe solid electrolyte. **(Right)** Creation and disruption of a pattern of missing oxygen atoms in a $SrTiO_3$ transition-metal oxide. Background pattern shows a micrograph of a semiconductor wafer with $SrTiO_3$ memory devices.

The most mature candidate is phase-change memory. Pioneered by Ovshinsky in the 1960s (*3*), it has garnered significant interest over the past few years and is now being actively pursued by all leading chip makers. Phase-change memory relies on a resistance change between the ordered crystalline state and a disordered amorphous form of a chalcogenide material such as $Ge_2Sb_2Te_5$. Electrical heating momentarily melts a small volume of the chalcogenide at about 600°C, which then, depending on the amplitude and duration of the electrical signal applied, solidifies into a crystalline low-resistance state or into an amorphous high-resistance state (*4*). These states represent the 1s and 0s of stored digital data.

The key ingredients of the second candidate, programmable metallization cells, are mobile metal ions embedded in an electrolyte glass matrix, for example, Ag or Cu in GeSe (*5*, *6*). Electrical pulses of opposite polarity applied to these memory cells switch the resistance between a low- and a high-resistance state. Electrochemical reduction and oxidation of the metal ions in the glass leads to creation and annihilation of a nanoscale metallic protrusion that forms a bridge between two electrodes.

Resistance-change memory in transition-metal oxides, ranging from perovskites such as $SrTiO_3$ to binary oxides such as NiO, has attracted the interest of the research community (*7*–*9*). In this third contender, electrical pulses of opposite polarity switch the resistance reversibly between a high- and a low-resistance state. The resistance switching was initially thought to be of electronic nature, for example, related to strongly correlated electrons in the transition-metal oxides or to charge trapping near the electrode interface. However, in view of the wide range of materials exhibiting this effect, an altogether different physical mechanism seems more likely. What all these materials have in common is a mixed-valence transition-metal ion (Ti^{3+}-Ti^{4+}, for example) and mobile oxygen vacancies. Movement of oxygen vacancies in the applied electrical field probably plays the dominant role (*10*). This oxygen-vacancy drift modulates the valence of the transition-metal ion and thus the conducting state.

How do the attributes and challenges of these contenders compare? All three have the potential of excellent scaling to the projected 32-nm lateral device features in 2013 and beyond. For programmable metallization cells, for example, researchers demonstrated that a metallic bridge can be scaled controllably down to 0.5 nm (*11*). A simple memory-cell structure (one-transistor one-resistor or one-diode one-resistor), combined with multiple-bits-per-cell storage, also guarantees a competitive storage density. In addition, the relatively fast write time (10-ns range) satisfies the requirements for a flash and DRAM replacement. Low-power operation is a challenge mainly for phase-change memory—an issue, however, that is alleviated as the devices get smaller. It is expected that the power dissipation required to melt the chalcogenide volume can be further reduced by appropriately tailoring the chalcogenide properties and memory-cell design (*12*).

The commercial success of the three contenders will hinge on reliability, especially as moving atoms around in the memory cells causes degradation and data-retention issues. Phase-change memory is the technology that is furthest advanced, with demonstrated manufacturability (*13*). A risk factor is the cycling endurance of ultimately scaled devices. Hence, we need experiments elucidating the melting and recrystallization behavior of nanoscale-volume chalcogenide glasses when interface effects start to prevail.

The other two candidates are at a "proof-of-concept" stage, which makes reliability assessment somewhat premature. For programmable metallization cells, the robustness of the cycling endurance and data-retention time at elevated temperatures must be addressed. For resistance-change memory in transition-metal oxides, the key challenge is reducing fluctuations in the switching parameters. A direct proof of whether oxygen vacancies are responsible for the resistance switching would be crucial. On the other hand, the transition-metal oxide concept offers compelling advantages in terms of compatibility with microprocessor fabrication technology. In addition, transition-metal oxides with their rich properties could possibly provide superior alternative resistance-change effects that are of electronic nature. One could envision memory effects based on, for example, a bandwidth-controlled metal-insulator-transition of Mott insulators (*14*), which is a first-order transition and exhibits a hysteresis.

Phase-change memory has emerged as the direct challenger of flash memory and maybe eventually also of DRAM, but it remains to be seen which approach will be the first to make its commercial debut.

References

1. International Technology Roadmap for Semiconductors, 2007 Edition, www.itrs.net/Links/2007ITRS/ExecSum2007.pdf
2. R. P. Feynman, *Eng. Sci.* **23**, 22 (1960).
3. S. R. Ovshinsky, *Phys. Rev. Lett.* **21**, 1450 (1968).
4. S. Lai, T. Lowrey, *IEEE IEDM 2001 Tech. Dig.*, 36.5 (2001).
5. M. N. Kozicki, M. Park, M. Mitkova, *IEEE Trans. Nanotechnology* **4**, 331 (2005).
6. R. Waser, M. Aono, *Nat. Mater.* **6**, 833 (2007).
7. S. Q. Liu, N. J. Wu, A. Ignatiev, *Appl. Phys. Lett.* **76**, 2749 (2000).
8. A. Beck *et al.*, *Appl. Phys. Lett.* **77**, 139 (2000).
9. I. G. Baek *et al.*, *IEEE IEDM 2004 Tech. Dig.* 23.6 (2004).
10. M. Janousch *et al.*, *Adv. Mater.* **19**, 2232 (2007).
11. K. Terabe *et al.*, *Nature* **433**, 47 (2005).
12. Y. C. Chen *et al.*, *IEEE IEDM 2006 Tech. Dig.*, 30.3 (2006).
13. J. H. Oh *et al.*, *IEEE IEDM 2006 Tech. Dig.*, 2.6 (2006).
14. M. Imada, A. Fujimori, Y. Tokura, *Rev. Mod. Phys.* **70**, 1039 (1998).

10.1126/science.1153909

NEUROSCIENCE

A Protoplasmic Kiss to Remember

During establishment of long-term memory, protein synthesis, regulated by neurotrophins, affects the morphology of synaptic structures.

Martin Korte

Capturing and storing information in an efficient and long-lasting way is a tremendous task for the brain. While processing a continuous flow of sensory information it must store memories, sometimes for a lifetime. What are the cellular foundations of this long-term storage capacity in the brain? One hypothesis is that functional changes in neurons are transformed into structural changes. The psychologist Donald Hebb proposed that both processes could be implemented if information is stored in connections (synapses) between neurons rather than within a single cell (*1*). On page 1683 in this issue Tanaka *et al.* (*2*) tackle the question of how functional changes are transformed into structural changes. Remarkably, it is the smallest element of a neuron's architecture—the dendritic spine—where these critical structural changes occur.

A neuron may contain many spines, branched protoplasmic extensions from dendrites that form synapses with other neurons. Spines conduct electrical signals when stimulated by connecting, presynaptic neurons (as occurs among pyramidal neurons in the mammalian hippocampus). Spine density, as well as the shape and extent of a neuron's dendritic arbor, strongly influences neuronal function and, in turn, is profoundly influenced by neuronal activity (*3*). Despite the wealth of data showing that neuronal activity controls the morphology and function of neuronal networks, the cellular and molecular mechanisms that translate activity into long-lasting structural and functional changes have remained largely unknown. Tanaka *et al.* observe functional plasticity and structural changes at single spines, without affecting neighboring spines, and unravel some of the underlying molecular mechanisms.

Tanaka *et al.* stimulated single spines of cultured rat pyramidal neurons by repetitively exposing them to the neurotransmitter glutamate. At the same time, postsynaptic electrical activity (spikes) were induced. Using this paired protocol, the authors observed a gradual and persistent enlargement of the spine head only when postsynaptic spikes were precisely correlated with glutamate release (see the figure). This enlargement occurred only in single, activated spines. Because of the high accuracy of glutamate uncaging by a precisely pointed laser beam (two-photon microscopy), neighboring spines were not affected. The electrophysiological results showed an increase in functional changes of synapses as well (glutamate-induced currents in spines were larger). In addition, whereas the spine-head volume increased with the paired protocol, the spine length was reduced. At the same time, the spine neck increased in thickness, making the spine environment less isolated from the underlying dendrite. The observed high correlation between pre- and postsynaptic activity agrees with the Hebbian rule that timing (associativity) of activity and input specificity is critical to transforming functional neuronal changes into structural changes, also referred to as spike-timing–dependent plasticity (*4*).

Protein synthesis can regulate synaptic plasticity (*5*), and indeed, Tanaka *et al.* could block the enlargement of spines by inhibiting protein synthesis. In addition, the authors show that the neurotrophin brain-derived neurotrophic factor (BDNF) is necessary and sufficient to induce long-lasting structural changes at dendritic spines. BDNF and its receptor, TrkB, are not only important modulators of activity-dependent synaptic plasticity (*6*), but maintain synaptic plasticity as well (*7*). Tanaka *et al.* focused on postsynaptic changes, as earlier studies have done (*8*), and conclude that BDNF release from a postsynaptic neuron depends on postsynaptic spiking, suggesting an autocrine function of BDNF. But they could not show the release of BDNF directly, due to the low abundance of BDNF in the brain (*9*). Other explanations for requiring this factor are possible. For example, BDNF can act presynaptically as well as postsynaptically (*10*), and therefore could change synaptic function and morphology on both sides of the synapse. Alternatively, because the TrkB receptor can also be activated by another receptor type in the spine,

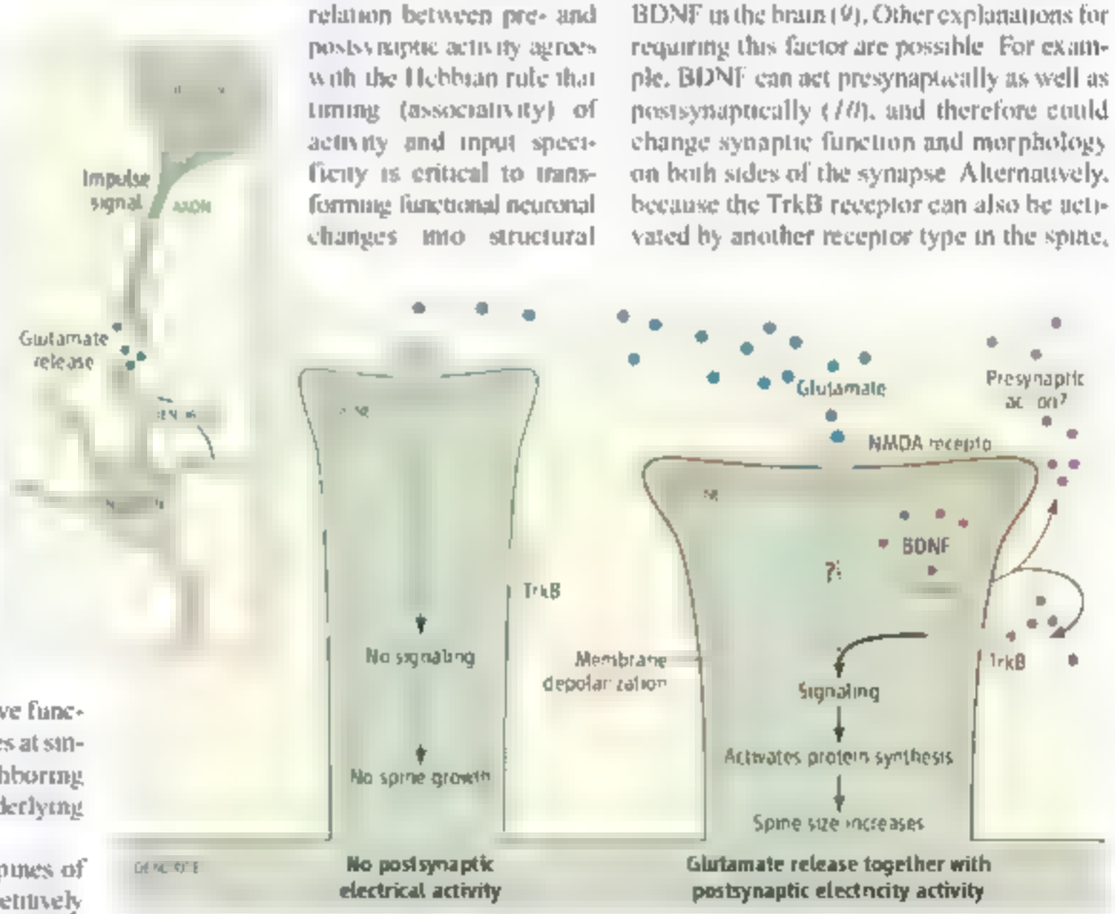

Spine growth and memory. When glutamate binds to postsynaptic *N*-methyl-D-aspartate (NMDA) receptors in the dendritic spine membrane and postsynaptic electrical signals are induced, there is a coincidence of pre- and postsynaptic activity. Only then is BDNF released in high amounts by the postsynaptic neuron, activating TrkB receptors in the spine. This initiates local protein synthesis necessary for structural changes in the spine, which may be linked to the formation of long-lasting memories in the hippocampus.

CREDIT: ADAPTED FROM MARTIN KORTE

Zoological Institute, Division of Cellular Neurobiology, TU Braunschweig, D-38106 Germany. E-mail: m.korte@tu-bs.de

such as a G protein–coupled receptor (*11*). TrkB could act as a coincidence detector of modulatory synaptic input and BDNF release. Nevertheless, the link between BDNF and possible local protein synthesis is important (*12*), as the latter is the bottleneck for the persistence of synaptic plasticity. Future research will need to determine if the newly manufactured proteins not only change the shape of a spine, but also "tag" a synapse for further activity-induced changes (*13*), or ensure that plastic processes can happen in the future (*14*).

It remains to be shown how TrkB receptor signaling can influence the cytoskeleton of a spine to change its morphology by regulating local protein synthesis. Tanaka *et al.* had to supply neurons with the cytoskeletal protein β-actin to observe the gradual spine enlargements. Ultimately, data from cultured neurons will need to be integrated with data obtained in vivo.

References

1. D. O. Hebb, *The Organization of Behavior* (Wiley, New York, 1949).
2. J.-I. Tanaka *et al.*, *Science* **319**, 1683 (2008).
3. R. Yuste, T. Bonhoeffer, *Annu. Rev. Neurosci.* **24**, 1071 (2001).
4. Y. Dan, M. M. Poo, *Physiol. Rev.* **86**, 1033 (2006).
5. U. Frey, M. Krug, K. G. Reymann, H. Matthies, *Brain Res.* **452**, 57 (1988).
6. M. M. Poo, *Nat. Rev. Neurosci.* **2**, 24 (2001).
7. H. Kang, A. A. Welcher, D. Shelton, E. M. Schuman, *Neuron* **19**, 653 (1997).
8. Y. Kovalchuk, E. Hanse, K. W. Kafitz, A. Konnerth, *Science* **295**, 1729 (2002).
9. T. Matsumoto *et al.*, *Nat. Neurosci.* **11**, 131 (2008).
10. A. Gartner *et al.*, *J. Neurosci.* **26**, 3496 (2006).
11. S. Wiese *et al.*, *Proc. Natl. Acad. Sci. U.S.A.* **104**, 17210 (2007).
12. G. Aakalu, W. B. Smith, N. Nguyen, C. Jiang, E. M. Schuman, *Neuron* **30**, 489 (2001).
13. U. Frey, R. G. M. Morris, *Nature* **385**, 533 (1997).
14. R. Fonseca, U. V. Nägerl, R. G. Morris, T. Bonhoeffer, *Neuron* **44**, 1011 (2004).

10.1126/science.1155748

GEOCHEMISTRY

Are Volcanic Gases Serial Killers?

Environmental consequences of ancient eruptions can be estimated by analysis of glass inclusions trapped in minerals present in lava flows.

Bruno Scaillet

Volatiles released by volcanic eruptions are often cited as a possible cause of major environmental changes. On a decadal time scale, at least, the connection between volcanic eruptions and climate was firmly established after the 1991 eruption of Mount Pinatubo, Philippines, whose climate aftermaths have been extensively documented and modeled (*1*). The remaining debate concerns the effect of magmatic volatiles on long-term climate trends (*2*). On page 1654 of this issue, Self *et al.* (*3*) fill in the picture of what gases have been released by volcanoes, and how much, during the so-called flood events. Such events are the most important volcanic eruptions that occurred on Earth. They are produced by mantle upwelling and its partial melting, resulting in massive basalt (a magma poor in silica) outpouring with volumes often exceeding 1 million km^3.

Earth volcanic activity is one of the two leading scenarios proposed to explain the pattern of mass extinctions in the Phanerozoic (the last 545 million years), the other involving asteroid impacts (*4*). To assess the volcanic hypothesis, we need to know the age and duration of volcanic events and the mass and nature of volatiles being released. Although decisive progress has been made in recent years concerning age and duration, confirming the geologically narrow interval (less than 1 million years) during which most flood basalt is discharged (*5*), almost no information is available on the latter aspects. As a result, the volatile yields of volcanic activity have been estimated by assuming that the volatile content of flood basalts is similar to that of their modern counterparts at mid-ocean ridges. However, there is no a priori reason why this should be so.

Self *et al.* (*3*) report the first analyses of sulfur in glass inclusions found in the Deccan basalts in west-central India. These ancient eruptions have been proposed by some as one of the important players of the Cretaceous-Tertiary mass extinction (*6*). The finding demonstrates unambiguously that the capacity of Deccan basalts to discharge sulfur into the atmosphere was similar to that of present-day erupting basalts. Trivial though this piece of evidence may seem, it now allows us to use with some confidence climate scenarios derived from the study of recent basalt outbursts, such as the 1783–1784 Laki eruption in Iceland (*7*), as a proxy for the likely envi-

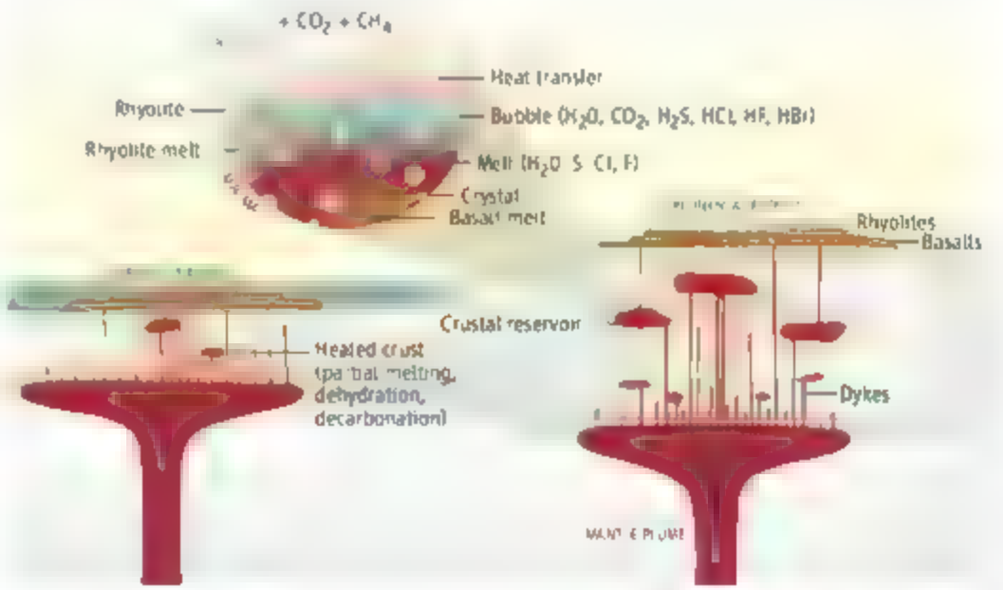

Volatile situation. The mantle plume hits the base of the crust, whether oceanic or continental, which, via dykes, intrusion, heats up, and eventually partially melts, producing magmas rich in silica (rhyolites). Local basalt accumulation in the upper crust produces reservoirs whose cooling may also yield rhyolite. Both basalt and rhyolite magmas, in addition to crystals hosting melt inclusions, may contain gas bubbles (**inset**) in which some volatile species (HCl, HBr, CO_2) may be concentrated. Heating by magmatic intrusions may release CH_4 or CO_2 species.

CREDIT: ADAPTED FROM BRUNO SCAILLET

Centre National de la Recherche Scientifique–Institut National des Sciences de l'Univers, Université d'Orléans, Institut des Sciences de la Terre Orléans, Orléans 45071, France. E-mail: bscaille@cnrs-orleans.fr

ronmental consequences related to catastrophic flood events (*8*), albeit on a much smaller scale.

This understanding of volatiles from the work of Self *et al.*, although clearly a decisive step forward, is far from complete, however. The authors have reasonably focused on quantifying one of the species to which climate is highly sensitive. Sulfur, along with CO_2, indeed reigns supreme in almost all models proposed so far to correlate mass extinctions with flood events, although each has opposite effects (*2*). Other volatiles may also have altered the climate, however, in particular halogens (F, Cl, Br, I). In addition to having regional devastating effects (*9*), halogens may dramatically affect both tropospheric and stratospheric chemistries, with severe impacts on the ozone layer.

According to Self *et al.*, the Deccan basalts were quite rich in Cl, and possibly in other halogens as well, as compared to their oceanic counterpart. Yet, their derived figure of 1 Tg (10^{12} g) of HCl per km^3 of erupted magma may well be a lower bound. Some researchers have proposed on the basis of calculations that basalt-forming floods may have been extremely H_2O and CO_2 rich, with combined amounts of up to 4 weight % (*10*). A consequence of such an elevated volatile content is that basalts may be saturated with gas at depth (see the figure), in which case the gas phase will store a considerable if not dominant part of the halogen budget, a factor not considered in climate models. Yet, given the colossal amounts of magma erupted, the amount of halogens delivered to the atmosphere may have been dramatic as well, and it is not certain that lessons derived from the Pinatubo eruption (*11*), which was three orders of magnitude smaller than the Deccan eruptions, equally apply to flood events. Quantitative evaluation of the amounts of F, Cl, and Br released during magmatic flood activity, and of their possible effects on atmospheric chemistry, should be a priority for future research.

Several uncertainties remain, unfortunately. So far, attention has been focused on the volatiles released by the basalt component. Yet, the composition of several flood provinces has two peaks (*12*), with a more or less prominent silicic component, whose volatile yield must also be evaluated. Contrary to the perceived wisdom (*2*), it has been shown that some silicic floods may have propelled enormous amounts of sulfur into the atmosphere, equivalent to those released by basalt (*13*). The reason lies in the different modes of silicic magma flood production, which in turn depend, among other things, on the locus of plumes that give rise to flood magmas (beneath the continental or oceanic crust) and on the frequency of basalt intrusion in the crust (*14*). A last complicating factor is due to thermal effects of basalt intrusion on crustal rocks. Upon heating, these may release additional volatiles such as CH_4 (*15*) or CO_2 (*16*), in amounts much larger than the pristine content of the magma.

Thus, the geological evidence suggests that the volatile-induced climate response to a flood event may not be unique, and the above list of potential influential factors has to be evaluated on a case-by-case basis. The possible large variation in release of volatiles from flood basalt eruptions offers an explanation as to why some of these massive magma outbursts are associated with worldwide biological crises while others are not (*2*). Besides highly precise geochronological and mass data, the complete elucidation of this particular volcano-climate connection needs careful and detailed petrological understanding of magmas erupted and of the rocks they have passed through, in addition to the determination of how the eruptions occurred. When such a consolidated database is available for each of the dozen or so flood sequences so far documented, then climate models may come into play and tackle the environmental consequences associated with these massive magma floods that have punctuated the last 350 million years. Then, and only then, will the geological community be in position to prove either right or wrong that putative causal link between mass extinctions and volcanism.

References

1. A. Robock, *Rev. Geophys.* **38**, 191 (2000).
2. P. Wignall, *Earth Sci. Rev.* **53**, 1 (2001).
3. S. Self, S. Blake, K. Sharma, M. Widdowson, S. Sephton, *Science* **319**, 1654 (2008).
4. L. W. Alvarez *et al.*, *Science* **208**, 1095 (1980).
5. V. E. Courtillot, P. R. Renne, *C. R. Geosci.* **335**, 113 (2003).
6. C. B. Officer *et al.*, *Nature* **326**, 143 (1987).
7. T. Thordarson, S. Self, *J. Geophys. Res.* **108**, 4011 (2003).
8. A. L. Chenet, F. Fluteau, V. Courtillot, *Earth Planet. Sci. Lett.* **236**, 721 (2005).
9. R. Stone, *Science* **306**, 1278 (2004).
10. R. A. Lange, *Geology* **30**, 179 (2002).
11. A. Tabazadeh, R. P. Turco, *Science* **260**, 1082 (1993).
12. S. E. Bryan *et al.*, *Geol. Soc. Am.* **362**, 97 (2002).
13. B. Scaillet, R. Macdonald, *J. Petrol.* **47**, 1413 (2006).
14. C. Annen, J. Blundy, R. J. S. Sparks, *J. Petrol.* **47**, 505 (2006).
15. G. J. Retallack, A. H. Jahren, *J. Geol.* **116**, 1 (2008).
16. G. Iacono-Marziano *et al.*, *Contrib. Mineral. Petrol.* 10.1007/s00410-007-0267-8 (2007).

10.1126/science.1155525

PLANETARY SCIENCE

Titan's Hidden Ocean

Christophe Sotin[1] and Gabriel Tobie[2]

Data from the Cassini-Huygens mission indicate that an ocean may exist beneath the solid surface of Saturn's moon Titan.

When the Cassini-Huygens mission began to observe Saturn's moon Titan in 2004, its surface was believed to be covered by a global hydrocarbon ocean. Yet the first radar images of its surface, taken by the Cassini spacecraft in October 2004, together with the data collected when the Huygens probe descended to Titan's surface in January 2005, showed most of it to be solid. Since then, geological features such as dunes, channels, lakes, impact craters, and putative cryo-volcanic structures have been documented. Three years after their discovery, Cassini is starting to observe these features for a second time. On page 1649 of this issue, Lorenz *et al.* report a systematic drift of these features, which leads them to conclude that Titan has an ocean buried below several tens of kilometers of ice (*1*).

Titan's dense methane-rich atmosphere makes it impossible to see the poles and use them to determine the spin axis. Scientists have assumed synchronous rotation (Titan always presents the same face to Saturn) and a spin axis perpendicular to the rotation plane of Titan around Saturn. However, using this reference frame, features observed by the Cassini radar instrument for the second time were displaced by several tens of kilometers. Using these data, Stiles *et al.* (*2*) have shown that Titan's obliquity is about 3° and that Titan spins 0.36° per year faster than synchronous spin. In 2005, Tokano and Neubauer (*3*) predicted Titan's spin rate to vary, because angular momentum is exchanged between the atmosphere and the icy

[1]Jet Propulsion Laboratory, California Institute of Technology, Pasadena, CA 91109, USA. E-mail: csotin@jpl.nasa.gov. [2]Laboratoire de Planétologie et Géodynamique, Université de Nantes, 44322 Nantes, France. E-mail: gabriel.tobie@univ-nantes.fr

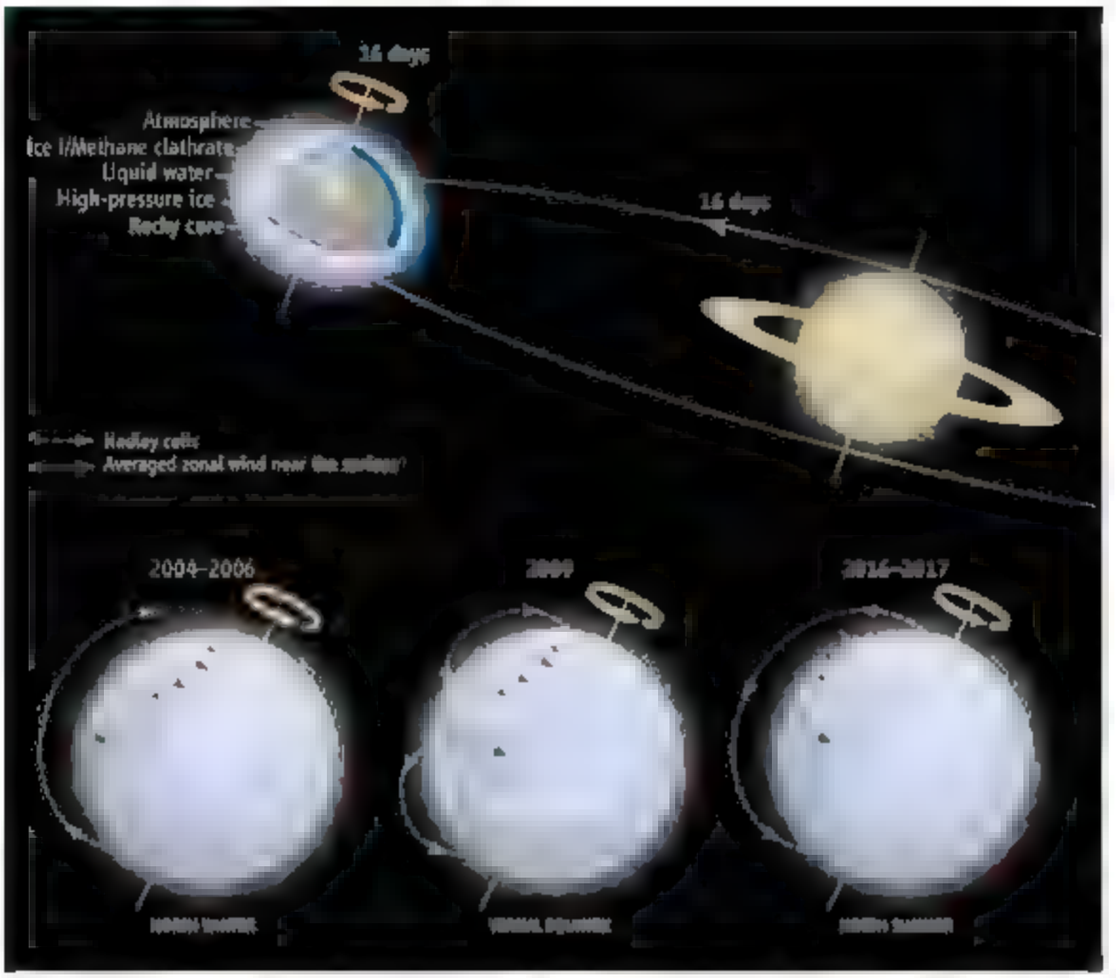

Exploring Titan. (**Top**) Titan orbits around Saturn within about 16 terrestrial days, as shown. Titan and the saturnian system travel around the Sun in about 30 years, and it is the orbit around the Sun that controls the seasonal cycle on Titan due to the obliquity of the Titan-Saturn system. Lorenz *et al.* suggest that an ocean may exist below the solid surface of Titan (see cut-open section), but other explanations of the observed results cannot yet be ruled out. (**Bottom**) During the nominal Cassini mission, it was winter in Titan's northern hemisphere (**left**). Seasonal variations of wind directions near the surface would explain why the observed spin rate is nonsynchronous, as discussed by Lorenz *et al.*, whose model predicts variations in the direction of the winds that affect the spin rate. These predictions may be checked if the Cassini mission is extended to cover the vernal equinox (**middle**) and the northern summer (**right**).

crust as the global wind circulation is seasonally modified (see the figure). Such a variation would not exist if the crust were coupled to the internal solid core.

Lorenz *et al.* now make the link between the model predictions (*3*) and the observations (*2*) and conclude that an internal ocean of liquid water is present. This finding is in agreement with previous models of Titan's evolution (*4*, *5*) that predicted an ammonia-rich deep ocean. If the presence of an ocean is confirmed, Titan would be the fourth object in the solar system with a deep ocean, after the Galileo mission found such liquid layers in Jupiter's moons Ganymede, Callisto, and Europa. Large reservoirs of water, a condition for life to form and develop, are thus a common feature in the solar system.

However, the observations and model predictions do not correlate very well [see figure 2 in (*1*)]. The discrepancies may result from an incomplete description of the seasonal atmospheric cycle and/or from effects in Titan's interior (*6*). Gravitational interaction with the deep interior and the gravitational field of Saturn could reduce the free motion of the icy crust and delay its differential rotation. Such gravitational couplings result from the nonspherical shape of the shell, which is elongated by tidal forces induced by Saturn. For highly viscous ice, the tidal bulge would point exactly to Saturn, prohibiting any motion of the crust relative to the reference system. The observed drift reported by Lorenz *et al.* indicates that the motion is permitted; hence, the mean viscosity of the lower crust must be low enough for the tidal bulge to remain pointed to Saturn, whereas the entire crust drifts eastward or westward depending on the season. The observed spin rate thus suggests not only the presence of an internal ocean, but also a soft lower crust.

Alternatively, recent results by Noyelles *et al.* (*7*) suggest that the apparent faster rotation of Titan may be the consequence of a periodical motion of the pole (wobble), on longer time scales than the seasonal forcing. For specific moment-of-inertia values, the combination of the spin and wobble motions could lead to the rotation period inferred by Lorenz *et al.* Another explanation may be a recent large impact, although there is no evidence for a major basin induced by an impact event in the past 1 million years.

Future observations by the Cassini mission will help to test the interpretation by Lorenz *et al.* Specifically, the predicted variations of the spin rate in the next 10 years can be checked by extending the Cassini mission (see the figure). If the spin rate variations do not change in the coming years, then another process must be responsible for the nonsynchronous state of Titan.

The finding that Titan is not in synchronous rotation is an important discovery of the Cassini mission. If the interpretation that Titan has an internal ocean is supported by other measurements, then Titan is a place where organics are produced and where liquid water is present. Data from Titan could then help to elucidate the formation of organic material in an icy satellite, and to address the question of whether this ocean could be habitable.

With its dunes, lakes, channels, mountains, and cryo-volcanic features, Titan is an active place that resembles Earth, with methane playing the role of water and ice that of silicates. The study of geological processes acting on these different materials by Cassini-Huygens and future missions will help us to understand the cycle of the elements and organic molecules that play a key role in the formation and evolution of life.

References and Notes

1. R. D. Lorenz *et al.*, *Science* **319**, 1649 (2008).
2. B. Stiles *et al.*, *Bull. Am. Astron. Soc.* **39**, 543 (2007).
3. T. Tokano, N. Neubauer, *Geophys. Res. Lett.* **32**, L24203 (2005).
4. O. Grasset, C. Sotin, *Icarus* **123**, 101 (1996).
5. G. Tobie *et al.*, *Nature* **440**, 61 (2006).
6. T. Van Hoolst *et al.*, *Icarus*, 10.1016/j.icarus.2007.12.011 (2008).
7. B. Noyelles *et al.*, *Astron. Astrophys.* **478**, 959 (2008).
8. This work was carried out at JPL, Caltech, under a contract with NASA.

10.1126/science.1155964

CREDIT: ADAPTED FROM CHRISTOPHE SOTIN AND GABRIEL TOBIE

Nanominerals, Mineral Nanoparticles, and Earth Systems

Michael F. Hochella Jr.,[1]* Steven K. Lower,[2] Patricia A. Maurice,[3] R. Lee Penn,[4] Nita Sahai,[5] Donald L. Sparks,[6] Benjamin S. Twining[7]

Minerals are more complex than previously thought because of the discovery that their chemical properties vary as a function of particle size when smaller, in at least one dimension, than a few nanometers, to perhaps as much as several tens of nanometers. These variations are most likely due, at least in part, to differences in surface and near-surface atomic structure, as well as crystal shape and surface topography as a function of size in this smallest of size regimes. It has now been established that these variations may make a difference in important geochemical and biogeochemical reactions and kinetics. This recognition is broadening and enriching our view of how minerals influence the hydrosphere, pedosphere, biosphere, and atmosphere.

Most physical, chemical, and biological processes on Earth are either influenced to some degree or fully driven by the properties of minerals. But with only about ~4500 mineral species presently described, not many relative to millions of prokaryotic and eukaryotic species combined, their diversity and range of influence may seem, by comparison, relatively modest. Minerals exert their influence by constituting the bulk of this rocky planet and having a wide range of composition and structure that is expressed in a marked diversity of physical and chemical properties. Now we are gaining a much better appreciation for another aspect of mineral diversity—that which is expressed in the nanoscale size range (*1*–*3*). Here, atomic and electronic structure of nanoparticles may vary with size even without a phase transformation, and surface-to-volume ratios change dramatically. Such particles are minerals that are as small as roughly 1 nm and as large as several tens of nanometers in at least one dimension. Limiting size in one, two, or three dimensions results in a nanofilm (or nanosheet), a nanorod, or a nanoparticle, respectively. Minerals can be found in all of these shapes, although this review will concentrate on nanoparticles. Nanominerals are defined here as minerals that only exist in this size range; that is, one will not find their equivalent at sizes larger than this. Well-known examples include certain clays as well as iron and manganese (oxyhydr)oxides (with ferrihydrite, an iron oxyhydroxide, as a type example). Mineral nanoparticles are minerals that can also exist in larger sizes, and these probably include most of all known minerals.

The importance of certain types of nanominerals and mineral nanoparticles, namely clays and the smallest mineral colloids, has been known for a long time. What has been generally recognized more recently is that nanominerals and mineral nanoparticles commonly behave differently as a function of their size within the nanoscale size range. Mineral nanoparticles also behave differently than larger micro- and macroscopic crystals of the same mineral. This observation violates aspects of the long-standing formal definition of a mineral. Although definitions vary somewhat, depending on the source, the general consensus is that minerals are naturally occurring, crystalline substances having a characteristic and defined chemical composition (or compositional range in the case of solid solutions). For any particular composition, each mineral expresses a set of specific physical and chemical properties. Nanominerals and mineral nanoparticles satisfy these criteria, except that even with a fixed composition, they express a range of physical and chemical properties depending on their size and shape.

Origin, Occurrence, and Distribution

Under the influence of either abiotic or biotic processes, all minerals go through a nanophase stage during formation. In most cases, this stage is transitory. But in cases where nucleation rates are high and growth rates are slow, as well as

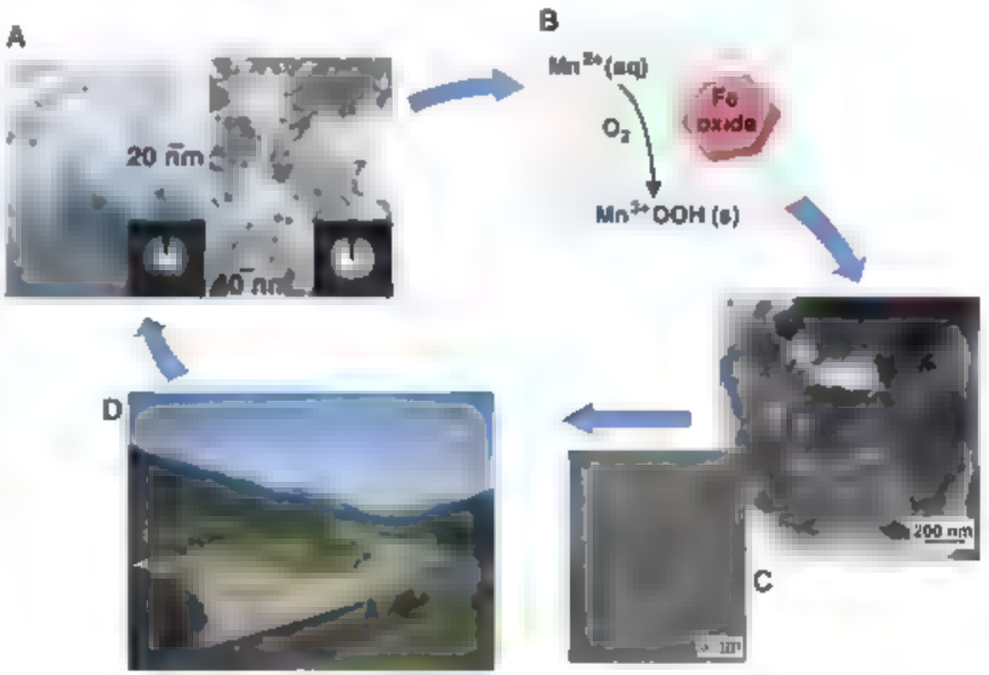

Fig. 1. An example of the cycle of nanomineralogy and nanogeoscience research. (**A**) Mineral nanoparticles (hematite in this case) of different sizes and/or shapes are synthesized (*23*) so that they can be systematically studied. (**B**) Wet chemical experiments that simulate some aspect of interest in a natural setting are run; in this case, hematite nanoparticles are used to catalyze the oxidation of aqueous Mn^{2+} resulting in the formation of a manganese oxyhydroxide (*23*). (**C**) Examples may be found in nature (*42*) that closely compare to systems studied in the lab (*23*): a Mn hydrous oxide nanomineral, a vernadite-like phase making up the darker areas and "strings" in the image to the right; nanocrystals of this mineral are shown at high resolution in the image to the left), which is intimately associated with ferrihydrite (the medium gray areas in the image to the right), contains relatively high concentrations of several toxic heavy metals and is important in toxic metal transport in the Clark Fork River Superfund Complex in Montana (**D**). With field observations, laboratory experiments are refined or created anew, back to (**A**)].

*Center for NanoBioEarth, Department of Geosciences, Virginia Polytechnic Institute and State University (Virginia Tech), Blacksburg, VA 24061–0420, USA. [2]School of Earth Sciences and School of Environment and Natural Resources, Ohio State University, Columbus, OH 43210, USA. [3]Department of Civil Engineering and Geological Sciences, University of Notre Dame, Notre Dame, IN 46556, USA. [4]Department of Chemistry, University of Minnesota, Minneapolis, MN 55455, USA. [5]Department of Geology and Geophysics, University of Wisconsin–Madison, Madison, WI 53706–1692, USA. [6]Center for Critical Zone Research, Department of Plant and Soil Sciences, University of Delaware, Newark, DE 19717–1303, USA. [7]Department of Chemistry and Biochemistry, University of South Carolina, Columbia, SC 29208, USA.

*To whom correspondence should be addressed. E-mail: hochella@vt.edu

where aggregated growth of mineral nanoparticles (4) is not a dominant process, nanominerals and mineral nanoparticles will form and can persist. Mineral nanophases forming under biotic processes, or nanobiomineralization, may involve bacterially driven redox reactions of aqueous species associated with some cell function, such as sequestering a toxic metal or storing a micronutrient, which often result in nanosize minerals (5, 6). Mineral weathering also commonly generates nanosized primary or secondary phases.

Nanominerals and mineral nanoparticles are common and widely distributed throughout the atmosphere, oceans, groundwater and surface waters, soils, in and/or on most living organisms, and even within proteins such as ferritin. Their occurrence is more limited in crustal or mantle rocks, but they do exist in these rocks, and they can even influence deep Earth processes. Although the overall mass distribution of nanominerals and mineral nanoparticles in the Earth system is not known at this time, the oceans may be the principal reservoir for them. Riverine, glacial, and aeolian supplies of nanoparticles to the world's oceans are large, with global biogeochemical consequences (7, 8).

In the atmosphere, the mass of mineral dust derived annually from windblown arid and semiarid lands, and secondarily from agricultural lands, far exceeds the average mass of mineral dust derived from volcanic emissions, as well as biological debris (9). The only large atmospheric inputs of natural particles that rival all of these sources are the halite and hydrous sulfate aerosols from sea spray (10). The total volume of atmospheric mineral particles is dominated by particles that are larger than 100 nm, but numerically, most are nanoparticles less than 50 nm in size (11). The cumulative surface area of these nanoparticles is considerably less than that of the larger particles, but it is still notable (11). Mineral dust, including mineral nanoparticles, is distributed globally from its source regions by way of atmospheric circulation patterns. Climate change is projected to play the key role in variations of mineral dust origins and distribution patterns of the future (12, 13).

In addition to mineral growth or weathering, nanoparticles can be generated by mechanical grinding associated with earthquake-generating faults in Earth's crust. The presence of fault-related fine-grained rock fragments, containing mineral nanoparticles down to 10 to 20 nm in size, is likely to be important in fault mechanics (14, 15). Nanomineralogy is also important in places where the presence of nanominerals and mineral nanoparticles would not necessarily be anticipated. For example, nanoparticles of the high-pressure silicates ringwoodite and wadsleyite play a central role in deep-focus earthquakes at ~300 to 700 km depths in Earth's mantle (16).

Beyond Earth, the presence of nanophase ferric oxides in martian soils and airborne dust has been suspected for several years based on data from spectral imagers onboard the Mars Viking and Pathfinder landers, as well as ground-based observations (17, 18). In chondritic meteorites and interplanetary dust particles, minute concentrations of diamond nanoparticles exist. These nanodiamonds are thought to represent presolar dust, likely forming in supernovae, but it is also suggested that they could form directly in the solar nebula (19) and in conjunction with other star types (20). Nanodiamonds average 3 nm in diameter, and grains as small as 1 nm (< 150 carbon atoms) have been observed (19).

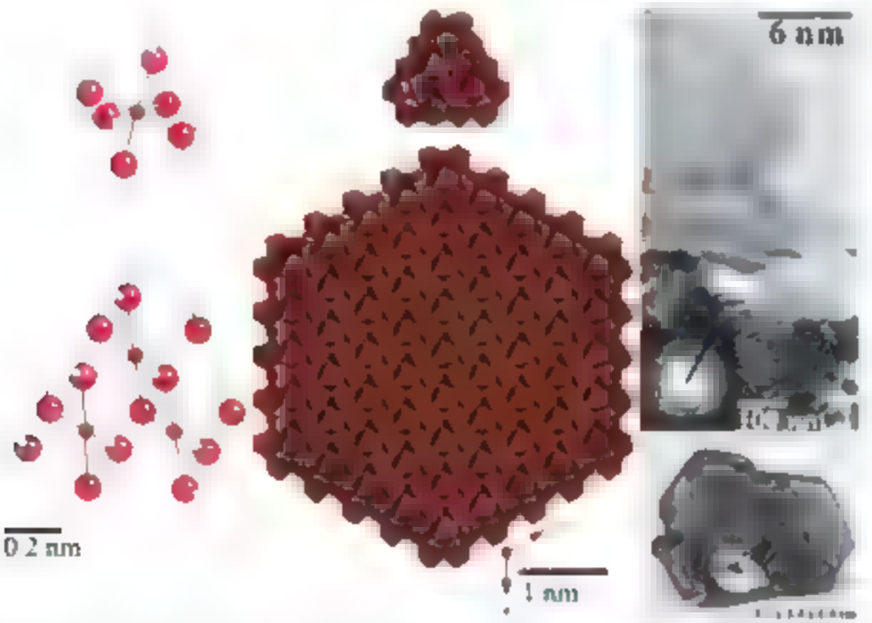

Fig. 2. Examples of how ferric iron occurs in the environment, ranging from the molecular to macroscopic scales. **(Left)** Molecular ferric oxide states, including an octahedrally coordinated monomer [hexaaquairon III (53), top] and oligomer [trimer cluster (54), bottom] with Fe^{3+} (smaller dark red spheres), oxygen (larger light red spheres), and hydrogen (light pink spheres). These molecules are hydrogen-terminated but should only be considered approximations of actual aqueous/environmental states. **(Middle)** Polyhedra, representations of 1- and 5-nm hematite (Fe_2O_3) nanoparticles. Each polyhedron represents an Fe^{3+} in octahedral coordination with oxygen. The thickness of the 5-nm particle should be typically several (roughly five to seven) octahedral layers (23) and that of the 1-nm particle should be just a few octahedral layers. **(Right)** (Top) HRTEM image of hematite nanoparticles from Namibia (Africa) (sample courtesy of the Smithsonian Institution research collection); (Middle) TEM image of an unoriented aggregate of 3- to 5-nm hematite crystals (stippled portion of the image) from an acid mine drainage site in Montana (USA) (55); (Bottom) photograph of macroscopic specular hematite (courtesy of R. Lavinsky).

Changes That Occur with Mineral Size

Current evidence suggests that—as with non-mineral metals, semiconductors, and insulating nanoparticles—nanominerals and mineral nanoparticles may show variations in their atomic structure relative to larger particles and as a function of size in the nanoscale regime (2, 5, 6). Many factors may be involved in these variations, including structurally disordered, strained, and/or reconstructed surfaces, as well as potential variations in surface topography and crystallographic surfaces that are exposed. Electronic structure variations are also expected, as observed for many other nanomaterials.

In small mineral nanoparticles, even the interior structure may be appreciably affected. Using a combination of extended x-ray absorption fine structure, wide-angle x-ray scattering, and pair distribution analyses, Gilbert and others (21) found that the atomic structure of 3.4-nm-diameter sphalerite (ZnS) nanoparticles deviated from that of bulk sphalerite, even though the surface was strongly passivated by a complexing ligand. A loss of structural coherence occurred at distances greater than 2 nm, suggesting that disrupted surface environments drive inhomogeneous internal strain. This results in structural stiffening that far exceeds what is expected by the mild overall bond-length contraction that is observed.

An example of structural variation as a function of particle size in the nanoregime can be garnered from a study of the nanomineral ferrihydrite (22), a common iron oxyhydroxide found in soils, oceans, surface waters, and groundwater. Individual crystallites of ferrihydrite are typically rounded and less than 10 nm in diameter. Pair distribution function analysis, derived from total x-ray scattering experiments and also calculated from refined atomic structure models, was used to gain insight into the structure of this important yet enigmatic phase. The results suggest that ferrihydrites with scattering domain sizes of 6, 3, and 2 nm have the same basic chemistry [$Fe_{10}O_{14}(OH)_2$], crystal structure with space group $P6_3mc$, cell dimensions a = ~5.95 Å

and c = ~9.06 Å, and an 80:20 ratio of octahedrally to tetrahedrally coordinated iron. However, as this nanomineral becomes smaller the a cell edge increases slightly (by 0.03 Å), the c cell edge decreases much more (by 0.16 Å), two of the three crystallographically distinct Fe sites show a decrease in occupancy, and the third Fe site (octahedral) remains fully occupied but shows increasing degrees of distortion. Like sphalerite nanoparticles (*21*), the atomic structure of ferrihydrite crystallites is probably influenced by surface relaxation driving internal disorder and strain (*22*). It is also interesting to consider that the 2-nm particles of ferrihydrite only contain ~ 20 unit cells, so a much higher percentage of Fe sites is at or near the surface versus that in the 6-nm particles with ~30 times the volume.

The Size Range of Nanominerals and Mineral Nanoparticles

The upper size range of nanominerals is likely to be quite variable, depending on the mineral. The upper size limit of mineral nanoparticles can be defined as the size above which the properties of the particles are indistinguishable from those of the bulk material, or (equivalently) the size where, as the mineral particles become smaller and smaller, properties begin to show variations relative to those of larger particles of the same mineral. This size should depend on the nature of the material (e.g., whether it is a metal, semiconductor, or insulator), the particle shape, and the property measured (e.g., whether it is chemical, electrical, optical, mechanical, or thermodynamic). In most cases, it is not known below what size these properties will begin to vary for which minerals, because, to date, few measurements of this type have been made. In a few cases where this information exists for affinities and rates of geochemically relevant reactions for certain iron oxide minerals, it has been suggested that surface area normalized variations are observed when size drops below a few tens of nanometers (*23*, *26*).

The lower size limit of nanominerals and mineral nanoparticles is also challenging to delineate. Minerals, by definition, are crystalline, which requires a repeating arrangement of atoms. Therefore, the smallest atomic clusters cannot qualify as nanominerals or mineral nanoparticles, but an atomic arrangement that is greater than a few unit cells in one or more dimensions would qualify. Using zinc, sulfur, and the mineral sphalerite as an example, one can start with an individual zinc ion dissolved in water: the hexaaqua Zn complex $[Zn^{2+}(H_2O)_6]$. In the presence of dissolved reduced sulfur, ZnS cluster complexes can form, for example, with the stoichiometry of $Zn_3S_3(H_2O)_6$ (*27*). Molecular modeling of this cluster shows that it has a diameter of about 0.7 nm (*27*). A single unit cell of sphalerite, containing Zn_4S_4, has a cubic unit-cell dimension of 0.54 nm with an atomic density greater than that of the cluster. The smallest nanoparticles of sphalerite that have been observed to date are about 1.5 nm in size, although there is no a priori reason not to expect smaller ones (*5*). From this analysis, one should expect the smallest sphalerite nanoparticles to be in the neighborhood of 1 nm in size, with larger ZnS cluster complexes also in this size range.

Reactivity and Stability

With variations in surface and near-surface atomic structure as a function of size, one can anticipate a concomitant change in the chemical interactions of nanominerals and mineral nanoparticles with their environment that does not scale with the total available surface area. Examples of this include the following (all rates are surface area normalized): 7-nm hematite (α-Fe_2O_3) nanocrystals catalyze the oxidation of aqueous Mn^{2+} one to two orders of magnitude faster than 37-nm hematite crystals (*23*), resulting in the rapid formation of Mn oxide minerals that are important heavy metal sorbents in water and soils; hydroquinone-driven reductive dissolution reactions of 5 × 64 nm goethite (α-FeO(OH)) are twice as fast compared with those of 22 × 367 nm goethite (*24*); 7-nm hematite shows a significantly increased sorption affinity for aqueous Cu^{2+} versus that of 25- and 88-nm hematite (*25*); and the reduction rate of hematite by *Shewanella oneidensis* MR-1 with lactate as the sole electron donor is an order of magnitude faster for 99-nm versus 11-nm nanoparticles (*26*).

Thermodynamic considerations in the nanorange are just as fascinating and critical to consider if we are to have a means for predicting the stability of nanophases under various Earth conditions, as well as to understand polymorphic phase transformations driven by size. Toward these goals, surface enthalpies of nanominerals and mineral nanoparticles, as well as enthalpies of phase transitions, have been measured for polymorphs of Al, Fe, Mn, Ti, and Zr oxides via high-temperature oxide-melt solution calorimetry and water adsorption calorimetry (*28*–*30*). At the nanoscale, three factors compete to stabilize a given polymorph: enthalpy of polymorphic transition, surface enthalpy, and enthalpy of hydration. In general, the polymorphs metastable for coarse particles have lower surface energies, leading to crossovers in phase stability as the particle size decreases. This provides a thermodynamic explanation of why nanoparticulate oxides often crystallize as one polymorph, whereas another polymorph is exhibited in coarser-grained material. It is important for future studies to make the thermodynamic predictions more relevant to Earth systems and to obtain systematic size-resolved thermodynamic data for systems of geochemical importance, including clays and carbonates.

Mineral solubility is a crucial property in predicting the fate of minerals and dissolved species in the environment. A modified version of the Kelvin equation predicts solubility dependence on size, stating that as particles get smaller through the nanorange of sizes, their solubilities increase exponentially (*6*). This implies that mineral nanoparticles in a dissolution setting would have short lifespans. However, it is not known how generally applicable this relationship is for minerals. Certain minerals are known to become less soluble as they get smaller (*31*). In addition, mineral nanoparticles of lepidocrocite (an iron oxyhydroxide) and $FePO_4 \cdot nH_2O$ have been formed at lower Fe:P ratios in solution than predicted by their bulk solubilities (*32*). This same study shows that in aqueous binary and ternary systems of Fe + PO_4 ± As, mixed nanophase coprecipitates form with the compositions $Fe[(OH)_3, PO_4] \cdot nH_2O$ and $Fe[(OH)_3, AsO_4, PO_4] \cdot nH_2O$. These nanophases do not have bulk counterparts or known solubilities. They are distinct from ferrihydrite or lepidocrocite with sorbed PO_4 and AsO_4, and are very similar to mixed metastable nanophases found in certain natural sedimentary environments (*32*).

Influence on Earth Chemistry

We start with an example that involves phytoplankton production levels in the open oceans, a process that provides a connection between nanoparticles, oceans, and global atmospheric and hydrospheric chemistry. Ocean phytoplankton play a critical role in influencing the amount of CO_2 in the atmosphere, and phytoplankton growth in large swaths of the global ocean has been shown to be limited by iron availability. Dissolved inorganic and organic complexes are typically thought to comprise the bioavailable pool of iron in the ocean. However, recent studies indicate that a significant fraction of the "dissolved" (<0.4 μm) iron in the ocean is actually composed of iron colloids and nanoparticles (*33*, *34*). Furthermore, this fraction contributes much of the observed variability in dissolved ocean iron concentrations (*35*). Oceanographic studies have typically used ultrafiltration membranes to define colloidal iron as the fraction greater than 20 to 25 nm, but researchers using electron microscopy have noted the presence of 2- to 20-nm particles at even higher concentrations (>10^9 ml^{-1}) (*36*, *37*). These particles appear to consist of organic compounds surrounding 2- to 5-nm mineral nanoparticles (*38*). Recent studies with high-resolution transmission electron microscopy (HRTEM) and electron energy-loss spectroscopy, however, have positively identified iron (oxyhydr)oxide nanoparticles 5 to 20 nm in diameter in glacial and riverine sediments (*7*, *8*). Iron associated with windblown mineral dust, including nanoparticulate dust, is also an important micronutrient input for phytoplankton (*13*). The input of iron within nanoparticles to the oceans has been estimated to far exceed riverine input of dissolved iron (*39*). Further, recent evidence suggests that iron within particulates contained in glacial sediments is bioavailable to marine phytoplankton and that this may be an increasingly important source in this century as icebergs are ejected from Antarctic shelves (*40*). Laboratory experiments

have shown that iron oxide nanoparticles can support the growth of osmotrophic phytoplankton after photoreduction or thermal dissolution (*41*), whereas mixotrophic phytoplankton may access mineral nanoparticles through direct ingestion (*42*).

Nanophase minerals also influence the movement of harmful heavy metals in Earth's near-surface environment via complex interactions involving rock, soil, water, air, and living organisms, in many cases overprinted by anthropogenic processes. For instance, lead, arsenic, copper, and zinc were mobilized over hundreds of kilometers within the Clark Fork River drainage basin, part of which makes up the Clark Fork River Superfund Complex in western Montana, the largest Superfund site in the United States. These metals are incorporated into and transported by a newly discovered nanocrystalline vernadite-like mineral (a manganese oxyhydroxide) along major portions of the river (*43*). This nanomineral likely forms as a result of the catalytic oxidation of aqueous manganese on ferrihydrite surfaces (*23*) (Fig. 1).

The movement of radionuclides (and other toxic metals) in the subsurface often defies laboratory- and thermodynamically based predictions that they should be essentially immobile (*44*). It has been shown that radionuclides can be carried over many kilometers in relatively short periods of time by colloids moving with groundwater. At a nuclear waste reprocessing plant in Mayak, Russia (one of the most contaminated nuclear sites in the world), plutonium has traveled several kilometers in the local groundwater system; 70 to 90% of the plutonium transport was attributed to nanoparticles less than 15 nm in size in the groundwater (*45*). The nanocarriers in this instance were primarily ferric iron oxides (not clays, calcite, rutile, or other nanomineral and mineral nanoparticle colloids that were also present).

The size dependence of the properties of atmospheric nanoparticles is just beginning to be explored. For example, atmospheric mineral nanoparticles [typically halite (NaCl) and hydrous sulfate evaporates from sea spray] are hygroscopic and act as water droplet nucleation and growth centers. This is a critical step in cloud formation. The size and density of the droplets dictate the solar radiation scattering ability and longevity of clouds, both important factors in influencing average global temperatures. The hygroscopic growth factor for NaCl nanoparticles decreases for sizes below 40 nm as a result of a size-dependent shape factor and the Kelvin effect that takes into account the change in surface tension as a function of surface curvature (*46*). Therefore, only relatively large mineral nanoparticles (>40 nm) are expected to contribute to cloud condensation nuclei.

Although minerals can carry human irritants and toxic materials in the atmosphere, many carriers are from anthropogenic sources, most notably particulates emitted from the combustion of fossil fuels (*47*) and many other emissions from the vast numbers of industries that are associated with metals (*48*). Many trace metals in airborne particles, including highly toxic metals such as cadmium, lead, and arsenic, occur in the very fine (<1-μm) to ultrafine (<100-nm) size fraction (*48*, *49*), and their distinctive properties will influence the bioavailability of the metals in these particles.

Elemental distribution and bioavailability, reaction pathways and catalysis, and mineral growth/solubility/weathering are all influenced by phenomena relevant to, with no equivalent phenomena at scales larger or smaller than, the nanoscale. A dissolved ion in aqueous solution behaves differently than that same ion in a 1-nm mineral, and both behave differently than that same ion in a 5-nm or larger mineral. Considering everything that passes through 200- or 2-nm filters as dissolved is not appropriate. Aqueous and gas-based reactions that occur on (or in conjunction with) a molecular cluster versus a small mineral nanoparticle versus a 50-nm or larger mineral particle, all with equivalent compositions (depicted in Fig. 2), are predicted to most often show significantly different pathways and kinetics.

Challenges for the Future

Measuring and understanding nanomineral and mineral nanoparticle origin (biotic or abiotic, natural or anthropogenic), geographic distribution, relevant nanochemistry, and overall influence and impact within the complex chemical and physical framework of Earth systems are all critical challenges for the future. For example, it is still not known whether metal oxide and other potentially catalytically active airborne nanoparticles can significantly modify atmospheric chemistry, even locally, as a result of nanomineral-gas heterogeneous chemical reactions (*11*). It is possible that important reactions may be driven under these specific circumstances and no other atmospheric scenario, especially where aerosols with very high nanomineral or mineral nanoparticle surface areas exist, or where reaction kinetics would be highly favorable on their surfaces. Very little information presently exists in this field. However, if discovered, such findings may be of fundamental interest and importance, much as was the discovery of the production of ozone-destroying chlorine compounds on the surface of polar stratospheric cloud aerosols (*50*).

The same general types of challenges remain in terrestrial and ocean systems. In addition, because nanoparticle aggregation is common in aqueous environments, one must also consider the formation and dispersion of aggregated states, and the transport of reactants to and products from reactive sites within aggregates. Further, when nanoparticles aggregate, it will be important to determine which properties are controlled by individual particles and which by the aggregate as a whole, and how the properties may change as aggregates form and dissociate.

All the complexities of nanomineral and mineral nanoparticle composition, structure, stability, and reactivity also apply to the human body, where normal and pathological mineralization (from the nanosize to the micron-size) affects the calcification of bones, teeth, arteries, and veins, as well as the formation of stones in the kidneys and joints (*51*). An equally important field is called nanotoxicology, defined as the safety evaluation of engineered nanostructures through a knowledge of the mechanisms and biokinetics of nanomaterials causing adverse effects in humans (*52*). The enormous impact of asbestos–human lung interactions gives some idea of the scope and importance of this one subfield. Nanominerals and mineral nanoparticles in the environment have been present throughout the evolutionary development of hominids, and our exposure to these through inhalation, ingestion, and dermal pathways are important foci of nanotoxicology.

The biogeochemical and ecological impacts of natural and synthetic nanomaterials are some of the fastest growing areas of research today, with not only vital scientific but also large environmental, economic, and political consequences (*3*).

References and Notes

1. J. F. Banfield, A. Navrotsky, Eds. *Nanoparticles and the Environment* (Mineralogical Society of America, Washington, DC, 2001).
2. G. A. Waychunas, C. S. Kim, J. F. Banfield, *J. Nanopart. Res.* **7**, 409 (2005).
3. M. S. Wiggenton, K. L. Haun, M. F. Hochella Jr., *J. Environ. Monit.* **9**, 1306 (2007).
4. R. L. Penn, J. F. Banfield, *Science* **281**, 969 (1998).
5. J. F. Banfield, H. Zhang, in (1), pp. 1–58.
6. B. Gilbert, J. F. Banfield, in *Molecular Geomicrobiology*, J. F. Banfield, J. Cervini-Silva, K. H. Nealson, Eds. (Mineralogical Society of America, Chantilly, VA, 2005), pp. 109–155.
7. S. W. Poulton, R. Raiswell, *Chem. Geol.* **218**, 203 (2005).
8. R. Raiswell *et al.*, *Geochim. Cosmochim. Acta* **70**, 2765 (2006).
9. J. H. Seinfeld, S. N. Pandis, *Atmospheric Chemistry and Physics* (Wiley, New York, 1998).
10. C. D. O'Dowd, M. H. Smith, I. E. Consterdine, J. A. Lowe, *Atmos. Environ.* **31**, 73 (1997).
11. C. Anastasio, S. T. Martin, in (2), pp. 293–349.
12. I. Tegen, M. Werner, S. P. Harrison, K. E. Kohfeld, *Geophys. Res. Lett.* **31**, L05105 (2004).
13. J. M. Prospero, P. J. Lamb, *Science* **302**, 1024 (2003).
14. B. Wilson, T. Dewers, Z. Reches, J. Brune, *Nature* **434**, 749 (2005).
15. O. Dor, Y. Ben-Zion, T. K. Rockwell, J. Brune, *Earth Planet. Sci. Lett.* **245**, 642 (2006).
16. H. W. Green II, P. C. Burnley, *Nature* **341**, 733 (1989).
17. J. F. Bell III *et al.*, *J. Geophys. Res.* **105**, 1721 (2000).
18. R. V. Morris *et al.*, *J. Geophys. Res.* **105**, 1757 (2000).
19. Z. R. Dai *et al.*, *Nature* **418**, 157 (2002).
20. A. B. Verchovsky *et al.*, *Astrophys. J.* **651**, 481 (2006).
21. B. Gilbert, F. Huang, H. Zhang, G. A. Waychunas, J. F. Banfield, *Science* **305**, 651 (2004).
22. F. M. Michel *et al.*, *Science* **316**, 1726 (2007).
23. A. S. Madden, M. F. Hochella Jr., *Geochim. Cosmochim. Acta* **69**, 389 (2005).
24. A. J. Anschutz, R. L. Penn, *Geochem. Trans.* **6**, 60 (2005).
25. A. S. Madden, M. F. Hochella Jr., T. P. Luxton, *Geochim. Cosmochim. Acta* **70**, 4095 (2006).
26. S. Bose *et al.*, in *Abstracts of Papers*, 232nd National Meeting of the American Chemical Society, San Francisco,

10 to 14 September 2006 (American Chemical Society, Washington, DC, 2006).
27. G. W. Luther, D. T. Rickard, *J. Nanopart. Res.* **7**, 389 (2005).
28. A. Navrotsky, in (*1*), pp. 73–103.
29. A. Navrotsky, *J. Chem. Thermodyn.* **39**, 2 (2007).
30. A. Navrotsky, L. Mazeina, J. Majzlan, *Science* **319**, 1635 (2008).
31. R. K. Tang, L. J. Wang, G. H. Nancollas, *J. Mater. Chem.* **14**, 2341 (2004).
32. N. Saha, Y. Lee, H. Xu, M. Ciardelli, J.-F. Gaillard, *Geochim. Cosmochim. Acta* **71**, 3193 (2007).
33. J. Wu, E. Boyle, W. Sunda, L.-S. Wen, *Science* **293**, 847 (2001).
34. J. Nishioka, S. Takeda, C. S. Wong, W. K. Johnson, *Mar. Chem.* **74**, 157 (2001).
35. B. A. Bergquist, J. Wu, E. A. Boyle, *Geochim. Cosmochim. Acta* **71**, 2960 (2007).
36. M. L. Wells, E. D. Goldberg, *Nature* **353**, 342 (1991).
37. M. L. Wells, E. D. Goldberg, *Limnol. Oceanogr.* **39**, 286 (1994).
38. M. L. Wells, E. D. Goldberg, *Mar. Chem.* **40**, 5 (1992).
39. S. W. Poulton, R. Raiswell, *Am. J. Sci.* **302**, 774 (2002).
40. K. L. Smith *et al.*, *Science* **317**, 478 (2007).
41. H. W. Rich, F. M. M. Morel, *Limnol. Oceanogr.* **35**, 652 (1990).
42. L. M. Nodwell, R. M. Price, *Limnol. Oceanogr.* **46**, 765 (2001).
43. M. F. Hochella Jr., T. Kasama, A. Putnis, C. Putnis, J. M. Moore, *Am. Mineral.* **90**, 718 (2005).
44. W. H. Penrose *et al.*, *Environ. Sci. Technol.* **24**, 228 (1990).
45. A. P. Novikov *et al.*, *Science* **314**, 638 (2006).
46. G. Bishop, I. M. Russell, P. R. Buseck, S. T. Martin, *Geophys. Res. Lett.* **33**, L07801 (2006).
47. M. Zheng *et al.*, *Atmos. Environ.* **39**, 3967 (2005).
48. S. Utsunomiya, K. A. Jensen, G. J. Keeler, R. C. Ewing, *Environ. Sci. Technol.* **38**, 2289 (2004).
49. L. E. Mayr, J. J. Bang, *Atmos. Environ.* **37**, 4795 (2003).
50. M. J. Molina, T. Tso, L. T. Molina, F. C. Wang, *Science* **238**, 1253 (1987).
51. M. Sahai, M. A. A. Schoonen, Eds. *Medical Mineralogy and Geochemistry* (Mineralogical Society of America, Chantilly, VA, 2006).
52. G. Oberdörster, E. Oberdörster, J. Oberdörster, *Environ. Health Perspect.* **113**, 823 (2005).
53. C. Jung *et al.*, *J. Chem. Soc. Dalton Trans.* **2002**, 1024 (2002).
54. K. M. Rosso, E. S. Ilton, *J. Chem. Phys.* **119**, 9207 (2003).
55. M. F. Hochella Jr., J. N. Moore, U. Golla, A. Putnis, *Geochim. Cosmochim. Acta* **63**, 3395 (1999).
56. We thank NSF, Directorate for Geosciences, for sponsoring the Nanogeosciences Working Group from which this paper originated. Support was also provided by NSF grants EAR02-21966 (Environmental Molecular Science Institute), DGE-0504196 (Integrative Graduate Education and Research Traineeship Program) CAREER-0346385, EAR-0346889, EAR-0525297, EAR-0544246, and OCE-0527062; U.S. Department of Energy grants DE-FG02-02ER15323 and DE-FG02-06ER15786; U.S. Department of Agriculture grant USDA 2005-35107-16105; and the Institute for Critical Technology and Applied Science at Virginia Tech. We acknowledge two anonymous reviewers for many important suggestions that improved this manuscript, as well as S. Bose, H. Green II, B. Lower, A. Madden, R. Mahajan, A. Navrotsky, and N. Woodward for very useful discussions.

10.1126/science.1141134

Size-Driven Structural and Thermodynamic Complexity in Iron Oxides

Alexandra Navrotsky,[1]* Lena Mazeina,[2] Juraj Majzlan[3]

Iron oxides occur ubiquitously in environmental, geological, planetary, and technological settings. They exist in a rich variety of structures and hydration states. They are commonly fine-grained (nanophase) and poorly crystalline. This review summarizes recently measured thermodynamic data on their formation and surface energies. These data are essential for calculating the thermodynamic stability fields of the various iron oxide and oxyhydroxide phases and understanding their occurrence in natural and anthropogenic environments. The competition between surface enthalpy and the energetics of phase transformation leads to the general conclusion that polymorphs metastable as micrometer-sized or larger crystals can often be thermodynamically stabilized at the nanoscale. Such size-driven crossovers in stability help to explain patterns of occurrence of different iron oxides in nature.

It is hard to find a process or environment in which iron oxides do not participate. From the surface of Mars to the depths of Earth, from old rusting factories to high-tech magnetic recording devices, from pigeon brains and magnetotactic bacteria to drug delivery systems, anhydrous and hydrated iron oxides are ubiquitous. They are constituents of rocks and soils, products of corrosion and bacterial processes, and sources of iron as a nutrient. They have many commercial applications: pigments, catalysts, medical devices, sensors, and recording media. Nanotechnology increasingly makes use of iron oxide nanoparticles and thin films.

Iron oxides exist in a bewildering variety of polymorphs (*1*). Anhydrous ferric oxides include hematite (α-Fe_2O_3), maghemite (γ-Fe_2O_3), and the less common ε- and β-Fe_2O_3. Fe_3O_4 (magnetite) and $Fe_{1-x}O$ (wustite) contain both ferric and ferrous iron. Maghemite and magnetite, both spinels, can form a continuous solid solution. The oxyhydroxides, nominally FeOOH, include goethite, lepidocrocite, akaganeite, and several other polymorphs. They often contain excess water. More oversized forms such as ferrihydrite, nominally $Fe(OH)_3$, have even more variable water content. Hydrated phases containing both ferrous and ferric iron include the green rusts, layered hydroxides with different anions in the interlayer. A further complication is that many iron oxides, both in nature and in the laboratory, are exceedingly fine-grained (nanophase) and therefore hard to characterize.

This complexity has meant that until recently, knowledge of the structural details, thermodynamics, and reactivity of iron oxides has been lacking. One could not understand or predict which phases form under what conditions, which polymorphs are stable and which metastable, and

[1]Peter A. Rock Thermochemistry Laboratory and Nanomaterials in the Environment, Agriculture, and Technology Organized Research Unit, University of California, Davis, CA 95616, USA. [2]Naval Research Laboratory, Washington, DC 20375, USA. [3]Institute of Mineralogy, Petrology and Geochemistry, Albert-Ludwigs-Universität Freiburg, D-79104 Freiburg, Germany.

*To whom correspondence should be addressed. E-mail: anavrotsky@ucdavis.edu

Table 1. Thermodynamic data for iron oxides. Enthalpies of formation (ΔH_f°) and Gibbs free energies of formation (ΔG_f°) are for conditions of 298 K and 1 bar. Surface enthalpies are given for anhydrous (ΔH_s) and hydrated ($\Delta H_s^{H_2O}$) surfaces. Most of the data are taken from the references cited. Values of Gibbs free energy without citations were calculated from corresponding values of standard enthalpies and entropies.

Oxide	ΔH_f° (kJ mol^{-1})	S° (J mol^{-1} K^{-1})	ΔS_f° (J mol^{-1} K^{-1})	ΔG_f° (kJ mol^{-1})	$\Delta H_s^{H_2O}$ (J m^{-2})	ΔH_s (J m^{-2})
Hematite, α-Fe_2O_3	−826.2 ± 1.3 (*31*)	87.4 ± 0.2 (*31*)	274.5 ± 0.3 (*31*)	−744.4 ± 1.3 (*31*)	0.75 ± 0.16 (*13*)	1.9 ± 0.3 (*18*)
Maghemite, γ-Fe_2O_3	−811.6 ± 2.2 (*4*)	93.0 ± 0.2 (*17*)	268.9 ± 0.3 (*17*)	−731.4 ± 2.0	0.57 ± 0.10 (*4*)	0.71 ± 0.13 (*4*)
ε-Fe_2O_3	−798 ± 7 (*15*)			−717.8 ± 6.6 (*15*)		
Goethite, α-FeOOH	−561.5 ± 1.5 (*12*)	59.7 ± 0.2 (*17*)	237.9 ± 0.2 (*17*)	−490.6 ± 1.5	0.60 ± 0.10 (*12*)	0.91 ± 0.09 (*18*)
Lepidocrocite, γ-FeOOH	−552.0 ± 1.6 (*10*)	65.1 ± 0.2 (*17*)	−232.5 ± 0.2 (*17*)	−482.7 ± 3.1	0.40 ± 0.16 (*10*)	0.62 ± 0.14 (*10*)
Akaganeite, β-FeOOH	−554.7 ± 1.9 (*11*)	53.8 ± 3.3 (*32*)	246.2 ± 3.3 (*32*)	−481.7 ± 1.9	0.34 ± 0.04 (*11*)	0.44 ± 0.04 (*11*)
Feroxyhyte, δ-FeOOH	−552.0 ± 1.0 (*13*)			−483.1 ± 1.3 (*13*)		
Ferrihydrite, $Fe(OH)_3$	−830.3 ± 2.0 (*15*)			−711.0 ± 2.0 (*15*)		

when and how they transform. These questions are important because each material has unique physical properties, chemical reactivity, and bioavailability. Furthermore, physical and chemical properties commonly change with particle size and degree of hydration. New structural, spectroscopic, and thermodynamic approaches are now enabling more sophisticated characterization and a more quantitative approach to phase stability. Here, we summarize thermodynamic data and discuss the current understanding of the factors affecting the occurrence and stability of various iron oxides. A key point is the importance of particle size and hydration in determining the energetics and in stabilizing, at the nanoscale, phases metastable in the bulk.

Synthesis, Structure, and Thermodynamic Properties

The synthesis and characterization of iron oxides with well-defined crystal structure, chemical composition, particle size, and hydration state are essential to determining their thermodynamic and kinetic parameters. Oxyhydroxides are normally obtained by precipitation from aqueous solution (*1*). Particle size is controlled by initial iron concentration, organic additives, pH, and temperature. Wet methods for synthesizing anhydrous iron oxides (Fe_2O_3 and/or Fe_3O_4) include those above as well as methods that use surfactants and templates (*2*, *3*) to prevent agglomeration. Dry methods, such as laser-induced pyrolysis of organometallic precursors (*4*) and ball milling (*5*), are effective for Fe_2O_3 and Fe_3O_4, especially for particle sizes less than 5 nm.

The structures of crystalline bulk iron oxides are well known (*1*). They are based on hexagonal or cubic packing of oxygen with iron ions occupying octahedral interstices. The exceptions are the structure of akaganeite, based on a body-centered cubic arrangement of oxygen, and those of maghemite and magnetite, containing abundant tetrahedral iron.

The structure of nanoparticles often varies as a function of their size and the surrounding medium. Hematite nanoparticles may vary in structure and may possess maghemite-like structures (i.e., tetrahedral defects near the surface) (*6*). The surface regions in lepidocrocite nanoparticles are sufficiently different from the bulk that their respective signals can be recognized in Mössbauer spectra (*6*). Recent studies of nanoakaganeite show that at very high surface areas, where particle size becomes comparable to a few unit cells, akaganeite may contain goethite-like structural features possibly related to the collapse of exposed tunnels (*7*).

Ferrihydrite is widespread and has the smallest particle size of all iron oxides. There are still debates about its structure. Is it a single phase with iron both octahedrally and tetrahedrally coordinated (*8*), or a mixture of phases with variable structure and crystallinity (*9*)? The nature of its extensive disorder is still controversial. Comparison of various results is further complicated because each synthesis potentially yields a slightly different product and the structural properties of the particles appear to be size-dependent. Also, during characterization, the particles may be altered by high vacuum and beam damage in the electron microscope. This complexity emphasizes the need to investigate the surface and bulk structure and energetics of not only perfect single crystals (not always available and, when available, not necessarily relevant to common materials) but also nanoparticles and poorly crystalline materials. Because of chemical and structural variability, it is also critical to determine chemical composition, including water content, surface area, and particle size (and its distribution). Once well-characterized materials are identified, physical, structural, spectroscopic, and thermodynamic studies on them can be compared and interpreted with reference to better-constrained variables. Much recent research is taking this direction and applying a combination of different techniques to the same well-characterized samples.

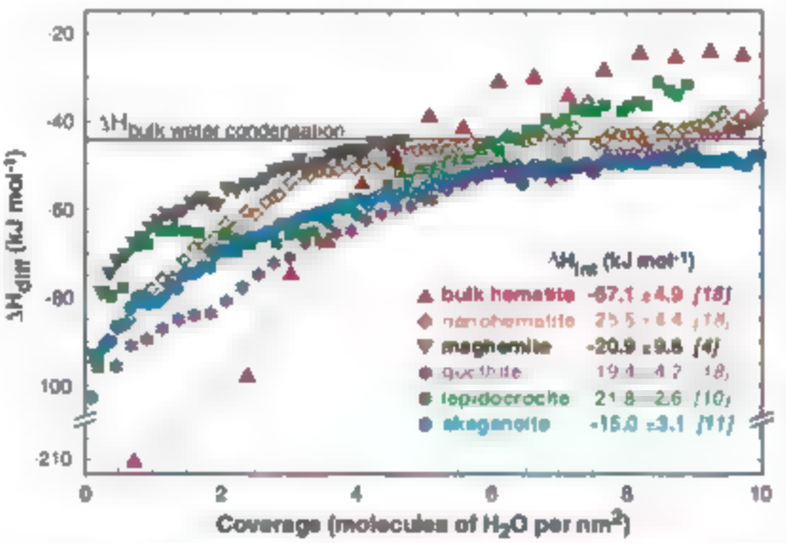

Fig. 1. Differential enthalpies of water vapor adsorption for different iron oxides, together with values of integral enthalpies of adsorption relative to liquid water. [Data from (*4*, *10*–*13*, *18*)]

The thermodynamics of formation of iron oxides, as of any materials, is governed by enthalpy (ΔH) and entropy (ΔS) terms, such that the Gibbs free energy (ΔG) is given by $\Delta G = \Delta H - T\Delta S$, where T is absolute temperature. Enthalpies of formation are determined by solution calorimetric techniques, with a molten oxide solvent used for anhydrous and moderately hydrated iron oxides, and aqueous acid for some heavily hydrated materials (*4*, *7*, *10*, *15*). New developments and significant improvements of sensitivity of older calorimetric techniques (*7*, *10*, *16*) enabled measurements of enthalpy differences between coarse- and fine-grained samples and studying the effects of hydration. Standard entropies (S°_{298}) are obtained from heat capacity measurements from cryogenic to room temperatures (*17*). Free energies can be obtained from aqueous solubility but, because of sample variability discussed above and the difficulty of obtaining reversed equilibrium, often make such measurements problematic. Thus, combining measured enthalpy and entropy to obtain free energy is generally a more reliable method (Table 1).

For coarse particles at ambient conditions, hematite is the most stable Fe_2O_3 polymorph, lower in Gibbs free energy than γ- or ε-Fe_2O_3, and goethite is the most stable FeOOH phase, lower in Gibbs free energy than a host of other oxyhydroxides (Table 1). However, the other polymorphs are not much higher in enthalpy and are similar in entropy. Thus, ΔG_f generally follows similar trends to ΔH_f and the other polymorphs are only slightly higher in Gibbs free energy. Therefore, being only slightly metastable, they are kinetically accessible when precipitated from aqueous solution. Moreover, they are often thermodynamically stabilized as small particles (see below).

Stability at the Nanoscale

Small particles are expected to have higher enthalpies and free energies than large crystals because of a positive surface energy. In contact with water and in most terrestrial environments, the particle surfaces are hydrated. Indeed, nanoparticles hold on to their water tenaciously. Thus, the thermodynamics of different polymorphs at the nanoscale will depend on the energetics of the bulk polymorphs, the particle size (or surface area), and the extent of hydration. To separate these factors, much recent effort has gone into combining solution calorimetry of well-characterized samples of different polymorphs (with known surface area and water content) with measurements of the heat of adsorption of water vapor (*10*, *13*, *15*, *18*). A new approach to measuring enthalpies of water adsorption combines a microcalorimeter coupled to a gas-adsorption analytical system (*19*). This combined system enables precise gas dosing, volumetric detection of amount of adsorbed water, and simultaneous measurement of heat effect and adsorption isotherm (amount of adsorbed water versus pressure). This method provides relatively rapid, automated, and high-resolution measurement of heat of adsorption as a function of surface coverage.

Figure 1 shows the differential heats of adsorption of water versus coverage for a number of iron oxides and oxyhydroxides, together with corresponding values of integral heats of adsorption. The integral adds all the differential heats up to a coverage where the heat of adsorption is simply the heat of condensation (−44 kJ per mole of H_2O) and further water is merely physisorbed. The water adsorption enthalpies for different FeOOH polymorphs show similar behavior. The values for maghemite and nano-hematite are also similar to those for oxyhydroxides. These similarities imply that surface bonding for water on all these phases is similar, and they suggest the possibility that all nanoparticle surfaces can be reconstructed to a relatively common structure. The most tightly held water at initial low coverage is bound more strongly than in the liquid by about 60 kJ mol^{-1}. Recent data suggest that coarse hematite behaves differently from hematite nanoparticles (see Fig. 1) and holds water more tightly than do nanoparticles by a factor of 2. Because the distribution of orientations of surface planes exposed and possible surface reconstruction in each sample cannot be quantified, comparisons of different samples are difficult. However, the strongly exothermic enthalpies suggest that H_2O on the larger particles may dissociate into tightly bound OH groups to satisfy incomplete bonding geometries on the initial surface. Such high-energy surface sites may never be made available on the nanoparticles because they cannot be fully dehydrated without coarsening, whereas coarse hematite can be outgassed at higher temperatures.

To derive surface enthalpy, one must separate the effect on measured enthalpy of surface area from that of water adsorption. This can be done in two ways. If one considers the water to be adsorbed with an enthalpy equal to its heat of condensation, then the resulting corrected solution calorimetric data (*14*), plotted versus the surface area (Table 1 and Fig. 2), produces the surface enthalpy of the hydrated surface as the slope of the linear fit (*10*, *12*). This is because any effects associated with differences in enthalpy of water adsorption, resulting from interaction of water with the surface and surface relaxation, are still included in the corrected enthalpy, because the reference state is taken as bulk liquid water. On the other hand, if one uses the measured integral heat of water adsorption to correct for the water adsorption enthalpy, one obtains the surface enthalpy of the anhydrous surface (Table 1 and Fig. 2). Surface energy, enthalpy, and free energy are expected to be very similar, especially at room temperature, and we make no serious distinction among these three terms. We also note that Fig. 2 has surface areas plotted in m^2 mol^{-1}, rather than showing particle size or area in m^2 g^{-1}. The former is necessary for the slope to represent a surface enthalpy and for the points of crossover to be meaningful.

One needs to know surface enthalpies for both hydrated (wet) and anhydrous (dry) surfaces because each is involved in different processes. Wet surfaces are appropriate for phase transformations and reactions in the ambient terrestrial environment (humid air, water, soil). In processes at higher temperatures (metamorphic, igneous, and technological reactions) or near-vacuum conditions (the surface of the Moon and Mars, various deposition chambers and electron microscopes), the enthalpy of the dry surface may be relevant.

Surface enthalpy (whether comparing wet or dry surfaces) is much higher for the anhydrous phases (oxides) than for any of the hydrous phases (oxyhydroxides). This is a general trend also seen in the alumina system (Al_2O_3 versus AlOOH) (*20*). A lower surface enthalpy allows oxyhydroxides to exist with larger surface areas and to be thermodynamically more competitive at smaller particle sizes. Figure 3 shows calculated dehydration curves for goethite to hematite ($2FeOOH = Fe_2O_3 + H_2O$) as a function of temperature and water pressure, for bulk and for 10-nm particles. If coarsening is slower than decomposition, the stability field of the hydrous phase (goethite) expands to significantly higher temperatures, allowing goethite to persist—as an equilibrium phase under the constraint of nearly constant particle size—to temperatures more than 100 K higher than those calculated by straightforward bulk thermodynamics. Once more, this difference emphasizes the need to take nanoscale phenomena into account when considering phase stability and reactivity.

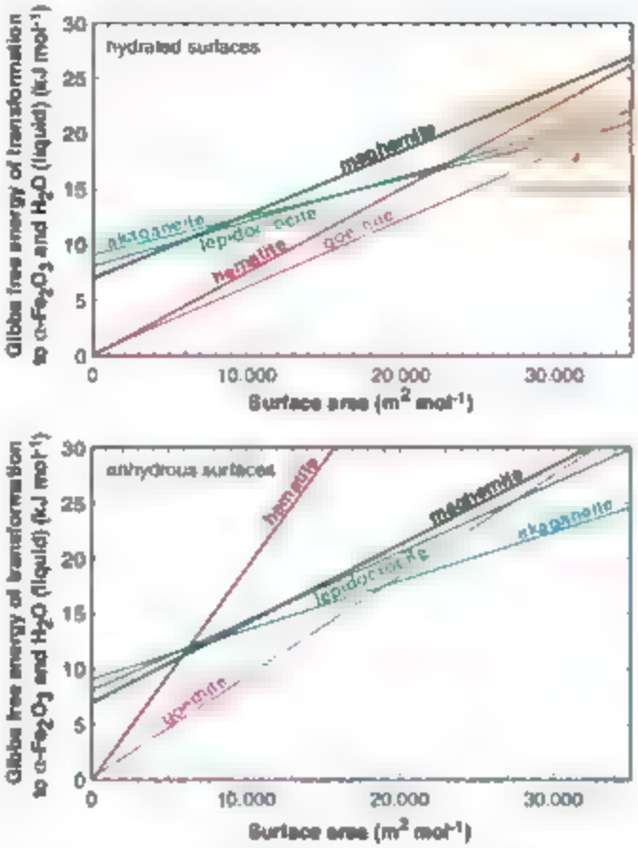

Fig. 2. Enthalpy, relative to coarse Fe_2O_3 (hematite) plus liquid water at 298 K, of various iron oxide and oxyhydroxide polymorphs as a formation of surface area per mole of $FeO_{1.5}$, FeOOH, or $Fe(OH)_3$. Lines are calculated from data in Table 1. Values for ferrihydrite are approximate because of sample variability and are represented as an elliptical area. Values of surface areas are plotted for formula units FeOOH (oxyhydroxides), $Fe(OH)_3$ (ferrihydrite), and $FeO_{1.5}$ (hematite and maghemite) for thermodynamic consistency when comparing different compositions. Corresponding values of surface areas (m^2 g^{-1}) and average particle size at the crossovers are discussed in the text.

Thermodynamic Control of Occurrences of Iron Oxides

Knowing the free energy of formation and the surface enthalpy (or free energy) of various iron oxides, one can predict their stability for a given surface area. Thermodynamic crossovers of the stability of iron oxides as a function of their particle size or surface area (Fig. 2) dominate these relations.

Goethite becomes thermodynamically stable relative to hematite and water at surface areas greater than about 15 m^2 g^{-1} (particle size 60 nm, assuming spherical particles). Lepidocrocite

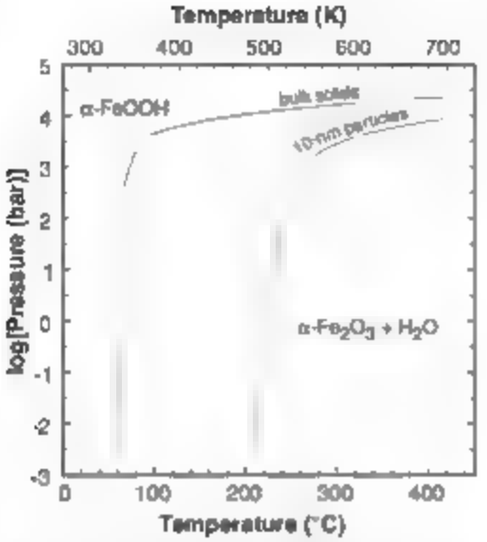

Fig. 3. Pressure-temperature diagram for the reaction α-FeOOH (goethite) = α-Fe_2O_3 (hematite) + H_2O (fluid). The curve at lower temperature shows the equilibrium among bulk solid phases and water (fluid implies liquid, vapor, or fluid above the critical point), whereas that at higher temperature shows equilibrium for 10-nm particles of hematite and goethite plus water.

becomes more energetically stable than maghemite and hematite at surface areas greater than 70 $m^2 g^{-1}$ (particle size 12 nm). Akaganeite becomes stable relative to goethite at surface areas greater than 200 $m^2 g^{-1}$ (particle size 5 nm).

The stability field of ferrihydrite overlaps those of many other iron oxides (hematite, maghemite, goethite, akaganeite, and lepidocrocite) (Fig. 2). At these high surface areas, ferrihydrite is thermodynamically very competitive with other iron oxides. This fact alone explains the ease with which ferrihydrite forms in a large variety of environments and persists if no coarsening occurs. Furthermore, variations in the structure of ferrihydrite, and much of the controversy about its structure, may arise because it can form from different oxyhydroxide precursors, over a range of particle sizes, and in a wide range of conditions.

The complex energetic crossovers shown in Fig. 2 are directly applicable to the occurrence of iron oxide minerals in soils. The most striking example is the hematite-goethite pair. Although the stable bulk assemblage at ambient conditions is hematite plus liquid water, Fig. 2 shows that almost any decrease in size leads to stabilization of goethite (*22*). Hence, particle size exerts major control over the relative stability and formation of hematite and goethite, even though soils represent a system that is too complex to be controlled just by a single variable.

The hematite-goethite equilibrium may be also shifted by variations in temperature, water activity, and the thermodynamics of Fe-Al substitution (*23*). The direct transformation of hematite to goethite or goethite to hematite has not been observed under ambient conditions, and long-term experiments documenting this transformation are lacking (*1*). However, water adsorption experiments have shown that hydrated hematite surfaces behave thermodynamically like the surfaces of goethite (*18*). Thus, perhaps the transformations may begin at the surfaces of nanoparticles, especially at temperatures somewhat above ambient. Transformation in either direction would then happen easily on the exposed goethite-like hydrated surfaces of either phase at the nanoscale. If the transformation occurs by a dissolution-reprecipitation process, those surfaces offer ample nucleation sites. The kinetic hindrance to coarsening below about 300°C ensures that the dehydration curve is that for small particles, with goethite stabilized to higher temperatures than in the bulk (Fig. 3).

Another natural laboratory with abundant iron oxides is the surface of Mars. The suspected presence of hematite was recently confirmed by in situ Mössbauer measurements (*24*). Earlier experiments performed on both Viking probes and Mars Pathfinder indicate that martian dust contains abundant maghemite (*25*). This maghemite is probably nanophase, with particle size of about 10 nm. The abundance of maghemite at the surface of Mars is readily explained by Fig. 2. Under dry conditions, as on Mars, maghemite particles become thermodynamically stable with respect to hematite particles at sizes of about 16 nm. Thus, maghemite nanoparticles are stable at the martian surface. Under wet conditions prevalent on Earth, the stabilization of maghemite is less pronounced, and goethite and other oxyhydroxides are competitive at the nanoscale. Although maghemite occurs in terrestrial soils (*26*), it is generally absent in older terrestrial sediments and rocks, both because of its limited stability in a hydrous environment and because of coarsening and transformation during burial and diagenesis.

During a possible solid-state akaganeite-goethite transformation involving biomineralization, the particle size of goethite is found to be bigger than that of akaganeite (*3*), supporting the stability crossovers presented here. According to recent structural observations (*7*), this transformation need not involve severe reconstruction, because fragments of the collapsed tunnels of akaganeite resemble structural blocks of goethite.

Transformation of lepidocrocite to goethite is not structurally straightforward, and only dissolution-reprecipitation mechanisms have been described in laboratory studies. The goethite is reported to have bigger particle size than the initial dissolving lepidocrocite (*27*). However, in natural systems, lepidocrocite crystals both larger and smaller than coexisting goethite have been reported (*28*, *29*). Goethite and lepidocrocite may often crystallize simultaneously from a ferrous iron source (*29*). Their further coarsening and or transformation depends on iron oxide thermodynamics but may also be influenced by temperature and the presence of silicates and carbonates (*1*).

Figure 2 also supports observations that lepidocrocite, especially when fine-grained, first transforms to maghemite (upon heating and/or in vacuum) and only then to hematite. This is consistent with the thermodynamic stability of maghemite relative to hematite at particle sizes less than about 16 nm. A direct size-driven phase transition between hematite and maghemite was observed with ball milling (*30*). It also supports the calculated size-related stability.

We conclude that the size-driven thermodynamic differences among iron oxide phases that are closely balanced in overall thermodynamic properties must be taken into account if we are to understand and predict the formation, stability, and transformation of these complex materials in geologic, environmental, and industrial settings.

References and Notes

1. R. M. Cornell, U. Schwertmann, *The Iron Oxides: Structure, Properties, Reactions, Occurrences and Uses* (Wiley-VCH, Weinheim, Germany, ed. 2, 2003).
2. J. A. Dahl, B. L. S. Maddux, J. E. Hutchison, *Chem. Rev.* **107**, 2228 (2007).
3. M. Nesterova, J. Moreau, J. F. Banfield, *Geochim. Cosmochim. Acta* **67**, 1185 (2003).
4. O. Bomati-Miguel, L. Mazeina, A. Navrotsky, S. Veintemillas-Verdaguer, *Chem. Mater.* **20**, 591 (2008).
5. H. Zhang, B. Gilbert, F. Huang, J. F. Banfield, *Nature* **424**, 1025 (2003).
6. E. De Grave, R. M. Persoons, D. G. Chambaere, R. E. Vandenberghe, L. H. Bowen, *Phys. Chem. Miner.* **13**, 83 (1986).
7. S. W. Deore, thesis, University of California, Davis (2006).
8. F. M. Michel *et al.*, *Science* **316**, 1726 (2007); published online 23 May 2007 (10.1126/science.1142525).
9. D. E. Janney, J. M. Cowley, P. R. Buseck, *Am. Mineral.* **86**, 327 (2001).
10. J. Majzlan, L. Mazeina, A. Navrotsky, *Geochim. Cosmochim. Acta* **71**, 615 (2007).
11. L. Mazeina, S. Deore, A. Navrotsky, *Chem. Mater.* **18**, 1830 (2006).
12. L. Mazeina, A. Navrotsky, *Clays Clay Miner.* **53**, 113 (2005).
13. J. Majzlan, thesis, University of California, Davis (2003).
14. A. Navrotsky, *Phys. Chem. Miner.* **24**, 222 (1997).
15. J. Majzlan, A. Navrotsky, U. Schwertmann, *Geochim. Cosmochim. Acta* **68**, 1049 (2004).
16. A. Navrotsky *et al.*, *Am. Mineral.* **79**, 1099 (1994).
17. J. Majzlan *et al.*, *Am. Mineral.* **88**, 846 (2003).
18. L. Mazeina, A. Navrotsky, *Chem. Mater.* **19**, 825 (2007).
19. S. V. Ushakov, A. Navrotsky, *Appl. Phys. Lett.* **87**, 164103/1 (2005).
20. J. Majzlan, A. Navrotsky, W. H. Casey, *Clays Clay Miner.* **48**, 699 (2000).
21. A. Navrotsky, *J. Chem. Thermodyn.* **39**, 2 (2007).
22. D. Langmuir, *Am. J. Sci.* **271**, 147 (1971).
23. J. Majzlan, A. Navrotsky, *Eur. J. Mineral.* **15**, 495 (2003).
24. G. Klingelhöfer *et al.*, *Science* **306**, 1740 (2004).
25. R. B. Hargraves *et al.*, *J. Geophys. Res.* **105**, 1819 (2000).
26. M. J. Singer, K. L. Verosub, P. Fine, J. TenPas, *Quat. Int.* **34**, 243 (1996).
27. J. Hiller, *Eidg. Tech. Hochsch.* **17**, 943 (1966).
28. H. Stanjek, *Z. Pflanzenernaehr. Bodenkd.* **150**, 314 (1987).
29. U. Schwertmann, R. W. Fitzpatrick, *Soil Sci. Soc. Am. J.* **41**, 1013 (1977).
30. M. Randrianantoandro, A. M. Mercier, M. Hervieu, J. M. Greneche, *Mater. Lett.* **47**, 150 (2001).
31. R. A. Robie, B. S. Hemingway, *U.S. Geol. Surv. Bull.* **2131** (1995).
32. B. Lang, thesis, Brigham Young University (2005).

33. Various aspects of the calorimetry described in this work were funded by the U.S. Department of Energy.

10.1126/science.1148614

Preparing and Motivating Behavior Outside of Awareness

Henk Aarts,* Ruud Custers, Hans Marien

The observation that the mere activation of the idea of a behavioral act moves the human body without the person consciously deciding to take action has long been a topic of scientific interest (*1*, *2*). Initially, this ideomotor principle was used to explain extraordinary actions such as compliance under hypnosis, automatic writing, dowsing, and swinging pendulums. Lately, research on social cognition and neuroscience has revealed that seeing or reading about a behavior available in the individual's repertoire increases the tendency to perform it, which has been interpreted as a result of the common code that action concepts share with motor programs. Whereas activating the mental representation of behavior outside of awareness—that is, subliminal priming—indeed prepares people to initiate rapidly the corresponding behavior, an important issue recently addressed is how such subliminal priming effects may acquire an intrinsic motivational property in the sense that people mobilize additional resources and actually spend effort on a task (*3*). We studied the emergence of such unconscious motivation by examining how subliminal priming of the action concept of physical exertion causes people to spend effort.

Building on research on the basic role of affective value in reward learning and motivation, we propose that the mechanism that turns subliminal priming of action concepts into motivation relies on the tagging of positive affect to the action concept (*3*). Specifically, we investigated that activating the behavior representation of exertion through subliminal priming prepares the execution of the corresponding behavior and that this priming actually motivates effortful behavior when that representation is co-activated with positively valenced stimuli that act as a reward signal. To test this, we subjected 42 participants to a priming task that enabled us to combine the subliminal priming of words representing exertion with briefly presented, although consciously visible positive words (Supporting Online Material (SOM) text). Accordingly, three different conditions were created: a (control) condition in which only positive stimuli were presented, a (priming) condition in which exertion was subliminally primed but not directly paired with positive stimuli, and a (priming-plus-reward) condition in which exertion was subliminally primed and immediately linked to positive stimuli.

After the manipulations, we recorded handgrip force, which allowed us to differentiate between action preparation and motivation. Participants were instructed to squeeze a hand grip for 3.5 s when the word "Squeeze" appeared on the screen. Results (Fig. 1) showed that participants in the priming and priming-plus-reward conditions started to squeeze earlier and increased their force faster than those in the control condition. The reaction time was shorter, and the initial slope toward the maximal force (rate of increase in applied force) was steeper in these two priming conditions. This faster initiation of the response to squeeze the hand grip and the faster development of force indicate that acting forcefully was more strongly prepared (*2*). Crucially, participants in the priming-plus-reward condition displayed more total effort (mean force over time) than those in the other two conditions, showing enhanced motivation (fig. S1 presents the mean scores on the three measures for each cell in the design).

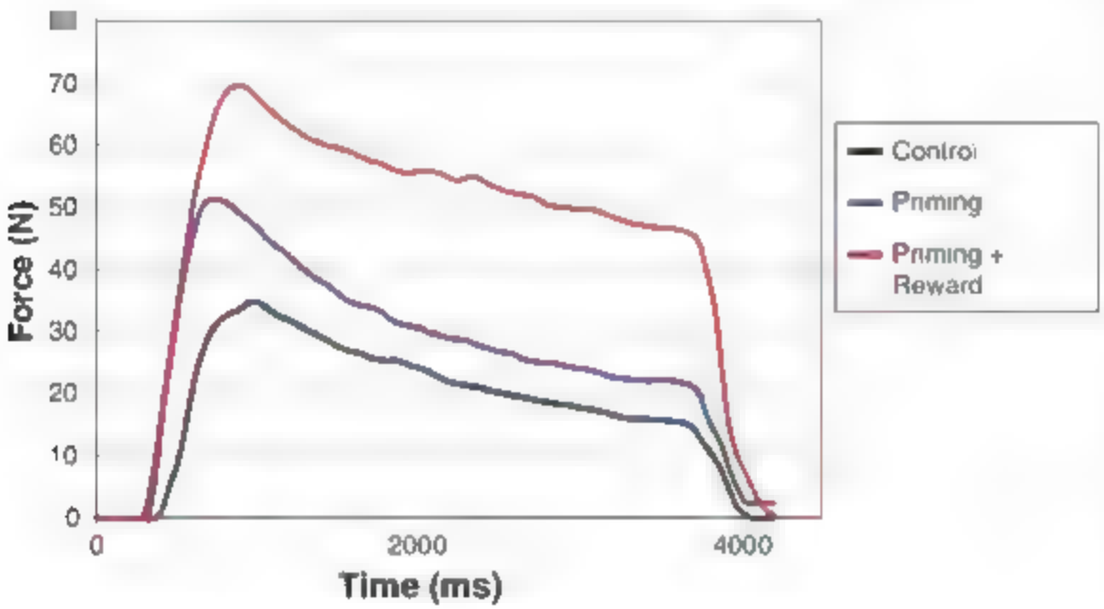

Fig. 1. Mean pattern of force over time as a function of the experimental treatments.

These results confirm that subliminally priming exertion prepares people to display forceful action, but when these subliminal primes are accompanied with a positive stimulus it motivates people to spend extra effort. Previous research on motivation agrees that positive affect acts as a motivator to engage in a task or behavior when it refers to a reward for performing the behavior, even if the reward is subliminally primed (*6*). We tested a more basic and content-free process by showing that such motivation also emerges when the activation of the behavior representation of exertion is directly accompanied by positive stimuli that do not explicitly pertain to the execution of the behavior itself but nevertheless act as reward signals. These effects occur even though participants were unaware of the behavioral primes and thereby of their contingency with the reward signals. This study thus demonstrates the human capacity to rely on mental processes in preparing and motivating behavior outside of awareness.

References and Notes

1. W. James, *The Principles of Psychology* (Macmillan, London, 1890).
2. M. Jeannerod, *The Cognitive Neuroscience of Action* (Blackwell, Malden, MA, 1997).
3. D. Wegner, *The Illusion of Conscious Will* (MIT Press, Cambridge, MA, 2002).
4. J. Bargh, *Eur. J. Soc. Psychol.* **36**, 147 (2006).
5. R. Custers, H. Aarts, *J. Pers. Soc. Psychol.* **89**, 129 (2005).
6. M. Pessiglione *et al.*, *Science* **316**, 904 (2007).
7. This work was financially supported by the Netherlands Organization for Scientific Research (VENI grant 451-06-014, VIDI grant 452-02-047, and VICI grant 453-06-002). We thank S. de Groot, L. Koopmans, and R. Renwinkel for helping with the experiment.

Supporting Online Material

www.sciencemag.org/cgi/content/full/319/5870/1639/DC1
Materials and Methods
Fig. S1
References and Notes

12 September 2007; accepted 7 January 2008
10.1126/science.1150432

Department of Psychology, Utrecht University, Heidelberglaan 1, 3584 CS Utrecht, Netherlands.

*To whom correspondence should be addressed. E-mail: h.aarts@uu.nl

Pattern Separation in the Human Hippocampal CA3 and Dentate Gyrus

Arnold Bakker,[1] C. Brock Kirwan,[2] Michael Miller,[3] Craig E. L. Stark[1,4]*

Pattern separation, the process of transforming similar representations or memories into highly dissimilar, nonoverlapping representations, is a key component of many functions ascribed to the hippocampus. Computational models have stressed the role of the hippocampus and, in particular, the dentate gyrus and its projections into the CA3 subregion in pattern separation. We used high-resolution (1.5-millimeter isotropic voxels) functional magnetic resonance imaging to measure brain activity during incidental memory encoding. Although activity consistent with a bias toward pattern completion was observed in CA1, the subiculum, and the entorhinal and parahippocampal cortices, activity consistent with a strong bias toward pattern separation was observed in and limited to the CA3/dentate gyrus. These results provide compelling evidence of a key role of the human CA3/dentate gyrus in pattern separation.

The medial temporal lobe (MTL) is critically involved in the ability to store and retrieve facts and events (declarative memory) (*1*). Theoretical models suggest that declarative memory relies on both the ability to orthogonalize overlapping or similar patterns of activation (pattern separation) and the ability to complete partial patterns or "clean up" similar patterns of activity into a single common representation (pattern completion) (*2*–*6*). Such models of the MTL have stressed the role of the hippocampus and, in particular, the dentate gyrus and its projections into the CA3 subregion in the process of pattern separation. Specifically, one computational model (*4*) proposed that the dentate gyrus creates a sparse, orthogonalized representation of its input from the entorhinal cortex and projects this into the CA3 via the mossy fibers. The model also suggests that the recurrent interconnected pyramidal cells of the CA3 subregion operate as an autoassociative network capable of reestablishing previously stored patterns of activation based on noisy or degraded cues (pattern completion) (*2*, *3*, *6*, *7*, *8*).

Only recently has empirical evidence been provided supporting the role of the hippocampus, and the dentate gyrus and CA3 in particular, in pattern separation. Rodent studies have shown striking differences in the stability of place cells in the CA1 and CA3 subfields in response to changes in the environment by means of early gene expression (*9*) and single cell recordings (*10*–*14*). Depending on the degree of change in the environment, distorted cues lead to either very similar neuronal representations (completion) or very dissimilar neuronal representations (separation), with the bias toward separation or completion varying across hippocampal subfields. In one example (*11*), rodents were exposed to enclosures of varying similarity during multiunit recording. In CA3, small changes in the enclosure resulted in the activation of a different, nonoverlapping set of neurons (separation). In contrast, CA1 neurons were relatively insensitive to change, with many (although not all) showing a strong overlap in activation between the different enclosures (with the degree of overlap correlated with enclosure similarity). Pattern separation and pattern completion can thus be observed in the rodent with a clear functional distinction between neuronal ensembles in the CA1 and CA3 subregions of the hippocampus.

Here, we used high-resolution functional magnetic resonance imaging (fMRI) (1.5 mm isotropic) to measure brain activity while subjects performed an incidental encoding task designed to parallel many of the rodent studies, including Leutgeb *et al.* (*11*), described above. Eighteen subjects viewed a series of pictures of everyday objects (making the task not overtly spatial). The series included 144 sets of slightly different pictures of the same object, as well as unrelated single pictures of objects used as foils (Fig. 1). Thus, on each trial a presented object could be either (i) new, (ii) a repetition of a previously shown object, or (iii) a slightly different version of a previously shown object (lure). All trials were presented in pseudorandom order with the limitation that a repeat or a lure trial would be presented within approximately 30 trials of each other. During each trial, subjects were not asked to determine whether the stimulus was a target, a repetition or a lure but rather were asked to make an unrelated determination about the object (whether it was typically an indoor or outdoor object). As such, the encoding was incidental and not overtly mnemonic, paralleling the studies in the rodent described above (*15*).

Although the resolution of 1.5 mm represents the likely limit for fMRI (*16*), it is still far too coarse to resolve the pattern of activity across individual neurons and assess pattern separation directly. However, if regions exhibit a change in activity with repetition, we can assess pattern separation versus pattern completion indirectly. We hypothesized that, if a given subregion was engaged in processes of pattern separation, the lure would more likely be treated like a new stimulus than a repetition and show activity similar to that for a first presentation of a stimulus. In contrast, if a given subregion was engaged in processes of pattern completion, the lure would be more likely treated as a repetition of the original stimulus and show activity consistent with a repetition.

Results. To examine the effects of the incidental encoding task, functional data from all trials were subjected to a two-way analysis of variance (ANOVA) with participants as a random factor and trial type (first presentation, first repeat, and first lure) as a fixed factor. Functional regions of interest (ROIs) were based on the resulting *F* maps and defined by setting a voxelwise threshold of $P < 0.05$ and a spatial extent threshold of a minimum ROI volume of 100 mm^3. This threshold is deliberately somewhat liberal because the clusters form the basis for a functional ROI analysis in which all voxels within each ROI are collapsed and the final alpha is set at $P < 0.05$.

This cluster analysis resulted in eight regions in which activity varied in some way with some form of repetition in the MTL (Fig. 2). Using ROI large deformation diffeomorphic metric mapping (ROI-LDDMM), segmentations of each subject's individual anatomy are used to align his or her brain to a high-resolution model consisting of bilateral segmentations of the CA1, the CA3/dentate gyrus (including CA2 and CA4), the subiculum, and the entorhinal, perirhinal, and parahippocampal cortices (*15*, *17*, *18*). The model is further used

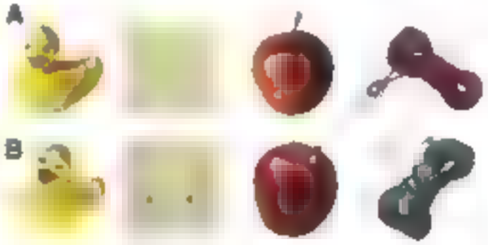

Fig. 1. Sample stimuli sets showing versions A and B of the same object.

[1]Department of Psychological and Brain Sciences, Johns Hopkins University, Baltimore, MD, USA. [2]Institute for Neural Computation, University of California at San Diego, San Diego, CA, USA. [3]Center for Imaging Science, Johns Hopkins University, Baltimore, MD, USA. [4]Center for the Neurobiology of Learning and Memory and Department of Neurobiology and Behavior, University of California at Irvine, Irvine, CA, USA.

*To whom correspondence should be addressed. E-mail: cestark@uci.edu

to localize each region identified in the group analysis (Fig. 2 and fig. S1). We cannot confidently isolate some regions from each other, and some activations cannot be confidently assigned to one region. In particular, we cannot confidently isolate CA3 from the dentate gyrus (DG) and therefore will refer to a single, combined region (CA3/DG) in discussing the results. In addition, if activity spans several regions (e.g., an ROI that covers both the CA1 and CA3/DG regions, as observed below), we prefer to acknowledge this ambiguity in localization rather than strictly adopting one location.

Using these techniques, the activations were localized to the right CA1 subregion of the hippocampus (CA1), bilateral CA3 dentate gyrus subregions of the hippocampus (CA3/DG), a region spanning both the left CA1 and CA3 dentate gyrus subregion of the hippocampus (CA1/3/DG), the left entorhinal cortex (EC), the right parahippocampal cortex (PHC), and finally the bilateral subiculum (Sub). Figure 2 shows these activities on representative coronal slices through the MTL. (Only the tip of the EC activity is shown. In more anterior slices, the activity extends well into the gyrus.) Mean activity within each of the ROIs was then calculated for the first presentation trials, the repeat trials, and the lure trials by collapsing all voxels within an ROI (Fig. 2). Reliable differences were observed between the three trial types in each ROI. In all but one of the ROIs, the repeat trials showed a lower mean activity compared with the first presentation and the lure trials. Only in the right parahippocampal cortex did the repeat trials show a greater mean activity compared with the first condition and the lure trials. In all, activity associated with lure trials was either in between the activity of the repetition trials and the first presentation trials or indistinguishable from the activity of the repetition trials or the first presentation trials. In response to the presentation of a lure, activity in the bilateral CA3/DG was significantly different from activity in response to a repeat presentation (right CA3/DG, $t_{17} = 5.147$, $P < 0.001$; left CA3/DG, $t_{17} = 6.463$, $P < 0.001$). Activity in response to the presentation of a lure stimulus in the bilateral CA3/DG was not significantly different from activity in response to a first presentation (right CA3/DG, $t_{17} = 1.89$, $P = 0.075$; left CA3/DG, $t_{17} = 0.165$, $P = 0.871$). This is in contrast to other areas of activation observed in the medial temporal lobe, where activity in response to the presentation of a lure was significantly different from activity in response to a first presentation (CA1/3/DG, $t_{17} = 3.151$, $P < 0.001$; left entorhinal cortex, $t_{17} = 3.697$, $P < 0.01$; right CA1, $t_{17} = 6.224$, $P < 0.001$) and not significantly different from the repeat presentation of a stimulus (CA1/3/DG, $t_{17} = 0.822$, $P = 0.422$; left entorhinal cortex, $t_{17} = 1.117$, $P = 0.279$; right CA1, $t_{17} = 1.25$, $P = 0.228$).

A simple bias score indexing how similar lure activity is to repetition [(first − lure) / (first − repetition)] can be used to assess the tendency toward completion (bias approaching 1) or separation (bias approaching 0) across regions. This bias score is shown in Fig. 3. A single bias score for each region is shown, collapsing across ROIs in the same region (e.g., bilateral CA3/DG). Bias scores for CA1, the region that spanned across the CA1/3/DG, the subiculum, and the entorhinal and parahippocampal cortices, ranged from 0.59 to 0.83. Thus, although somewhat mixed and not purely connoting completion, lure stimuli were treated more like true repetitions than first presentations of stimuli. In stark contrast, the bias score of 0.15 in the CA3/DG showed that lure stimuli were treated almost exactly the same as the presentation of a novel stimulus, consistent with a strong bias toward pattern separation.

Discussion. We used high-resolution fMRI to study processes of pattern separation in the human MTL by scanning subjects while they performed an incidental encoding task using pictures of common objects. Embedded in the task were direct repetitions of pictures and lure stimuli that were only similar to previously presented objects. A bias toward pattern separation was observed in the CA3/DG, and biases toward completion were observed in several MTL regions, including CA1.

Our design used an incidental encoding task with no overt behavioral assessment of whether or not pattern separation occurred on a given trial. This was done both to more closely parallel the rodent literature and to remove any explicit memory components from the task that might confound our findings. In an explicit memory task, correctly rejecting the lure as only similar to, but not the same as, the target could provide behavioral evidence that pattern separation occurred. However, as previously suggested (*18*), this approach does not allow us to clearly isolate processes of pattern separation. If subjects are aware of the pattern separation demands of the task, the subject might employ a "recall to reject" strategy (*8*). This strategy implies that when presented with a lure, subjects first retrieve the original presentation from memory (thereby performing pattern completion) and subsequently compare the representations to determine whether the stimulus is a lure or a target. The subject can then make a determination based on the comparison between the stimulus and the representation of the initial presentation retrieved

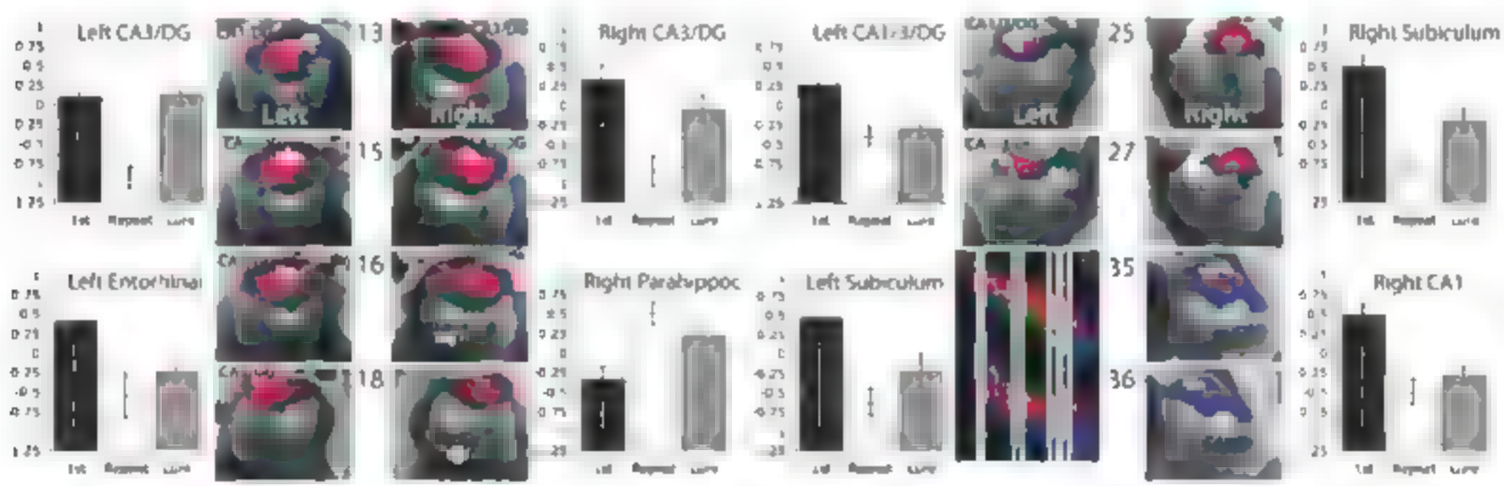

Fig. 2. Anatomical location and mean activity in the three task conditions for each of the eight MTL regions of interest. A model segmentation of hippocampal subfields is overlaid on each brain slice to indicate the location of the subiculum (green), CA1 (blue), and CA3/DG (red). Regions of activity within the MTL are shown in white and labeled within each slice (PHC, parahippocampal cortex; EC, entorhinal cortex). Regions of activity outside the MTL (not part of the analysis) are shown in black. Three-dimensional rendering (lateral, superior view) shows the location of each slice (white lines). The distance of each slice from the anterior commissure (*y* = 0 in Talairach coordinates) is indicated for each slice as well (*y* = −13 to 36 mm). The thicker white lines represent two adjoining slices. Bar graphs show mean activity (summed beta coefficients) in each ROI for each trial condition.

from memory. As such, this task does not rely merely on pattern separation but also on pattern completion and even processes of encoding and retrieval. Our indirect measure that simply examines activity for lure items relative to first presentations and repetitions is not only closer to the free exploration of an environment used in the rodent studies but also suffers far less from this difficulty.

Our observation of activity consistent with pattern separation specifically in the CA3 DG subregion of the hippocampus is consistent with computational models that have stressed the role of the dentate gyrus in particular in creating sparse orthogonalized representations (*2*, *4*, *6*, *8*). Although high-resolution fMRI allows us to study these processes within the hippocampus, the resolution remains insufficient to distinguish the neuronal activity of the dentate gyrus from the activity of the CA3 subregion, so these two areas were combined and treated as one. As such, task-related activity of the dentate gyrus cannot be distinguished from activity of the CA3 subregion, and processes of pattern separation cannot be ascribed specifically to the dentate gyrus. However, because the sparse orthogonalized representations created by the dentate gyrus are projected predominantly to the CA3 subregion, one would expect to observe activity related to processes of pattern separation in both subregions of the hippocampus. Animal studies have shown pattern separation signals in both the dentate gyrus and the CA3 subregion (*14*, *19*, *20*). Thus, our findings remain consistent with both the computational models and the animal studies described earlier.

There are limitations to our method. First, if pattern separation was present in a region, but overall activity remained stable across the various repetition conditions, we would fail to detect pattern separation in this region. Indeed, all findings in this study are dependent on a change in blood oxygen level dependent (BOLD) activity across the conditions in our task (e.g., dropping activity with repetition of the stimulus), because fMRI is based on contrasts and is sensitive only to differences across conditions.

Second, pattern separation and pattern completion are processes that are not limited to the MTL (*21*, *22*). Indeed, one could argue that pattern separation and pattern completion occur in all sensory modalities in response to different or similar stimuli. It is thus possible that activity in the CA3 DG reflects the mere processing of patterns already separated elsewhere in the brain rather than active pattern separation. Although computational models and animal studies suggest the CA3 DG serves an active role in pattern separation, the current data do not allow us to differentiate unequivocally between these possibilities.

Third, because novelty, recency, and familiarity signals have played important roles in understanding the MTL (*23*), we must consider the present results in light of these codes. Each of the regions showed activity consistent with novelty (and recency) detection in that simple repetition was associated with less activity than the first presentation (with the exception that the parahippocampal cortex showed an inverted signal, increasing activity with repetition). In the regions outside the CA3 DG, the same change in activity was observed for lures, whereas the CA3 DG responded with elevated activity. These results would be consistent with the hypothesis that the same pattern of activity was present (i.e., the same neurons were firing and no pattern separation occurred) but at rates that coded for novelty. The novelty coding in the CA3 DG must be less tolerant of small changes than other regions. Although a plausible account of our data, this view is inconsistent with several other sources of data. It is inconsistent with the pattern of novelty signals typically observed in the hippocampus (*23*). We observed multiple patterns in the hippocampus, and it is not clear that the CA3 DG would best be interpreted as coding for item-place (or similar) associations. Further, the simpler pattern of activity that is consistent with novelty signals was not observed in the perirhinal cortex. Finally, this account would ignore the data showing that neuronal activity in the dentate gyrus and the CA3 subregion of the hippocampus does in fact exhibit changes in the representation as the environment changes (*11*, *14*). Our results are in no way inconsistent with novelty signals in the hippocampus that differ from novelty signals elsewhere in the MTL (*23*). However, we suggest that the present results are more indicative of pattern separation and completion and that they are not synonymous with various novelty codes.

With the ability to perform fMRI with sufficiently high resolution, pattern separation can be observed in the human MTL and even specifically be ascribed to the bilateral CA3 DG subregions of the hippocampus. These findings provide compelling evidence of a key role of the human CA3 DG in pattern separation and further evidence supporting the computational models' account of hippocampal function. The process of pattern separation is central to and heavily taxed by many of the functions ascribed to the hippocampus in various cognitive theories (e.g., recollection, episodic memory, and conjunctive memory). We suggest that an understanding of the division of labor within the MTL and between the MTL and other structures will require a greater understanding of how pattern separation and completion function throughout the MTL and elsewhere in the cortex.

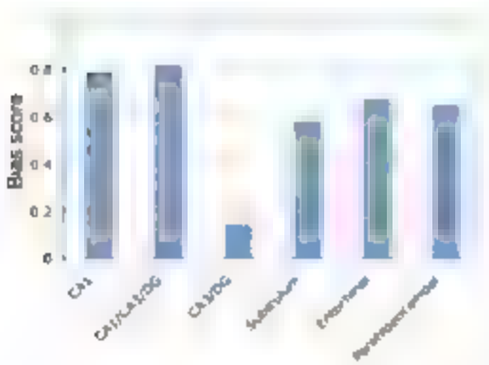

Fig. 3. Bias scores in the MTL. A single bias score for each of the six different areas in the MTL was calculated by collapsing the bias scores for multiple ROIs in the same area. Bias scores closer to 0 connote separation, scores closer to 1 connote completion.

References and Notes

1. L. R. Squire, C. E. L. Stark, R. E. Clark, *Annu. Rev. Neurosci.* **27**, 279 (2004).
2. D. Marr, *Philos. Trans. R. Soc. London Ser. B* **262**, 23 (1971).
3. R. C. O'Reilly, J. L. McClelland, *Hippocampus* **4**, 661 (1994).
4. A. Treves, E. T. Rolls, *Hippocampus* **4**, 374 (1994).
5. J. L. McClelland, N. H. Goddard, *Hippocampus* **6**, 654 (1996).
6. R. C. O'Reilly, J. W. Rudy, *Psych. Rev.* **108**, 311 (2001).
7. D. G. Amaral, M. P. Witter, *Neuroscience* **31**, 571 (1989).
8. K. A. Norman, R. C. O'Reilly, *Psychol. Rev.* **110**, 611 (2003).
9. A. Vazdarjanova, J. F. Guzowski, *J. Neurosci.* **24**, 6489 (2004).
10. I. Lee, D. Yoganarasimha, G. Rao, J. J. Knierim, *Nature* **430**, 456 (2004).
11. S. Leutgeb, J. K. Leutgeb, A. Treves, M. Moser, E. I. Moser, *Science* **305**, 1295 (2004).
12. S. Leutgeb, J. K. Leutgeb, M. B. Moser, E. I. Moser, *Curr. Opin. Neurobiol.* **15**, 738 (2005).
13. T. J. Wills, C. Lever, F. Cacucci, N. Burgess, J. O'Keefe, *Science* **308**, 873 (2005).
14. J. K. Leutgeb, S. Leutgeb, M. B. Moser, E. I. Moser, *Science* **315**, 961 (2007).
15. Materials and methods are available as supporting material on *Science* Online.
16. J. S. Hyde, B. B. Biswal, A. Jesmanowicz, *Magn. Reson. Med.* **46**, 114 (2001).
17. C. B. Kirwan, C. K. Jones, M. Miller, C. E. L. Stark, *Hum. Brain Mapp.* **28**, 959 (2007).
18. C. B. Kirwan, C. E. Stark, *Learn. Mem.* **14**, 625 (2007).
19. P. E. Gilbert, R. P. Kesner, I. Lee, *Hippocampus* **11**, 626 (2001).
20. T. J. McHugh *et al.*, *Science* **317**, 94 (2007).
21. R. L. Buckner *et al.*, *Neuron* **20**, 285 (1998).
22. P. Rotshtein, R. N. A. Henson, A. Treves, J. Driver, R. J. Dolan, *Nat. Neurosci.* **8**, 107 (2005).
23. M. W. Brown, J. P. Aggleton, *Nat. Rev. Neurosci.* **2**, 51 (2001).

24. This work was supported by NSF grant BCS 0544959 to C.S. and NIH grant P41 RR15241-01A1 and NIMH grant RO1 E800975-01 to M.M.

Supporting Online Material

www.sciencemag.org/cgi/content/full/319/5870/1640/DC1
Materials and Methods
Fig. S1
References

12 November 2007; accepted 14 February 2008
10.1126/science.1152882

Low-Magnetic-Field Control of Electric Polarization Vector in a Helimagnet

Shintaro Ishiwata,[1]* Yasujiro Taguchi,[2] Hiroshi Murakawa,[1] Yoshinori Onose,[1,3] Yoshinori Tokura[1,2,3]

The mutual control of the electric and magnetic properties of a solid is currently of great interest because of the possible application for novel electronic devices. We report on the low-magnetic field (for example, B values of ±30 millitesias) control of the polarization (P) vector in a hexaferrite, $Ba_2Mg_2Fe_{12}O_{22}$, which shows the helimagnetic spin structure with the propagation vector k_0 parallel to [001]. The B-induced transverse conical spin structure carries the P vector directing perpendicular to both B and k_0, in accord with the recently proposed spin-current model. Then, the oscillating or multidirectionally rotating B produces the cyclic displacement current via the flexible handling of the magnetic cone axis.

For device applications, there is increasing interest in enhancing the coupling between the electric and magnetic dipole moments for the magnetoelectric (ME) effect (*1*–*3*). With the recent discovery of large ME effects in transition-metal oxides such as $TbMnO_3$ (*4*), considerable effort has been devoted to magnetically frustrated systems with a long-period magnetic structure (*5*–*8*). The large ME effect in such systems is often observed in the course of magnetic-field–induced phase transitions with field magnitudes of a few teslas. For applications, however, it will be necessary to generate and control the ME effects at room temperature and by low magnetic fields.

Explanations for the microscopic origin of the nontrivial coupling between the polarization (P) and the transverse spiral spin structure have been proposed (*9*–*12*). According to the spin-current model (*9*), the non-collinear arrangement of the adjacent spins can produce the polarization of electron density at the bonds between them through the superexchange interaction, and the expression of the polarization reads as $Ae_{i,j} \times (S_i \times S_j)$. Here, A is a scalar determined by the exchange interaction and the spin-orbit interaction. The spins S_i and S_j reside on the adjacent sites along the unit vector $e_{i,j}$, and the term $S_i \times S_j$ corresponds to the magnitude of dissipationless spin supercurrent along $e_{i,j}$ (*9*). This mechanism of polarization generation may be viewed as representing the duality that the charge or spin current produces the magnetic or electric dipole. When the inevitable electron-lattice coupling is explicitly taken into account, this mechanism is also considered the inverse effect of Dzyaloshinsky-Moriya interaction (*10*). The spin-current model can explain the ferroelectricity induced by the transverse-spiral (cycloidal) spin orders, in which every spin pair lining up along the propagation vector k_0 ($e_{i,j} \perp k_0$) produces the unidirectional local P and hence the total macroscopic P ($\sum_{i,j} \| k_0 \propto (S_i \times S_j) \| k_0$), as observed for $(Tb, Dy)MnO_3$ (*13*–*15*).

As exemplified by the case of a spinel $CoCr_2O_4$, the above model is applicable to transverse conical ferrimagnets (the cone axis is perpendicular to k_0), wherein ferromagnetic and ferroelectric moments are coupled with each other (*16*). By contrast, materials with a proper screw or a longitudinal conical spin structure cannot yield the spin current–induced polarization (Fig. 1, B and C) because $\sum S_i \times S_j \| k_0$. Nevertheless, they can be the potentially tunable ME materials by making use of an external magnetic field (B) stabilizing a conical spin structure, in which the cone axis deviates from k_0 (Fig. 1D). This allows us to control both the magnitude and the direction of the ferroelectric polarization via controlling the direc-

[1]Multiferroics Project, Exploratory Research for Advanced Technology (ERATO), Japan Science and Technology Agency (JST), care of Department of Applied Physics, University of Tokyo, Hongo, Tokyo 113-8656, Japan. [2]Cross-Correlated Materials Research Group (CMRG), Frontier Research System (FRS), RIKEN, Wako 351-0198, Japan. [3]Department of Applied Physics, University of Tokyo, Hongo, Tokyo 113-8656, Japan.

*To whom correspondence should be addressed. E-mail: ishiwata@riken.jp

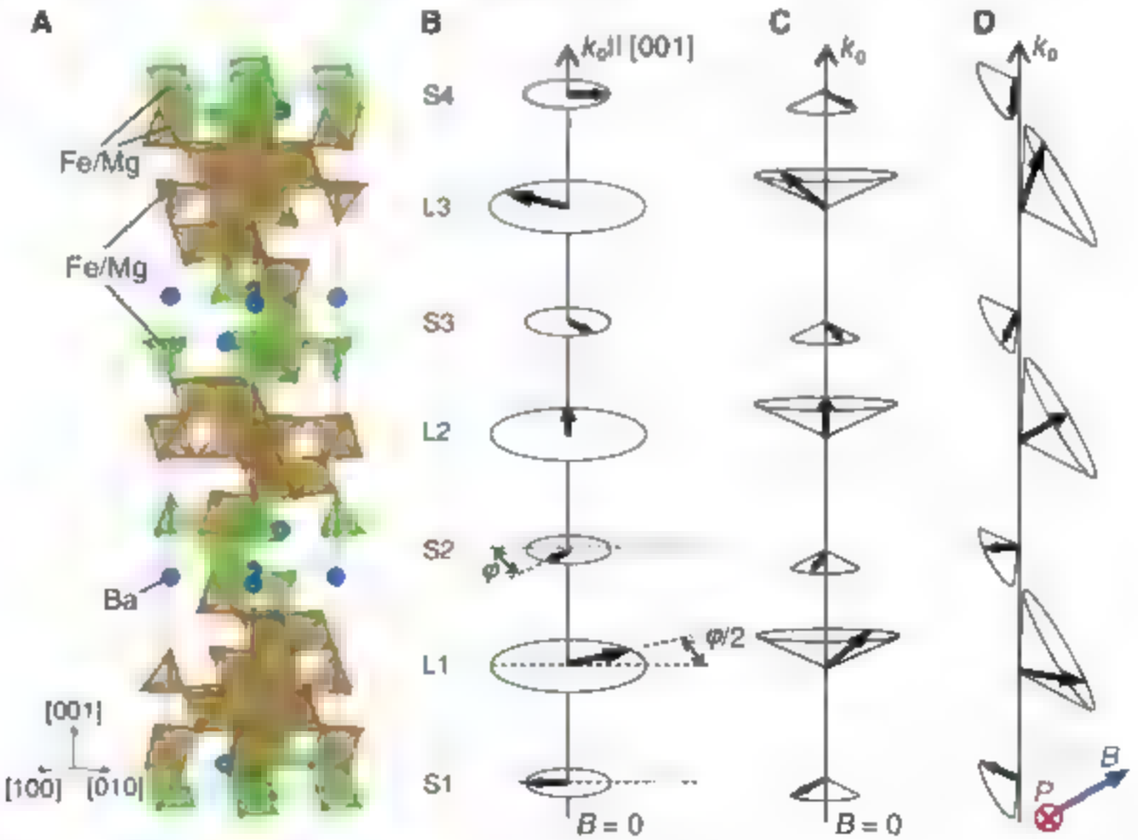

Fig. 1. (**A**) Schematic crystal structure of $Ba_2Mg_2Fe_{12}O_{22}$. The magnetic structure consists of alternate stacks of L blocks (brown) and S blocks (green) having large and small magnetic moments, respectively. Illustrations of helicoidal spins (represented by arrows) (**B**) with proper screw ($50 < T < 195$ K), (**C**) longitudinal conical ($T < 50$ K), and (**D**) slanted conical ($T < 195$ K and $B \sim 30$ mT) spin structures.

tion of the cone axis by relatively weak B. Here, we demonstrate a control of the ferroelectric polarization vector P ($\perp B$ and k_0) in a longitudinal conical helimagnet $Ba_2Mg_2Fe_{12}O_{22}$ having weak spin anisotropy by handing the cone axis with rotating B of several tens of millitesla (mT).

Recently, magnetoplumbite-related hexaferrites have been suggested as promising candidates for ME materials with a high magnetic-ordering temperature, and it was found that a Y-type hexaferrite $Ba_{0.5}Sr_{1.5}Zn_2Fe_{12}O_{22}$ (BSZFO) shows a B-induced polarization that can be rotated around the hexagonal axis by the external B (*17*). BSZFO undergoes a thermal transition from a ferrimagnetic state to a helicoidal state at 319 K, below which several successive magnetic field–induced transitions occur (*18*). All the phases, except for the collinear ferrimagnetic phase above ~2 T, have a long-period magnetic structure with a propagation vector k_0 parallel to the hexagonal axis ($\parallel [001]$). However, the ferroelectric polarization was observed only in the particular phase, which is stable at around 1 T. Thus, this ferroelectric phase is seemingly a unique phase, and the link between the magnetic structures in this phase and in zero field is not clear. In the present compound, $Ba_2Mg_2Fe_{12}O_{22}$ (BMFO), we have found the existence of a flexibly tunable ferroelectric phase in a much weaker magnetic-field region, that is, the transverse conical phase, which is continuously connected by the small magnetic fields from the magnetic structure in zero field, while keeping the sense of the spin helix. [See (*19*) for details of sample preparation and measurements.]

The crystal structure of BMFO is compatible with the Y-type hexaferrite having the centric space group $R\bar{3}m$, composed of alternate stacks of L blocks and S blocks along [001] (Fig. 1A). Within each block, the spins aligned ferrimagnetically within the [001] plane yield a large magnetic moment on the L block and a small magnetic moment on the S block [the former is 2.8-fold larger than the latter (*20*)]. This material is ferrimagnetic below 553 K and adopts a proper screw spin structure with k_0 along [001] below 195 K (Fig. 1B). The turn angle φ between the moments on the same kind of the adjacent blocks is about 70° at 9 K (*21*). We also found a spin reorientation transition to a longitudinal conical state at around 50 K (Fig. 1C), which showed up as the onset of the spontaneous magnetization along [001] (Fig. 2B inset). According to previous studies (*20*), competitive nature among superexchange interactions around the boundary between the L and the S blocks is responsible for the screw-type spin structure and, perhaps, for the reorientation transition as well.

The magnetic phase diagram for BMFO as functions of temperature and B ($\parallel [100]$) is shown in Fig. 2A. In addition to the proper screw state (and the longitudinal conical state below about 50 K) at $B = 0$, there are four kinds of magnetic phases, unexpectedly, three of them (FE1, FE2, and FE3) are ferroelectric phases, and the other one (PE) is a paraelectric phase (Fig. 2C). As typified in Fig. 2B in the case of 5 K, these phases are distinguishable by the plateaus in the M-B curve. M/M_s (M_s denotes the saturation magnetization) increases as 0 (proper screw, $B \sim 0$ T) → 0.25 (FE1, $0 \text{ T} < B < \sim 60$ mT) → 0.45 (FE2, ~ 60 mT < B < 0.12 T) → 0.75 (FE3, ~0.12 T < B < ~3.8 T) → 1 (PE, $B >$ ~3.8 T). Although the magnetic structures of BMFO under magnetic fields have not been characterized as yet, the resemblance to BSZFO with regard to the M-B and P-B curves convinces us of the occurrence of similar sequential phase transitions.

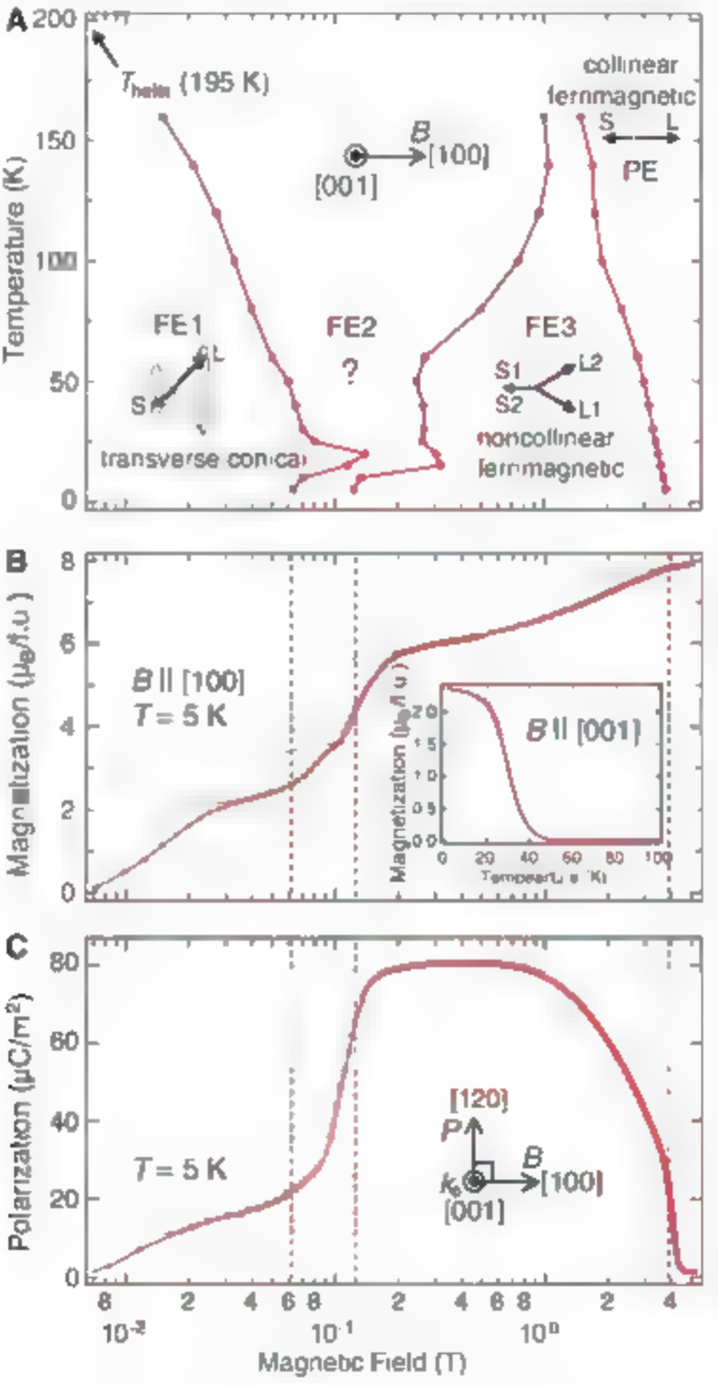

Fig. 2. (**A**) Magnetoelectric phase diagram of $Ba_2Mg_2Fe_{12}O_{22}$ in magnetic field (B) along [100] as determined by magnetization curves at selected temperatures. (**B**) Magnetization along [100] and (**C**) electric P as a function of B. (Inset) A temperature-dependent magnetization along [001] measured in a zero-field heating run after field cooling with $B = 5$ T. All the B-dependent data in (A) to (C) were collected on increasing B. Plausible spin configurations are shown within the area of each phase. Dashed lines indicating phase boundaries at 5 K are appended over (B) and (C).

Within each block, the spins aligned ferrimagnetically within the [001] plane yield a large magnetic moment on the L block and a small magnetic moment on the S block [the former is 2.8-fold larger than the latter (*20*)]. This material is ferrimagnetic below 553 K and adopts a proper screw spin structure with k_0 along [001] below 195 K (Fig. 1B). The turn angle φ between the moments on the same kind of the adjacent blocks is about 70° at 9 K (*21*). We also found a spin reorientation transition to a longitudinal conical state at around 50 K (Fig. 1C), which showed up as the onset of the spontaneous magnetization along [001] (Fig. 2B inset). According to previous studies (*20*), competitive nature among superexchange interactions around the boundary between the L and the S blocks is responsible for the screw-type spin structure and, perhaps, for the reorientation transition as well.

The magnetic phase diagram for BMFO as functions of temperature and B ($\parallel [100]$) is shown in Fig. 2A. In addition to the proper screw state (and the longitudinal conical state below about 50 K) at $B = 0$, there are four kinds of magnetic phases, unexpectedly, three of them (FE1, FE2, and FE3) are ferroelectric phases, and the other one (PE) is a paraelectric phase (Fig. 2C). As typified in Fig. 2B in the case of 5 K, these phases are distinguishable by the plateaus in the M-B curve. M/M_s (M_s denotes the saturation magnetization) increases as 0 (proper screw, $B \sim 0$ T) → 0.25 (FE1, $0 \text{ T} < B < \sim 60$ mT) → 0.45 (FE2, ~ 60 mT < B < 0.12 T) → 0.75 (FE3, ~0.12 T < B < ~3.8 T) → 1 (PE, $B >$ ~3.8 T). Although the magnetic structures of BMFO under magnetic fields have not been characterized as yet, the resemblance to BSZFO with regard to the M-B and P-B curves convinces us of the occurrence of similar sequential phase transitions.

As the applied B increased (Fig. 2C), P increased in accordance with the increase of M and reached a maximum in FE3 (~80 μC/m^2), followed by the collapse at the phase boundary between the FE3 and the spin-collinear ferrimagnetic PE phases. Notably, the ferroelectric polarization was observable even in the FE1 phase near $B = 0$, in contrast to BSZFO, which showed the ferroelectric polarization only in the intermediate (~1 T) field-induced phase (perhaps corresponding to the $B \cong 1$ T phase in BMFO). Accordingly, the magnetic structures of BMFO in the low B region, especially for FE1, should be different from the likes of the fan spin structure proposed for the low-field phase in BSZFO (*18*). Instead, FE1 should have a transverse conical spin structure with a cone axis nearly parallel to B (as illustrated in Fig. 2A). This is ascertained by the fact that in the FE1 phase both the external field and the spin anisotropy are weak, the cone axis should follow the direction of magnetic field with the turn angle of the spins unchanged. Note that k_0 is always parallel to the unique axis [001], irrespective of the direction of B. The emergence

of P perpendicular to both k_0 ([001]) and the transverse cone axis (B) strongly suggests that the spin-current model holds for FE1.

In order to clarify the relationship between P and the conical or other long-period spin structures propagating along [001], we studied the B direction dependence of P under rotating B values of 30 mT, 0.1 T, and 1 T within the planes normal to [001] (horizontal rotation, Fig. 3, A to D) and normal to [120] (vertical rotation; Fig. 3, E to H). Before the measurements, B was first set to −1 T and then increased to a positive value for FE1 (30 mT), FE2 (0.1 T), or FE3 (~1 T).

First, we noticed from Fig. 3, B and F, that in B = 30 mT both the ϕ- and θ-dependent P values follow nearly sinusoidal curves. Given that the applied field and the magnetic anisotropy are weak, the cone axis should follow the direction of B while keeping the spin helicity intact. Then, on the basis of the spin-current model, the direction of P is expected to be perpendicular to both B and k_0 (Fig. 3A), and its magnitude is proportional to sinθ (Fig. 3E), in agreement with the observed feature. The slight deviation from the sinusoidal curve reflects the weak but finite magnetic anisotropy that drags the cone axis slightly away from the direction of B and causes the hysteretic behavior, as observed in the angle-increasing and -decreasing runs.

The same dependence of P with almost no hysteresis can also be observed in B = 1 T (Fig. 3D). This behavior is essentially the same as that reported for BSZFO (*17*). Actually, M ⊥ k_0 for FE3 is quite close to that for the intermediate-field (~1 T) ferroelectric phase of BSZFO with the noncollinear ferrimagnetic structure with k_0 = (0, 0, 3/2). In the case of θ dependence, on the other hand, P suddenly vanished around θ = 70°, and it never recovered to the usual state afterward, indicating the occurrence of a transition to the collinear ferrimagnetic PF phase (Fig. 3H). Similarly, although P under the horizontally rotating B of 0.1 T showed the nearly sinusoidal behavior (Fig. 3C), that for the vertical one was quite different, and its magnitude tended to be reduced as the external B rotated across the [001] axis (Fig. 3G). These results highlight the robust stability of FE1 against the all-directional B, or conversely that the P vector in FE1 is highly tunable by a rotating small B.

Next, we show cyclic oscillation of the displacement current in BMFO under the small oscillating B applied along [100] at 5 K. As shown in Fig. 4, A and B, the displacement current and P oscillate with changing its sign and keeping almost the same amplitude. This behavior resembles the case of a conical magnet $CoCr_2O_4$ (*16*), which exhibits the reversal of P upon the reversal of the magnetization M (or the cone axis). This feature has been interpreted in terms of clamping between the P and M domains across the Bloch-type domain walls. However, BMFO shows quite a different mechanism of the magnetic reversal of P. While B oscillates, the longitudinal conical spin structure tends to appear at around B = 0, as shown schematically in the upper part of Fig. 4. Due to the presence of this longitudinal (M // k_0) conical state at B = 0, the spin helicity as defined as $\Sigma k_0(S_i \times S_j)$ should be preserved on traversing the B = 0 point. This process leads to the reversal of P with the reversal of B($\perp k_0$). [Note that the two states with M // k_0 are degenerate at B = 0. Nevertheless, the spin helicity around B = 0 is the same, leading to the identical consequence about the P reversal.

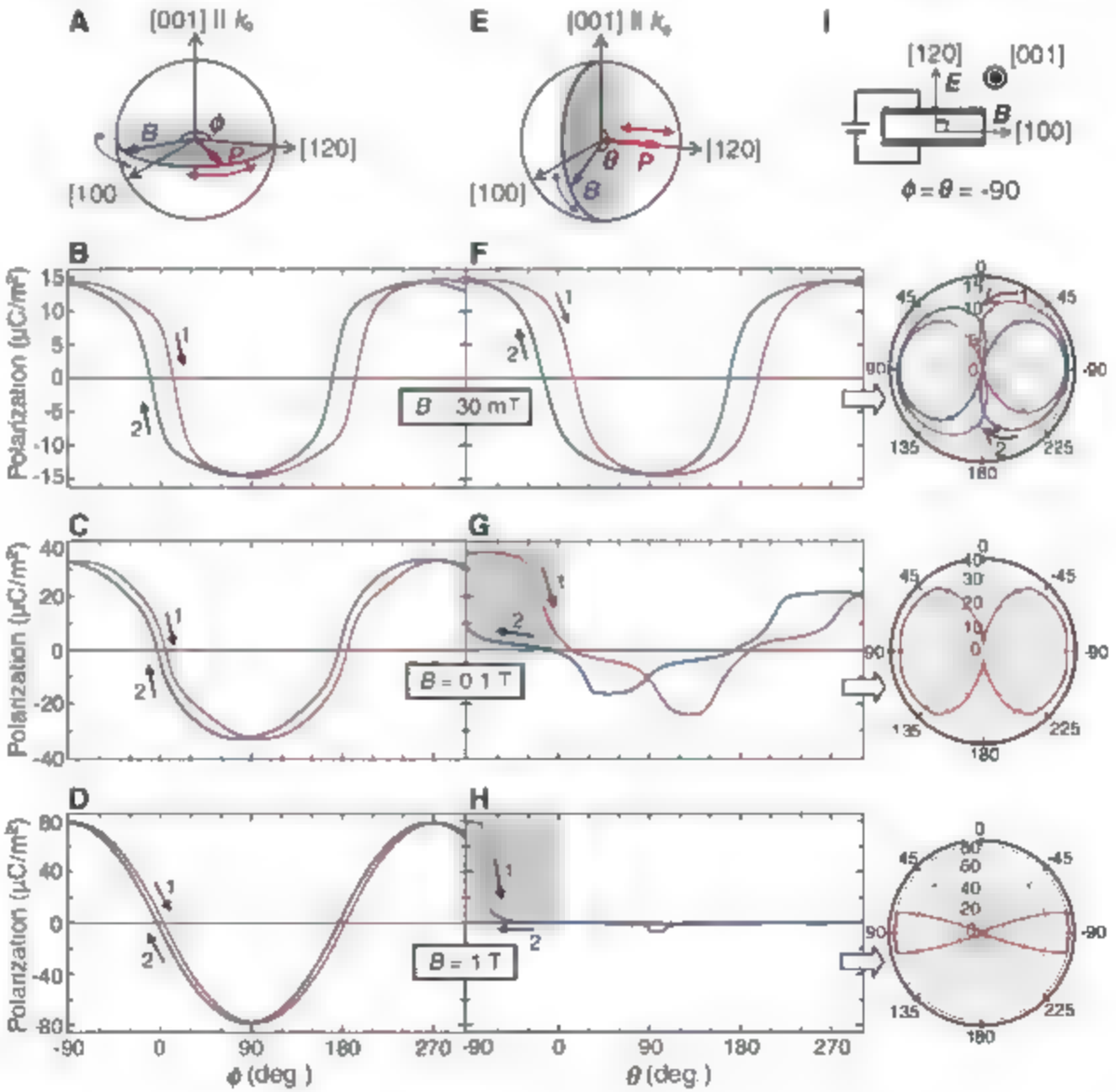

Fig. 3. (A) Schematic configurations for the measurements of ME polarization under the horizontally rotating B and (E) that under the vertically rotating B. ϕ and θ are defined as the relative angles between B and [120] and between B and [001], respectively. (B) to (D) ϕ and (F) to (H) θ dependence of the ME polarization under the rotating B of [(B) and (F)] 30 mT, [(C) and (G)] 0.1 T, and [(D) and (H)] 1 T. The polar plots of P of (F) FE1, (G) FE2, and (H) FE3 are appended to the right of each panel. The polar plots for (G) and (H) were made by symmetrical operations of the data in the angular region, −90 ≤ θ ≤ 0, highlighted by shadows. The arrows with numbers indicate the direction of experimental sequences. (I) Schematics of the configuration for the poling process (E denotes the poling electric field). All the data were collected at 5 K.

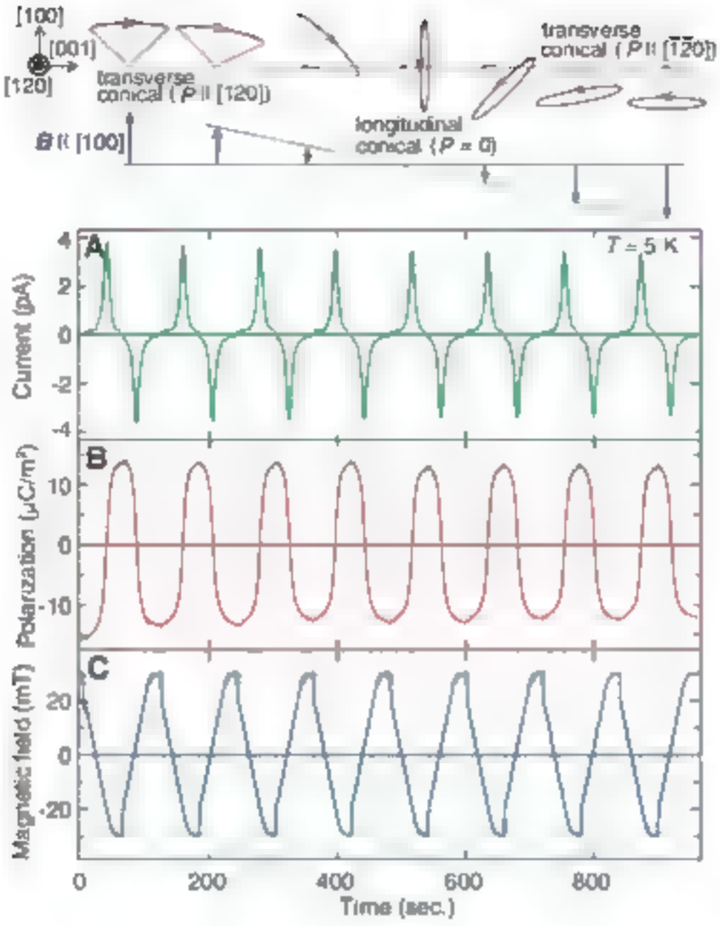

Fig. 4. (**A**) Oscillating displacement current, (**B**) cyclic reversal of the ferroelectric polarization, and (**C**) periodically changing B parallel to [100] plotted as a function of time. The drawings at the top schematically show the temporal change of the spin cone and helicity while oscillating B.

similar to the case of B rotation around [120], (fig. S1).

We have found the magnetically induced ferroelectric phases at low B in a hexaferrite $Ba_2Mg_2Fe_{12}O_{22}$ and succeeded in flexibly controlling the P vector in the transverse conical spin phase by handling the cone axis with rotating B of several tens of mT. Considering the high helimagnetic ordering temperature of Y-type hexaferrites (up to above room temperature), our results offer a possible route to field-tunable room-temperature multiferroics.

References and Notes

1. J. Wang *et al.*, *Science* **299**, 1719 (2003).
2. M. Fiebig, *J. Phys. D* **38**, R123 (2005).
3. Y. Tokura, *Science* **312**, 1481 (2006).
4. T. Kimura *et al.*, *Nature* **426**, 55 (2003).
5. G. Lawes *et al.*, *Phys. Rev. Lett.* **95**, 087205 (2005).
6. T. Kimura, J. C. Lashley, A. P. Ramirez, *Phys. Rev. B* **73**, 220401 (2006).
7. S. Park, Y. J. Choi, C. L. Zhang, S.-W. Cheong, *Phys. Rev. Lett.* **98**, 057601 (2007).
8. I. Arima, *J. Phys. Soc. Jpn.* **76**, 073702 (2007).
9. H. Katsura, N. Nagaosa, A. V. Balatsky, *Phys. Rev. Lett.* **95**, 057205 (2005).
10. I.A. Sergienko, E. Dagotto, *Phys. Rev. B* **73**, 094434 (2006).
11. M. Mostovoy, *Phys. Rev. Lett.* **96**, 067601 (2006).
12. A. B. Harris, T. Yildirim, A. Aharony, O. Entin-Wohlman, *Phys. Rev. B* **73**, 184433 (2006).
13. Y. Yamasaki *et al.*, *Phys. Rev. Lett.* **98**, 147204 (2007).
14. M. Kenzelmann *et al.*, *Phys. Rev. Lett.* **95**, 087206 (2005).
15. I. Arima *et al.*, *Phys. Rev. Lett.* **96**, 097202 (2006).
16. Y. Yamasaki *et al.*, *Phys. Rev. Lett.* **96**, 207204 (2006).
17. T. Kimura, G. Lawes, A. P. Ramirez, *Phys. Rev. Lett.* **94**, 137201 (2005).
18. H. Momozawa, Y. Yamaguchi, *J. Phys. Soc. Jpn.* **62**, 1292 (1993).
19. Materials and Methods are available on *Science* Online.
20. H. Momozawa, Y. Yamaguchi, M. Mita, *J. Phys. Soc. Jpn.* **55**, 1350 (1986).
21. H. Momozawa, Y. Nagao, S. Utsumi, M. Abe, Y. Yamaguchi, *J. Phys. Soc. Jpn.* **70**, 2724 (2001).

22. The authors thank N. Nagaosa and I. Arima for useful comments and Y. Tokunaga for experimental support and discussions.

Supporting Online Material

www.sciencemag.org/cgi/content/full/319/5870/1643/DC1
Materials and Methods
References

21 December 2007; accepted 14 February 2008
10.1126/science.1154507

Observation of Giant Diffusivity Along Dislocation Cores

Marc Legros,[1]† Gerhard Dehm,[2] Eduard Arzt,[3]* T. John Balk[4]

Diffusion of atoms in a crystalline lattice is a thermally activated process that can be strongly accelerated by defects such as grain boundaries or dislocations. When carried by dislocations, this elemental mechanism is known as "pipe diffusion." Pipe diffusion has been used to explain abnormal diffusion, Cottrell atmospheres, and dislocation-precipitate interactions during creep, although this rests more on conjecture than on direct demonstration. The motion of dislocations between silicon nanoprecipitates in an aluminum thin film was recently observed and controlled via in situ transmission electron microscopy. We observed the pipe diffusion phenomenon and measured the diffusivity along a single dislocation line. It is found that dislocations accelerate the diffusion of impurities by almost three orders of magnitude as compared with bulk diffusion.

Defects such as vacancies, impurities, dislocations, grain boundaries, and precipitates control several material properties (e.g., resistivity, magnetic coercivity, and strength). Of these defects, dislocations have motivated numerous studies, because their intrinsic ability to multiply and to propagate determines many mechanical properties of metals and alloys. In addition, dislocation lines can act as fast paths for diffusing atoms, and this elemental phenomenon, known as pipe diffusion (*1*), is thought to originate from the disordered core region that lowers the activation energy for diffusion (*2*, *3*). This concept of a fast diffusion path in crystalline solids has been extended to screw or mixed-character dislocations (*1*, *4*) and, collectively, to arrays of dislocation (i.e., grain boundaries) (*5*, *6*). By creating a short circuit pathway, pipe diffusion can potentially affect various types of material behavior involving dislocations, impurities, and precipitates [e.g., creep (*7*), dynamic strain aging (*8*, *9*), crystal nucleation (*10*), or Ostwald ripening (*11*)]. It becomes critical when diffusion paths are short, as in thin films and nanocrystals (*12*, *13*).

The measurement of diffusion through the core of a single dislocation was performed by Volin *et al.* (*14*), with the use of ex situ transmission electron microscopy (TEM) to study the transfer of vacancies between a void and the surfaces of an aluminum foil. Aside from this case, the phenomenon is either indirectly confirmed (*15*) or at best measured through grain boundaries treated as arrays of dislocations (*16*).

[1]CEMES-CNRS, Toulouse 31055, France. [2]Erich Schmid Institute of Materials Science, Austrian Academy of Sciences, Department Materials Physics, University of Leoben, 8700 Leoben, Austria. [3]Max Planck Institute for Metals Research, 70569 Stuttgart, Germany. [4]Department of Chemical and Materials Engineering, University of Kentucky, Lexington, KY 40506, USA.

*Present address. INM–Leibniz Institute for New Materials, 66123 Saarbrücken, Germany.

†To whom correspondence should be addressed. E-mail: legros@cemes.fr

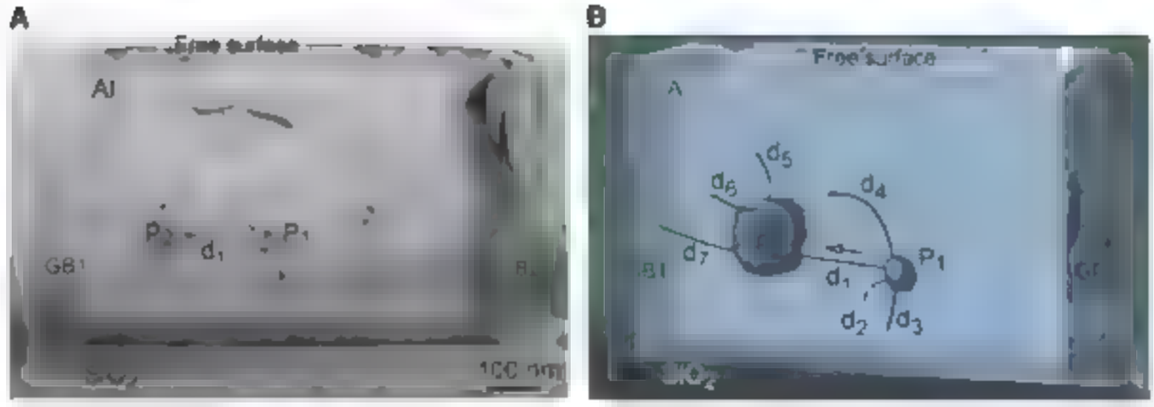

Fig. 1. Typical configuration of Si precipitates and dislocations observed by in situ TEM to study pipe diffusion. (**A**) TEM micrograph showing precipitates P_1 and P_2 connected by a dislocation segment d_1 in an aluminum grain at 623 K. (**B**) Three-dimensional sketch of the configuration observed in (A). The dislocation segments d_2 to d_7 connect the precipitates to the free surfaces or the boundary of the grain (GB1 and GB2) and do not participate in the diffusion of Si from P_1 to P_2. The larger arrow in (B) indicates the direction of the Si atom flux. The corresponding video (movie S1) and crystallographic information (fig. S1) are available as supporting material on *Science* Online

Diffusion is a thermally activated process, and the pipe diffusivity D_p can be described by the following equation

$$D_p = D_{p_0} \exp\left(\frac{Q_p}{kT}\right) \qquad (1)$$

where k is the Boltzmann constant, T is absolute temperature, and D_{p_0} and Q_p are the pre-exponential factor and activation energy for pipe diffusion that we want to determine.

TEM samples were thinned down as cross-sectional wedges until the Al layer containing the precipitates and the underlying Si substrate was 200 to 300 nm thick. The Al layer remains as a 400- to 500-μm-long electron-transparent thin beam (*17*) consisting of columnar grains ("bamboo structure"). The goal of our in situ TEM heating experiments is to stabilize, within an Al grain, a dislocation between two Si precipitates of different size (see d_1, P_1, and P_2 in Fig. 1) and to maintain this configuration at a constant temperature. Dislocation motion is controlled via the difference in coefficient of thermal expansion between the Al film and the Si substrate. The driving force for Si atom diffusion from smaller to larger precipitates [Ostwald ripening (*18*)] is the difference between the Gibbs free energy of each precipitate that is, their chemical potential μ_r due to surface curvature

$$\mu_r = \frac{2\Omega\gamma}{r} \qquad (2)$$

Here, r_i is the radius of precipitate i, Ω is the atomic volume of Si, and γ is the surface energy.

In Fig. 2, five precipitates labeled P_1 to P_5 and two dislocation segments d_1 and d_2 are monitored during an experiment at 623 K. Precipitates P_1 and P_2 are connected by the dislocation segment d_1, whereas d_2 links precipitates P_2 and P_5, the latter precipitate being located just underneath the free surface of the Al film. This configuration remained stable for about 1 hour, allowing us to observe the evolution of the Si precipitates in the Al matrix. As compared with others of similar size (e.g., P_4), precipitate P_1 dissolves much faster (Fig. 2, A to D). This is because its Si atoms channel quickly toward precipitate P_2 through dislocation segment d_1. The volume evolution of precipitates P_1 and P_2 is plotted in Fig. 2E. Once all the Si atoms are transferred from P_1 to P_2, dislocation d_1 is released and moves to the closest surface (Fig. 2, D and F). Figure 2F summarizes the positions and dimensions of P_1, P_2, P_5, d_1

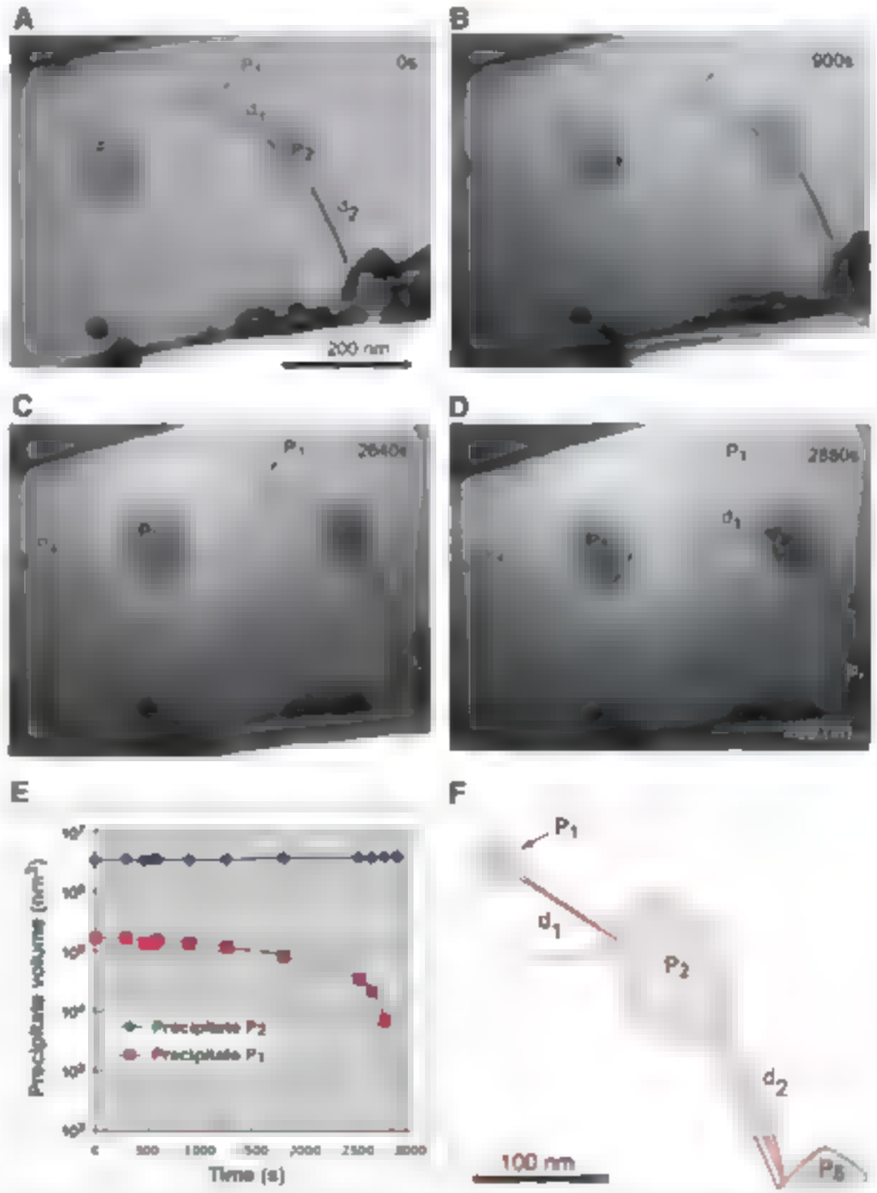

Fig. 2. In situ TEM observation of precipitate dissolution through a dislocation. T = 623 K. (**A** to **D**) Still micrographs: P_1 to P_5 are Si precipitates, and d_1 and d_2 are dislocation segments. Only P_1 dissolves abnormally fast because d_1 acts as a short circuit for diffusion. In (D) d_1 is released once P_1 has completely dissolved. (**E**) Evolution of precipitate volume for P_1 and P_2 as a function of time. (**F**) Sketch of the evolution of P_1, P_2, d_1, and d_2 size and position from (A) to (D).

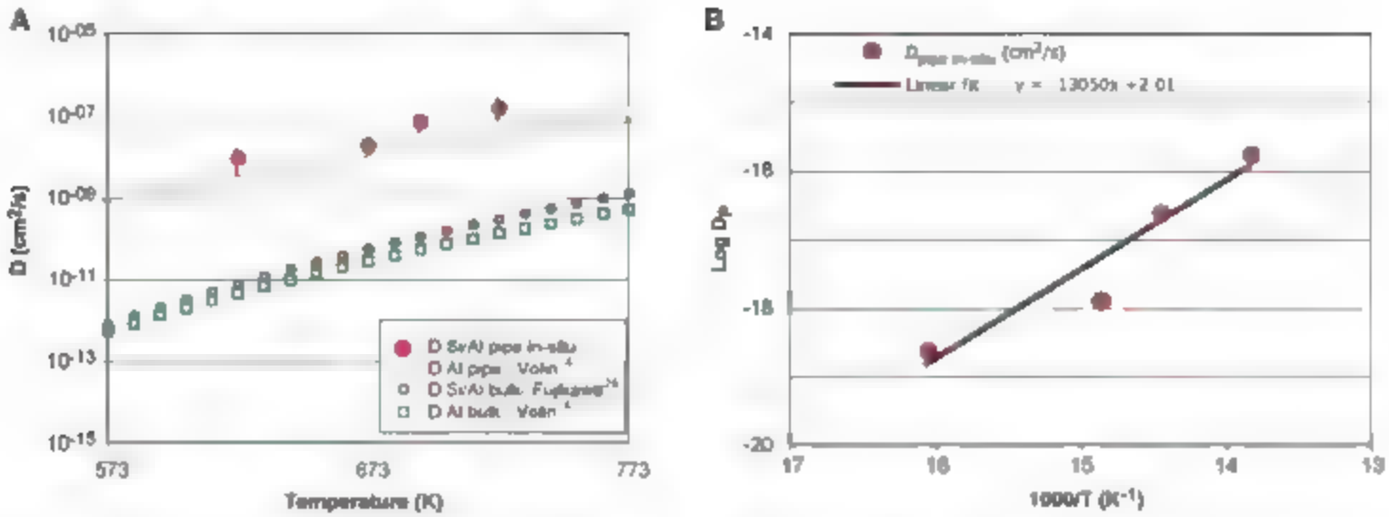

Fig. 3. Evolution of diffusivity (D) as a function of temperature. (**A**) Comparison of pipe and bulk diffusivity for Si in Al between 573 and 773 K. Curves composed of open squares (lattice self-diffusion of Al), open circles (lattice diffusion of Si in Al), and open triangles (Al pipe self-diffusion) are plotted according to previous experimental data (*14*, *29*). Filled red circles represent the pipe diffusivity found in the present study. Error bars calculated from the SD found on D_p values were added to these filled circles as vertical bars. (**B**) Logarithmic plot of D_p versus $1/T$. The fitted line is used to determine the pipe diffusion activation energy (*17*).

and d_2 from the micrographs in Fig. 2, A to D. The size of all precipitates, except P_1, remained apparently constant, and precipitate P_1, while fixed in place, dissolved faster on the side connected to the dislocation. We conclude from this that Si diffusion around the particle surface is not rate-limiting for pipe diffusion.

The atomic flux density J_p simply derives from the volume evolution dV_1/dt of the smallest precipitate participating in pipe diffusion (i.e., P_1)

$$J_p = \frac{dV_1}{dt}\frac{1}{\Omega s_p} \qquad (3)$$

The "pipe cross section" s_p is usually calculated from the dislocation Burgers vector **b**. The atomic flux density is also related to the pipe diffusivity D_p

$$J_p = \frac{D_p \Delta\mu}{\Omega k T \Delta l} \qquad (4)$$

with $\Delta\mu$ being the difference in chemical potential between precipitates P_1 and P_2 and with Δl being their distance. This equation explains why the volumic reaction of P_1 accelerates at the end of dissolution (Fig. 2F): As the radius of P_1 diminishes, the gradient of chemical potential between P_1 and P_2 increases, accelerating diffusion (Fig. 2E). Combining Eqs. 2 to 4 leads to an expression for D_p that depends only on V_1, r_1, r_2, and Δl

$$D_p = \frac{kT}{2\Omega\gamma s_p}\frac{dl}{dt}\left(\frac{1}{r_2}-\frac{1}{r_1}\right)^{-1}\Delta l \qquad (5)$$

This relation for D_p results from the simple form of Gibbs free energy (Eq. 2) in which we have neglected the strain energy of Si precipitates. The absence of notable strain gradients near the Si precipitates can be verified by analyzing the TEM bright-field contrast around the spherical precipitates (*19*) (Fig. 2) and the neighboring dislocation displacements and bowing. This lack of strain gradients during the pipe diffusion process is more understandable in the thin-foil geometry of this study. The growth of large precipitates should occur normal to the TEM thin foil (200 to 300 nm thick in general), that is, in the direction where potential elastic strains are lowest. This is because a free surface is always close to the larger precipitates, which have a diameter of about 100 nm. As a result, the monitored area of larger precipitates is not expected to vary significantly during in situ experiments, which is indeed the case (*17*).

Altogether, five successful experiments were carried out, two at 623 K (Figs. 1 and 2) and one each at 673 K, 693 K (movie S1), and 723 K. At 623 K, the experiment described in Fig. 2 leads to a value of $D_p = 1.2 \times 10^{-8}$ cm²/s whereas that in Fig. 1 gives $D_p = 8.2 \times 10^{-9}$ cm²/s. This shows that consistent results are reached for experiments repeated at the same temperature, even with dissimilar precipitate and dislocation configurations. Figure 3, A and B, presents the four values of D_p resulting from these experiments, plotted as filled red circles. The error bars correspond to the SD, primarily resulting from the term dl/dt (*17*). For each temperature, this SD never exceeded 50% of the calculated median values of D_p.

The surface energy γ of the precipitates and the pipe cross section s_p can also alter the value of D_p. We choose $\gamma = 1.2$ J/m², a mean value lying between (i) the experimentally measured surface energy of pure Si (*20*) and of Al-Si interface (~1 J/m²) (*21*) and (ii) the theoretically predicted Si {111} surface energy (1.15 < γ < 1.9 J/m²) (*22*, *23*). These studies also indicate that the close-packed planes of Si have similar surface energies.

The pipe cross section s_p characterizes the higher diffusivity core region of the dislocation. Recent observations of Cottrell atmospheres around dislocations via atom probe tomography give an upper limit of the radial extent of impurities (*24*, *25*), but these diameters (1.5 to 3 nm) cannot be directly related to s_p. Picu and Zhang (*26*) simulated the pipe diffusion of Mg in dissociated dislocations in Al and found that diffusion was confined within a region bounded by two adjacent {111} planes and by the dissociation width (i.e., with a radius of 0.28 to 0.68 nm²), depending on the character and splitting of the dislocation. This means that most of the accelerated diffusion does not permeate beyond the first atomic neighbors around the dislocation core. The actual core structure of a ½<110> dislocation in Al is still under debate (*27*), and high-resolution TEM images show compact cores with spreading less than **2b** (*28*). For the pipe cross section, we therefore considered a disk with radius equal to the Burgers vector of a perfect a/2 <110> dislocation (b = 0.28 nm), yielding $s_p = 0.25$ nm². This value corresponds to diffusion confined inside the compact core of a perfect a/2 <110> dislocation and also to the value adopted in the review by Balluffi and Granato (*16*), which allows for relevant comparison. Finally, we have not systematically determined the dislocation character, which could also influence the value of Q_p. A dislocation analysis of the configuration described in Figs. 1 and 2 is shown in figs. S1 and S2 and shows that the dislocation responsible for pipe diffusion (d_1) has mixed character in this case.

For comparison, the graph in Fig. 3A includes the bulk diffusivity of Si in Al (*29*), the self-diffusivity of Al, and the pipe diffusivity of vacancies in Al (*14*). In the temperature range investigated, the pipe diffusivity is about three orders of magnitude higher than that for bulk and is similar in magnitude to the Al vacancy pipe diffusion deduced from Volin *et al.* (*14*) by a nondirect experimental method. The logarithmic plot of D_p as a function of $1/T$ in Fig. 3B allows the calculation of both the pre-exponential factor D_{p_0} and the activation energy Q_p for pipe diffusion via Eq. 1. A linear curve fit of the four points in Fig. 3B yields $D_{p_0} = 7$ cm²/s and $Q_p = 108$ kJ/mol. This energy is very close to the simulated value of $Q_p = 108.8$ kJ/mol for Mg diffusion through 60° dislocations (*26*). For comparison,

the experimental bulk values for diffusion of Si in Al are $D_0 = 2$ cm^2/s and $Q = 136$ kJ mol (29). The pre-exponential factor D_{Pa} is thus larger than those found in the literature (14–29), but the activation energy, which indicates how easily pipe diffusion occurs, is 20% smaller than that for bulk diffusion of Si in Al (29). Also, the activation energy for interstitials (108 kJ mol) is higher than that for vacancies (82 kJ mol) (14), indicating easier diffusion of vacancies (3).

Confirming previous theoretical studies, the present in situ TEM experiments establish that dislocations can transport atoms at rates orders of magnitude faster than bulk diffusion in a crystal. Quantifying the diffusivity and activation energy of a single dislocation should help to understand low-angle grain boundary diffusion, accelerated precipitate growth, and high-temperature creep in many alloys. A more fundamental insight into the detailed interactions between a dislocation and migrating vacancies/interstitials is also expected.

References and Notes

1. G. R. Love, *Acta Metall.* **12**, 731 (1964).
2. J. Huang, M. Meyer, V. Pontikis, *Phys. Rev. Lett.* **63**, 628 (1989).
3. J. Rabier, M. P. Puls, *Philos. Mag. A* **59**, 533 (1989).
4. R. W. Balluffi, R. M. Thomson, *J. Appl. Phys.* **33**, 817 (1962).
5. W. A. Swansiger, W. Lojkowski, M. W. Grabski, *Acta Metall.* **34**, 599 (1986).
6. P. Goudeau, C. Teymonie, P. Lacombe, *C. R. Acad. Sci. Paris* **246**, 1209 (1958).
7. A. B. Pandey, R. S. Mishra, A. G. Paradkar, Y. R. Mahajan, *Acta Mater.* **45**, 1297 (1997).
8. C. Schwink, A. Hartmann, *Mater. Sci. Eng. A* **234–236**, 1 (1997).
9. Y. Brechet, Y. Estrin, *Acta Metall. Mater.* **43**, 955 (1995).
10. W. Luo, C. Shen, Y. Wang, *Acta Mater.* **55**, 2579 (2007).
11. R. D. Vengrenovich, Y. V. Gudyma, S. V. Yarema, *Scripta Mater.* **46**, 363 (2002).
12. L. Klinger, E. Rabkin, *Interface Sci.* **8**, 197 (1998).
13. P. Komninou, J. Stoemenos, G. Nouet, T. Karakostas, *J. Cryst. Growth* **203**, 103 (1999).
14. I. E. Volin, K. H. Lie, R. W. Balluffi, *Acta Metall.* **19**, 263 (1971).
15. X. Tang, K. P. D. Lagerlöf, A. H. Heuer, *J. Am. Ceram. Soc.* **86**, 560 (2003).
16. R. W. Balluffi, A. V. Granato, in *Dislocations in Solids*, F. R. N. Nabarro, Ed. (North Holland, Amsterdam, vol. 13, 1979), pp. 23–131.
17. Materials and methods are available as supporting material on *Science* Online.
18. F. W. Voorhees, *Annu. Rev. Mater. Sci.* **22**, 197 (1992).
19. L. H. Zhang, E. Johnson, U. Dahmen, *Acta Mater.* **53**, 3635 (2005).
20. J. M. Bermond, J. J. Métois, X. Egéa, F. Floret, *Surf. Sci.* **330**, 48 (1995).
21. E. Ogris, A. Wahlen, H. Lüchinger, P. J. Uggowitzer, *J. Light Met.* **2**, 263 (2002).
22. M. Bernstein, E. Kaxiras, *Phys. Rev. B* **56**, 10488 (1997).
23. B. C. Bolding, H. C. Andersen, *Phys. Rev. B* **41**, 10568 (1990).
24. D. Blavette, E. Cadel, A. Fraczkiewicz, A. Menand, *Science* **286**, 2317 (1999).
25. K. Thompson, P. L. Flaitz, P. Ronsheim, D. J. Larson, T. F. Kelly, *Science* **317**, 1370 (2007).
26. B. C. Pan, D. Zhang, *Acta Mater.* **52**, 161 (2004).
27. S. G. Srinivasan *et al.*, *Phys. Rev. Lett.* **94**, 125502 (2005).
28. M. J. Mills, P. Stadelmann, *Philos. Mag. A* **60**, 355 (1989).
29. S.-I. Fujikawa, K.-I. Hirano, Y. Fukushima, *Metall. Trans. A* **9**, 1811 (1978).

30. M.L. thanks C. Bonales, O. Thomas, and P. Gergaud for helpful discussions and the supply of initial samples. This work was supported by the recurrent financial support from the Centre National de la Recherche Scientifique (CNRS) and occurred in the frame of the ESTEEM (Enabling Science and Technology through European Electron Microscopy) European network.

Supporting Online Material

www.sciencemag.org/cgi/content/full/319/5870/1646/DC1
Materials and Methods
SOM Text
Figs. S1 and S2
References
Movie S1

15 October 2007; accepted 15 February 2008
10.1126/science.1151771

Titan's Rotation Reveals an Internal Ocean and Changing Zonal Winds

Ralph D. Lorenz,[1]* Bryan W. Stiles,[2] Randolph L. Kirk,[3] Michael D. Allison,[4] Paolo Persi del Marmo,[5] Luciano Iess,[6] Jonathan I. Lunine,[4] Steven J. Ostro,[2] Scott Hensley[2]

Cassini radar observations of Saturn's moon Titan over several years show that its rotational period is changing and is different from its orbital period. The present-day rotation period difference from synchronous spin leads to a shift of ~0.36° per year in apparent longitude and is consistent with seasonal exchange of angular momentum between the surface and Titan's dense superrotating atmosphere, but only if Titan's crust is decoupled from the core by an internal water ocean like that on Europa.

Titan's massive atmosphere modifies its surface in many ways—notably by aeolian (wind) transport forming sand dunes and by fluvial erosion forming river channels—and it has been predicted (*1*) that angular momentum exchange between the surface and atmosphere might lead to seasonal variations in Titan's spin rate or length of day (LoD). Changes in wind patterns lead to a seasonal change (*2*, *3*) in Earth's LoD of ~1 ms, superimposed on longer-term variations in LoD due to gravitational tidal torque from the Moon. On Mars, a seasonal variation in LoD of ~1 ms measured by lander radio tracking (*4*) occurs as a result of the redistribution of mass in the CO_2 frost cycle. Also, a gravitational libration of Mercury revealing a liquid core was recently observed by planetary radar (*5*). These effects are quite subtle, but on Titan, a small body with a massive atmosphere, the changes can be substantial. Global Circulation Model (GCM) predictions of seasonal changes in LoD (*1*) are of some tens to hundreds of seconds (Titan's sidereal LoD is nominally equal to the orbit period of 1,377,684 s, or ~15.945 solar Earth days). This change leads to displacements of surface features from their expected positions by tens to hundreds of kilometers over time scales of a Titan season (about one-fourth of the 29.5-year Saturn orbital period), easily detectable by radar mapping.

The high spatial resolution (<0.5 km) of images from the Cassini radar instrument, coupled with the geometric precision relative to an external reference frame afforded by radar imaging, has recently allowed Titan's spin state to be determined with great accuracy (*6*–*8*). In synthetic aperture radar (SAR) imaging acquired by Cassini between October 2004 and May 2007, there are 19 regions on Titan that are observed in more than one swath. Two independent analyses—one (*6*) using 150 manually determined landmark features, which are displaced by up to 30 km between swaths if the locations are computed with the previously assumed pole position and a synchronous rotation, and another (*7*) using numerical correlation of four overlapping images—both indicate a spin rate of 22.5781° per day, or 0.36° per year faster than synchronous spin. These analyses also determine the pole position, indicating an obliquity of Titan's pole from its orbital plane around Saturn of 0.3°. This is small enough to be meteorologically unimportant relative to the Saturn system obliquity that drives Titan's seasons (the ring plane, itself inclined by ~0.3° to Titan's orbital plane about Saturn, is inclined to Saturn's orbit around the Sun by some 26.7°, close to the present obliquities of Mars and Earth of 25.2° and 23.5°, respectively). Although the pole position (expected to precess on century-to-millennium time scales because of gravitational torques in the saturnian system) may provide constraints on Titan's internal structure, notably if Titan is in a dynamically relaxed spin-orbit equilibrium [a so-called "Cassini State," e.g., (*9*–*11*)] we focus here on the spin rate.

First, we note that Titan's spin-down time is short (<10^8 years) relative to the age of the solar system, so in the absence of external torques it should be in an asymptotic end state with synchronous rotation (*12*). Indeed, less accurate

[1]Space Department, Johns Hopkins University Applied Physics Laboratory, Laurel, MD 20723, USA. [2]Jet Propulsion Laboratory, California Institute of Technology, Pasadena, CA 91109, USA. [3]U.S. Geological Survey, Flagstaff, AZ 86001, USA. [4]NASA Goddard Institute for Space Studies, New York, NY 10025, USA. [5]Università La Sapienza, 00184 Rome, Italy. [6]Lunar and Planetary Laboratory, University of Arizona, Tucson, AZ 85721, USA.

*To whom correspondence should be addressed. E-mail: ralph.lorenz@jhuapl.edu

determinations (*13*, *14*) of Titan's spin are consistent with synchronous or near-synchronous spin. However, transfer of angular momentum between the atmosphere and surface can cause short-term (seasonal) variations about this long-term synchronous baseline that have eluded detection by prior methods. Overall nonsynchroneity of Titan's atmosphere, surface, and interior would require external forcing via an implausibly large recent impact and would be difficult to reconcile with the combined constraints of our measurements and prior determinations (*8*).

If Titan were a solid, uniform undifferentiated body, it would have a moment of inertia about its rotation axis $C = 3.4 \times 10^{35}$ kg m^2 = 0.4 MR^2 where M is the planetary mass and R is the radius. If it differentiated into a rocky core with an ice mantle (*15*), then $C \sim 2.7 \times 10^{35}$ kg m^2 ~0.33 MR^2. On the other hand, the moment of inertia of an ice crust alone, mechanically decoupled from the deep interior of silicates and high-pressure ice by a liquid layer of water or water-ammonia, is much lower, only ~2.2×10^{34} kg m^2 for a crust 70 km thick. These possibilities may be compared with the moment of inertia of the atmosphere I_{atm}, taken as a spherical shell using the surface air density of 5.3 kg m^{-3} and scale height of H = 25 km: $I_{atm} = 4.9 \times 10^{31}$ kg m^2. In other words, the moment of inertia of the crust may be only 400 times that of the atmosphere (by contrast, this ratio is ~10^6 for Earth).

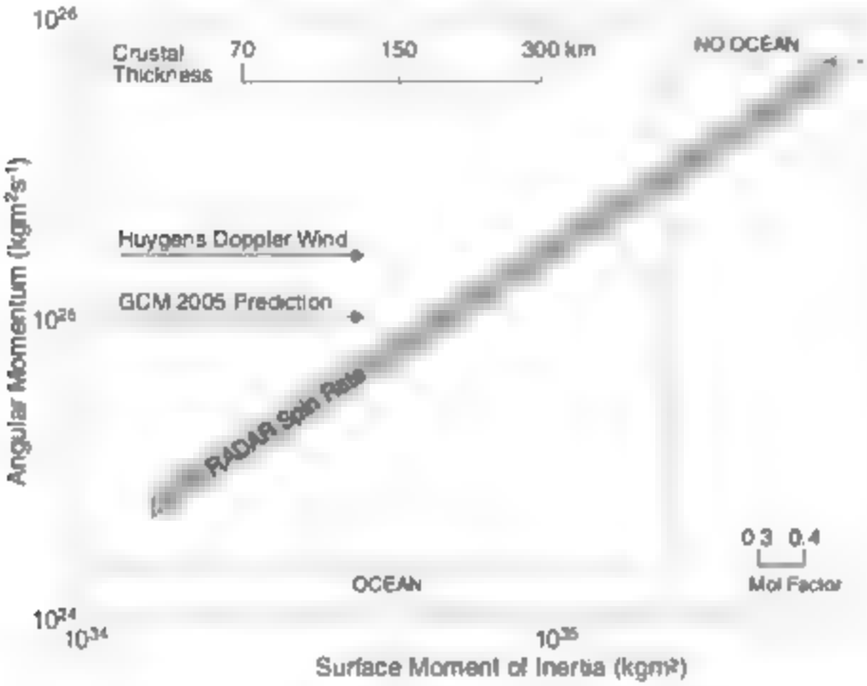

Fig. 1. The radar determination of spin rate offset from synchronous rotation (shaded diagonal line) is equivalent to a determination of the ratio between angular momentum deposition (ordinate) and the moment of inertia attached to the surface (abscissa). The observed rate requires either that the crust is decoupled from the interior or that exceptional variations in atmospheric angular momentum occur. The GCM prediction is from (*1*). The Huygens Doppler Wind Experiment probe assumes that the atmosphere rotates as a solid body, a more probable cosine-latitude dependence would drop the angular momentum by a factor of 2. Atmospheric angular momentum values are for motion relative to Titan's surface. MoI, moment of inertia.

Although all models, telescopic observations, and the measurements by the Huygens probe (*16*) indicate consistently prograde winds in the upper levels of the atmosphere, the lowest scale height of the atmosphere may experience a seasonal reversal at some latitudes. This reversal is predicted (*1*) to almost balance the rest of the atmosphere, such that the total angular momentum budget relative to the surface varies by ~80% about a mean of ~1.5×10^{25} kg m^2 s^{-1} (in an inertial frame the angular momentum varies only by ~10%, dominated by the rotational velocity of Titan itself). The effect on the LoD relates to the ratio of this angular momentum change to the crustal moment of inertia (Fig. 1). If the angular momentum change is as predicted, it is clear that Titan's crust must be decoupled from its interior. The same conclusion can be drawn even if the atmospheric angular momentum observed by the probe (adopting a wind speed proportional to cosine of latitude) were completely exchanged with the surface. Only if the atmospheric angular momentum were to change by almost an order of magnitude relative to what was measured (for which there is no observational support) could a solid Titan be accommodated; this scenario might also require unphysical changes in total kinetic energy.

The existence of an internal water-ammonia ocean that mechanically decouples the crust from the interior has been long predicted by cosmochemical and thermal models (*17*, *18*) and has even been considered to be potentially habitable (*19*). Internal oceans have been detected magnetically on Europa and Callisto (*20*) and are also presumed to exist on Ganymede.

We note that the present magnitude of our drift is slightly smaller (0.36° per year) than the 0.6° per year predicted (*1*). This difference points to one or more model assumptions that might be adjusted to achieve better agreement; for example, gravitational coupling between the crust and a possibly nonspherical solid core could affect the rotation history, or the ice crust may be thicker than the 70 km assumed. A factor of ~2 increase in thickness can be readily accommodated in thermal models by uncertainties in internal heat flow. Indeed, other evidence points to the crust not being thin. The 440-km-diameter impact structure Menrva (*21*) does not appear to have penetrated the crust in the manner of ice-breaching impacts on Europa. This implies that the crust was thicker than one-third the diameter of the transient cavity (about two-thirds of the final diameter) when the crater formed, or at least 100 km.

The spin rate also appears to be accelerating, relative to synchronous spin, by 0.05° per day every 100 years (Fig. 2). The mere existence of observable change supports the thin-crust inter-

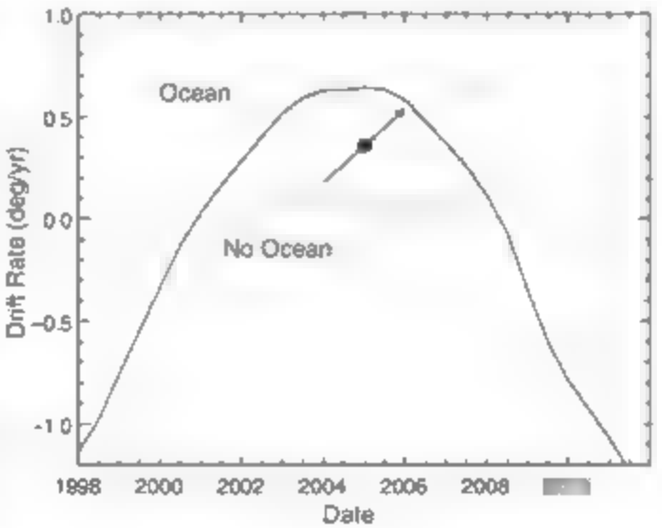

Fig. 2. Solid circle plus arrow shows our measured longitude drift (relative to assumed synchronous rotation) and its rate of change as measured on Cassini flybys TA to T28. Predicted drift rates are much smaller (dotted line) if Titan is a solid body. The drift and its rate of change are the same magnitude and sign, but lagging by ~2 years, the predicted rotation if Titan's crust is decoupled from the interior (solid line). Further observations in the 2008–2010 time frame, during the proposed extended mission of Cassini, may confirm the predicted decline and reversal of the drift (dashed line).

pretation above. This change is similar to that predicted (*1*) but is apparently delayed by ~2 years, which suggests that GCMs may merit refinement. An unavoidable deficiency in present Titan GCMs is the lack of surface topography, so atmospheric torque is assumed to be attributable only to skin friction. However, it is known that there are kilometer-high mountain chains on Titan (*22*) and that a pressure field can exert a torque on the surface via pressure differences across mountain chains [e.g., (*2*, *23*)]. Another assumption that bears further examination is that of complete decoupling from the ocean. Friction at the bottom of the ice layer would allow the ocean to act as another angular momentum reservoir, generally providing a higher apparent moment of inertia than the ice crust alone, but likely increasing the complexity of the spin history.

Regardless of the details, an important and robust conclusion of this study is that the spin period can be expected to vary substantially over time scales of a few years, and indeed other data (*8*) show that the rate of change of spin rate must have been different over the past couple of decades. Taking the phase-lagged model as a guide, Titan's spin should peak during the proposed extended mission (2008–2010) and then begin to decline. We predict that other anticipated Cassini results, such as determination of the tidal Love number k_2 (*12*) from radio tracking (*24*), will be consistent with an internal aqueous ocean. Induced magnetic fields in such an ocean, which might independently constrain the ice thickness and ocean conductivity (*25*), will be difficult to detect on Cassini flybys, although a future dedicated Titan orbiter-lander mission could succeed. Such a mission would itself provide new rotation measurements of this body, which combines the astrobiological appeal of a subsurface water ocean on an organic-rich icy satellite with solid-body rotation effects driven by atmospheric dynamics that are more profound than those observed on the terrestrial planets.

References and Notes

1. L. Iess, P. Rimlinger, *Geophys. Res. Lett.* **32**, L24201 (2005).
2. R. Hide, M. T. Birch, L. V. Morrison, D. J. Shea, A. A. White, *Nature* **286**, 114 (1980).
3. J. P. Peixoto, A. H. Oort, *Physics of Climate* (AIP Press, New York, 1992).
4. W. M. Folkner, C. F. Yoder, D. N. Yuan, E. M. Standish, R. A. Preston, *Science* **278**, 1749 (1997).
5. J. L. Margot, S. J. Peale, R. F. Jurgens, M. A. Slade, I. V. Holin, *Science* **316**, 710 (2007).
6. B. Sicardy *et al.*, *Bull. Am. Astron. Soc.* **39**, 543 (2007).
7. P. Peralta de Medina, L. Iess, G. Picardi, R. Seu, B. Bertotti, *Bull. Am. Astron. Soc.* **39**, 543 (2007).
8. See supporting material on *Science* Online.
9. B. G. Bills, *Icarus* **175**, 233 (2005).
10. P. Goldreich, *Astron. J.* **71**, 1 (1961).
11. R. Greenberg, S. Weidenschilling, *Icarus* **58**, 186 (1984).
12. W. D. Sears, J. I. Lunine, R. Greenberg, *Icarus* **105**, 259 (1993).
13. P. H. Smith *et al.*, *Icarus* **119**, 336 (1996).
14. J. Richardson, R. D. Lorenz, A. McEwen, *Icarus* **170**, 113 (2004).
15. F. Sohl, H. Hussmann, B. Schwentker, T. Spohn, R. D. Lorenz, *J. Geophys. Res.* **108**, 10.1029/2003JE002044 (2003).
16. M. K. Bird *et al.*, *Nature* **438**, 800 (2005).
17. D. J. Stevenson, *Eur. Space Agency Spec. Publ. ESA SP-338* (1992), pp. 29–33.
18. O. Grasset, C. Sotin, F. Deschamps, *Planet. Space Sci.* **48**, 617 (2000).
19. A. D. Fortes, *Icarus* **146**, 444 (2000).
20. C. Zimmer, K. K. Khurana, M. G. Kivelson, *Icarus* **147**, 329 (2000).
21. C. Elachi *et al.*, *Nature* **441**, 709 (2006).
22. J. Radebaugh *et al.*, *Lunar Planet. Sci. Conf.* **XXXVII**, 1007 (2006).
23. R. M. White, *J. Meteorol.* **6**, 353 (1949).
24. N. Rappaport, B. Bertotti, G. Giampieri, J. D. Anderson, *Icarus* **126**, 313 (1997).
25. K. Hand, C. Chyba, *Icarus* **189**, 424 (2007).

26. We thank those who designed, developed, and operate the Cassini/Huygens mission, and in particular our colleagues on the Cassini radar team. Cassini is a joint endeavor of NASA, ESA, and the Italian Space Agency (ASI) and is managed by the Jet Propulsion Laboratory, California Institute of Technology, under a contract with NASA.

Supporting Online Material

www.sciencemag.org/cgi/content/full/319/5870/1649/DC1
Materials and Methods
Figs. S1 to S3
References

11 October 2007; accepted 24 January 2008
10.1126/science.1151639

Chloride-Bearing Materials in the Southern Highlands of Mars

M. M. Osterloo,[1]* V. E. Hamilton,[1] J. L. Bandfield,[2]† T. D. Glotch,[3] A. M. Baldridge,[2]‡ P. R. Christensen,[2] L. L. Tornabene,[4] F. S. Anderson[1]

Chlorides commonly precipitate during the evaporation of surface water or groundwater and during volcanic outgassing. Spectrally distinct surface deposits consistent with chloride-bearing materials have been identified and mapped using data from the 2001 Mars Odyssey Thermal Emission Imaging System. These deposits are found throughout regions of low albedo in the southern highlands of Mars. Geomorphologic evidence from orbiting imagery reveals these deposits to be light-toned relative to their surroundings and to be polygonally fractured. The deposits are small (< ~25 km^2) but globally widespread, occurring in middle to late Noachian terrains with a few occurrences in early Hesperian terrains. The identification of chlorides in the ancient southern highlands suggests that near-surface water was available and widespread in early Martian history.

On Earth, chlorides are formed by precipitation from evaporating surfaces (e.g., saline lakes) or groundwater hydrothermal brines, as volcanic sublimates (e.g., at fumaroles) and by efflorescence (direct crystallization onto sediment grains forming crusts) (*1*). Typically, chloride deposits produced by precipitation have large surface relief and polygonal to blocky morphologies, whereas efflorescence tends to produce thin crusts (*1*). For terrestrial evaporite systems, the most important variable for the resultant brine composition and saline mineral assemblages is the composition of the dilute water at the onset of concentration (evaporation) (*2*). Generally, chlorides in terrestrial settings occur in alkaline environments and are the last minerals to precipitate out of saline brines, preceded by various carbonates, sulfates, and silica. On Mars, saline minerals (including various chlorides) are predicted to form from acidic fluids derived from basaltic weathering (*3*). Geologic environments that contain saline minerals are of key interest to the exobiology community because they are potentially areas of biological activity and chemical sedimentation, which is optimal for the preservation of biological signatures and a high priority for future exploration by orbiting and landed missions (*4*).

Using Mars Odyssey Thermal Emission Imaging System (THEMIS) data (*5*), as well as supporting data from the Mars Global Surveyor (*6*) and Mars Reconnaissance Orbiter (*7*), we have identified a compositional unit on Mars that contains a mineralogical component likely attributable to chloride salts. We initially identified these deposits because of their spectral distinctiveness in false-color, decorrelation stretched (DCS), THEMIS daytime infrared radiance images (*8*). The deposits range in area from ~1 km^2 to ~25 km^2 and generally are topographically lower than the immediate surrounding terrain. The spectrally distinct deposits commonly exhibit irregular outlines (Fig. 1A) and occur less commonly in small craters and sinuous channels (Fig. 1, B to D). Our examination of the THEMIS daytime infrared data set has revealed ~200 of these deposits throughout the low albedo, mid-to-low latitude southern highlands (Fig. 2), corresponding to mid-

[1]Hawai'i Institute of Geophysics and Planetology, University of Hawai'i, 1680 East West Road, Honolulu, HI 96822, USA. [2]School of Earth and Planetary Exploration, Arizona State University, Tempe, AZ 85287, USA. [3]Department of Geosciences, Stony Brook University, Stony Brook, NY 11794, USA. [4]Lunar and Planetary Laboratory, University of Arizona, Tucson, AZ 85721, USA.

*To whom correspondence should be addressed. E-mail: osterloo@higp.hawaii.edu

†Present address: Department of Earth and Space Sciences, University of Washington, Johnson Hall 070, Box 351310, Seattle, WA 98195-1310, USA.

‡Present address: Jet Propulsion Laboratory, MS 183-501, 4800 Oak Grove Drive, Pasadena, CA 91109, USA.

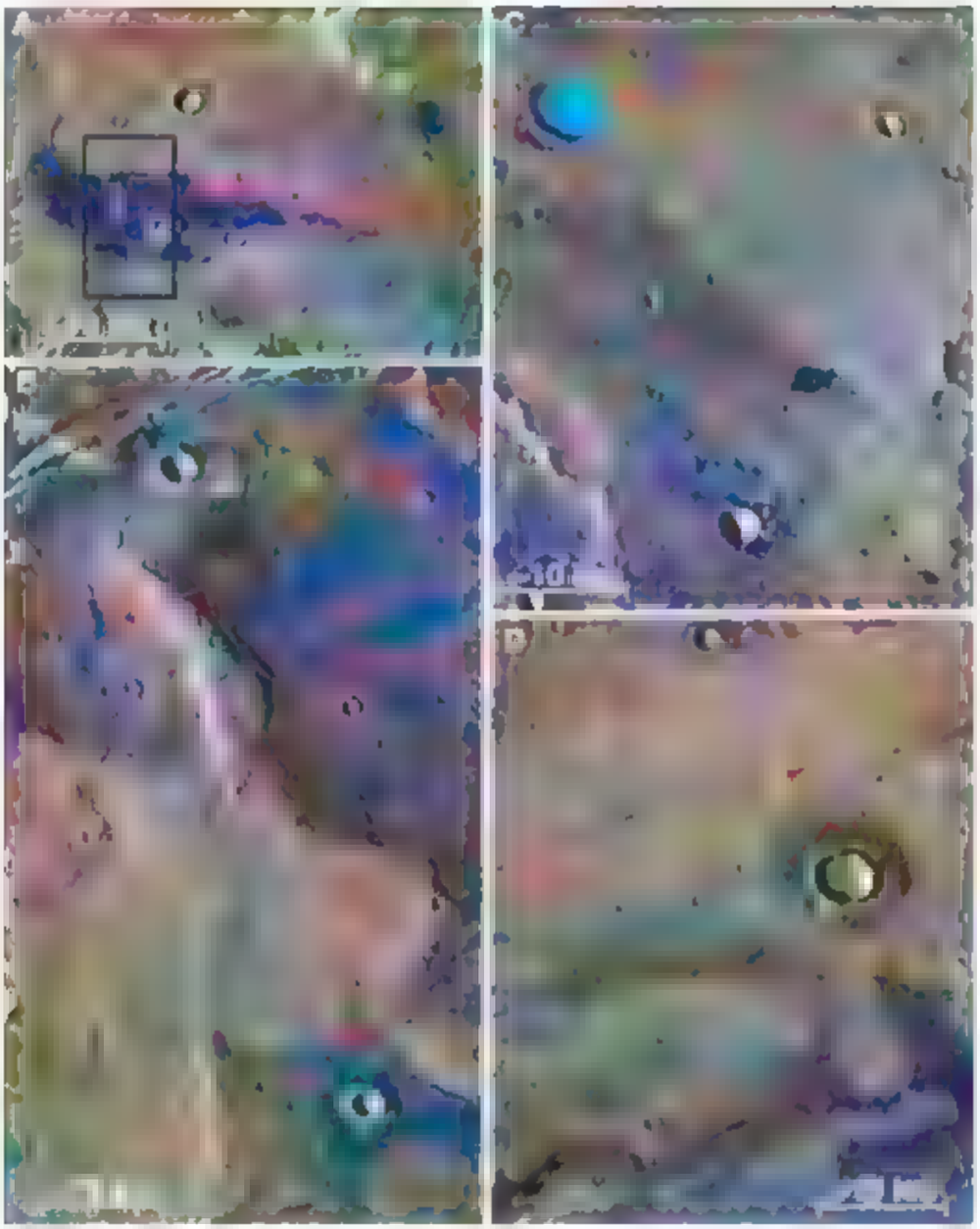

Fig. 1. All images are THEMIS 8/7/5 DCS radiance images. (**A**) I08831002 (~221.0° E, ~38.8° N) showing spectrally distinct materials in blue. Red boxes indicate areas averaged for spectral analysis, and the black box indicates HiRISE coverage. (**B**) I07808003 (~205.5° E, ~32.7° N) showing spectrally distinct materials following sinuous paths, abutting Sirenum Fossae, and occurring in low-lying areas near craters. (**C**) I07815002 (~4.1° E, 28.0° N) showing spectrally distinct materials filling a small crater as well as occurring as patches. (**D**) Spectrally distinct materials following sinuous path in I07830004 (~290.8° E, 34.0° N).

Fig. 2. Global distribution of spectrally distinct materials overlain on TES Lambert albedo and MOLA shaded relief.

Noachian (~3.9 to ~3.8 billion years ago (Gya)) terrains and the Hesperian ridged plains unit (~3.7 to ~3.5 Gya) (*9*).

THEMIS surface emissivity spectra (*10*) of the deposits show that they have a spectral shape that is unlike any previously studied surface type (*11*–*14*). Whereas the regional materials (Fig. 3A) exhibit a basaltic spectral shape, the distinct deposits are characterized by higher emissivity across the 1260 to 900 cm^{-1} range and exhibit a featureless spectral slope toward lower wave numbers. Higher spectral resolution (10 cm^{-1} sampling) Thermal Emission Spectrometer (TES) data can be used to further constrain the mineralogy of these surfaces, although at lower spatial resolution (~3 × 6 km minimum) (*8*). In Terra Sirenum, the spectrum of the spectrally distinct material is similar to that of the surrounding terrain in that it exhibits a shape similar to that of a basalt, but it differs in having a negative spectral slope (Fig. 3B). The basaltic shape is attributable to the large spatial area measured by TES relative to THEMIS, which leads to subpixel mixing and dilution of the spectrally distinct material by the regional basaltic materials. Spectral ratios were used to remove features common to both spectra and derive a residual spectral shape that represents the difference between the two materials (*15*). The resulting ratio spectrum is relatively featureless and slopes toward lower wave numbers, as shown in Fig. 3B. A slight residual "hump" in the ratio spectrum between ~1330 and 830 cm^{-1} resembles the basaltic shape (inverted) and is attributable to a difference in spectral contrast between the two spectra, both of which include basaltic materials. Therefore, we conclude that the spectral character of the spectrally distinct deposits is nearly featureless and inconsistent with previously derived TES surface shapes (*8*, *11*–*14*). Quantitative linear deconvolution and factor analysis/target transformation analyses of the TES data also indicate that phases with weak spectral features and negative slopes are candidates for the component that is responsible for the spectrally distinct materials, although there is no phase in our spectral library (which contains >200 rock and mineral phases, including phyllosilicates and sulfates, (*16*)) that results in a good model fit (*8*).

A negative spectral slope in mid-infrared emissivity spectra can arise from errors in the derivation of temperature in the process of converting radiance (a temperature-dependent parameter) to emissivity (which is independent of temperature) (*8*, *17*). The separation of temperature and emissivity relies on the assumption that the observed radiance represents a single or narrow range of temperatures (e.g., a few degrees K) and that the emissivity of the materials is unity at some point in the spectral range. We find no evidence for large temperature variations at the 100 m pixel scale of the THEMIS instrument that would introduce such temperature errors (*8*). However, if the observed materials do not exhibit unit emissivity (as assumed at some point in the wave number range used to determine the target temper-

ature), incorrect temperatures may be derived during the conversion of radiance to emissivity (8). For materials having a maximum emissivity less than unity, the target temperature will be underestimated and a slope will be imparted to the resulting emissivity spectrum (17).

Virtually all silicate phases (and most carbonate, sulfate, and oxide phases) exhibit near-unit emissivity at some point in the 1350 to 300 cm^{-1} range used for the TES temperature-emissivity separation (18); however, some chlorides have relatively featureless spectra in this range (8, 19, 20). One or more chlorides as a component of the Martian materials would reduce emissivity, causing incorrect temperature derivation and introducing a slope in the emissivity spectrum. Chloride salts have been identified on Earth in infrared multispectral data on the basis of similar observations; for example, the presence of halite was accurately inferred in Death Valley, California, by a lack of spectral features in high-resolution MODIS (Moderate Resolution Imaging Spectroradiometer) ASTER (Advanced Spaceborne Thermal Emission and Reflection Radiometer) Airborne Simulator (MASTER) which covers a similar wavelength range as the THEMIS instrument (8, 21). Based on the observed Martian spectra, the assumption of unit emissivity during TES and THEMIS data reduction, the laboratory measurements of the behavior of chloride salts, and similar terrestrial identifications, we interpret these spectrally distinct materials to be chloride-bearing deposits.

Further insight into the nature and origin of the putative chloride-bearing deposits is provided by visible images from THEMIS (5), the High Resolution Imaging Science Experiment (HiRISE) (7), and the Mars Orbiter Camera (MOC) (6), topography from the Mars Orbiter Laser Altimeter (MOLA) (22), and thermal inertia from THEMIS nighttime data (23). MOC images (~2.95 m/pixel) of the Terra Sirenum deposit and other deposits across the southern highlands show that the chloride-bearing materials are light-toned, in addition, they exhibit patterned-ground and etched-terrain morphologies. Higher spatial resolution (~25.3 cm/pixel) HiRISE images of the materials in Terra Sirenum also show the putative chloride-bearing materials to be light-toned and highly fractured and to have an etched morphology that may indicate cemented aeolian bedforms (Fig. 4, A and B). The chloride-bearing materials appear to have been exposed by erosion of dark materials, which are observed bordering the light-toned deposit (Fig. 4A).

The pervasive polygonal fracturing observed in the HiRISE image is irregular, with variable diameters (Fig. 4B.). The fractures defining the polygons crosscut ridges and valleys and occur along ridge crests, indicating that the surface is an indurated material (Fig. 4C). Thermal inertia derived from THEMIS nighttime infrared observations indicates that the chloride-bearing material in Terra Sirenum has a thermal inertia close to 400 J $m^{-2} K^{-1} s^{-1/2}$, whereas values for the surrounding terrain are substantially lower (180 to 280) (23). The values for the putative chloride-bearing deposits are consistent with a mean particle size of fine gravel (2 to 4 mm) (24). However, thermal inertia is not a uniquely interpretable parameter, and values in this range also are consistent with smaller-grained particles that are cemented together (25). The latter is consistent with the generally crusty to indurated appearance for the chloride-bearing deposits observed in the MOC and HiRISE imagery.

The relationship between the putative chloride-bearing materials and craters is complex. A number of small (<300 m diameter), highly degraded craters appear to predate the chloride-bearing materials in Terra Sirenum, indicated by polygonal fractures crosscutting the crater rims and sidewalls (Fig. 4C). Larger craters (~300 to 900 m) in the same area appear to have excavated through the materials, covering them with ejecta (Figs. 1A and 4A). In other locations, chloride-bearing materials fill the floors of degraded craters but do not fill nearby, less degraded craters (Fig. 1C). In Terra Sirenum, a small crater ~500 m in diameter shows the light-toned, putative chloride-bearing materials in cross-section and reveals that the stratigraphic unit containing the putative

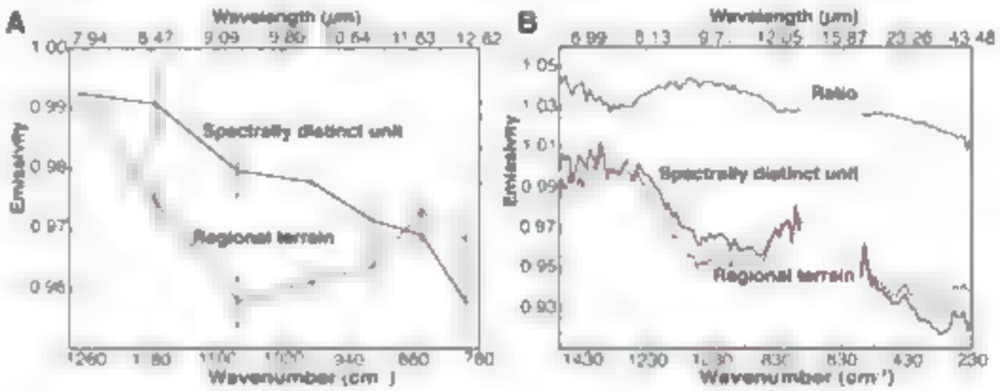

Fig. 3. (**A**) THEMIS surface spectra from image I08831002 in Terra Sirenum. (**B**) TES data for the spectrally distinct materials and the surrounding terrain. The ratio of the spectrally distinct surface to the surrounding terrain is shown at top.

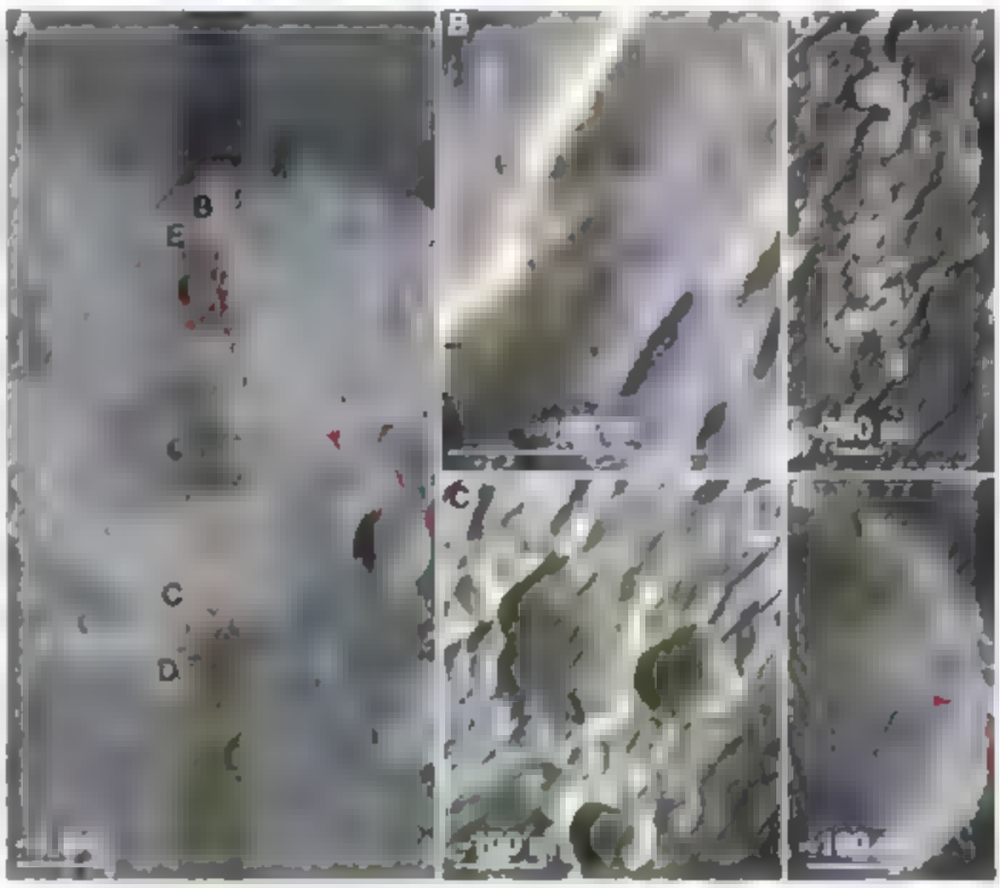

Fig. 4. (**A**) HiRISE image PSP_003160_1410, which includes the location of color data, locations of color inset images are indicated by red boxes. Crater ejecta overlie the light-toned materials, as indicated by the red arrows. (**B**) Polygonal fractures. (**C**) Chloride-bearing material appears to post-date small, degraded craters. (**D**) Small patches of chloride-bearing material with ambiguous stratigraphic relationships. (**E**) Light-toned materials are visible in the wall of this ~500-m-diameter crater.

chloride-bearing materials has a substantial thickness (Fig. 4E) (*8*).

On a global scale, the chloride-bearing materials occur at a wide range of elevations, ranging from roughly −3 to 3 km. MOLA gridded elevation data show that individual deposits not located in crater floors commonly occur in local topographic lows relative to the immediate surrounding terrain. As described previously, many of the deposits occur as small, isolated patches, in conjunction with their locally low elevations, this suggests they most likely represent unconformable units. Additionally, within a region containing several deposits, the putative chloride-bearing materials may occur at different elevations relative to each other, indicating that the formation postdates the stratigraphy, although it may also suggest the presence of multiple units in the stratigraphy.

On the basis of our observations, a number of inferences can be drawn about how the putative chloride-bearing deposits might have formed on the Martian surface. The widespread distribution of the deposits suggests that the climatological-hydrological conditions that facilitated their deposition were global in scale. However, ocean-scale bodies of water would appear to be inconsistent with the deposits' concentration in the cratered southern highlands. Alone, local-scale processes such as fumarolic activity are unlikely to produce the observed global distribution and differing morphologies of the deposits. Similarly, efflorescence alone does not account for the observed polygonal morphologies of the deposits, which are more consistent with desiccation cracks in thick salt deposits forming through precipitation. The occurrences of putative chloride-bearing materials in crater floors and in association with channels suggest that many of the putative chloride-bearing materials were precipitated from brines. Crater floors are ideal locations for ponding and evaporation of brines trapped from surface runoff or by the intersection of groundwater with the surface. Additionally, impact melting and mobilization of subsurface groundwater (or ground ice) could also be a viable mechanism for the production of chlorides. Based on our observations, we believe that the majority of the deposits were formed by chloride precipitation processes, although it is likely that in various locations, some of the materials are efflorescent salts or volcanic sublimates or were precipitated from hydrothermal brines (*8*). Locations where the stratigraphic relationship between the putative chloride-bearing materials and surrounding terrain is not clear (Fig. 4D) may be candidates for reactivation and/or modification of the original deposits by efflorescence.

The abundance of these deposits indicates that the formation of chloride salts on Mars has been an important process (*26*, *27*). The deposition of widespread chloride-bearing materials in the ancient southern highland terrains of Mars is further evidence of the presence of extensive reservoirs of surface and/or subsurface groundwater in the planet's early history (*8*).

References and Notes

1. T. M. Goodall, C. P. North, K. W. Glenn, *Sedimentology* **47**, 99 (2000).
2. H. P. Eugster, L. A. Hardie, in *Saline Lakes*, A. Lerman, Ed. (Springer-Verlag, New York, 1978), pp. 237–293.
3. M. J. Rosca, S. M. McLennan, *Earth Planet. Sci. Lett.* **241**, 23 (2006).
4. J. D. Farmer, D. J. Des Marais, *J. Geophys. Res.* **104**, 26977 (1999).
5. P. R. Christensen *et al.*, *Space Sci. Rev.* **110**, 85 (2004).
6. M. C. Malin *et al.*, *J. Geophys. Res.* **97**, 7699 (1992).
7. A. S. McEwen *et al.*, *J. Geophys. Res.* **112**, E05S02 (2007).
8. Materials and methods are available as supporting material on *Science* Online.
9. W. K. Hartmann, G. Neukum, *Space Sci. Rev.* **96**, 165 (2001).
10. J. L. Bandfield, A. D. Rogers, M. D. Smith, P. R. Christensen, *J. Geophys. Res.* **109**, E10008 (2004).
11. J. L. Bandfield *et al.*, *Science* **287**, 1626 (2000).
12. M. T. Mellon *et al.*, *Science* **302**, 627 (2003).
13. P. R. Christensen *et al.*, *J. Geophys. Res.* **105**, 9623 (2000).
14. J. L. Bandfield, M. D. Smith, *Icarus* **161**, 47 (2003).
15. S. W. Ruff, P. R. Christensen, *J. Geophys. Res.* **107**, 5127 (2002).
16. P. R. Christensen *et al.*, *J. Geophys. Res.* **105**, 9735 (2000).
17. S. W. Ruff, P. R. Christensen, P. W. Barbera, D. L. Anderson, *J. Geophys. Res.* **102**, 14899 (1997).
18. P. R. Christensen, Calibration Report for the Thermal Emission Spectrometer (TES) for the Mars Global Surveyor Mission, Mars Global Surveyor Project (Jet Propulsion Laboratory, Pasadena, CA, 1999).
19. M. D. Lane, P. R. Christensen, *Icarus* **135**, 528 (1998).
20. V. C. Farmer, *The Infrared Spectra of Minerals* (Mineralogical Society, London, 1974).
21. A. M. Baldridge, J. D. Farmer, J. E. Moersch, *J. Geophys. Res.* **109**, E12006 (2004).
22. M. T. Zuber *et al.*, *J. Geophys. Res.* **97**, 7781 (1992).
23. J. B. Bandfield, *Nature* **447**, 64 (2007).
24. M. A. Presley, P. R. Christensen, *J. Geophys. Res.* **102**, 6551 (1997).
25. F. D. Palluconi, H. H. Kieffer, *Icarus* **45**, 415 (1981).
26. G. W. Brass, *Icarus* **42**, 20 (1980).
27. P. L. Knauth, D. M. Burt, *Icarus* **158**, 267 (2002).

28. We are grateful to the members of the THEMIS team at Arizona State University and the Mars Odyssey team at the Jet Propulsion Laboratory. We thank K. Nowicki for help with THEMIS data processing and M. Lane for the use of chloride samples and spectra. We also thank our anonymous reviewers for insightful, thorough, and constructive comments. Funding for this work was provided by NASA grant NNX06AE15G and the Mars Odyssey Science Office. Funding for V.E.H. was provided by grants from the Mars Odyssey Participating Scientist, the Mars Data Analysis, and the Planetary Geology and Geophysics programs.

Supporting Online Material

www.sciencemag.org/cgi/content/full/319/5870/1651/DC1
Materials and Methods
Figs. S1 and S2
References

18 September 2007; accepted 28 January 2008
10.1126/science.1150690

Sulfur and Chlorine in Late Cretaceous Deccan Magmas and Eruptive Gas Release

Stephen Self,* Stephen Blake, Kirti Sharma, Mike Widdowson, Sarah Sephton

Large-volume pahoehoe lava flows erupted 67 to 65 million years ago, forming the Deccan Traps, India. The impact of these flood basalt eruptions on the global atmosphere and the coeval end-Cretaceous mass extinction has been uncertain. To assess the potential gas release from this volcanism, we measured sulfur and chlorine concentrations in rare glass inclusions inside crystals and on glassy selvages preserved within lavas. Concentrations range from ~1400 parts per million of S and 900 parts per million of Cl in inclusions down to a few hundred parts per million in the lava. These data indicate that eruptions of Deccan lavas could have released at most 0.103 weight % of S, yielding up to 5.4 teragrams of SO_2 per cubic kilometer of lava. A more conservative estimate is 0.07 weight % of S and 0.04 weight % of Cl, yielding 3.5 teragrams of SO_2 and 1 teragram of HCl for every cubic kilometer of lava erupted. The flows were very large in volume, and these results imply that huge amounts of S and Cl gases were released. The environmental impact from even individual eruptions during past flood basalt activity was probably severe.

Earth's most voluminous subaerial volcanic eruptions, both individual events and groups of closely spaced eruptions, happened during the formation of flood basalt provinces (*1*, *2*). These eruptions would have had a widespread environmental impact only through the release of gases, primarily S and Cl and possibly F (*3*). Of these, S gas releases are important in modern basaltic eruptions for causing atmospheric sulfate aerosol clouds, with well-documented climatic, weather, and other environmental effects (*4*), the distribution and severity of which have been replicated by modeling (*5*). By contrast, amounts of CO_2 released to the atmosphere even by flood basalt volcanism are thought to have been insufficient, when compared to the natural atmospheric reservoir, to have caused noticeable radiative effects (*2*, *6*). However, missing from these considerations have been directly measured data from the lavas that would constrain the amount of gas added to the atmosphere. The S and Cl contents of the magmas can be assessed indirectly by using a petrologic method (*7*, *8*) that has been validated by satellite-based measurements of SO_2 from recent eruptions of basaltic magma (*9*).

Here, we present direct determinations of S and Cl in glass inclusions in crystals in ancient basaltic lavas of the late Mesozoic, ~67 to 65 million years ago (Ma), Deccan flood basalt

province, India (*10*) (table S1) and discuss the potential amounts of degassed volatiles released by these eruptions. We examined phenocryst- or microphenocryst-bearing tholeiitic Deccan basalt lavas (Fig. 1) in thin section to identify those that contained glass (melt) inclusions in which the original, pre-eruption, volatile content might be preserved (*9*, *11*). Only one partial major-element analysis of a Deccan glass inclusion [including H_2O by Fourier transform infrared (FTIR) spectroscopy, but excluding S] has been published (*12*). After scrutinizing some 150 thin sections spanning all major main Deccan stratigraphic formations, we found only four samples that contained crystals with glass inclusions free of cracks, bubbles, or crystallites and that gave electron microprobe analyses with acceptable totals (98 to 101 weight (wt) %).

The four samples are from lava lobes positioned in three stratigraphic units exposed in the Matheran-Nasik area northeast of Mumbai: the Jawhar, Neral, and Thakurvadi Formations of the Kalsubai Subgroup (table S1). The glass inclusions are in (i) microphenocrysts of olivine (Fig. 1A) in a group of small pāhoehoe toes (Fig. 1B) and plagioclase crystals from a thicker sheet lobe lying above the toes (possibly both are from the same lava flow field) in the Neral Formation, collected near Neral (samples MG4 and MG5); (ii) phenocrysts of plagioclase from the altered glassy selvage of a lava lobe within the Thakurvadi Formation, collected near Igatpuri (sample Big1); and (iii) a phenocryst of plagioclase from a lava lobe in the upper part of the Jawar Formation, collected near Nasik (sample Thg3). Only lobes from which sample MG4 came had quenched glassy selvages sufficiently well preserved for residual volatile contents to be measured. Similar samples from outer selvages of modern basaltic lavas (*13*, *14*) represent magma that has degassed at the vent and has undergone a small amount of crystallization to a few millimeters beneath the quenched lava surface. The rarity of glassy material is unsurprising considering the age and the tropical environment of the Deccan lavas.

The whole-rock compositions of our samples (table S3) are typical of those of their respective formations. Analyzed glass compositions are slightly more evolved than the whole rocks due to in situ crystallization. Results (table S3 and fig. S1) indicate that the pre-eruption magmatic melt phase contained ≤1400 parts per million (ppm) of S. However, some inclusions have lower S concentrations, 400 to 800 ppm, suggesting that they were trapped in crystals that grew after the magma had already partially degassed, possibly in the conduit during transport to the surface [compare with inclusions in olivines from basaltic lavas formed in the ongoing activity at Kilauea volcano, Hawaii (*15*)]. The highest chlorine content of the inclusions is 900 ppm, and, within one lava, Cl content appears to be more variable than the contents of S. The average degassed concentrations of S and Cl in the one lava selvage glass (MG4; n = 33) are 370 ± 70 (1 σ) (range of 550 to 250) and 220 ± 80 ppm, respectively. The highest S contents are comparable to those of undegassed midocean ridge basalt (MORB) samples displaying the same FeO_{total} (Fig. 2). The S content of the degassed MG4 matrix is comparable with values in degassed subaerial modern-historic tholeiitic basaltic lavas and pyroclastics (*7*–*9*).

Amounts of S and Cl degassed from the magma during eruption can be estimated by comparing the S and Cl contents of glassy lava

Volcano Dynamics Group, Department of Earth and Environmental Sciences, Open University, Milton Keynes MK7 6AA, UK.

*To whom correspondence should be addressed. E-mail: stephen.sell@open.ac.uk

Fig. 1. Photo of 500-m-high stack of Deccan lava flows in the Mahabaleshwar area, dark bands are cores of large pahoehoe sheet lobes. [Photo, M. Widdowson.] (**A**) Back-scatter electron image of rounded glass inclusions (20 to 50 μm across) in euhedral olivine crystal (200 μm across) from Deccan lava sample MG4. (**B**) Neral Formation pahoehoe lobes from which sample MG4 came; tape is extended 10 cm. [Photo, S. Sell.]

selvages, representing degassed magma, and glass inclusions in crystals, representing melts trapped before and/or during degassing. The difference between the highest S concentration in an inclusion (1400 ppm) and the average lava selvage in MG4 (370 ppm) amounts to 1030 ppm of S, equivalent to the release of about 5.4 Tg of SO_2 km^{-3} of lava erupted. However, the matrix glass in MG4 is more evolved than that found in glass inclusions (table S3), indicating that the difference in volatile content includes the effects of variable degrees of syn- and posteruptive crystal growth, not just degassing. This result agrees with findings from glass inclusions and matrix glasses in tholeiitic lavas of the Columbia River Basalts (*11*) and Iceland (*7*).

A more-accurate estimate of the amount of S and Cl released can be calculated by taking account of amounts of crystallization between inclusion entrapment and quenching of the glass matrix (*11*, *16*). By using the approach in (*16*), we found the mass of sulfur released as a percentage of the mass of lava erupted to be 0.071‰ ± 0.007‰ in the case of MG4 and 0.059‰ ± 0.005‰ in the case of MG5, if this lava degassed to the same extent as MG4, a reasonable assumption given the uniformly low S contents of glasses from basaltic lava selvages (*8*). These values translate to 3.3 to 3.8 Tg of SO_2 km^{-3} of lava erupted. For Cl, the mean concentration in MG4 matrix is 0.02 wt %, comparing this with the highest Cl concentration in a glass inclusion (0.09 wt %) (*16*) implies that 0.04 wt % of Cl was lost, a yield of 1 Tg of HCl km^{-3} of lava. Actual amounts degassed likely varied between the values estimated by these two approaches.

Deccan values for S release are slightly less than those inferred during eruption of the Miocene age (~15 Ma) Roza lava in the Columbia River province, United States (*11*), which are ≤1500 ppm of S (average of 1370 ppm) and ≤130 ppm of Cl, equating to a maximum SO_2 release of 7.7 (average of 7.0) Tg per km^3 of lava erupted. The Roza magma had higher Fe than the Deccan examples and is thus expected to have had higher concentrations of dissolved S, but the Deccan magmas evidently released more Cl gas per unit volume of magma erupted.

Observations and measurements of S degassing from historic basaltic eruptions (*7*, *8*) imply that 75% of the gas released from the magma escapes at the vents and is lofted to the mid- to high troposphere and to the lower stratosphere, especially when vigorous fire-fountaining occurs (*4*). The remaining 25% of lost gas escapes from the lava as it flows over the ground to form a low-lying sulfate aerosol cloud or "vog."

Our estimates are most applicable to eruptions that generated the lower Deccan lava formations but may be appropriate for many eruptions during emplacement of the main province. Between 1×10^6 and 2×10^6 km^3 [recently estimated to be 1.3×10^6 km^3 (*17*)] of lava was erupted over ~0.5 to 0.8 million years (*18*, *19*). However, long-term time-averaged gas release rates are meaningless in regard to atmospheric perturbations because of the pulsatory nature of volcanism. Durations of pulses of Deccan eruptive activity are not known, but the eruptions were huge, yielding up to several 1000 km^3 of lava (*20*). An eruption of 1000 km^3 would have released between 5.4×10^3 and 3.6×10^4 Tg of SO_2. This amount would have been released, by analogy with the Roza eruption, over time periods of years to decades (*21*). Accordingly, an eruptive volume twice that emplaced over the same time period would yield annual releases up to and exceeding 1000 Tg of SO_2. Thus, a semi-persistent gas release of hundreds to thousands of teragrams of SO_2 per year can be envisaged for each Deccan eruption. The values for Cl, and possibly S, may be minima because of the possibility of an excess gas phase coexisting with the melt at precrystallization pressures (*22*).

Annual gas-release rates for flood-basalt activity proposed here are several times larger than recent anthropogenic emissions of SO_2, ~80 Tg of S, and more than an order of magnitude greater than the current global background volcanic SO_2 emission rate, ~10 Tg of S (*23*, *24*). The climatic and hazardous effects of massive Deccan gas discharges via aerosols, acid rain, or ozone depletion should form important topics for future studies. Current models do not permit analysis of the formation of aerosols or their atmospheric circulation and potential radiative effects 65 Ma. Moreover, extrapolation from changes caused by modern stratospheric Plinian eruptions such as Pinatubo 1991 may be misleading because of differences in duration of the injections and in factors such as rise heights of volcanic plumes and formation rates and lifetimes of aerosols in a Late Cretaceous atmosphere. If the effects of the 8-month-long Laki 1783 eruption (SO_2 yield of ~120 Tg) can be used as a guideline (*4*, *5*, *25*, *26*), then maintained releases of 1000 Tg of SO_2 $year^{-1}$ would cause damaging atmospheric perturbations. These results provide a quantitative basis for future modeling of the environmental impact of flood basalt volcanism and its role in major biosphere changes during Earth history (*2*, *27*).

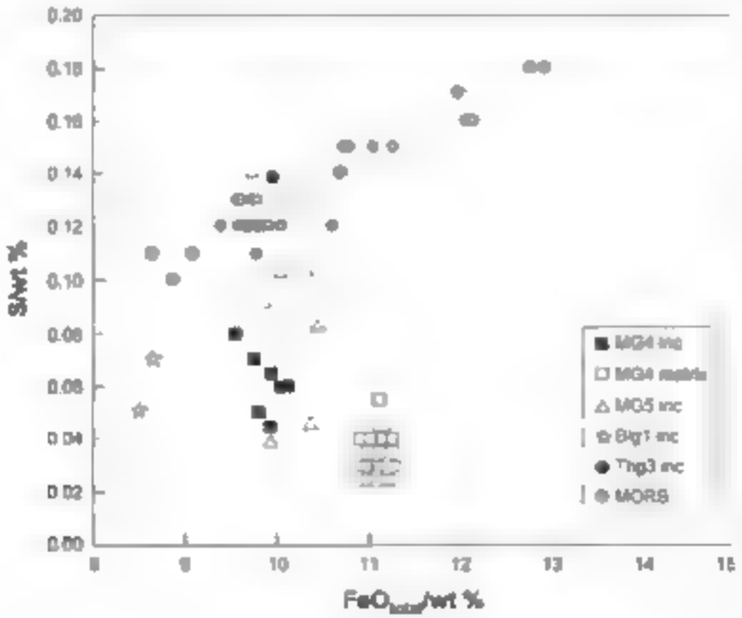

Fig. 2. Plot of S versus FeO_{total} for Deccan inclusions and matrix glass data; MORB data is from (*28*).

References and Notes

1. S. Self, A. E. Jay, M. Widdowson, L. P. Keszthelyi, *J. Volcanol. Geothermal Res.* in press.
2. P. B. Wignall, *Earth Sci. Rev.* **53**, 1 (2001).
3. M. M. Palmer, H.-U. Schmincke, H.-F. Graf, *J. Volcanol. Geothermal Res.* **115**, 511 (2002).
4. Th. Thordarson, S. Self, *J. Geophys. Res.* **108**, 10.1029/2001JD002042 (2003).
5. L. Oman *et al.*, *J. Geophys. Res.* **111**, D12209 10.1029/2005JD006899 (2006).
6. S. Self, Th. Thordarson, M. Widdowson, *Elements* **1**, 283 (2005).
7. Th. Thordarson, S. Self, N. Oskarsson, T. Hulsebosch, *Bull. Volcanol.* **58**, 205 (1996).
8. Th. Thordarson, S. Self, D. J. Miller, G. Larsen, E. G. Vilmundardottir, in *Volcanic Degassing*, C. Oppenheimer, D. M. Pyle, J. Barclay, Eds., vol. 213 of *Geological Society of London Special Publications* (Geological Society of London, London, 2003), pp. 103–123.
9. K. Sharma, S. Blake, S. Self, A. Krueger, *Geophys. Res. Lett.* **31**, L13612 10.1029/2004GL019688 (2004).
10. Materials and methods are available on Science Online.
11. Th. Thordarson, S. Self, *J. Volcanol. Geothermal Res.* **74**, 49 (1996).
12. F. Sano, T. Fujii, S. S. Deshmukh, T. Fukuoka, S. Aramaki, *J. Petrol.* **42**, 2175 (2001). These authors reported 0.8 wt % water in a glass inclusion, by FTIR. We have obtained an FTIR analysis of 0.5 wt % water in an olivine-hosted glass inclusion in sample MG4.
13. C. Ore, J. D. Winter, *J. Volcanol. Geothermal Res.* **142**, 285 (2005).
14. M.-N. Guilbaud, S. Blake, T. Thordarson, S. Self, *J. Petrol.* **48**, 10.1093/petrology/egm017 (2007).
15. C. R. Thornber, *Can. Mineral.* **39**, 239 (2001).
16. For a total mass of magma erupted, M, the mass of S released during degassing is

$$M_{S\,lost} = M[(1 - X_{crystals})S_{crystals} - (1 - X_{lava})S_{lava}] \quad (1)$$

where $S_{crystals}$ and S_{lava} are the S concentrations in the melt at depth, before any degassing as measured in the glass inclusions, and in the degassed matrix glass in the lava, respectively. X is the mass fraction of crystals present and is estimated by the amount of enrichment of an incompatible element with respect to the whole-rock concentration such that $(1 - X_{crystals}) = I_w/I_{rock}$, where I_w and I_{rock} are the concentrations of a highly

recent anthropogenic emissions of SO_2, ~80 Tg of S, and more than an order of magnitude greater than the current global background volcanic SO_2 emission rate, ~10 Tg of S (*23*, *24*). The climatic and hazardous effects of massive Deccan gas discharges via aerosols, acid rain, or ozone depletion should form important topics for future studies. Current models do not permit analysis of the formation of aerosols or their atmospheric circulation and potential radiative effects 65 Ma. Moreover, extrapolation from changes caused by modern stratospheric Plinian eruptions such as Pinatubo 1991 may be misleading because of differences in duration of the injections and in factors such as rise heights of volcanic plumes and formation rates and lifetimes of aerosols in a Late Cretaceous atmosphere. If the effects of the 8-month-long Laki 1783 eruption (SO_2 yield of ~120 Tg) can be used as a guideline (*4*, *5*, *25*, *26*), then maintained releases of 1000 Tg of SO_2 $year^{-1}$ would cause damaging atmospheric perturbations. These results provide a quantitative basis for future modeling of the environmental impact of flood basalt volcanism and its role in major biosphere changes during Earth history (*2*, *27*).

incompatible element in the whole rock and in any nondegassed inclusion in which the sulfur value $S_{chamber}$ has been measured. Similarly, $(1 - X_{lava})$ is equal to f_m/f_{lava}, and we obtain by substitution

$$M_{S,init} = M_{lava}(S_{chamber}/I_{chamber} - S_{lava}/I_{lava}) \quad (2)$$

Of the components analyzed by electron microprobe, TiO_2, K_2O, and P_2O_5 are candidates for the incompatible species. However, K_2O is variable in the MG4 matrix and may have been affected by weathering and alteration. By contrast, TiO_2 and P_2O_5 are immobile and, because TiO_2 is much more abundant than P_2O_5 and can be more precisely measured, it has been chosen as I. Co-genetic inclusions that have not degassed will share the same $S_{chamber}/I_{chamber}$ ratio if a sulfide phase is absent or minor. For example, data on MORB from the Juan de Fuca ridge (26) show near-constant S/TiO_2 despite being S-saturated. In fig. S1, three MG5 inclusions share the highest S/TiO_2 ratio (0.0664 ± 0.0019), and two of these have high Cl. MG4 matrix glass has S/TiO_2 = 0.0207 ± 0.0038 (n = 33). The whole-rock TiO_2 contents are 1.55 wt % for MG4 and 1.29 wt % for MG5.

17. A. E. Jay, M. Widdowson, *J. Geol. Soc.* **165**, 177 (2008).
18. V. Courtillot, P. Renne, *C. R. Geosci.* **335**, 113 (2003).
19. A.-L. Chenet, X. Quidelleur, F. Fluteau, V. Courtillot, S. Bajpai, *Earth Planet. Sci. Lett.* **263**, 1 (2007).
20. S. Self, M. Widdowson, T. Thordarson, A. E. Jay, *Earth Planet. Sci. Lett.* **248**, 517 (2006).
21. T. Thordarson, S. Self, *J. Geophys. Res.* **103**, 27411 (1998).
22. B. Scaillet, R. Macdonald, *J. Petrol.* **47**, 1413 (2006).
23. H.-F. Graf, B. Langmann, J. Feichter, *Chem. Geol.* **147**, 131 (1998).
24. J. Haywood, O. Boucher, *Rev. Geophys.* **38**, 513 (2000).
25. J. Gratian, *Lithos* **79**, 343 (2005).
26. A.-L. Chenet, F. Fluteau, V. Courtillot, *Earth Planet. Sci. Lett.* **236**, 721 (2005).
27. V. Courtillot, *Evolutionary Catastrophes, The Science of Mass Extinctions* (Cambridge Univ. Press, Cambridge, 1999).
28. E. A. Mathez, *J. Geophys. Res.* **81**, 4269 (1976).

29. We thank UK Natural Environment Research Council for funding this work (grant NER/B/S/2003/00246), A. Jay for help with sample collection and geochemical analyses, and S. Sethna for general support of our fieldwork in India. We thank the four anonymous reviewers for their helpful comments.

Supporting Online Material

www.sciencemag.org/cgi/content/full/319/5870/1654/DC1
Materials and Methods
Fig. S1
Tables S1 to S4
References

9 November 2007; accepted 1 February 2008
10.1126/science.1152830

Atmospheric Hydroxyl Radical Production from Electronically Excited NO_2 and H_2O

Shuping Li, Jamie Matthews, Amitabha Sinha*

Hydroxyl radicals are often called the "detergent" of the atmosphere because they control the atmosphere's capacity to cleanse itself of pollutants. Here, we show that the reaction of electronically excited nitrogen dioxide with water can be an important source of tropospheric hydroxyl radicals. Using measured rate data, along with available solar flux and atmospheric mixing ratios, we demonstrate that the tropospheric hydroxyl contribution from this source can be a substantial fraction (50%) of that from the traditional $O(^1D) + H_2O$ reaction in the boundary-layer region for high solar zenith angles. Inclusion of this chemistry is expected to affect modeling of urban air quality, where the interactions of sunlight with emitted NO_x species, volatile organic compounds, and hydroxyl radicals are central in determining the rate of ozone formation.

Hydroxyl radicals are the single most important oxidant in the atmosphere because they are the agent primarily responsible for removing the majority of gases emitted into the atmosphere by natural and anthropogenic activity (*1*–*6*). Hence, accurate modeling of the oxidizing (or cleansing) capacity of the atmosphere requires knowledge of all substantial sources of these radicals. Studies of the upper troposphere and polar regions have reported discrepancies between model predictions and measured HO_x (where $HO_x = OH + HO_2$) concentrations associated with chemistry specific to high solar zenith angles (*7*–*9*). These differences not only highlight the difficulty of measuring atmospheric OH concentrations but also the potential variability arising from incomplete accounting of all major sources and sinks of the radical. Recently, several unconventional photodissociative sources of HO_x have been reported (*10*, *11*). Here, we show that the bimolecular reaction of electronically excited nitrogen dioxide (denoted by NO_2^* and generated by the absorption of visible light) with water molecules can lead to substantial OH radical production. The fact that the reaction is initiated by the portion of the solar flux that readily penetrates into the lower atmosphere over a broad range of zenith angles, combined with the relatively large concentrations of NO_2 and water in the troposphere, suggests that this source will be an important addition to the tropospheric OH budget.

The primary production mechanism of tropospheric OH radicals is through the photolysis of ozone, which generates $O(^1D)$ atoms at wavelengths $\lambda \leq 320$ nm. Although most of these excited atoms are deactivated through collisions with background gases, a small fraction of them are able to react with water to form OH radicals (*6*, *12*).

$$O_3 + h\nu(\leq 320\ \text{nm}) \rightarrow O(^1D) + O_2 \quad (1)$$

$$O(^1D) + M \rightarrow O(^3P) + M \quad (2)$$

(where M is N_2 or O_2)

$$O(^1D) + H_2O \rightarrow 2OH \quad (3)$$

In reaction 2, h is Planck's constant and ν is the wave's frequency. When a steady-state approximation is applied to the $O(^1D)$ atoms, a kinetics analysis of the above reaction sequence gives the production rate for OH (R_{OH}) by this mechanism as

$$R_{OH} = 2j_1k_3[H_2O][O_3]/(k_2[M] + k_3[H_2O]) \quad (4)$$

In Eq. 4, j_1 is the O_3 photolysis rate to form $O(^1D)$, k_2 is the rate constant for collisional deactivation of $O(^1D)$ by "air," k_3 is the rate constant for the reaction of $O(^1D)$ with water, and $[H_2O]$ is the concentration of H_2O. An important constraint associated with the above mechanism is that it requires the absorption of ultraviolet (UV) light. There are situations, however, such as those corresponding to high tropospheric solar zenith angles, where the sunlight traverses an extended optical path through the atmosphere, resulting in the incoming solar flux being greatly depleted of its UV component because of scattering and absorption. For these scenarios, alternate OH production mechanisms involving photochemical processes occurring at longer wavelengths can become important. Electronic excitation of NO_2 by visible light provides the molecule with sufficient energy to overcome the 39.8 kcal/mol endothermicity associated with the $NO_2 + H_2O$ reaction (*13*). Thus, the reaction of NO_2^* with water can be a major source of tropospheric OH radicals.

To better appreciate the OH-generating potential of this mechanism, we note that NO_2 has a broad absorption spectrum between 250 and 650 nm with a maximum near 410 nm. Absorption of radiation by NO_2 at wavelengths shorter than 420 nm leads to photodissociation and the formation of $O(^3P)$ atoms in the atmosphere (*13*, *14*). In contrast, excitation at longer wavelengths ($\lambda >$ 420 nm) leads to the formation of NO_2^* with fluorescence lifetimes of 40 to 60 μs (*15*). The long lifetimes of these states arise from the mixing of the B^2B_1 and A^2B_2 excited electronic states with the X^2A_1 ground electronic state (*16*).

Upon photoexcitation to these long-lived electronic states, most of the excited NO_2 will be quenched by collisions with N_2 and O_2 for which the quenching rate constants are known to be 2.7×10^{-11} and 3.0×10^{-11} cm^3 molecule^{-1} s^{-1}, respectively (*17*–*19*). However, because water is a tropospheric trace gas of relatively large abun-

Department of Chemistry and Biochemistry, University of California, San Diego, 9500 Gilman Drive, La Jolla, CA 92093–0314, USA.

*To whom correspondence should be addressed. E-mail: asinha@ucsd.edu

dance, some of the photoexcited NO_2 molecules can also collide with water. Water quenches NO_2* efficiently with a rate constant of ~1.7 × 10^{-10} cm^3 $molecule^{-1}$ s^{-1} (*17*, *19*); however, there has been no previous report of any OH radical formation from the reaction of NO_2* and H_2O (*20*). If a substantial fraction of the NO_2* reacts with water, then the following mechanism for OH formation becomes possible

$$NO_2 + h\nu\ (\lambda > 420\ nm) \rightarrow NO_2^* \quad (5)$$

$$NO_2^* + M \rightarrow NO_2 + M \quad (6)$$
(where M is N_2, O_2, or H_2O)

$$NO_2^* + H_2O \rightarrow OH + HONO \quad (7)$$

Apart from OH radicals formed directly through reaction 7, photolysis of the HONO reaction product can also give rise to additional OH

$$HONO + h\nu\ (\lambda < 390\ nm) \rightarrow OH + NO \quad (8)$$

Applying a steady-state approximation to NO_2* in the above reaction sequence produces a rate of OH formation through this mechanism of

$$R_{OH} = 2\phi_5 k_5[NO_2][H_2O]/(k_5[H_2O] + k_6[M]) \quad (9)$$

In the above expression, j_5 is the photoexcitation rate constant for NO_2, k_6 is the total collisional quenching rate constant of NO_2* by air, and k_7 is the rate constant for the NO_2* + H_2O reaction. A comparison of Eqs. 9 and 4 shows that if k_7 is sufficiently large and the HONO molecule formed in reaction 7 is also photolyzed, then the yield of OH from the NO_2* + H_2O reaction can be a sizable fraction of that arising from the $O(^1D)$ + H_2O reaction, especially under conditions of low UV flux.

To test the viability of the above mechanism, we carried out laboratory studies consisting of rate measurement for the NO_2* + H_2O reaction in conjunction with laser-induced fluorescence (LIF) detection of the OH product. The experimental apparatus we used has been described previously (*21*) and, along with the procedure for the kinetics measurement, is detailed further in the supporting online material (SOM) (*22*).

Although long-lived NO_2* can be formed by means of excitation over the entire region between 420 and 640 nm, we focused our study between 560 and 640 nm. This region was chosen because NO_2 is known to have relatively strong sequential multiphoton transitions over the 420 to 540 nm range, which can result in the production of electronically excited oxygen atoms (*20*, *23*). Furthermore, studies of collisional energy transfer from NO_2* suggest that the average amount of energy transferred from NO_2* to its collision partners increases as the internal energy of the NO_2* is increased (*24*). This, in turn, can potentially increase the effective temperature of the reaction zone.

We minimized these problems by working at the longer wavelengths. The formation of OH radicals from reaction 7 was confirmed by its characteristic LIF spectrum. Figure 1A shows the OH spectrum generated by exciting the reaction mixture with light at 590 nm while scanning the probe laser wavelength. As shown in Fig. 1B, replacing H_2O with D_2O gives the OD signal. To confirm that the OH was indeed from reaction 7, we carried out several diagnostic measurements (*22*) that, taken together, confirmed our hypothesis. First, the time dependence of the OH product appearance, relative to the excitation-laser pulse, was measured and found to be consistent with that expected for a bimolecular reaction and not prompt photodissociation. This finding ruled out the possibility that the detected OH arises from photolysis of impurities such as HONO or nitric acid that can form in NO_2-water mixtures through heterogeneous chemistry (*25*, *26*). In separate experiments (*22*), we confirmed the absence of these species in our starting reaction mixture. Second, excitation-laser power-dependence measurements at 565 and 590 nm confirmed that the OH product yield varies linearly with laser power over the range of 4.5 to 50 mJ. This finding is consistent with a single-photon excitation process involving the absorption of a visible photon by NO_2 to form NO_2*, followed by its reaction with H_2O to form OH radicals. It also suggests that a contribution to the OH signal from a secondary reaction of NO_2* with energized water molecules (produced through collision with NO_2*) is not substantial, as this would require a squared dependence on the laser power. As a final diagnostic, we recorded NO_2 action spectra (Fig. 1C). The spectra were generated by scanning the excitation laser over the region from 560 to 640 nm while monitoring the yield of OH products in the indicated quantum state. The photoacoustic spectrum of NO_2 was simultaneously recorded with a portion of the excitation laser. As shown in Fig. 1C, the peaks and valleys in the action spectra match well with those in the photoacoustic spectrum as well as the reference absorption spectrum (*27*), thus establishing that the OH signal is due to the reaction of photoexcited NO_2. Subsequently, we investigated the dependence of the OH signal on H_2O concentration and measured the rate of reaction for reaction 7.

We carried out the rate measurements under short time conditions using pseudo first-order kinetics, and the analysis and assumptions made are outlined in the SOM (*22*). Briefly, the kinetics associated with OH formation from reaction 7 can be expressed as

$$d[OH]_7/dt = k_7[NO_2^*][H_2O] \quad (10)$$

When the reaction time Δt is kept short, the above differential equation becomes

$$\Delta[OH]_7 = k_7[NO_2^*][H_2O]\Delta t \quad (11)$$

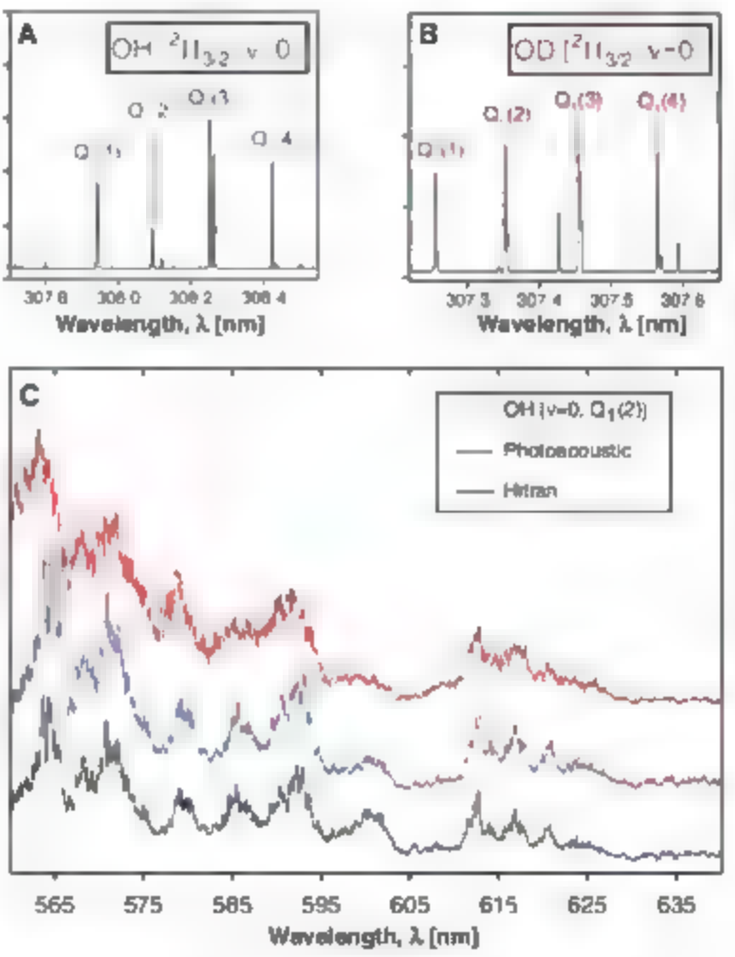

Fig. 1. (**A**) Partially relaxed product OH radical LIF spectra from the reaction of NO_2* with H_2O. $^2\Pi_{3/2}$ is the OH spin-orbit state, *v* is the OH vibrational level, and $Q_1(n)$ is the rotational branch. (**B**) Partially relaxed OD transitions result when H_2O is replaced with D_2O. (**C**) Comparison of NO_2 photoacoustic and action spectra. The action spectrum is obtained by monitoring the indicated OH product quantum state as a function of the excitation-laser wavelength. A reference NO_2 absorption spectrum from the HITRAN database (*27*) is also shown for comparison.

Further, assuming that the starting concentration of H_2O is in excess over NO_2^*, the above equation can be written in terms of a pseudo–first-order rate constant $k_7^1 = k_7[H_2O]$ giving (27)

$$\Delta[OH]_P = k_7^1[NO_2^*]\Delta t \quad (12)$$

Figure 2 shows a plot of the measured pseudo–first-order reaction rate constant k_7^1 versus H_2O concentration, the slope of which yields the bimolecular rate constant $k_7 = 1.7 \times 10^{-13}$ cm^3 molecule^{-1} s^{-1}. This value was confirmed at three separate wavelengths (565, 590, and 612.5 nm), all of which gave similar rates. We estimated the uncertainty in our rate constant to be ~50%.

Having determined the rate constant, we could then estimate the tropospheric OH contribution from the $NO_2^* + H_2O$ source. For this analysis, we assumed that the reaction occurs over the entire region from 420 to 640 nm with the same rate constant. Figure 3A shows plots of the rate of OH production from the $NO_2^* + H_2O$ reaction as a function of altitude for various solar zenith angles. For this analysis, we used Eq. 9, in which the variation in solar flux is taken into account using the computer code of (28). The variation in reactant concentration with altitude is from the data of (29), associated with a fairly clean region of the North American continent. The dashed lines in Fig. 3A correspond to ground-level NO_2 concentrations of ~400 parts per trillion (ppt), whereas the solid lines correspond to concentrations of 1 part per billion (ppb). As the figure illustrates, the reaction's influence is largest near the boundary layer, where the concentrations of water and NO_2 are highest. We found that the OH production rate from this reaction can reach as high as 5000 to 40,000 molecules cm^{-3} s^{-1}. Urban environments typically are even more polluted, and their ground-level NO_2 concentrations can readily exceed 10 ppb, resulting in a concomitant increase in the contributions from reaction 7. It is also interesting to compare the relative OH production rates from the $NO_2^* + H_2O$ reaction versus that from the $O(^1D) + H_2O$ reaction [considered to be the primary source of atmospheric OH (6)] by taking the ratio of Eqs. 9 and 4. These results illustrate that the contribution from the $NO_2^* + H_2O$ reaction is largest relative to the $O(^1D) + H_2O$ source for high solar zenith angles, reaching anywhere from 11 to 52% of that from the $O(^1D)$ source (Fig. 3B).

The present findings demonstrate that NO_2^* can react with water molecules to form OH radicals. The measured rate for this reaction is sufficiently fast for it to be an important source of OH in the tropospheric boundary layer. Inclusion of this previously unrecognized source chemistry will impact models addressing urban air pollution where the concentration of ground-level ozone, a major component of smog, is dictated by a complex set of reactions involving volatile organic compounds (VOCs) and NO_x (NO_x = $NO_2 + NO$) species generated from motor-vehicle exhaust and industrial emissions, along with visible sunlight driven photochemistry (2, 6). The efficiencies of these ground-level ozone-generation schemes depend on the concentration of OH radicals present to initiate reactions involving VOC's (6). Finally, the $NO_2^* + H_2O$ reaction may also help to explain discrepancies between measured and predicted HO_x concentrations reported in arctic regions (9). The elevated levels of OH and HONO observed from arctic snowpacks under conditions of high solar zenith angles are consistent with the products expected from the $NO_2^* + H_2O$ reaction.

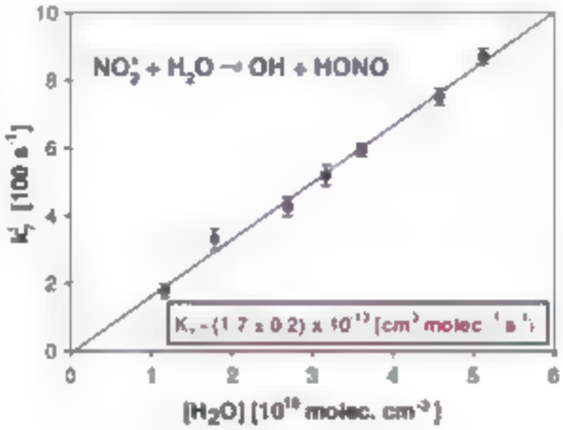

Fig. 2. Plot of the pseudo–first-order rate constant k_7^1 versus H_2O concentration. The line's slope gives the bimolecular rate constant k_7. Error bars indicate the precision of the data. We estimate the overall uncertainty in the rate constant to be ±50%.

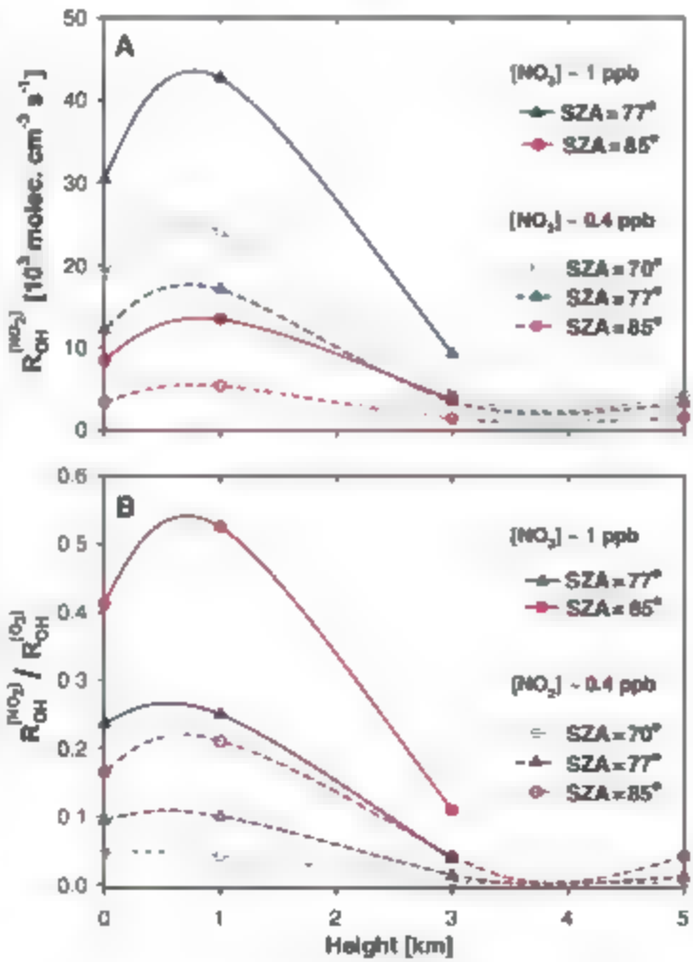

Fig. 3. (A) Rate of production of OH solely from the $NO_2^* + H_2O$ reaction as a function of altitude and various solar zenith angles. The rates were calculated from Eq. 9. In this analysis, we assume that the HONO formed in reaction 7 is also photolyzed. The dashed lines correspond to a ground-level NO_2 concentration of ~400 ppt (29), whereas the solid lines correspond to a more polluted situation with an NO_2 concentration of ~1 ppb. The ground-level water concentration was taken to be 10 torr. (B) Comparison of relative tropospheric OH production rates from the $NO_2^* + H_2O$ reaction versus the $O(^1D) + H_2O$ reaction. The ratio of rates from these two sources, calculated by taking the ratios of Eqs. 9 and 4, is plotted as a function of altitude and solar zenith angle.

References and Notes

1. B. J. Finlayson-Pitts, J. N. Pitts Jr., *Atmospheric Chemistry* (Wiley, New York, 1986).
2. G. P. Brasseur, J. J. Orlando, G. S. Tyndall, *Atmospheric Chemistry and Global Change* (Oxford Univ. Press, New York, 1999).
3. H. Levy II, *Planet. Space Sci.* **20**, 919 (1972).
4. P. J. Crutzen, *Pure Appl. Geophys.* **106–108**, 1385 (1973).
5. J. A. Logan, M. J. Prather, S. C. Wofsy, M. B. McElroy, *J. Geophys. Res.* **86**, 7210 (1981).
6. P. S. Monks, *Chem. Soc. Rev.* **34**, 376 (2005).
7. P. O. Wennberg *et al.*, *Geophys. Res. Lett.* **26**, 1373 (1999).
8. R. J. Salawitch, P. O. Wennberg, G. C. Toon, B. Sen, J. F. Blavier, *Geophys. Res. Lett.* **29**, 1762 (2002).
9. F. Domine, P. B. Shepson, *Science* **297**, 1506 (2002).
10. D. J. Donaldson, G. J. Frost, K. H. Rosenlof, A. F. Tuck, V. Vaida, *Geophys. Res. Lett.* **24**, 2651 (1997).
11. J. Matthews, A. Sinha, J. S. Francisco, *Proc. Natl. Acad. Sci. U.S.A.* **102**, 7449 (2005).

12. P. H. Wine, A. R. Ravishankara, *Chem. Phys. Lett.* **77**, 103 (1981).
13. S. P. Sander, *et al.*, *Chemical Kinetics and Photochemical Data for Use in Stratospheric Modeling, Evaluation No. 14, JPL Publ. 02-25* (NASA Jet Propulsion Laboratory, Pasadena, CA, 2003).
14. C. M. Roehl *et al.*, *J. Phys. Chem.* **98**, 7837 (1994).
15. C. G. Stevens, M. W. Swagel, R. Wallace, R. N. Zare *Chem. Phys. Lett.* **18**, 465 (1973).
16. A. E. Douglas, *J. Chem. Phys.* **45**, 1007 (1966).
17. H. Okabe, *Photochemistry of Small Molecules* (Wiley, New York, 1978).
18. V. M. Donnelly, D. G. Keil, F. Kaufman, *J. Chem. Phys.* **71**, 659 (1979).
19. J. A. Thornton, P. J. Wooldridge, R. C. Cohen, *Anal. Chem.* **72**, 528 (2000).
20. J. N. Crowley, S. A. Carl, *J. Phys. Chem. A* **101**, 4178 (1997).
21. G. Dutton, R. J. Barnes, A. Sinha, *J. Chem. Phys.* **111**, 4976 (1999).
22. Materials and methods are available as supporting material on Science Online.
23. K. Shibuya, H. Nagai, T. Imajo, K. Obi, I. Tanaka, *J. Chem. Phys.* **85**, 5061 (1986).
24. G. V. Hartland, D. Qin, H. L. Dai, C. Chen, *J. Chem. Phys.* **107**, 2890 (1997).
25. B. J. Finlayson-Pitts, L. M. Wingen, A. L. Sumner, D. Syomin, K. A. Ramazan, *Phys. Chem. Chem. Phys.* **5**, 223 (2003).
26. K. A. Ramazan *et al.*, *J. Phys. Chem. A* **110**, 6886 [illegible].
27. L. S. Rothman *et al.*, *J. Quant. Spectrosc. Radiat. Transf.* **82**, 5 (2003).
28. S. Madronich, S. Flocke, J. Zeng, I. Petropavlovskikh, J. Lee-Taylor, *Tropospheric Ultraviolet-Visible Model, version 4* (National Center For Atmospheric Research, Boulder, CO, 2006).
29. H. B. Singh *et al.*, *J. Geophys. Res.* **112**, D12S04 (2007).
30. We thank the Donors of the American Chemical Society Petroleum Research Fund and NSF Chemistry for partial support of this research.

Supporting Online Material

www.sciencemag.org/cgi/content/full/319/5870/1657/DC1
Materials and Methods
Figs. S1 to S4
References and Notes

9 October 2007; accepted 30 January 2008
10.1126/science.1151443

Synchronous Aggregate Growth in an Abundant New Ediacaran Tubular Organism

Mary L. Droser[1]* and James G. Gehling[2]

The most abundant taxon of the Neoproterozoic soft-bodied biota near Ediacara, South Australia, occurs as clusters of similarly sized individuals, which suggests synchronous aggregate growth by spatial... Tubes of *Funisia dorothea* gen. et sp. nov. were anchored within the shallow, sandy sea bed and lived in dense, typically monospecific concentrations. Tubes were composed of modular serially repeating elements. Individuals grew by adding serial elements to the tubular body and by branching of tubes. Their construction and close-packed association imply likely affinity within the Porifera or Cnidaria. These data suggest that several of the most successful marine invertebrate ecological strategies known today were in place in Earth's oldest known metazoan ecosystems before the advent of skeletonization and widespread predation.

Both the structure and associations of Neoproterozoic Ediacaran fossils from near the Flinders Ranges, South Australia, provide information on the complex ecological makeup of Earth's first metazoan habitats (*1*). The fossil-bearing Ediacara Member of the Rawnsley Quartzite lies 50 to 500 m below a basal Cambrian disconformity and consists of shallow marine, thin- to medium-bedded quartz sandstone (*2*). We excavated beds within the Ediacara Member of the Rawnsley Quartzite at the Ediacara Conservation Park (South Ediacara) and on Nilpena Station of South Australia (fig. S1) to reveal details of the form, diversity, and distribution of these taxa.

A large diversity of fossils in original growth position occurs on successive bedding planes within the more than 150 m^2 excavated. Tubular fossils, representing an undescribed structural organization, are more abundant than any other previously described element of the Ediacara biota (*1*). They occur on nearly all excavated beds and densely on 3 of the 10 beds excavated at Nilpena and 2 of the beds at South Ediacara.

[1]Department of Earth Sciences, University of California, Riverside, CA 92521, USA. [2]South Australia Museum, North Terrace, Adelaide, South Australia 5000, Australia.

*To whom correspondence should be addressed. E-mail: Mary.droser@ucr.edu

Funisia dorothea gen. et sp. nov. (see supporting online material) is preserved exclusively on the base of beds, as are nearly all fossils in these strata (Fig. 1). Unlike most elements of the Ediacara Biota (*3*), *Funisia* is preserved in positive relief, either as flattened casts formed when sand entered the body cavity (Fig. 1, A and D), or as casts of the collapsed body that was impressed into the underlying biomat (Fig. 1, E and G). Collapse and casting is the most common preservation mode because sand rarely fills more than a few centimeters of each tubular body (Fig. 1A). Removal of internal casts leaves an external mold in the overlying bed. In the best-preserved specimens, individual serial units show faint, offset concentric wrinkles that suggest collapse of a thin integument during burial, rather than ornamentation (Fig. 1, E and G).

Funisia is up to 30 cm long and 12 mm in diameter and is divided longitudinally into serial units 6 to 8 mm in length throughout the length of the tube (Figs. 1 and 2). The serial units are defined by constrictions perpendicular or gently oblique to the axis of the tube. Particularly when tubes are bent or curved, constrictions give the tube the appearance of being a spiral, but examination of material preserved nearly in three dimensions (3D) (Fig. 1, D, E, and G) confirms serial segmented construction. In compacted and poorly preserved tubes, or external molds, a scalloped-shaped tube outline, rather than the impression of individual segments, is typically preserved (Fig. 1, A, I, and J). Where *F. dorothea* covers the surface, the degree of overlapping is such that individual tubes are deformed by composite preservation (Figs. 1, I and J), and under very poor preservation, the sides of the tube appear as parallel lines (Fig. 1A).

Tube widths range from 2 to 12 mm and are consistent on individual bedding surfaces. These structures were originally interpreted to be strings of fecal pellets (*4*), but this has since been discounted on the basis of the presence of branching and orientation of specimens (*5*). Units within the tube taper progressively in width toward the axis, suggestive of growth by terminal addition (*6*) (Fig. 1, E and G). Individuals can occur within dense assemblages, sometimes greater than 1000/m^2 (Fig. 1, I and J). Here, individual tubes of similar size may radiate from a single area of origin (Fig. 1I). In such dense assemblages, tubes completely cover the surface and may overlap or crisscross in a felted manner (Fig. 1, I and J) but most commonly occur in parallel, close-packed groups of 5 to 15 individuals (Fig. 1, A and C). Such groups do not show alignment with current lineations or ripple crests that occur on top of the beds, which suggests that the position of these fossils is not a reflection of transport or reorientation by currents. Rather, they are the result of smothering by sandy event beds in the wake of storm activity (*2*). Branching is rare, but in such instances, the last common serial unit is expanded and branches remain tightly packed (Fig. 1H).

Tube attachment structures ranging in diameter from 1 to 8 mm are preserved as invaginate bosses on bed soles (Fig. 1, B, C, D, and I). Serially constricted tubes are directly connected to attachment structures (Fig. 1D). The marked modality of size and morphology suggest that different developmental cohorts are preserved (Fig. 1C). Attachment structures of a similar size and developmental stage are spatially clustered within individual bedding surfaces (Fig. 1C). Clustered attachment points are not typically closely packed, but three-dimensionally preserved examples recording the basal several millimeters of the tube demonstrate a hexagonal close packing

within millimeters of vertical growth (Fig. 1, B and F). Individual attachments occur without close neighbors but are not common. The size and morphology of attachments range from small knobs 1 to 3 mm in width to well-developed structures that are casts of tube ends with concave hollows (Fig. 1, B, C, D, and I). These structures occur on both ripple crests and troughs and originally extended below the interface between water and substrate. They are clearly attachment discs rather than cross sections through the tubes. Ediacaran preservation consists entirely of casts and molds. Cross sections are confined to broken, three-dimensionally cast specimens within a bed. Furthermore, there would be some ellipses preserved, and it would not be possible for the tube to be sectioned and still cast by sand.

Like the well-known Ediacaran fronds (7), *Funisia* tubes are typically preserved without holdfasts attached. In life position (Fig. 2), attachment structures are interpreted to have been situated within or beneath a microbial mat. Where they are cast by sand, the corresponding tube was ripped off by storm activity, allowing sediment to enter the hollow holdfast (Fig. 1C). Alternatively, the holdfast was molded below the mat-bound sediment, and the tube was cast within the overlying sediment or preserved as a collapsed impression at the base of the sediment that engulfed the specimen (Fig. 1B).

The phylogenetic affinity of *F. dorotheae* is problematic. The morphology is consistent throughout all well-preserved specimens and serial units are a 3D character rather than features of external ornamentation. However, the lack of evidence for polypoid openings or pores in the body wall limits our understanding of its taxonomic affinities. Although it is difficult to place these fossils within Metazoa, the morphology and ecology are suggestive of stem-group cnidarians or ponterans. The tightly packed nature of the tubes and attachment structures (Fig. 1I), as well as the rarity of branching, eliminates an algal origin because these characteristics are inconsistent with the maximization of surface area crucial for a photosynthetic habit.

The branching patterns and rarity of branching of *Funisia* is consistent with metazoan asexual budding. The consistency of tube widths on individual bedding surfaces (Fig. 1, A, I, and J), the densely packed nature of the attachment structures, and the clustering pattern of developmental stages of attachment structures on individual bedding planes suggests that the juveniles settled as aggregates in a series of limited cohorts.

These solitary organisms thus exhibit growth by addition of serial units to tubes and by the division of tubes, and dispersed propagation by the production of spats. Among living organisms, spat production is almost ubiquitously the result of sexual reproduction but is known to occur rarely in association with asexual reproduction (*8*). Hence, despite its morphological simplicity, the Neoproterozoic *F. dorotheae* provides evidence of a variety of growth modes and a complex arrangement for the propagation of new individuals. In living organisms, synchronous aggregate growth may result from a variety of factors, including response to competition, sediment disturbance, and heterogeneity of the substrate, and has the advantage of reducing competition for space between clones and can also decrease gamete wastage (*9*, *10*). It may also reduce vulnerability to predation (*9*). Borings in the calcified *Cloudina* may demonstrate predation in the latest Ediacaran (*11*). Furthermore, close

Fig. 1. *Funisia dorotheae* gen. et sp. nov. preserved as external casts, internal casts, and external molds on bed bases. (**A**) Holotype set of subparallel tubes SAM P40725, internal casts, external mold where casts have separated, and as convex casts of collapsed specimens demonstrating various taphonomic variants, including well-preserved serial units, scalloped edge outlines (arrow), and parallel edged outlines. (**B**) Close-packed set of attachment points (lower left) showing typical convex rim and indented center with or without boss, one with cast of part of tube (arrow); SAM P42681. (**C**) Growth by branching; SAM P40726. (**D**) Attachment points with serially constricted tubes, field specimen E505. (**E** and **G**) Specimens showing growth by terminal addition; SAM P41508. (**F**) Two sets of attachment points demonstrating different stages of development. (**H**) Enlargement of lower right part of surface in Fig. 2I showing crossed tubes with serial constrictions (arrows). (**I**) Layered, close-packed specimens radiating from clusters of attachment points (examples marked by arrows); SAM P40309. (**J**) Densely packed surface with both scalloped and parallel edge preservation; part of very large field specimen, Nilpena. Scale bars, 2 cm.

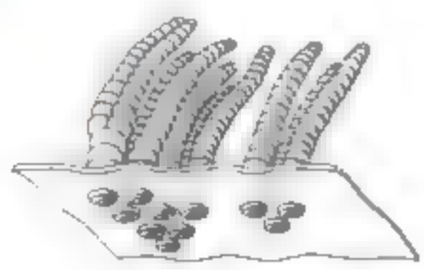

Fig. 2. Reconstruction of *Funisia* in life position with holdfast beneath mat substrate.

packing also imparts protection from current damage and/or high-energy events and allows for selection of most favorable sites for attachment and growth to adulthood (*12*).

Aggregation is not uncommon among some elements of the Ediacara biota and is present in the frond holdfast *Aspidella*. These typically occur in dense assemblages, but in contrast to *F. dorothea*, their size distribution is consistent with continuous recruitment (*1*, *13*, *14*) rather than periodic cohort growth. The terminal Neoproterozoic calcified tubes *Cloudina* and *Namacalathus* also show evidence of aggregation (*15*), but there is no indication of distinct cohorts.

These data demonstrate that even morphologically simple Ediacaran organisms had multiple modes of growth and propagation, reminiscent of several of the most successful marine invertebrate ecological strategies today (*16*). These systems were in place in Earth's oldest known metazoan ecosystems before the ecological pressures that accompanied the advent of skeletonization and extensive predation.

References and Notes

1. M. L. Droser, J. G. Gehling, S. R. Jensen, *Palaeogeogr. Palaeoclimatol. Palaeoecol.* **232**, 131 (2006).
2. J. G. Gehling, *Precambrian Res.* **100**, 65 (2000).
3. J. G. Gehling, *Palaios* **14**, 40 (1999).
4. M. F. Glaessner, *Lethaia* **2**, 369 (1969).
5. M. L. Droser, J. G. Gehling, S. R. Jensen, Eds., *Ediacaran trace fossils: Truth and false* (Peabody Museum of Natural History, New Haven, CT, 2005), pp. 125–138.
6. D. K. Jacobs, M. C. Hughes, S. T. Fitz-Gibbon, C. J. Winchell, *Evol. Dev.* **7**, 498 (2005).
7. J. G. Gehling, M. L. Droser, S. R. Jensen, B. N. Runnegar, Eds., *Ediacara Organisms. Relating Form to Function* (Yale Peabody Museum, New Haven, CT, 2005).
8. D. G. Fedak, *Can. J. Zool.* **80**, 1735 (2002).
9. J. B. C. Jackson, in *Biotic interactions in Recent and Fossil Benthic Communities*, M. J. S. Tevesz, P. L. McCall, Eds. (Plenum Press, New York, 1983), vol. 3, pp. 39–120.
10. D. J. Crisp, in *Biology and Systematics of Colonial Organisms*, G. P. Larwood, B. R. Rosen, Eds. (Academic Press, New York, 1979), pp. 319–327.
11. S. Bengston, Z. Yue, *Science* **257**, 1645 (1992).
12. G. Wörheide, A. M. Solé-Cava, J. N. A. Hooper, *Comp. Biol.* **45**, 377 (2005).
13. K. J. Peterson, B. Waggoner, J. W. Hagadorn, *Integr. Comp. Biol.* **43**, 127 (2003).
14. J. G. Gehling, G. M. Narbonne, M. A. Anderson, *Palaeontology* **43**, 427 (2000).
15. J. E. Amthor *et al.*, *Geology* **31**, 431 (2003).
16. L. J. Holtz, K. A. Beauchamp, *Mar. Biol.* **116**, 129 (1993).

17. This research was supported by a National Science Foundation grant (EAR-0074021) and a NASA grant (NNG04G142G NASA Exobiology Program) to M.L.D. and an Australian Research Council Grant (DP0453393) to J.G.G. We are indebted to J. Fargher and R. Fargher for access to their property and permission to excavate fossiliferous beds. Fieldwork was facilitated by D. Rice, S. Jensen, J. Paterson, M. Draugis, M. E. Draugis, R. Droser, and members of the Waterhouse Club. M. Hughes, R. Wood and S. Xiao provided helpful comments. D. Garson constructed Fig. 2.

Supporting Online Material

www.sciencemag.org/cgi/content/full/319/5870/1660/DC1
SOM Text
Fig. S1

5 November 2007; accepted 1 February 2008
10.1126/science.1152595

Orrorin tugenensis Femoral Morphology and the Evolution of Hominin Bipedalism

Brian G. Richmond[1,2]* and William L. Jungers[3]

Bipedalism is a key human adaptation and a defining feature of the hominin clade. Fossil femora discovered in Kenya and attributed to *Orrorin tugenensis*, at 6 million years ago, purportedly provide the earliest postcranial evidence of hominin bipedalism, but their functional and phylogenetic affinities are controversial. We show that the *O. tugenensis* femur differs from those of apes and *Homo* and most strongly resembles those of *Australopithecus* and *Paranthropus*, indicating that *O. tugenensis* was bipedal but is not more closely related to *Homo* than to *Australopithecus*. Femoral morphology indicates that *O. tugenensis* shared distinctive hip biomechanics with australopiths, suggesting that this complex evolved early in human evolution and persisted for almost 4 million years until modifications of the hip appeared in the late Pliocene in early *Homo*.

Bipedalism is one of very few human characteristics that appears to have evolved at the base of the hominin clade [species more closely related to modern humans than to any other living species (*1*)]. Recent fossil discoveries have apparently pushed back the origin of the hominin clade into the late Miocene, to 6 to 7 million years ago (Ma). The oldest known potential hominin fossils, attributed to *Sahelanthropus tchadensis*, come from Toros-Menalla in Chad and are biostratigraphically dated to ~7 Ma (*2*). Currently, *Sahelanthropus* is only known from craniodental evidence, and although the position of the foramen magnum suggests that it was bipedal (*3*), postcranial fossils are needed to confirm this conclusion. The next oldest potential hominin remains were discovered in 2000 by Senut, Pickford, and colleagues (*4*) from localities (5.7 to 6.0 Ma) in the Lukeino Formation in Kenya (*5*, *6*) and attributed to *Orrorin tugenensis*. Of the fossils assigned to *O. tugenensis*, three fragmentary femora (BAR 1002'00, 1003'00, and 1215'00) are critical pieces of evidence because they are interpreted as having derived characteristics indicating bipedalism (*7*). However, some of these features are also found in nonbipedal primates and are therefore inconclusive (*8*). Similarly, a study of the femora based on computerized tomography (*9*) suffered from poor image resolution and does not provide convincing evidence of bipedality (*10*). The discoverers have also cited the femora in formulating hypotheses about early hominin phylogenetic relationships (*4*), but these have been disputed (*8*, *11*, *12*). Thus, the morphology of the *O. tugenensis* femora is critical to our understanding of the origin of bipedalism and phylogenetic relationships of the earliest hominin taxa, yet the functional and phylogenetic implications of their morphology remain highly controversial. We present here a quantitative, morphometric (shape) comparison of the most complete *O. tugenensis* femur, BAR 1002'00, of a young adult.

When compared to the proximal femora of a large and diverse sample of great apes, modern humans (including small-bodied adult individuals from African Pygmy and Andaman Islander populations), as well as Plio-Pleistocene hominin femora (*13*), the *O. tugenensis* femur (BAR 1002'00) more closely resembles femora attributed to early hominin taxa (*Australopithecus* and *Paranthropus*) than do those of extant apes, fossil *Homo*, and modern humans. Multivariate analyses of shape (canonical variates, cluster analysis, and principal components analysis) reveal that modern human proximal femora are distinct from those of extant great apes primarily in having a relatively large head and short distance between the head and lesser trochanter. Canonical variates axis 1 (Fig. 1A) is a contrast vector driven by these distinguishing features of shape (table S1), and the non-*Homo* fossil hominins (including BAR 1002'00) occupy an intermediate position in this part of multivariate space. The second axis separates orangutans from African apes, modern humans, and all the fossils. Orangutans have relatively large femoral heads (related to mobility rather than more pronounced weight support) combined with narrow femoral shafts, a combination of features not seen in modern or fossil hominin femora. The third axis, driven by neck length and breadth, and shaft breadth, serves to separate early hominin femora from those of extant apes, modern humans, and fossil *Homo* taxa. BAR 1002'00 resembles the early hominin femora, which are characterized in this and previous analyses by a combination of long and

[1]Center for the Advanced Study of Hominid Paleobiology, Department of Anthropology, The George Washington University, 2110 G Street, NW, Washington, DC 20052, USA. [2]Human Origins Program, National Museum of Natural History, Smithsonian Institution, Washington, DC 20560, USA. [3]Department of Anatomical Sciences, Stony Brook University, Stony Brook, NY 11794–8081, USA.

*To whom correspondence should be addressed. E-mail: bgrich@gwu.edu

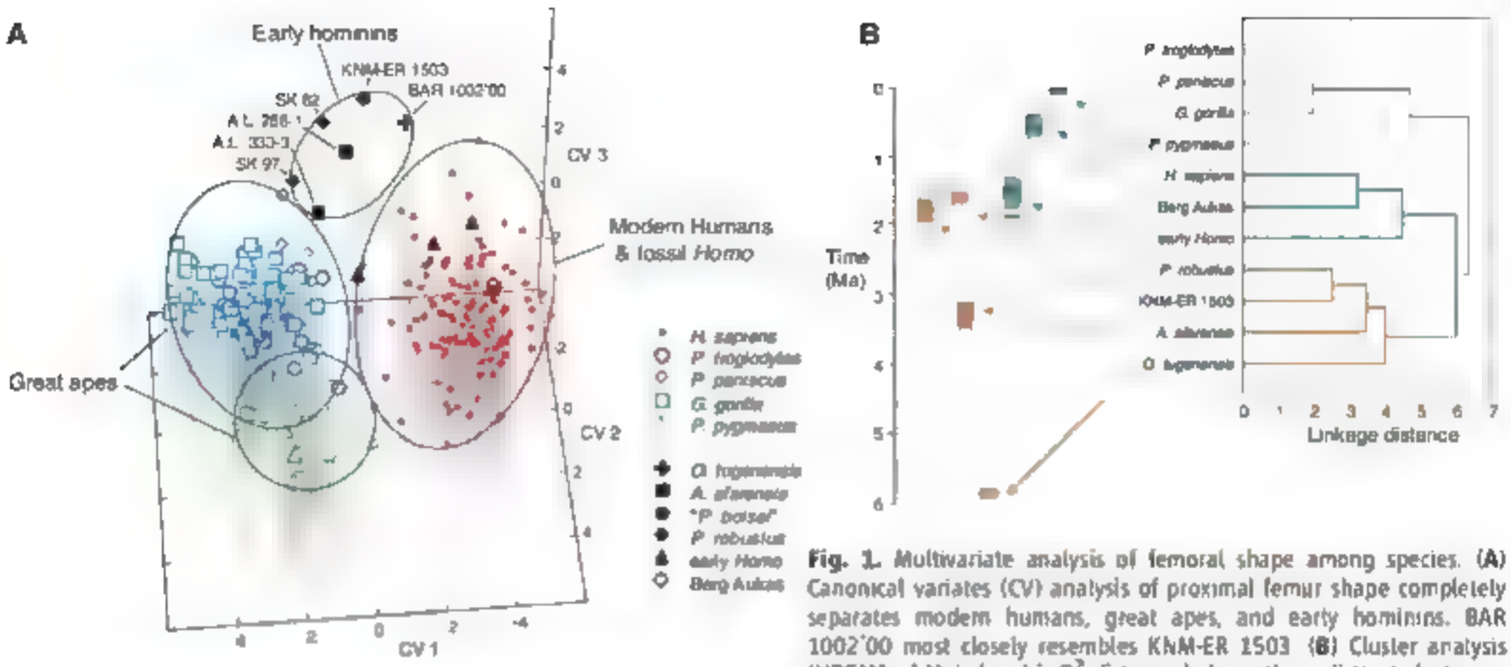

Fig. 1. Multivariate analysis of femoral shape among species. **(A)** Canonical variates (CV) analysis of proximal femur shape completely separates modern humans, great apes, and early hominins. BAR 1002'00 most closely resembles KNM-ER 1503. **(B)** Cluster analysis (UPGMA of Mahalanobis D^2 distances) shows three distinct clusters: a great ape cluster, a cluster of modern and fossil *Homo*, and a cluster of BAR 1002'00 and early hominins. The early hominin femoral morphology exhibited by BAR 1002'00 appears to persist for more than 4 million years, with a major change in hip structure in early *Homo*.

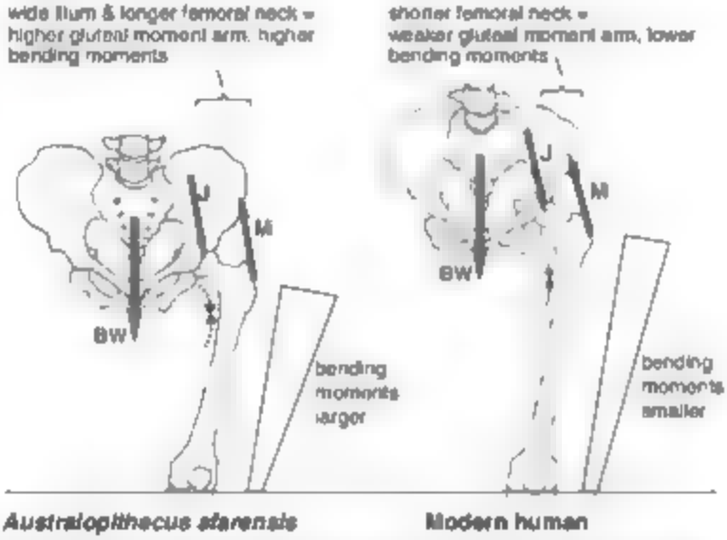

Fig. 2. Hominin hip biomechanics. Distinctive features of the early hominin hip (**left**) are part of a biomechanical complex in which the tendency of the body weight force (BW) to pull down the trunk during gait is counteracted by the gluteal muscle force acting on the pelvis. Compared to modern humans (**right**), the wider iliac blade and longer femoral neck of the early hominin hip (left) result in greater moment arms for the gluteal muscle force (M). They also result in greater femoral shaft bending moments from the joint reaction force (J), which in turn are related to greater mediolateral shaft robusticity to withstand the elevated compressive stresses along the medial side of the proximal femoral shaft. Thus, the long femoral neck, wide proximal shaft, and possibly the small femoral head are part of a biomechanical complex. (Vector and bending moment illustrations not to scale.)

anteroposteriorly constricted necks, mediolaterally broad shafts, and smaller heads (relative to modern humans) (*14*, *17*). This morphological complex is not merely an allometric consequence of the small size of many of the fossils (fig. S3), including A.L. 288-1 and BAR 1002'00 (*18*), as the small-bodied modern humans and apes in this sample do not resemble the early hominins. Three distinct clusters summarize these affinities (Fig. 1B): modern humans and fossil *Homo* form a group that is linked to a cluster of *Australopithecus*, *Paranthropus*, and *O. tugenensis*, and these two groups are joined by a more distant cluster of extant apes.

The features (long, narrow neck and broad proximal shaft) characterizing *O. tugenensis* and australopith (*19*) femora are not biomechanically independent, and reflect differences in hip morphology related to gait mechanics. Modern human gait is distinct from the kinematics of bipedalism in other primates in several ways, including very little lateral displacement and a slight drop in the contralateral hip during stance phase (*20*, *21*). These characteristics are made possible in part by the flared, short iliac blade and by the recruitment of the lesser gluteal muscles on the ipsilateral side, which counteract the tendency of the body weight force to lower the contralateral hip (Fig. 2). The very flaring ilia and long femoral necks of australopiths improve the gluteal muscle lever arm and thus counter the torque of body weight (*17*), but the long necks also increase the bending moment on the proximal femoral shaft. These elevated bending moments are resisted by the greater mediolateral width of the femoral diaphysis, especially proximally where bending moments are highest (*22*).

O. tugenensis shares this uniquely archaic hominin morphological pattern, thus providing strong evidence that *O. tugenensis* was adapted to bipedalism 6 million years ago (Fig. 3). This evidence is functionally consistent with other morphological features believed to be linked to bipedalism in the *O. tugenensis* femora, including a marked obturator externus groove, the presence of an intertrochanteric line, vertical gluteal tuberosity (third trochanter), and a slightly enlarged head (*7*). BAR 1002'00 bears distinct markings for the medial and lateral extents of the vastus musculature, but it lacks the prominent, raised linea aspera that is distinctive of modern and fossil *Homo* femora. In this manner, BAR 1002'00 resembles some australopith femora [e.g., A.L. 288-1ap (*23*)]. The relative femoral head size of BAR 1002'00 is intermediate between, and overlaps with, the distribution of *Pan* and *Homo* femora; the femoral head of BAR 1002'00 is large compared to *Australopithecus*, *Paranthropus*, and African ape femora, but relatively smaller than those of orangutans and fossil and modern *Homo* (fig. S6). Furthermore, the difference between BAR 1002'00 and *Australopithecus* and *Paranthropus* in relative femoral head size is within the expected level of intraspecific variation based on extant standards.

To investigate how proximal femur shape has changed over the course of human evolutionary

Fig. 3. Morphological comparisons among femora of or attributed to (**A**) *P. troglodytes* (**B**) *O. tugenensis* (BAR 1002'00) (**C** and **D**) *Paranthropus robustus* (SK 97 and SK 82, reversed), (**E**) *A. afarensis* (A.L. 288-1ap), (**F**) *Paranthropus boisei* (KNM-ER 1503, reversed) (**G**) early *Homo* (KNM-ER 1481), and (**H**) modern *H. sapiens*. Like other early hominin femora (C to F), BAR 1002'00 (B) is distinct from those of modern humans (H) and great apes (A) in having a long, anteroposteriorly narrow neck and wide proximal shaft. Early *Homo* femora (G) have larger heads and broader necks compared to early hominins. In addition to these features, modern human femora (H) have short necks and mediolaterally narrow shafts. Scale bar, 2 cm.

history, we plotted against time the multivariate shape Mahalanobis D^2 distance between each fossil femur and the mean shape of *Homo sapiens* femora. Distances are consistently high until the appearance in the late Pliocene and early Pleistocene of femora attributed to *Homo* (fig. S4). The early *Homo* femora retain the primitively long necks and broad shafts (*16*, *24*), suggesting the retention of relatively broad ilia (*24*), but more closely resemble modern human femora in having larger heads and broader necks. In conjunction with significantly greater femoral length (*25*), these features provide evidence of a transition to a more modern humanlike bipedal gait including greater speed and energetic efficiency compared to earlier hominins (*16*, *26*–*29*). Further changes in femoral anatomy (e.g., shorter neck, narrower shaft) occur in the genus *Homo* in the Middle Pleistocene and can be linked in part to obstetrical factors (*24*).

In light of the marked changes in femoral anatomy from at least 2 Ma to the present, the close morphological similarity between femora of *O. tugenensis* at 6 Ma and *Australopithecus* and *Paranthropus* in the later Pliocene is especially pronounced (figs. 3 and 3 and table S3). Accordingly, the early hominin taxa, *Orrorin* has the smallest Mahalanobis D^2 distance from the modern human centroid. BAR 1002'00 is much closer to all early hominin taxa than to the modern human centroid in shape space (table S3). The external morphology of *O. tugenensis* provides no indications of differences in bipedal gait compared to *Australopithecus* or *Paranthropus*. This suggests that the pattern of bipedal gait characteristic of australopiths evolved very early in the human lineage, and perhaps they were also the characteristics of the first bipedal hominins. This form of bipedalism appears to have persisted as a successful locomotor strategy for as long as 4 million years (fig. 1B). Additional lower limb fossils from the late Miocene and early Pliocene will be needed to test this hypothesis.

Similarities in femoral morphology, however, do not rule out possible differences in overall repertoires of postional behavior. Upper limb fossils of *O. tugenensis* retain morphological features related to arboreal climbing, including a pronounced humeral brachioradialis flange and a curved proximal manual phalanx (*4*). The included angle measured on BAR 349'00 (proximal phalanx) is 52°, significantly greater than those of modern humans and *Macaca mulatta* (*t* test, $P < 0.05$), and significantly lower than those of orangutans (fig. S5). In degree of curvature, BAR 349'00 most closely resembles *Pan troglodytes*. The *Pan*-like curvature of the proximal phalanx close to the *Pan-Homo* last common ancestor supports the hypothesis that bipedalism evolved from an ancestor adapted to orthograde and vertical climbing, consistent with a climbing and knuckle-walking repertoire (*30*), rather than an orangutan-like arboreal specialist (*31*). Therefore, while *O. tugenensis* was bipedal, it most probably also climbed trees (*4*), presumably to forage, build nests, and seek refuge. Whether arboreality played a greater role in the locomotor repertoire of *O. tugenensis* in comparison to *Australopithecus* remains unresolved. The available evidence of internal cortical morphology of BAR 1002'00 (*7*, *9*) leaves open the possibility that *O. tugenensis* had a pattern of neck bone cortical thickness that differed from the human-like pattern observed in *Australopithecus* (*32*) and would be consistent with the use of a wider range of hip joint postures like those used by great apes during climbing. The external anatomy of BAR 1002'00 indicates bipedality, but is also consistent with a locomotor repertoire involving an appreciable scansorial component (*33*, *34*).

The similarity between *O. tugenensis* and australopith femora weakens support for scenarios in which *O. tugenensis* is ancestral to *Homo* to the exclusion of *A. afarensis* (*4*). Instead, the overall primitive hominin morphology of the *O. tugenensis* femur, along with primitive dental anatomy, is consistent with the more parsimonious hypothesis that it is a basal member of the hominin clade. In sum, the comparative biomechanical anatomy of *O. tugenensis* femora suggests that *O. tugenensis* is a basal hominin adapted to bipedalism, and current evidence suggests that an *Australopithecus*-like bipedal morphology evolved early in the hominin clade and persisted successfully for most of human evolutionary history.

References and Notes

1. B. A. Wood, B. G. Richmond, *J. Anat.* **196**, 19 (2000).
2. M. Brunet *et al.*, *Nature* **434**, 752 (2005).
3. C. P. Zollikofer *et al.*, *Nature* **434**, 755 (2005).
4. B. Senut *et al.*, *C. R. Acad. Sci. Paris Ser. II a* **332**, 137 (2001).
5. A. L. Deino, L. Tauxe, M. Monaghan, A. Hill, *J. Hum. Evol.* **42**, 117 (2002).
6. Y. Sawada *et al.*, *C. R. Palevol* **1**, 293 (2002).
7. M. Pickford, B. Senut, D. Gommery, J. Treil, *C. R. Palevol* **1**, 1 (2002).
8. D. R. Begun, *Science* **303**, 1478 (2004).
9. K. Gabi *et al.*, *Science* **305**, 1450 (2004).
10. J. C. Ohman, C. O. Lovejoy, T. D. White, *Science* **307**, 845 (2005).
11. L. C. Aiello, M. Collard, *Nature* **410**, 526 (2001).
12. C. J. Cela-Conde, F. J. Ayala, *Proc. Natl. Acad. Sci. U.S.A.* **100**, 7684 (2003).
13. Materials and methods are available as supporting material on *Science* Online.
14. M. H. Day, *Nature* **221**, 230 (1969).
15. A. C. Walker, *J. Hum. Evol.* **2**, 545 (1973).
16. H. M. McHenry, R. S. Corruccini, *Am. J. Phys. Anthropol.* **49**, 473 (1978).
17. C. O. Lovejoy, K. G. Heiple, A. H. Burstein, *Am. J. Phys. Anthropol.* **38**, 757 (1973).
18. M. Nakatsukasa, M. Pickford, N. Egi, B. Senut, *Primates* **48**, 171 (2007).
19. We use "australopith" as a vernacular term to refer to *Australopithecus* and *Paranthropus* species, following (*1*).
20. F. A. Jenkins, *Science* **178**, 877 (1972).
21. J. T. Stern Jr., R. L. Susman, *Am. J. Phys. Anthropol.* **55**, 153 (1981).
22. C. B. Ruff, in *Primate Locomotion: Recent Advances*, E. Strasser, J. G. Fleagle, A. Rosenberger, H. M. McHenry, Eds. (Plenum, New York, 1998), pp. 449–469.
23. T. D. White *et al.*, *Nature* **440**, 883 (2006).
24. C. B. Ruff, *Am. J. Phys. Anthropol.* **98**, 527 (1995).
25. B. G. Richmond, L. C. Aiello, B. A. Wood, *J. Hum. Evol.* **43**, 529 (2002).
26. D. R. Carrier, *Curr. Anthropol.* **25**, 483 (1984).
27. W. L. Jungers, *J. Hum. Evol.* **17**, 247 (1988).
28. K. L. Steudel-Numbers, *J. Hum. Evol.* **51**, 445 (2006).
29. M. D. Sockol, D. A. Raichlen, H. Pontzer, *Proc. Natl. Acad. Sci. U.S.A.* **104**, 12265 (2007).
30. B. G. Richmond, D. R. Begun, D. S. Strait, *Yrbk. Phys. Anthropol.* **116**, 70 (2001).
31. S. K. Thorpe, R. L. Holder, R. H. Crompton, *Science* **316**, 1328 (2007).
32. C. O. Lovejoy, R. S. Meindl, J. C. Ohman, K. G. Heiple, T. D. White, *Am. J. Phys. Anthropol.* **119**, 97 (2002).
33. J. T. J. Stern Jr., R. L. Susman, *Am. J. Phys. Anthropol.* **60**, 279 (1983).
34. J. T. J. Stern Jr., *Evol. Anthropol.* **9**, 113 (2000).

35. This research was supported by The George Washington University, Stony Brook University, and the NSF. We gratefully acknowledge the assistance of the curators at the numerous institutions housing the extant and fossil collections used in this study. We also thank M. Pickford and B. Senut for helpful discussions, and B. Wood, J. Stern, D. Strait, M. Nakatsukasa, and the anonymous reviewers for constructive comments on our manuscript.

Supporting Online Material
www.sciencemag.org/cgi/content/full/319/5870/1662/DC1
Figs. S1 to S6
Tables S1 to S3
References

14 December 2007; accepted 22 February 2008
10.1126/science.1154197

Activation of FOXO1 by Cdk1 in Cycling Cells and Postmitotic Neurons

Zengqiang Yuan,[1*†] Esther B. E. Becker,[1*] Paola Merlo,[1] Tomoko Yamada,[1] Sara DiBacco,[1] Yoshiyuki Konishi,[1] Erik M. Schaefer,[2] Azad Bonni[1‡]

Activation of cyclin-dependent kinase 1 (Cdk1) has been linked to cell death of postmitotic neurons in brain development and disease. We found that Cdk1 phosphorylated the transcription factor FOXO1 at Ser^{249} in vitro and in vivo. The phosphorylation of FOXO1 at Ser^{249} disrupted FOXO1 binding with 14-3-3 proteins and thereby promoted the nuclear accumulation of FOXO1 and stimulated FOXO1-dependent transcription, leading to cell death in neurons. In proliferating cells, Cdk1 induced FOXO1 Ser^{249} phosphorylation at the G_2/M phase of the cell cycle, resulting in FOXO1-dependent expression of the mitotic regulator Polo-like kinase (Plk). These findings define a conserved signaling link between Cdk1 and FOXO1 that may have a key role in diverse biological processes, including the degeneration of postmitotic neurons.

The protein kinase Cdk1 is a key mediator of neuronal cell death. This is relevant to brain development and degeneration (*1*–*6*). As a major apoptotic kinase, Cdk1 might be expected to orchestrate a program of gene expression that activates the cell death machinery. Because Cdk1 resides in the cytoplasm in neurons (*1*, *5*, *6*), we reasoned that Cdk1 might regulate gene expression through proteins that shuttle between the cytoplasm and nucleus. The FOXO transcription factors undergo nucleocytoplasmic shuttling and control cell death (*7*, *8*). We therefore investigated the role of FOXO proteins in propagating the Cdk1 cell death signal to the nucleus in postmitotic neurons.

FOXO1 contains a conserved putative Cdk1 phosphorylation site within the forkhead domain at Ser^{249} (fig. S1A). Cdk1 catalyzed the phosphorylation of FOXO1 in vitro (Fig. 1A) (*9*). Cdk1 also phosphorylated the FOXO1 forkhead domain (FOXO1FD) in vitro, but failed to phosphorylate a FOXO1FD mutant in which Ser^{249} was replaced with alanine (FOXO1FD S249A) (fig. S1B). We generated an antibody that specifically recognizes FOXO1 that is phosphorylated at Ser^{249} (*9*). The phosphoS249-FOXO1 antibody recognized recombinant FOXO1 or FOXO1FD that was phosphorylated by Cdk1 in vitro but did not recognize unphosphorylated FOXO1 or the FOXO1FD S249A mutant that was incubated with Cdk1 in vitro (Fig. 1B and fig. S1C). We expressed cyclin B and Cdk1 in 293T cells together with FOXO1 or a S249A FOXO1 mutant. Immunoblotting of total lysates or FOXO1 immunoprecipitates of transfected cells revealed that Cdk1 increased the amount of phosphorylated FOXO1 at Ser^{249} in cells (Fig. 1C and fig. S1D). In other experiments, depletion of endogenous Cdk1 by RNA interference (RNAi) reduced the FOXO1 phosphorylation in cells (Fig. 1D and fig. S1E), which suggested a requirement for endogenous Cdk1 in the FOXO1 phosphorylation at Ser^{249} in cells.

We tested whether the activation of endogenous Cdk1 induced the phosphorylation of endogenous FOXO1 at Ser^{249} in neurons. Endogenous Cdk1 is activated in cerebellar granule neurons upon inhibition of membrane depolarization (*1*, *3*). We found that the amount of FOXO1 Ser^{249} phosphorylation was higher in neurons deprived of membrane-depolarizing concentrations of KCl (5 mM KCl) than in neurons maintained in depolarizing medium (30 mM KCl) (Fig. 1E). The Cdk1 inhibitor roscovitine reduced the FOXO1 Ser^{249} phosphorylation in neurons deprived of depolarization (Fig. 1E). Thus, endogenous Cdk1 appears to mediate activity deprivation–induced phosphorylation of endogenous FOXO1 at Ser^{249} in neurons.

The identification of Cdk1-induced phosphorylation of FOXO1 at Ser^{249} led us to test whether the FOXO1 phosphorylation mediated the ability of Cdk1 to trigger cell death in neurons. Because endogenous Cdk1 is required for apoptosis of activity-deprived neurons (*1*, *3*), we determined the role of FOXO1 in apoptosis of neurons deprived of activity. We transfected neurons with the U6 loop RNAi or control U6 plasmid. FOXO RNAi reduced the expression of FOXO1 in primary granule neurons and

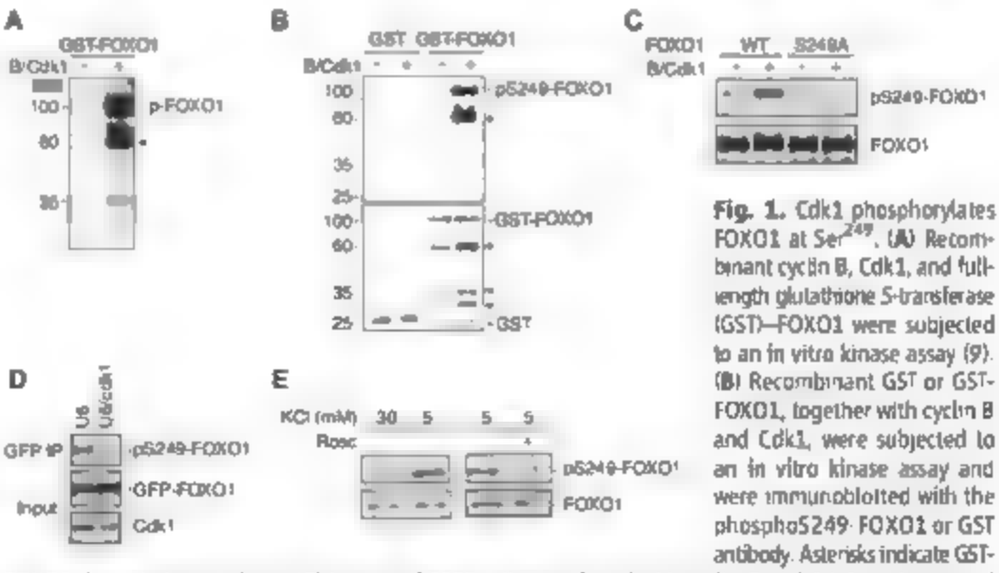

Fig. 1. Cdk1 phosphorylates FOXO1 at Ser^{249}. (**A**) Recombinant cyclin B, Cdk1, and full-length glutathione *S*-transferase (GST)–FOXO1 were subjected to an in vitro kinase assay (*9*). (**B**) Recombinant GST or GST-FOXO1, together with cyclin B and Cdk1, were subjected to an in vitro kinase assay and were immunoblotted with the phosphoS249-FOXO1 or GST antibody. Asterisks indicate GST-FOXO1 degradation products. (**C**) Lysates of 293T cells transfected with cyclin B and Cdk1 or the control vector together with the green fluorescent protein (GFP) fusion protein GFP-FOXO1 or the GFP-FOXO1S249A mutant, were immunoblotted with the phosphoS249-FOXO1 antibody or a mouse monoclonal FOXO1 antibody. (**D**) Lysates of Neuro2A cells transfected with the control U6 or U6/cdk1 RNAi plasmid and GFP-FOXO1 were immunoprecipitated with the GFP antibody and immunoblotted with the phosphoS249-FOXO1 antibody. Lysates were also immunoblotted with the GFP or Cdk1 antibody. (**E**) Lysates of granule neurons maintained in membrane-depolarizing medium (30 mM KCl) or in which depolarization was inhibited (5 mM KCl) in the presence of the Cdk1 inhibitor roscovitine (10 μM) or its vehicle dimethyl sulfoxide (DMSO), were immunoblotted with the phosphoS249-FOXO1 or FOXO1 antibody.

[1]Department of Pathology, Harvard Medical School, 77 Avenue Louis Pasteur, Boston, MA 02115, USA. [2]Center for Signal Transduction, Cellular Analysis Business Unit/BioDiscovery Division, Invitrogen Corporation, 94 South Street, Hopkinton, MA 01748, USA.

*These authors contributed equally to this work.
†Present address: Institute of Biophysics, Chinese Academy of Sciences, 15 Datun Road, Beijing 100101, China.
‡To whom correspondence should be addressed. E-mail: azad_bonni@hms.harvard.edu

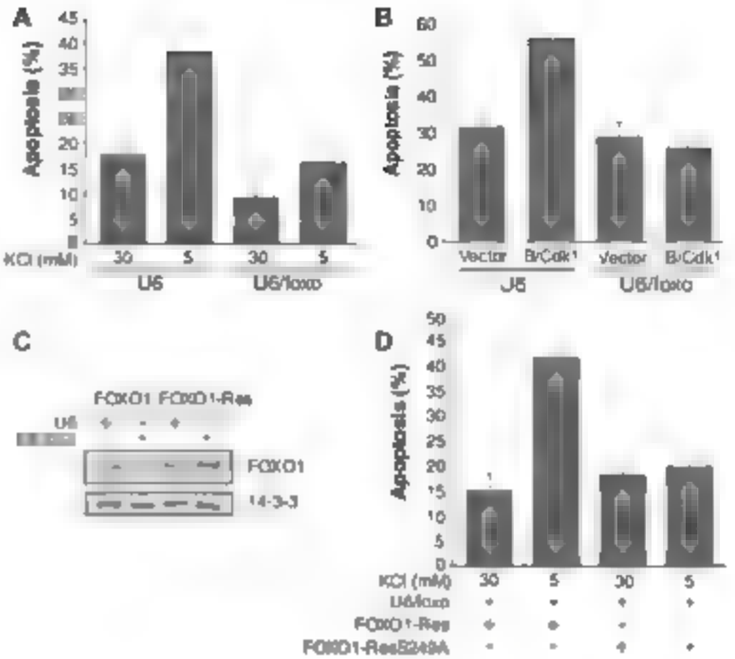

Fig. 2. Cdk1-FOXO1 signaling mediates activity deprivation–induced neuronal death. (**A**) Granule neurons transfected with the U6/foxo RNAi or control U6 plasmid were placed in membrane-depolarizing medium (30 mM KCl) or deprived of membrane depolarization (5 mM KCl) for 30 hours and subjected to analysis of cell death (9). FOXO RNAi attenuated activity deprivation–induced neuronal cell death [mean ± SEM, $n = 4$; $P < 0.005$, analysis of variance (ANOVA) followed by Fisher's PLSD post hoc test] but not cell death in depolarized neurons (see also fig. S2C). (**B**) Granule neurons transfected with the U6/foxo RNAi or control U6 plasmid, together with cyclin B and Cdk1 or the control vector, were analyzed as in (A). FOXO RNAi inhibited cyclin B and Cdk1–induced cell death (mean ± SEM, $n = 3$; $P < 0.005$, ANOVA followed by Fisher's PLSD post hoc test). (**C**) Lysates of COS cells transfected with the U6/foxo RNAi or control U6 plasmid together with FOXO1 or an RNAi-resistant rescue form of FOXO1 (FOXO1-Res) were immunoblotted with a FOXO1 or 14-3-3 antibody (9). (**D**) Granule neurons transfected with the U6/foxo RNAi plasmid together with FOXO1-Res or the FOXO1-Res5249A mutant were analyzed as in (A). FOXO1-Res, but not FOXO1 Res5249A, induced cell death in activity-deprived neurons in the background of FOXO RNAi (mean ± SEM, $n = 3$; $P < 0.05$, ANOVA followed by Fisher's PLSD post hoc test).

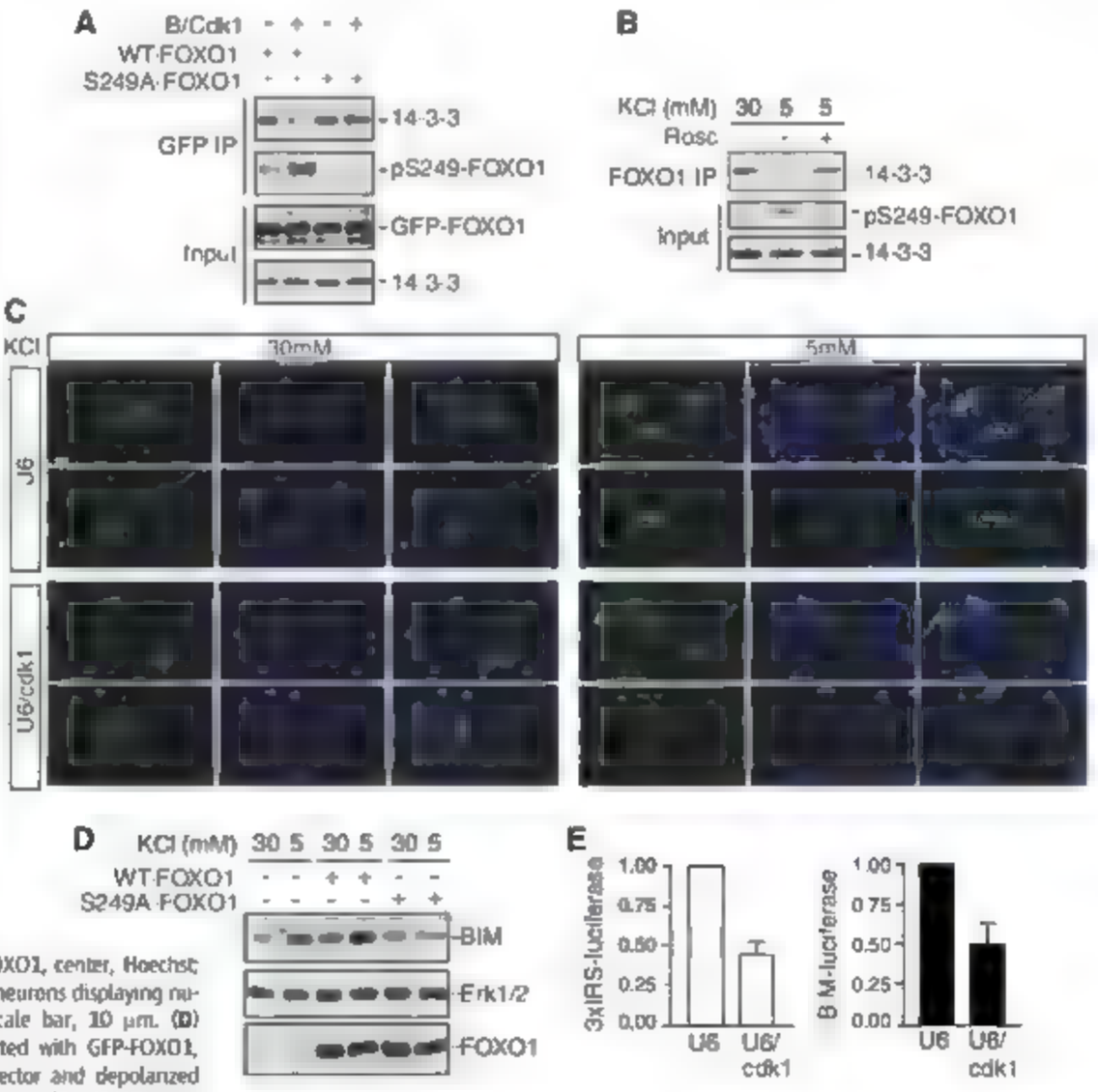

Fig. 3. FOXO1 Ser^{249} phosphorylation disrupts the FOXO1 14-3-3 interaction and promotes nuclear accumulation of FOXO1, leading to activation of transcription. (**A**) Lysates of 293T cells transfected with GFP-FOXO1 or GFP-FOXO1S249A, together with cyclin B and Cdk1 or the control vector, were immunoprecipitated with the GFP antibody and immunoblotted with the 14-3-3 or phosphoS249-FOXO1 antibody. Lysates were also immunoblotted with the GFP or 14-3-3 antibody. (**B**) Lysates of granule neurons maintained in depolarizing medium (30 mM KCl) or deprived of depolarization (5 mM KCl), in the presence of the Cdk1 inhibitor roscovitine (10 μM) or its vehicle (DMSO), were immunoprecipitated with the FOXO1 antibody and immunoblotted with the 14-3-3 antibody. Lysates were immunoblotted with the phosphoS249-FOXO1 or 14-3-3 antibody. (**C**) Granule neurons transfected with GFP-FOXO1 together with the U6/cdk1 RNAi or control U6 plasmid maintained in depolarizing medium (30 mM KCl) or deprived of depolarization (5 mM KCl) were analyzed by fluorescence microscopy. Representative images are shown (left, GFP-FOXO1; center, Hoechst; right, merged). Arrowheads indicate neurons displaying nuclear localization of GFP-FOXO1. Scale bar, 10 μm. (**D**) Lysates of granule neurons transfected with GFP-FOXO1, GFP-FOXO1S249A, or the control vector and depolarized (30 mM KCl) or deprived of depolarization (5 mM KCl) were immunoblotted with the BIM, Erk1/2, or FOXO1 antibody. (**E**) Granule neurons transfected with the U6/cdk1 RNAi or control U6 plasmid together with the 3xIRS-luciferase (left) or BIM-luciferase (right) reporter gene and tk-renilla were deprived of depolarization and subjected to luciferase assays. Cdk1 knockdown reduced the expression of the 3xIRS (mean ± SEM, $n = 3$; $P < 0.001$, t test) and BIM-luciferase (mean ± SEM, $n = 3$; $P < 0.005$, t test) reporter gene.

protected neurons against cell death induced by suppression of depolarization (Fig. 2A and fig. S2A) (*9*). FOXO RNAi also suppressed the ability of expression of cyclin B and Cdk1 to induce cell death in neurons (Fig. 2B). To determine the importance of the phosphorylation of FOXO1 at Ser^{249} in activity deprivation–induced neuronal apoptosis, we constructed an expression plasmid encoding an RNAi-resistant form of FOXO1 (FOXO1-Res) (*9*). Whereas FOXO RNAi induced depletion of FOXO1 encoded by wild-type cDNA, FOXO RNAi failed to induce efficient depletion of FOXO1-Res (Fig. 2C). Expression of FOXO1-Res triggered apoptosis in FOXO-depleted neurons deprived of activity (Fig. 2D). By contrast, a FOXO1-Res mutant in which Ser^{249} was replaced with alanine (FOXO1-ResS249A) failed to effectively induce neuronal cell death in the background of FOXO RNAi (Fig. 2D). Thus, the Ser^{249} phosphorylation appears to be required for the ability of FOXO1 to mediate activity deprivation–induced neuronal apoptosis.

We characterized the mechanism by which the Cdk1-induced phosphorylation of FOXO1 at Ser^{249} stimulates FOXO1-dependent neuronal cell death. Ser^{249} lies within a conserved short FOXO1 peptide motif that includes the Akt site of phosphorylation, Ser^{256} (fig. S1A). Because Ser^{256}–phosphorylated FOXO1 interacts with 14-3-3 proteins, leading to FOXO1's cytoplasmic sequestration and inhibition (*7*, *8*), we tested whether phosphorylation of FOXO1 at Ser^{249} might regulate FOXO1's interaction with 14-3-3 proteins. Although FOXO1 or its forkhead domain interacted efficiently with 14-3-3 proteins, expression of Cdk1 reduced these interactions (Fig. 3A and fig. S3A). However, Cdk1 failed to inhibit the interaction of FOXO1S249A with 14-3-3 proteins (Fig. 3A). Cdk1 did not affect Ser^{256} phosphorylation in FOXO1 or its forkhead domain (fig. S3, A and B), which suggests that the Ser^{249} phosphorylation inhibits the interaction of Ser^{256}–phosphorylated FOXO1 with 14-3-3 proteins.

To ascertain whether endogenous Cdk1 might regulate the interaction of endogenous FOXO1 with 14-3-3 proteins in neurons, we assayed the association of these proteins in granule neurons in the presence or absence of membrane depolarization. In depolarized neurons, endogenous FOXO1 interacted with endogenous 14-3-3 proteins (Fig. 3B). However, withdrawal of depolarization, which stimulates the activity of endogenous Cdk1 in neurons (*1*, *3*), reduced the interaction (Fig. 3B). The Cdk1 inhibitor roscovitine blocked the ability of activity deprivation to disrupt FOXO1's association with 14-3-3 proteins (Fig. 3B). These findings suggest that endogenous Cdk1-induced phosphorylation of FOXO1 at Ser^{249} releases FOXO1 from sequestration by 14-3-3 proteins in neurons.

Because 14-3-3 proteins sequester FOXO proteins in the cytoplasm (*7*, *8*), we characterized the consequences of the Ser^{249} phosphorylation on the subcellular localization of FOXO1. Whereas FOXO1 was localized predominantly in the cytoplasm in depolarized neurons, FOXO1 accumulated in the nucleus in neurons deprived of activity (Fig. 3C and fig. S4, A to C). Depletion of endogenous Cdk1 by RNAi reduced the nuclear accumulation of FOXO1 in activity-deprived neurons (Fig. 3C and fig. S4, A to C). In other experiments, expression of cyclin B and Cdk1 triggered the nuclear accumulation of wild-type FOXO1 but not FOXO1S249A in neurons (fig. S5). These results suggest that Cdk1-induced phosphorylation of FOXO1 Ser^{249} stimulates the nuclear accumulation of FOXO1 in neurons.

The finding that Ser^{249}-phosphorylated FOXO1 accumulates in the nucleus led us to test whether Cdk1-FOXO1 signaling might activate FOXO-dependent transcription. Overexpression of Cdk1 augmented the ability of FOXO1, but not of FOXO1S249A, to stimulate the expression of a luciferase reporter gene controlled by a FOXO-responsive promoter (3xIRS-luciferase) in granule neurons (fig. S6) (*9*). Withdrawal of membrane depolarization induced the endogenous expression of the FOXO-responsive apoptotic gene *BIM* in granule neurons (Fig. 3D). Expression of FOXO1S249A, but not of FOXO1, reduced the induction of endogenous BIM expression upon activity deprivation (Fig. 3D). Depletion of endogenous Cdk1 by RNAi in neurons reduced the expression of both the 3xIRS-luciferase reporter gene and a reporter gene controlled by the BIM promoter (Fig. 3E). Together, these results suggest that endogenous Cdk1-induced phosphorylation of FOXO1 at Ser^{249} stimulates FOXO1-dependent transcription, leading to BIM expression and consequent neuronal cell death.

Overexpression of the Cdk1-related protein kinase Cdk2 was reported to phosphorylate FOXO1 at Ser^{249}, thereby inducing the nuclear exclusion and inhibition of FOXO1 in prostate cancer cells (*10*). We found that overexpression of Cdk2 or Cdk1 stimulated FOXO1-dependent transcription and failed to promote the nuclear export of

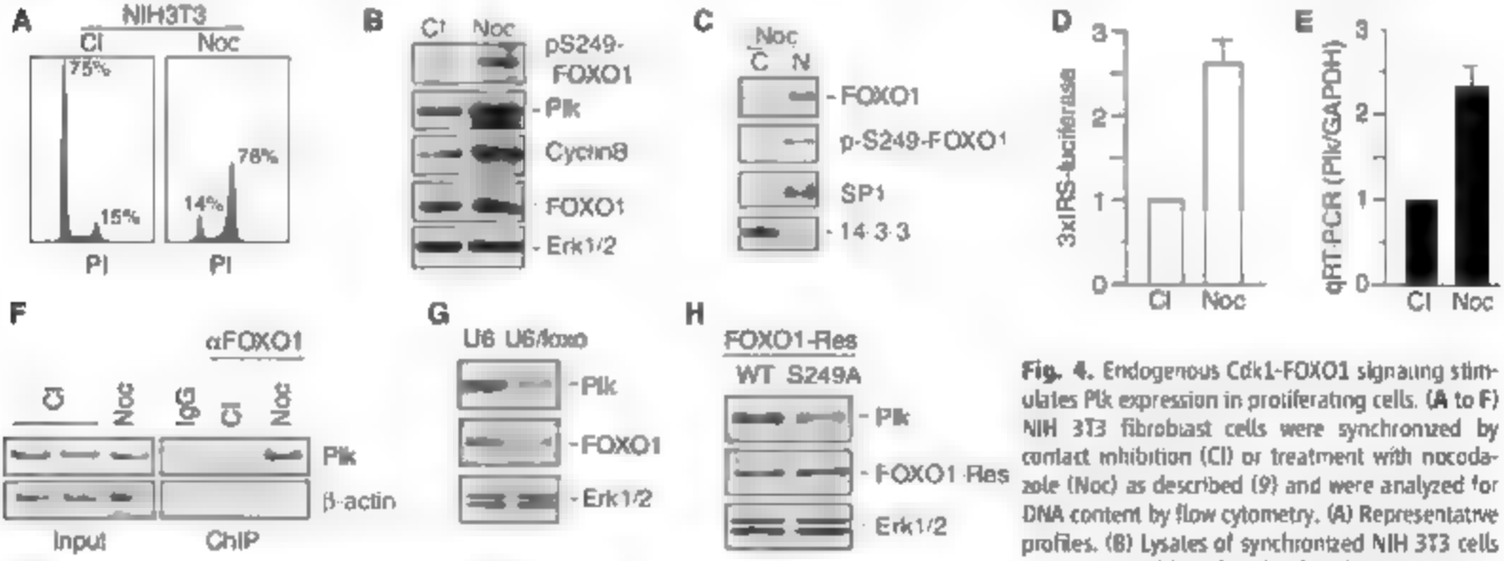

Fig. 4. Endogenous Cdk1-FOXO1 signaling stimulates Plk expression in proliferating cells. (**A** to **F**) NIH 3T3 fibroblast cells were synchronized by contact inhibition (CI) or treatment with nocodazole (Noc) as described (*9*) and were analyzed for DNA content by flow cytometry. (**A**) Representative profiles. (**B**) Lysates of synchronized NIH 3T3 cells were immunoblotted with phospho5249-FOXO1, Plk1, cyclin B, FOXO1, or Erk1/2 antibody. (**C**) Lysates of NIH 3T3 cells synchronized in G_2/M were fractionated into cytoplasmic and nuclear components and immunoblotted with the FOXO1, phospho5249-FOXO1, SP1, or 14-3-3 antibody. The 14-3-3 and SP1 proteins indicate the cytoplasmic and nuclear compartments, respectively. (**D**) NIH 3T3 cells transfected with 3xIRS-luciferase reporter gene and synchronized as in (A) were subjected to luciferase assay. FOXO-dependent reporter expression was increased in G_2/M-enriched relative to G_0/G_1-enriched NIH 3T3 cells (mean ± SEM, $n = 5$, $P < 0.01$, *t* test). (**E**) The amount of Plk mRNA was induced in G_2/M-enriched relative to G_0/G_1-enriched NIH 3T3 cells (mean ± SEM, $n = 3$; $P < 0.001$, *t* test). (**F**) Chromatin immunoprecipitation analysis of synchronized NIH 3T3 cells, using a rabbit immunoglobulin G control or a FOXO1 antibody. (**G**) NIH 3T3 cells transfected with U6-GFP/foxo RNAi or U6-GFP control RNAi plasmid were sorted on the basis of GFP expression. Lysates of sorted cells were immunoblotted with the Plk, FOXO1, or ERK1/2 antibody. (**H**) NIH 3T3 cells transfected with U6-GFP/foxo RNAi plasmid and FOXO1-Res or FOXO1-ResS249A were sorted on the basis of GFP expression. Lysates of sorted cells were analyzed as in (G).

FOXO1 in diverse cell types, including prostate cancer cells (figs. S7 and S8) (9). We confirmed that overexpression of Cdk2 induced phosphorylation of FOXO1 at Ser^{249} (fig. S9A). However, the FOXO1 Ser^{249} phosphorylation was not reduced in Cdk2-deficient fibroblasts (fig. S9, B and C) (9), which suggests that endogenous Cdk2 may not be uniquely required for the FOXO1 Ser^{249} phosphorylation in proliferating cells.

To determine the consequences of endogenous FOXO1 Ser^{249} phosphorylation in proliferating cells, we characterized the FOXO1 phosphorylation in distinct phases of the cell cycle in which Cdk1 activity is low (G_0 or G_1) or high (G_2-M) in synchronized DU 145 prostate cancer cells (fig. S10), NIH 3T3 fibroblasts (Fig. 4), and murine embryonic fibroblasts (MEFs) (fig. S11). Endogenous FOXO1 phosphorylation was low in cells enriched for the G_0 or G_1 phase and high in cells enriched for the G_2-M transition of the cell cycle (Fig. 4B and figs. S10B, S11B, and S12). These findings suggest that phosphorylation of endogenous FOXO1 at Ser^{249} coincides with endogenous Cdk1 activity in the cell cycle.

We assessed the effect of phosphorylation of endogenous FOXO1 at Ser^{249} on the subcellular localization of FOXO1 in proliferating cells. In subcellular fractionation assays, endogenous FOXO1 and Ser^{249}-phosphorylated FOXO1 in particular were associated with the nuclear fraction in G_2-M–enriched cells (Fig. 4C and figs. S10C and S11C). We also assessed the effect of phosphorylation of endogenous FOXO1 at Ser^{249} on FOXO-dependent transcription in proliferating cells. Expression of the FOXO-responsive reporter gene was higher in G_2-M–enriched cells than in G_0/G_1–enriched cells (Fig. 4D and figs. S10D and S11D).

The gene promoter of the mitotic regulator Polo-like kinase (Plk) harbors conserved FOXO binding sites, and Plk transcription is induced by FOXO3 at the G_2-M transition (*11*). We therefore tested whether the gene encoding Plk might represent a direct target of FOXO1 in proliferating cells. Plk mRNA and protein levels were higher at the G_2-M transition than in the G_0/G_1 phase of the cell cycle (Fig. 4, B and E, and figs. S10, B and E, and S11, B and E). In addition, FOXO1 occupied the Plk gene promoter at G_2-M but not at G_0/G_1 (Fig. 4F and fig. S10F). FOXO RNAi reduced endogenous Plk levels in cells (Fig. 4G). Expression of the RNAi-resistant FOXO1-Res, but not FOXO1-ResS249A, restored Plk expression in cells in the background of FOXO RNAi (Fig. 4H and fig. S13). These results suggest that the gene encoding Plk represents a G_2-M–specific target gene of Ser^{249}-phosphorylated FOXO1 in proliferating cells.

Our study reveals an intimate and conserved signaling link between the protein kinase Cdk1 and the transcription factor FOXO1. Cdk1 phosphorylates FOXO1 at Ser^{249} and thereby disrupts FOXO1's interaction with 14-3-3 proteins, driving FOXO1 into the nucleus to activate a cell death program of gene expression in neurons. Cdk1-FOXO1 signaling also operates at the G_2-M transition of the cell cycle in proliferating cells and thereby stimulates the expression of the mitotic regulator Plk. The Cdk1-FOXO1 signaling pathway may thus have diverse functions in cellular homeostasis, including regulation of neuronal death and degeneration in brain development and disease.

References and Notes

1. Y. Kanoshi, M. Lehtinen, N. Donovan, A. Bonni, *Mol. Cell* **9**, 1005 (2002).
2. E. B. Becker, A. Bonni, *Prog. Neurobiol.* **72**, 1 (2004).
3. M. Kurita, T. Kuwajima, T. Nishimura, K. Yoshikawa, *J. Neurosci.* **26**, 12003 (2006).
4. V. Khurana *et al.*, *Curr. Biol.* **16**, 230 (2006).
5. I. Vincent, G. Jicha, M. Rosado, D. W. Dickson, *J. Neurosci.* **17**, 3588 (1997).
6. J. Busser, D. S. Geldmacher, K. Herrup, *J. Neurosci.* **18**, 2801 (1998).
7. L. P. Van Der Heide, M. F. Hoekman, M. P. Smidt, *Biochem. J.* **380**, 297 (2004).
8. B. M. Burgering, G. J. Kops, *Trends Biochem. Sci.* **27**, 352 (2002).
9. See supporting material on *Science* Online.
10. H. Huang, K. M. Regan, Z. Lou, J. Chen, D. J. Tindall, *Science* **314**, 294 (2006).
11. B. Alvarez, A. C. Martinez, B. M. Burgering, A. C. Carrera, *Nature* **413**, 744 (2001).

12. We thank J. W. Harper, S. Puram, and other members of the Bonni laboratory for helpful discussions and critical reading of the manuscript. Supported by a pilot grant from the Paul Glenn Laboratories (A.B.), NIH grant NS047188 (A.B.), and a Uehara Memorial Foundation fellowship (T.Y.).

Supporting Online Material

www.sciencemag.org/cgi/content/full/319/5870/1665/DC1
Materials and Methods
SOM Text
Figs. S1 to S13
References

30 October 2007; accepted 21 February 2008
10.1126/science.1152337

TDP-43 Mutations in Familial and Sporadic Amyotrophic Lateral Sclerosis

Jemeen Sreedharan,[1,*] Ian P. Blair,[3,4,*] Vineeta B. Tripathi,[1,*] Xun Hu,[1] Caroline Vance,[1] Boris Rogelj,[1] Steven Ackerley,[1,2] Jennifer C. Durnall,[3] Kelly L. Williams,[3] Emanuele Buratti,[5] Francisco Baralle,[5] Jacqueline de Belleroche,[6] J. Douglas Mitchell,[7] P. Nigel Leigh,[1] Ammar Al-Chalabi,[1] Christopher C. Miller,[1,2] Garth Nicholson,[3,4,8] Christopher E. Shaw[1,†]

Amyotrophic lateral sclerosis (ALS) is a fatal motor neuron disorder characterized pathologically by ubiquitinated TAR DNA binding protein (TDP-43) inclusions. The function of TDP-43 in the nervous system is uncertain, and a mechanistic role in neurodegeneration remains speculative. We identified neighboring mutations in a highly conserved region of *TARDBP* in sporadic and familial ALS cases. $TARDBP_{M337V}$ segregated with disease within one kindred and a genome-wide scan confirmed that linkage was restricted to chromosome 1p36, which contains the *TARDBP* locus. Mutant forms of TDP-43 fragmented in vitro more readily than wild type and, in vivo, caused neural apoptosis and developmental delay in the chick embryo. Our evidence suggests a pathophysiological link between TDP-43 and ALS.

Amyotrophic lateral sclerosis (ALS, also known as Lou Gehrig's disease) is a relentlessly progressive and ultimately fatal adult-onset disorder characterized pathologically by the degeneration of motor neurons in the brain and spinal cord (*1*). ALS is familial in 5 to 10% of cases (FALS) with an autosomal dominant pattern of inheritance. Mutations in CuZn superoxide dismutase (*SOD1*) are known to cause ALS, and are detected in ~20% of FALS and 3% of sporadic ALS (SALS) cases (*2*, *3*). Mice transgenic for mutant human *SOD1* develop selective motor neuron degeneration because of a toxic gain of function (*4*). Pure FALS kindreds have been linked to chromosome 18q (*5*), 16q (*6*), and 20p (*7*). Other dominant kindreds that have a phenotypic spectrum ranging from pure ALS to pure frontotemporal lobar dementia (FTLD) and individuals who have features of both disorders have been linked to chromosome 9p and 9q (*8*–*10*), but no pathogenic mutations have been identified in these kindreds.

The presence of ubiquitinated inclusions (Ubis) in the perikaryon and proximal axon of surviving spinal motor neurons is the pathological hallmark of ALS and indicates a failure of the proteasome to recycle damaged proteins (*11*). Ubis are also prominent in cortical neurons within the frontal and temporal lobes in patients with tau-negative frontotemporal lobar dementia (FTLD-U). Many individuals who present with a pure ALS phenotype will have pathological features of FTLD-U and vice versa, which also provides a circumstantial link between FTLD and ALS (*12*). The TAR DNA binding protein (TDP-43) is the major protein in Ubis in FTLD-U and ALS (*13*, *14*). A phosphorylated 25-kD C-terminal fragment of TDP-43 and high-molecular-mass ubiquitinated aggregates are enriched in detergent-resistant fractions of FTLD-U and ALS brains. It is noteworthy that those neurons with cytoplasmic inclusions have a substantial loss of nuclear TDP-43, which raises the possibility that cleavage of full-

length TDP-43 and cytoplasmic sequestration might play a mechanistic role in neurodegeneration. TDP-43 inclusions are seen in glia and its deposition has been observed in many different neurodegenerative disorders (*15*–*18*); however claims of a pathophysiological role for TDP-43 aggregation in ALS have been challenged (*19*).

To investigate the role of TDP-43 in ALS pathogenesis we screened 54 index FALS cases for mutations in *TARDBP*, the gene encoding TDP-43 (*20*). *SOD1*, *VAPB*, *ANG*, *Dynactin*, and *CHMP2B* mutations had been excluded from these cases. We identified a missense mutation in exon 6 of *TARDBP* in the index case from kindred ALS85 (Fig. 1A), a Caucasian family of English descent. The mutation is predicted to result in substitution of valine for methionine at codon 337 (M337V) (*21*) and resides in a strongly phylogenetically conserved region of TDP-43 (Fig. 1C). The mutation segregated with disease and was present in four other affected individuals in three branches and two generations of the extended kindred and was absent from nine unaffected siblings.

Family ALS85 demonstrated autosomal dominant inheritance with male-to-male transmission apparent. Four of five affected individuals had definite ALS by the El Escorial criteria (*22*), and another recently symptomatic individual had probable ALS. Three had limb-onset ALS, and two had bulbar-onset ALS. The mean age of symptom onset was 47 years (range 44 to 52). Mean disease duration was 5.5 years (range 4 to 7) from symptom onset to death. The obligate carrier (who died aged 54 from severe coronary atheroma) was reported by family members to have had gait disturbance and declining upper limb strength consistent with ALS. There was no history of dementia or any atypical features in the kindred.

We next conducted a genome-wide scan in this kindred. DNA was available from 23 members of the kindred, including 5 affected individuals (4 males and 1 female). By analysis of single-nucleotide polymorphism (SNP) genotypes, we identified linkage to chromosome 1p36, which contains the *TARDBP* locus, with a parametric multipoint logarithm of the odds ratio for linkage (lod) score of 2.04 (Fig. 2A). Fine mapping across the region with microsatellite markers confirmed linkage with a maximal two-point lod score of 2.73 at D1S450 (table S1) and a highly significant multipoint lod score of 2.93 (Fig. 2B). These lod scores approach the simulated maximum power to detect linkage in this kindred (simulated maximal lod score of 2.98). Only one other locus on chromosome 15 generated a lod score of >1 (fig. S1), but fine mapping with microsatellite markers confidently excluded linkage to this region (table S1). Analysis of the microsatellite markers spanning the chromosome 1p36 region revealed a clear haplotype that segregated with the mutation and disease (Fig. 2C). Recombinant events in two unaffected individuals (II.4 and II.8) defined the telomeric limit as D1S2795. Recombination in one affected individual (III.8) defined the centromeric limit as D1S228. This linked region spanning 16.5 cM (~8.2 Mb) contains 97 genes in total including *TARDBP* and the 1009 A>G mutation.

We next sought to determine the frequency of TDP-43 mutations by sequencing all six exons in a cohort of 200 British SALS cases. We identified a missense mutation in exon 6 (991 C>A) which is 18 base pairs upstream of the familial mutation and predicted to be a substitution of lysine for glutamine (Q331K) (Fig. 1B). This mutation was found in a man who developed limb-onset ALS at age 72 with a disease duration of 3 years. No mutations were detected in a screen of all six exons of *TARDBP* from 90 British Caucasian controls, which emphasizes the high degree of evolutionary conservation seen. Because Q331K and M337V are unlikely to be benign polymorphisms, we proceeded to study the functional effect of these two mutations.

We screened all six exons of *TARDBP* in two further cohorts: 172 Australian Caucasian SALS cases and 172 controls, as well as 200 British Caucasian controls. A further mutation was detected in exon 6 in an Australian SALS case (881 G>C); the mutation was predicted to be a substitution of alanine for glycine (G294A) (Fig. 1B). The patient was a man who developed limb onset ALS at age 65, with a disease duration of 5 years and no atypical features. One nonsynonymous change in a single control was identified in exon 3 (269 C>T), predicted to be a substitution of valine for alanine (A90V) (fig. S2). This individual was a healthy 53-year-old Caucasian male. Last, we sequenced exon 6 of *TARDBP* in an additional 390 British and Australian Caucasian controls and found no mutations. Mutations were detected in exon 6 in 3 out of 526 ALS cases and 0 out of 1262 controls ($P = 0.025$ by Fischer's exact test).

In order to assess the functional significance of these mutations, we expressed tagged TDP-43_{WT}, TDP-43_{Q331K}, and TDP-43_{M337V} in Chinese hamster ovary (CHO) cells. Immunofluorescent staining of cells 48 hours after transfection demonstrated abundant expression of transfected TDP-43. No obvious differences in subcellular distribution or aggregation were observed between wild-type and mutant proteins. Using the lactate dehydrogenase (LDH) assay, we saw no significant increase in cell death in CHO cells transfected with either TDP-43 mutant when compared with wild type. Probing immunoblots of the cytoplasmic fraction for the N-terminal Myc tag revealed numerous fragments varying in molecular weight from ~14 to ~45 kD (Fig. 3A). Quantitative analysis of the most prominent bands demonstrated a nonsignificant increase in the 14-kD band in the mutants and a

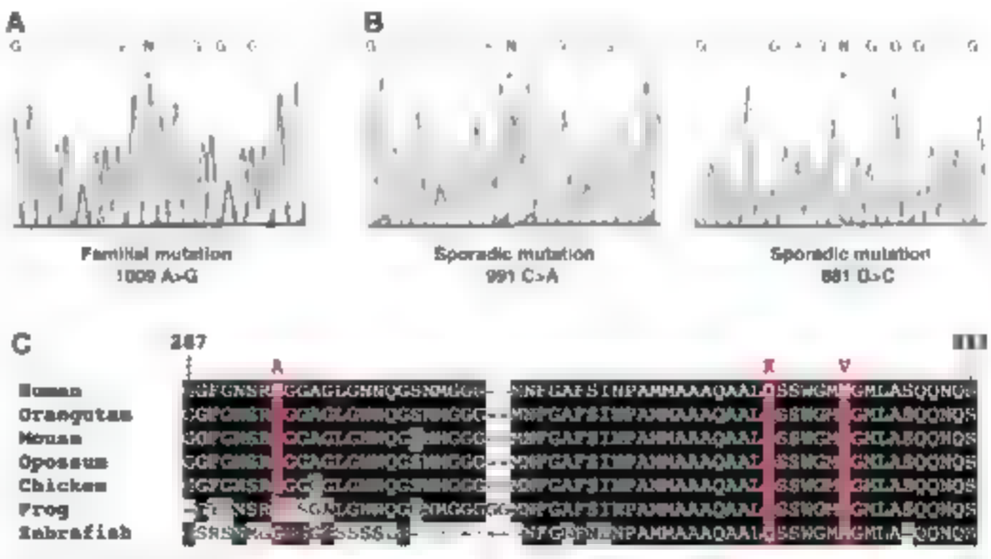

Fig. 1. Identification of three missense mutations in exon 6 of *TARDBP*. (**A**) DNA sequence demonstrating a single base substitution (asterisk) changing the wild-type adenine at 1009 to guanine, valine substituting for methionine (M337V). (**B**) Two additional mutations were found in sporadic ALS cases: 991 C>A, lysine substituted for glutamine (Q331K); and 881 G>C, alanine substituted for glycine (G294A). (**C**) A sequence alignment of amino acids 287 to 347 of TDP43 from diverse vertebrate species is shown. Identical amino acids have a black background, similar amino acids are gray, and mutation sites are red.

[1]Department of Clinical Neuroscience, King's College London, Medical Research Council (MRC) Centre for Neurodegeneration Research, and Institute of Psychiatry, London, SE5 8AF, UK. [2]Department of Neuroscience, King's College London, MRC Centre for Neurodegeneration Research, and Institute of Psychiatry, London, SE5 8AF, UK. [3]Northcott Neuroscience Laboratory, Australian and New Zealand Army Corps (ANZAC) Research Institute, Concord, NSW, 2137, Australia. [4]Faculty of Medicine, University of Sydney, Sydney, NSW, 2139, Australia. [5]International Centre for Genetic Engineering and Biotechnology, Padriciano 99, 34012 Trieste, Italy. [6]Division of Neurosciences and Mental Health, Faculty of Medicine, Imperial College London, and Charing Cross Hospital, London, W6 8RF, UK. [7]Department of Neurology, Royal Preston Hospital, Preston, PR2 9HT, UK. [8]Molecular Medicine Laboratory, Concord Repatriation General Hospital, Concord, NSW, 2139, Australia.

*These authors contributed equally to this work.
†To whom correspondence should be addressed. E-mail: chris.shaw@iop.kcl.ac.uk

significant increase in the 18-kD band when compared with wild-type TDP-43 (Fig. 3B, WT versus Q331K, $P < 0.01$ and WT versus M337V $P < 0.05$).

We next investigated the effects of TDP-43 mutants in chick embryos. This model allows DNA to be efficiently delivered directly into the neural tube by electroporation, which permits in vivo analysis of neural tissue expressing transfected genes (23). We expressed tagged TDP-43_{WT}, TDP-43_{Q331K}, and TDP-43_{M337V} in the spinal cords of Hamburger Hamilton (HH) stage 14 chick embryos (Fig. 4, D to F). $SOD1_{WT}$ and the ALS-linked $SOD1_{G93A}$ mutant were used as controls. Embryos expressing TDP-43_{Q331K} and TDP-43_{M337V} showed a dramatic reduction in maturation compared with TDP-43_{WT}, with a failure to develop normal limb and tail buds (Fig. 4, A to C). Chick embryo development proceeded normally over 48 hours with TDP-43_{WT}, $SOD1_{WT}$, and $SOD1_{G93A}$ but at 24 hours only 5 to 15% of those embryos expressing mutant TDP-43 had reached the normal stage of maturation (Fig. 4J, $P < 10^{-4}$). Terminal deoxynucleotidyl transferase mediated deoxyuridine triphosphate biotin nick end labeling (TUNEL) staining demonstrated a significant increase in

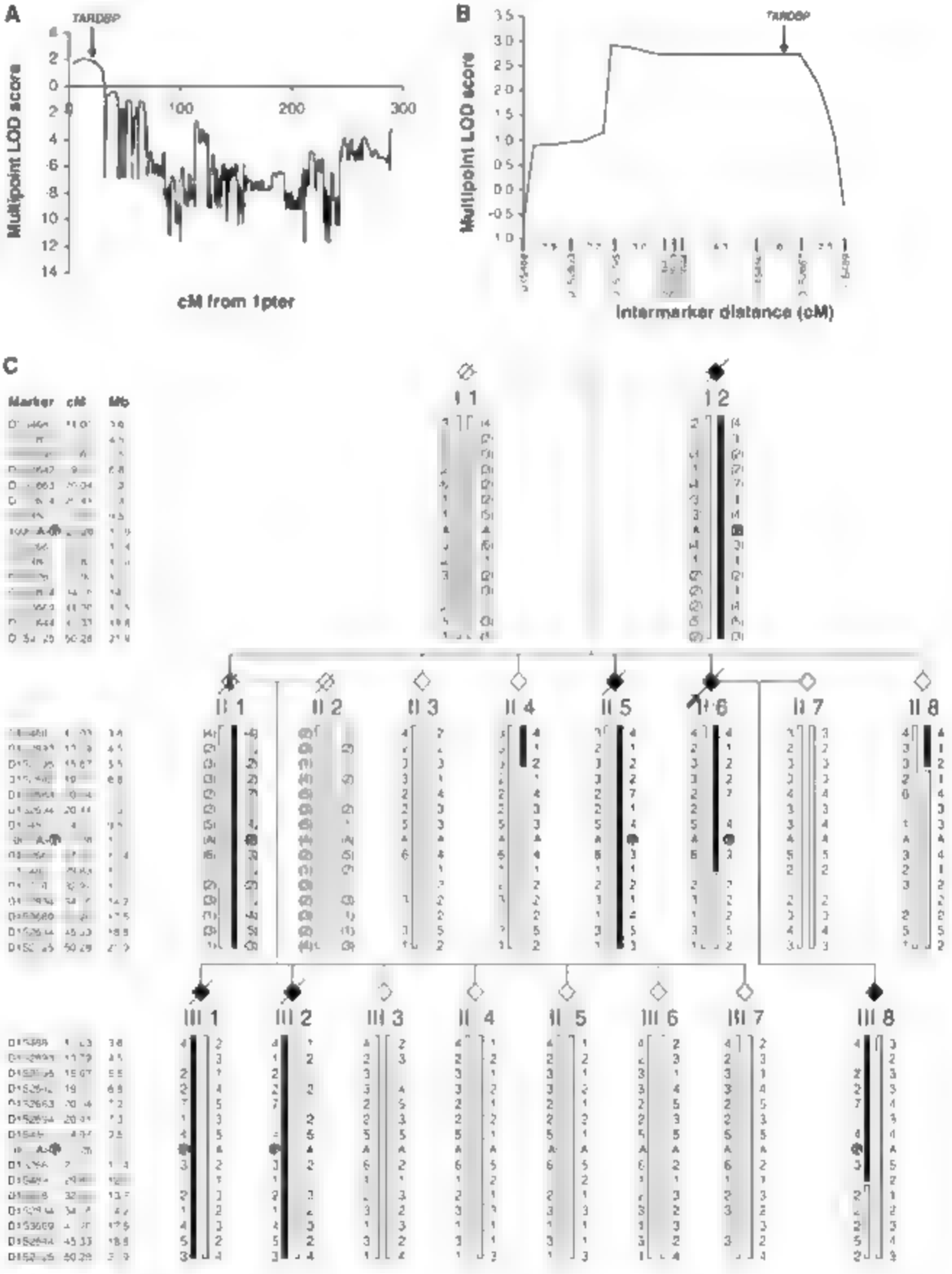

Fig. 2. Mutation in *TARDBP* cosegregates with disease in kindred ALS85. (**A**) Linkage analysis of Affymetrix 10K SNP array data demonstrated linkage to chromosome 1p36. (**B**) Linkage to the region containing *TARDBP* was confirmed by using microsatellite markers. (**C**) The ALS85 pedigree is shown. Affected individuals are indicated by black symbols. The proband is indicated by the arrow. Unaffected individuals have open symbols. II:1 (vertical bar) was an obligate carrier with an anecdotal history of ALS. Slashed symbols indicate deceased subjects. Gender has been omitted for confidentiality. Microsatellite markers are shown in chromosomal order, with their genetic and physical locations. Genotypes for each individual are given with inferred genotypes in parentheses. The haplotype segregating with disease is indicated by the black bar. The 1009 A>G *TARDBP* mutation is indicated by a white "G" on a black background.

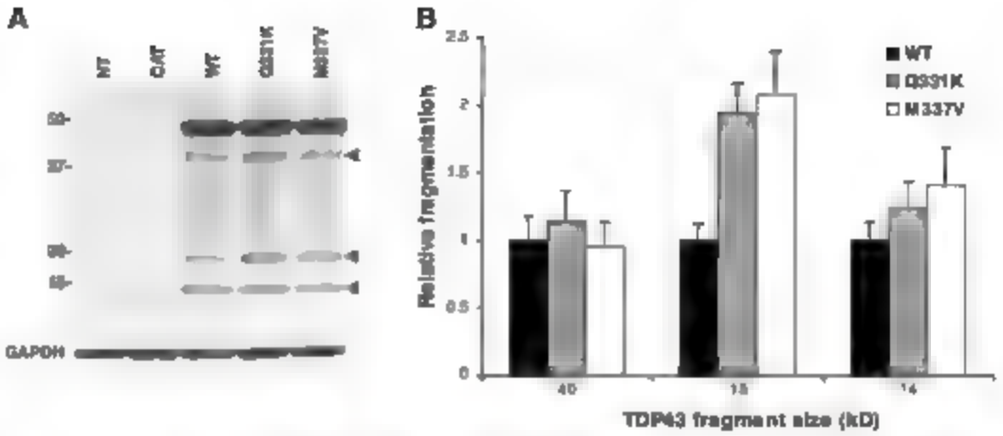

Fig. 3. Immunoblots of cytoplasmic fractions from CHO cells transiently transfected with wild-type and mutant TDP-43. (**A**) Probing for the N-terminal Myc tag shows numerous fragments that were absent in controls (NT, nontransfected, and CAT chloramphenicol acetyl transferase–transfected). The dominant bands were at 40, 18, and 14 kD. (**B**) Quantitative analysis of Myc-immunoreactive bands. Densitometry of bands was conducted using Odyssey. Results are means ± SEM for eight experiments.

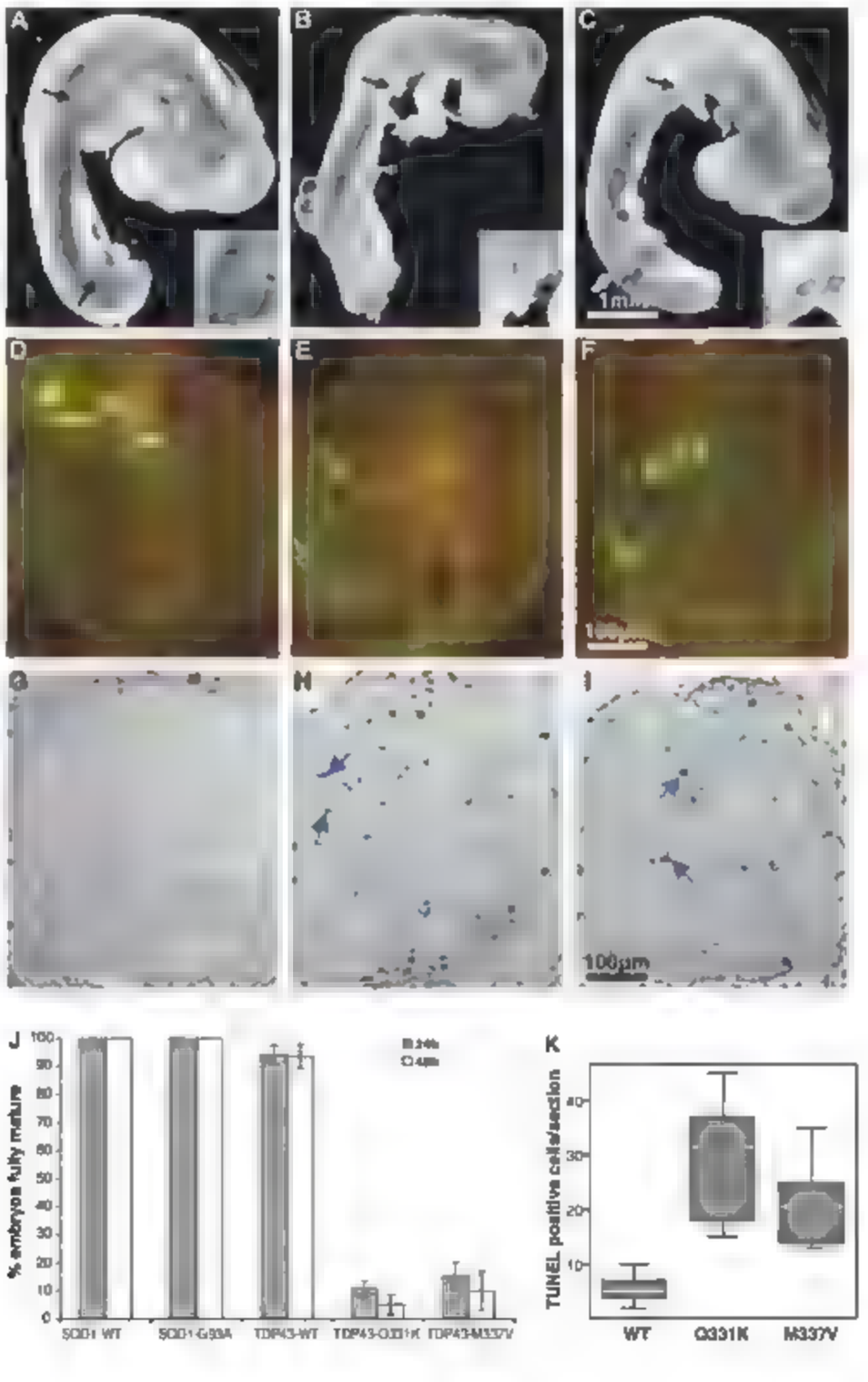

Fig. 4. Mutant TDP-43 causes chick embryonic developmental delay. Chick embryo spinal cords were transfected with plasmids encoding wild-type TDP-43 (**A**, **D**, and **G**); mutant Q331K (**B**, **E**, and **H**); or M337V (**C**, **F**, and **I**). Embryo images and sections shown were taken 24 hours post electroporation. Embryos expressing $TDP43_{WT}$ developed normal limb (black arrows) and tail buds (**A**); those expressing mutant TDP-43 did not (**B** and **C**). Magnified images of upper limb buds are shown in insets. (**D**) to (**F**) Transverse sections of chick spinal cord double-stained with hemagglutinin (HA)–specific (green) and Myc-specific (red) antibodies to the tags on transfected TDP-43 constructs. Unilateral TDP-43 construct expression in spinal cord neural cells occurs after embryo electroporation. The majority of the cells in the transfected region have the characteristic phenotype of neuroepithelial cells. (**G**) to (**I**) TUNEL staining of sections shown in (**D**) to (**F**) demonstrates apoptotic nuclei (blue arrows). (**J**) The percentage of embryos that matured normally (reached HH stage 15 or 17 after 24 hours and 48 hours, respectively) is shown. Data were generated from analysis of 49 embryos in each treatment group. (**K**) Quantification of apoptosis. TUNEL-positive cells in five sections per embryo (two embryos per transfection) were counted.

the number of apoptotic nuclei in embryos expressing either mutant TDP-43 when compared with wild type (Fig. 4, G to I and K, $P < 0.0001$). These results suggest a toxic gain of function or dominant negative effect of mutant TDP-43.

TDP-43 is a ubiquitously expressed nuclear protein capable of binding DNA and RNA, which regulates transcription and splicing but may also be involved in microRNA biogenesis, apoptosis and cell division (*24*). The C-terminal domain binds heterogeneous ribonuclear proteins and inhibits splicing of the cystic fibrosis transmembrane conductance regulator mRNA (*25*). The accumulation of hyperphosphorylated TDP-43 fragments in the perikaryon of neurons in FTLD-U and ALS is accompanied by a substantial loss of TDP-43 from the nucleus (*13, 14*). The sequestration of TDP-43 would be predicted to disrupt the regulation of transcription and splicing, which may account for the 1.5-fold increase in TDP-43 mRNA seen in FTLD-U brains (*26*). The identification of TDP-43 mutations that result in increased fragmentation and toxicity to neural cells strongly supports a pathophysiological role for TDP-43 misaccumulation in ALS. Robust linkage to the *TARDBP* locus in kindred ALS84 adds crucial evidence that the M337V mutation is pathogenic.

The G294A, Q331K, and M337V mutations are all localized to a highly conserved region of the C terminus of TDP-43 known to be involved in protein-protein interactions (*25*). The Q331K mutation in particular creates a new protein kinase A site, which may result in abnormal phosphorylation. The G294A mutation interrupts a glycine-rich motif characteristic of all heterogeneous nuclear ribonucleoproteins and may interfere with RNA binding and gene suppression (*27*).

Three other studies have failed to identify *TARDBP* mutations in FTLD and ALS (*28–30*). Our findings suggest that although mutations are rare they may be pathogenically linked to ALS. Parallels exist with other neurodegenerative disorders where the identification of rare familial mutations in the β-amyloid precursor protein in Alzheimer's disease and α-synuclein in Parkinson's disease has dramatically advanced studies into the pathogenesis of a predominantly sporadic disease. Elucidating the biochemical processes responsible for the increased fragmentation of TDP-43 and its toxicity to neural tissues may provide important insights into disease mechanisms that underlie ALS.

References and Notes

1. C. E. Shaw, A. Al-Chalabi, N. Leigh, *Curr. Neurol. Neurosci. Rep.* **1**, 69 (2001).
2. D. R. Rosen *et al.*, *Nature* **362**, 59 (1993).
3. C. E. Shaw *et al.*, *Neurology* **49**, 1612 (1997).
4. M. E. Gurney *et al.*, *Science* **264**, 1772 (1994).
5. S. Hadano *et al.*, *Nat. Genet.* **29**, 166 (2001).
6. D. M. Ruddy *et al.*, *Am. J. Hum. Genet.* **73**, 390 (2003).
7. P. C. Sapp *et al.*, *Am. J. Hum. Genet.* **73**, 397 (2003).
8. B. A. Hosler *et al.*, *JAMA* **284**, 1664 (2000).
9. C. Vance *et al.*, *Brain* **129**, 868 (2006).
10. M. Morita *et al.*, *Neurology* **66**, 839 (2006).
11. P. N. Leigh *et al.*, *Brain* **114**, 775 (1991).
12. A. M. Lipton, C. L. White III, E. H. Bigio, *Acta Neuropathol. (Berlin)* **108**, 379 (2004).
13. M. Neumann *et al.*, *Science* **314**, 130 (2006).
14. T. Arai *et al.*, *Biochem. Biophys. Res. Commun.* **351**, 602 (2006).
15. C. Amador-Ortiz *et al.*, *Ann. Neurol.* **61**, 435 (2007).
16. M. Hasegawa *et al.*, *Brain* **130**, 1386 (2007).
17. H. Nakashima-Yasuda *et al.*, *Acta Neuropathol. (Berlin)* **114**, 221 (2007).
18. S. H. Freeman, T. Spurlock-Jones, B. T. Hyman, J. H. Growdon, M. P. Frosch, *J. Neuropathol. Exp. Neurol.* **67**, 62 (2008).
19. J. D. Rothstein, *Ann. Neurol.* **63**, 382 (2007).
20. Materials and methods are available as supporting material on *Science* Online.
21. Single letter abbreviations for the amino acid residues are as follows: A, Ala; C, Cys; D, Asp; E, Glu; F, Phe; G, Gly; H, His; I, Ile; K, Lys; L, Leu; M, Met; N, Asn; P, Pro; Q, Gln; R, Arg; S, Ser; T, Thr; V, Val; W, Trp, and Y, Tyr.
22. B. R. Brooks, R. G. Miller, M. Swash, T. L. Munsat, *Amyotroph. Lateral Scler. Other Motor Neuron Disord.* **1**, 293 (2000).
23. G. D. Ghadge *et al.*, *Neurobiol. Dis.* **21**, 194 (2006).
24. E. Buratti, F. E. Baralle, *Front. Biosci.* **13**, 867 (2008).
25. E. Buratti *et al.*, *J. Biol. Chem.* **280**, 37572 (2005).
26. M. Mishra *et al.*, *Acta Neuropathol. (Berlin)* **114**, 81 (2007).
27. M. M. Abhyankar, C. Urekar, P. P. Reddi, *J. Biol. Chem.* **282**, 36143 (2007).
28. S. Rollinson *et al.*, *Neurosci. Lett.* **419**, 1 (2007).
29. A. Schumacher *et al.*, *Neurobiol. Aging*, published online 3 July 2007 10.1016/j.neurobiolaging.2007.05.022 in press.
30. I. Gijselinck *et al.*, *Neurobiol. Aging*, published online 3 July 2007 10.1016/j.neurobiolaging.2007.11.002 in press.

31. This publication is dedicated to the memory of Steven Ackerley, an outstanding young scientist. We thank the patients and families who have contributed to this project and to B. Coote, C. Cecere, J. Gardham, the MRC Neurodegenerative Diseases Brain Bank and the Australian Motor Neurone Disease (MND) DNA Bank for assistance in sample collection. This work was supported by grants from The Wellcome Trust, European Union contract LSHM-CT 2003 503330 (APOPIS); American ALS Association, Motor Neurone Disease Association, UK Medical Research Council, UK, the Middlemass family, Jack Cigman, King's College Hospital Charity, the Psychiatry Research Trust of the Institute of Psychiatry, and the Motor Neurone Disease Research Institute of Australia (MNDRIA).

Supporting Online Material

www.sciencemag.org/cgi/content/full/1154584/DC1
Materials and Methods
SOM Text
Figs. S1 to S4
Tables S1 to S3
References

26 December 2007; accepted 19 February 2008
Published online 28 February 2008;
10.1126/science.1154584
Include this information when citing this paper.

A Nitric Oxide–Inducible Lactate Dehydrogenase Enables *Staphylococcus aureus* to Resist Innate Immunity

Anthony R. Richardson,[1] Stephen J. Libby,[1] Ferric C. Fang[1,2]*

Staphylococcus aureus is one of the most successful human pathogens, colonizing 2 billion individuals worldwide and causing invasive infections even in immunocompetent hosts. *S. aureus* can evade multiple components of host innate immunity, including the antimicrobial radical nitric oxide ($NO^{\bullet}$) produced by activated phagocytes. We show that *S. aureus* is capable of metabolically adapting to nitrosative stress by expressing an $NO^{\bullet}$-inducible L-lactate dehydrogenase (*ldh1*, SACOL0222) divergently transcribed from the $NO^{\bullet}$-detoxifying flavohemoglobin (*hmp*). L-Lactate production allows *S. aureus* to maintain redox homeostasis during nitrosative stress and is essential for virulence. $NO^{\bullet}$-inducible lactate dehydrogenase activity and $NO^{\bullet}$ resistance distinguish *S. aureus* from the closely related commensal species *S. epidermidis* and *S. saprophyticus*.

Enzymatic generation of radical nitric oxide ($NO^{\bullet}$) by NO synthase is one of the most broad-spectrum mechanisms of host resistance to pathogenic microorganisms (*1*). $NO^{\bullet}$ synthesis is observed in patients with staphylococcal infections (*2*), and *S. aureus* stimulates $NO^{\bullet}$ production by human phagocytes (*3*). Moreover, high $NO^{\bullet}$ concentrations are found in the nasopharynx (*4*), the primary site of *S. aureus* colonization. $NO^{\bullet}$ and its congeners can modify a variety of cellular targets, including heme and nonheme iron, protein thiols, tyrosine residues, lipids, and DNA (*5–9*). Despite the abundance of potential $NO^{\bullet}$ targets, *S. aureus* is able to resist the antimicrobial actions of $NO^{\bullet}$ through a coordinated nitrosative stress response that includes the Hmp flavohemoglobin and enzymes involved in hypoxic or anaerobic metabolism (*10*). Mutant strains lacking a two-component regulatory system, SrrAB, which controls the transition to hypoxic anaerobic metabolism, are extremely sensitive to nitrosative stress (*10*).

The ability to replicate in the presence of $NO^{\bullet}$ distinguishes *S. aureus* from many other bacterial pathogens (fig. S1), including the commensal species *S. epidermidis* and *S. saprophyticus* (Fig.

[1]Department of Laboratory Medicine, University of Washington, Seattle, WA 98195, USA. [2]Department of Microbiology, University of Washington, Seattle, WA 98195, USA.
*To whom correspondence should be addressed. E-mail: fcfang@u.washington.edu

1A). $NO^{\bullet}$ resistance is a general trait of *S. aureus* observed in methicillin-susceptible (MSSA) and methicillin-resistant (MRSA) clinical isolates from both hospital and community-acquired (CA-MRSA) settings (Fig. 1A).

To gain insights into the metabolic state of *S. aureus* growing under nitrosative stress, we assessed end-product excretion for 4 hours after exogenous $NO^{\bullet}$ treatment. Under aerobic conditions, *S. aureus* primarily excreted acetate, whereas fermenting cells produced a mixture of mainly L-lactate, ethanol, and formate (Fig. 1B). However, upon $NO^{\bullet}$ exposure, respiring cells ceased acetate production and fermenting cells no longer excreted measurable amounts of ethanol or formate (Fig. 1B). Moreover, $NO^{\bullet}$ exposure resulted in almost exclusive production of L-lactate from both respiring and fermenting *S. aureus* (Fig. 1B), which suggests that nitrosative stress restricts available glucose catabolic pathways. These results are consistent with increased lactate dehydrogenase gene expression observed in *S. aureus* exposed to $NO^{\bullet}$ or anaerobiosis (Fig. 1C) (*10*, *11*). Interestingly, although both *S. epidermidis* and *S. saprophyticus* exhibited increased lactate dehydrogenase activity under anaerobic conditions, neither species displayed lactate dehydrogenase activity after treatment with $NO^{\bullet}$ (Fig. 1C). Thus, $NO^{\bullet}$-inducible lactate dehydrogenase activity is specific to *S. aureus* and correlates with the ability to replicate during nitrosative stress (Fig. 1, A and C).

$NO^{\bullet}$ can inhibit aerobic respiration by competitively binding to cytochrome hemes of the terminal oxidases (*12*). Indeed, exposure of *S. aureus* to $NO^{\bullet}$ completely inhibited oxygen consumption until Hmp-mediated scavenging lowered $NO^{\bullet}$ to submicromolar levels (Fig. 2A). Therefore, reducing equivalents generated from glucose oxidation during nitrosative stress must be handled in a respiration-independent manner, as occurs by the reduction of pyruvate to lactate (Fig. 1D). Although $NO^{\bullet}$-dependent inhibition of respiration poses a redox stress leading to increased L-lactate excretion, this cannot account for the absence of acetate production during nitrosative stress. To investigate this phenomenon, we determined enzyme activities in cell-free extracts in the presence or absence of increasing $NO^{\bullet}$ concentrations (Fig. 2B). Both L- and D-lactate dehydrogenase activities were found to be resistant to $NO^{\bullet}$, but pyruvate dehydrogenase (PDH) activity was extremely $NO^{\bullet}$-sensitive. Inhibition of PDH limits the generation of acetyl coenzyme A (CoA), thereby restricting acetate production (Fig. 1D). Thus, in addition to overcoming the redox stress created by impaired respiration, $NO^{\bullet}$-treated *S. aureus* must adapt to a lower overall adenosine triphosphate (ATP) yield.

In glucose-fermenting *S. aureus*, pyruvate can serve as an electron acceptor, generating lactate from three different lactate dehydrogenases (Fig. 1D). Acetyl-CoA production proceeds via the pyruvate formate-lyase (PFL) reaction, which converts pyruvate to formate rather than CO_2 and thus does not consume oxidized nicotinamide adenine dinucleotide (NAD^+) (Fig. 1D). Excess acetyl-CoA is converted to ethanol by an iron-containing alcohol dehydrogenase (ADH), regenerating twice as much oxidizing power as lactate production (Fig. 1D). The tendency of fermenting cells to forgo the additional ATP yield from acetate production in favor of NAD^+-generating ethanol synthesis underscores the importance of redox balance in nonrespiring cells (Fig. 1, B and D). PFL is inhibited at physiologically relevant $NO^{\bullet}$ concentrations (Fig. 2B), thereby limiting acetyl-CoA production and accounting for the absence of ethanol excretion despite the $NO^{\bullet}$ resistance of ADH (Fig. 1B and Fig. 2B). By limiting ethanol production, $NO^{\bullet}$

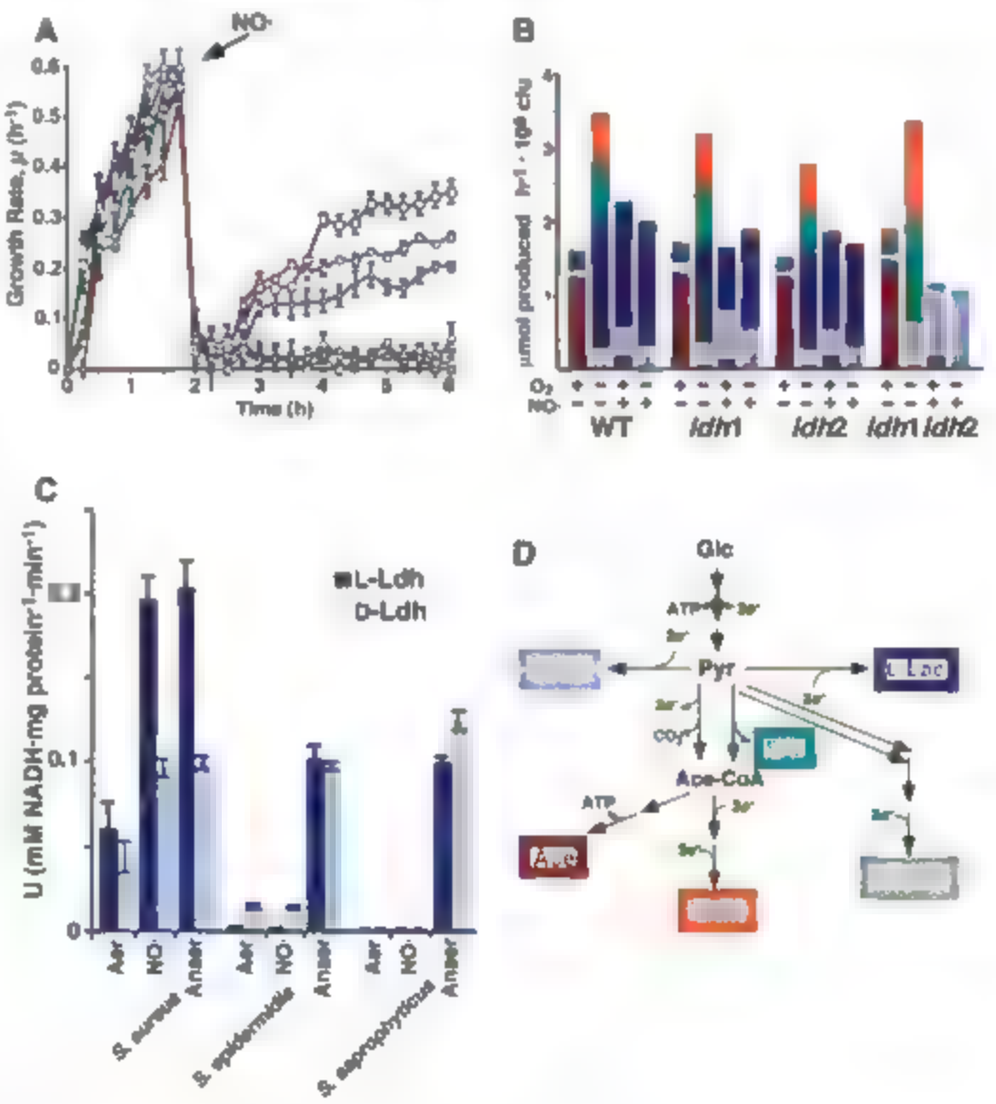

Fig. 1. Metabolic adaptation of *S. aureus* to nitrosative stress. (**A**) Growth rate μ ($hour^{-1}$) of *S. aureus* strains COL (blue circles), Newman (blue diamonds), and MW2 (blue squares); *S. epidermidis* strains 6293 (cyan circles) and 6903 (cyan diamonds); and *S. saprophyticus* strains C1L3 (red circles) and C1L4 (red diamonds) in PN medium (*10*) after $NO^{\bullet}$ exposure. (**B**) Metabolite excretion profile of *S. aureus* COL and derivatives grown in PN medium aerobically ($+O_2$) or anaerobically ($-O_2$) in the presence or absence of $NO^{\bullet}$. Data represent average rates of acetate (red), L-lactate (dark blue), D-lactate (light blue), ethanol (orange), or formate (cyan) production ($hour^{-1} \cdot 10^9$ CFU) during 4 hours of $NO^{\bullet}$ stress. (**C**) D- and L-lactate dehydrogenase activity in cell-free extracts from cultures grown in PN medium aerobically (Aer), aerobically with $NO^{\bullet}$, or anaerobically (Anaer). (**D**) Pyruvate metabolism in *S. aureus*. Glucose (Glc) is oxidized to pyruvate (Pyr), which can be converted to D- or L-lactate (D-Lac, L-Lac) or oxidatively decarboxylated, generating CO_2 and acetyl-CoA (Ace-CoA). Acetyl-CoA is converted to acetate (Ace) to generate ATP. Anaerobically, pyruvate can be converted to 2,3-butanediol (2,3-But) or to formate (For) and acetyl-CoA, the latter of which can be reduced to ethanol (EtOH).

eliminates an efficient mechanism of NAD^+ regeneration, forcing fermenting cells to rely on L-lactate dehydrogenase to maintain redox homeostasis (Fig. 1D).

The importance of lactate dehydrogenase activity in maintaining redox homeostasis in both aerobically and anaerobically cultured cells undergoing nitrosative stress is demonstrated by the inability of an *ldh1 ldh2* mutant to maintain a physiological balance of NAD^+ and its reduced form NADH in the presence of $NO^•$ (Fig. 2C). Thus, the $NO^•$-resistant metabolic state achieved by *S. aureus* growing under nitrosative stress requires the induction of L-lactate dehydrogenase activity. Transcript levels of *ldh2* (SACOL2618) were relatively abundant under aerobic growth and were modestly induced by anaerobiosis, but remained unchanged during nitrosative stress (Fig. 2D). In contrast, *ldh1* expression was virtually undetectable in aerobic cultures but predominated upon $NO^•$ exposure (Fig. 2D and fig. S2). Accordingly, inactivation of *ldh1* measurably impaired staphylococcal growth during nitrosative stress in both aerobically and anaerobically cultured cells (Fig. 3A). Both Ldh1 and Ldh2 are resistant to $NO^•$ (fig. S2); thus, constitutive Ldh2 activity can partially compensate for the loss of Ldh1. However, the complete loss of L-lactate production in an *ldh1 ldh2* mutant eliminated the ability of *S. aureus* to grow in the presence of $NO^•$ (Fig. 1B and Fig. 3A). Furthermore, providing the *ldh1* gene in trans significantly enhanced the growth rate of both *ldh1* and *ldh1 ldh2* mutants in the presence of $NO^•$ (Fig. 3B). Collectively, these data show that adaptation to the metabolic constraints imposed by $NO^•$ under both aerobic and hypoxic conditions is critical for *S. aureus* resistance to nitrosative stress. $NO^•$-inducible *ldh1* appears to be primarily responsible for the metabolic adaptation of *S. aureus* to nitrosative stress in vitro and is present in all *S. aureus* genomes sequenced to date.

To determine the importance of $NO^•$ adaptation in staphylococcal pathogenesis, we compared the virulence of wild-type *S. aureus* and isogenic L-lactate dehydrogenase–deficient mutants in a murine sepsis model. Intravenous (iv) injection of C57BL/6 mice with 5×10^7 colony-forming units (CFU) of wild-type *S. aureus* induced arthritic symptoms by day 3, followed by 2 weeks of progressive disease (Fig. 4A). Whereas an *ldh2* mutation alone had no discernible effect on virulence, strains lacking the $NO^•$-inducible *ldh1* gene were measurably attenuated and *ldh1 ldh2* mutants were essentially avirulent (Fig. 4A). Furthermore, the *ldh1* and *ldh1 ldh2* mutant strains exhibited competitive disadvantages (by a factor of 4 and a factor of 67, respectively) when coadministered with wild-type *S. aureus* (Fig. 4A, inset).

Histological examination of infected renal tissue 5 days after inoculation revealed massive abscesses surrounding bacterial microcolonies (Fig. 4B). By day 5, abscesses were significantly larger and more numerous in mice inoculated with wild-type *S. aureus* relative to *ldh1* or *ldh1 ldh2* mutants (Fig. 4B and fig. S4). The reduced mortality, decreased abscess formation, and competitive disadvantage exhibited by the *ldh1*

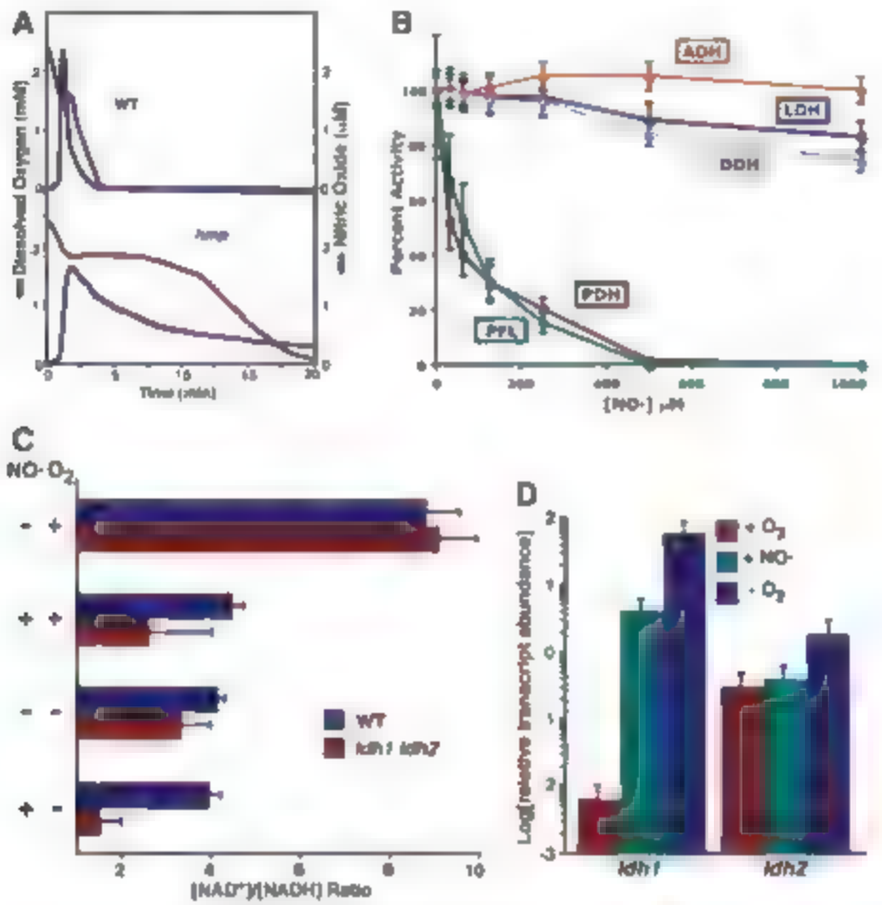

Fig. 2. Physiological consequences of $NO^•$ exposure in *S. aureus*. (**A**) $NO^•$ inhibition of staphylococcal respiration. Oxygen consumption was measured in cell suspensions in sealed vessels as loss of dissolved oxygen (red) by means of a Clark-type electrode. The presence of $NO^•$ (blue) was simultaneously monitored via an $NO^•$-specific probe and was enzymatically scavenged from the cell suspension in a Hmp-dependent manner; compare top trace (wild type, WT) with the bottom trace from *hmp* mutant cells. (**B**) Percent enzyme activity in cell-free extracts as a function of $NO^•$ concentration. PDH, pyruvate dehydrogenase; LDH, L-lactate dehydrogenase; DDH, D-lactate dehydrogenase; ADH, alcohol dehydrogenase; PFL, pyruvate formate lyase. Enzymatic activity assays are described in (*17*) and fig. S3. (**C**) Redox state of cells measured as NAD^+/NADH ratio during aerobic and anaerobic growth in the presence or absence of $NO^•$. Nucleotide extraction and quantification were performed as described in (*17*). (**D**) Transcript levels of *ldh1* and *ldh2* under varying environmental conditions. We used quantitative real-time reverse transcription polymerase chain reaction to compare *ldh1* and *ldh2* transcript levels via a $\Delta\Delta C_t$ algorithm outlined in (*17*). Values represent transcript levels relative to those of *rpoD*, encoding the sigma-70 subunit of RNA polymerase.

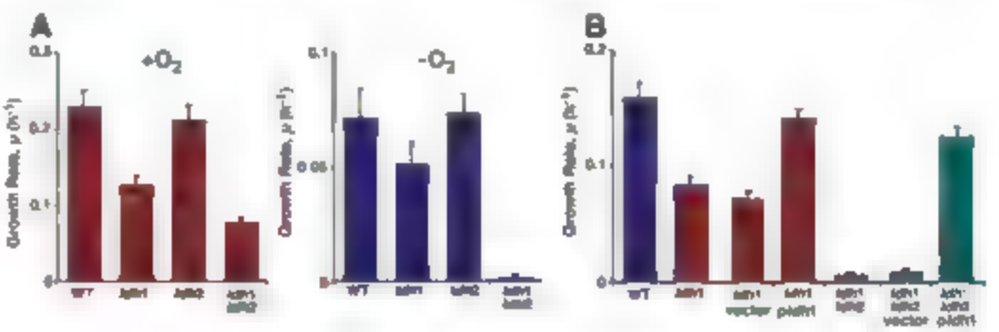

Fig. 3. Role of L-lactate dehydrogenase activity in *S. aureus* $NO^•$ resistance. (**A**) Growth rate μ (hour^{-1}) of *S. aureus* COL and derivatives grown aerobically (left) or anaerobically (right) in PN medium in the presence of $NO^•$. (**B**) Complementation of observed $NO^•$ sensitivity in *ldh1* and *ldh1 ldh2* *S. aureus* Newman, with p*ldh1* harboring the *ldh1* allele from *S. aureus* expressed from its endogenous promoter.

mutant were not apparent in congenic C57BL/6 *iNOS*$^{-/-}$ mice lacking the ability to produce inflammatory NO$^{\bullet}$ (Fig. 4 and fig. S4). Additionally, L-lactate dehydrogenase activity is necessary for *S. aureus* to resist the cytostatic effects of host NO$^{\bullet}$ in cultured murine macrophages (fig. S5). Thus, NO$^{\bullet}$-inducible *ldh1* allows *S. aureus* to evade host-derived NO$^{\bullet}$. Although the attenuation of *ldh1 ldh2* mutants was partially abrogated in *iNOS*$^{-/-}$ mice, virulence was not fully restored (Fig. 4A). Together, these data suggest that an NO$^{\bullet}$ independent requirement for L-lactate dehydrogenase activity during infection can be met by either *ldh1* or *ldh2*, but NO$^{\bullet}$ resistance specifically requires high-level L-lactate dehydrogenase activity provided by *ldh1*.

This work has identified novel enzymatic targets of NO$^{\bullet}$ and provided insights into the metabolic state of *S. aureus* growing in the presence of host-derived NO$^{\bullet}$. NO$^{\bullet}$ inhibits respiration as well as acetyl-CoA generation by PDH and PFL. Although the mechanism by which NO$^{\bullet}$ inhibits PDH and PFL is uncertain, preferential reactivity of NO$^{\bullet}$ with sulfhydryl groups and metals (*13*) suggests several possible molecular targets. The PDH complex requires the sulfhydryl-containing cofactor lipoamide and the coordinate activity of four redox-active thiols to catalyze the oxidative decarboxylation of pyruvate (*14*). PFL is an oxygen-labile enzyme whose active site contains both glycyl and thiyl radical moieties during catalysis (*15*). Moreover, PFL activation requires an additional enzyme, PflA, which contains an iron-sulfur cluster (*16*).

Metabolic adaptation to circumvent NO$^{\bullet}$-mediated cytostasis is essential for the full virulence of *S. aureus* in an immunocompetent host. Whether *S. aureus* is residing within an aerobic or hypoxic niche within the host, NO$^{\bullet}$ restricts available options to regenerate oxidizing power. A key adaptive response of *S. aureus* during nitrosative stress is the induction of *ldh1* encoding the dominant L-lactate dehydrogenase (Fig. 2D and fig. S2). Interestingly, NO$^{\bullet}$ induction of *ldh1* is independent of the SrrAB two-component system, thereby implicating other mechanisms for the NO$^{\bullet}$ sensitivity of the *srrAB* mutant (*10*). The *ldh1* allele is absent from coagulase-negative *S. epidermidis* and *S. saprophyticus* (fig. S6), and consequently neither species exhibits NO$^{\bullet}$-inducible L-lactate dehydrogenase activity nor grows under nitrosative stress (Fig. 1, A and C). Thus, *S. aureus* has evolved NO$^{\bullet}$-inducible L-lactate dehydrogenase activity through the acquisition of *ldh1*, which is divergently transcribed from the NO$^{\bullet}$-scavenging flavohemoglobin encoded by *hmp*.

The *hmp-ldh1* locus comprises a *S. aureus* specific NO$^{\bullet}$-resistance cassette that both detoxifies host-derived NO$^{\bullet}$ and circumvents its detrimental metabolic consequences. The pathogenic nature of *S. aureus* hinges on a previously unappreciated feature of its redox metabolism: the ability to induce homolactic fermentation during nitrosative stress.

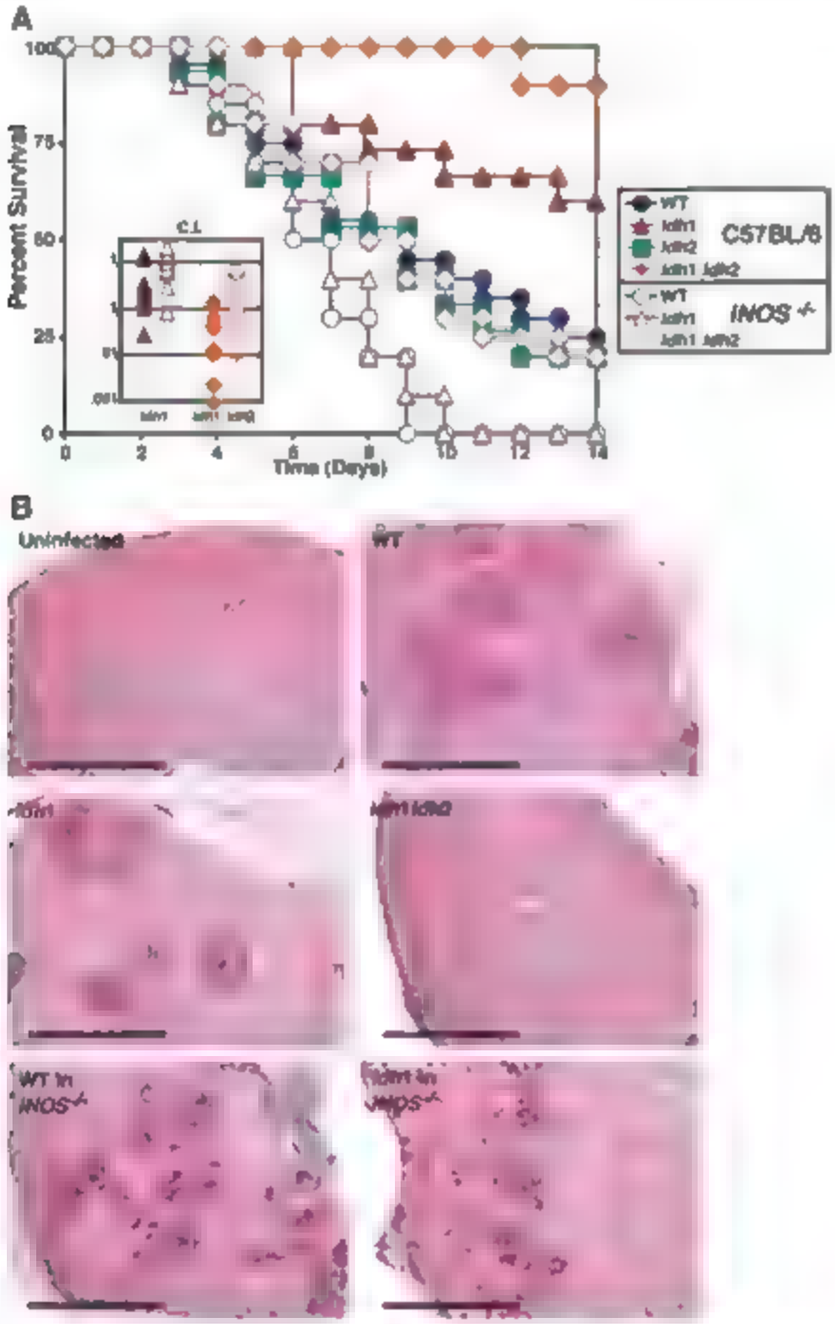

Fig. 4. Role of NO$^{\bullet}$-induced L-lactate dehydrogenase activity in *S. aureus* virulence. (**A**) Survival of 6-week-old female C57BL/6 and isogenic *iNOS*$^{-/-}$ mice inoculated iv with 5×10^7 CFU of *S. aureus* strain Newman and mutant derivatives. Inset: Competitive indices [C.I. = (mutant$_{out}$/wild-type$_{out}$)/(mutant$_{IN}$/wild-type$_{IN}$)] of *ldh1* or *ldh1 ldh2* mutants coinfected iv with wild-type *S. aureus* strain Newman. Mice were injected with 10^7 CFU of 1:1 mixtures of mutant and wild-type bacteria, kidneys were harvested at 5 days after infection, homogenized, sonicated to disrupt *S. aureus* aggregates, and plated to determine viable CFU counts. Colonies were patched onto selective medium to determine the ratio of mutant to wild-type bacteria in renal tissue. (**B**) Histology of infected murine renal tissue. Female C57BL/6 mice were inoculated iv with 10^7 CFU of *S. aureus* strain Newman or indicated derivatives. Tissue was harvested 5 days after infection, formalin-fixed, paraffin-embedded, then stained with hematoxylin and eosin. Scale bar, 1 mm.

References and Notes

1. F. C. Fang, *Nat. Rev. Microbiol.* **2**, 820 (2004).
2. K. C. Choi *et al.*, *Adv. Perit. Dial.* **14**, 173 (1998).
3. A. H. Shay *et al.*, *J. Infect. Dis.* **187**, 700 (2003).
4. J. A. Andersson, A. Cervin, S. Lindberg, R. Uddman, L. O. Cardell, *Acta Otolaryngol.* **122**, 861 (2002).
5. A. R. Butler, I. L. Megson, *Chem. Rev.* **102**, 1155 (2002).
6. C. E. Cooper, *Biochim. Biophys. Acta* **1411**, 290 (1999).
7. R. Radi, J. S. Beckman, K. M. Bush, B. A. Freeman, *Arch. Biochem. Biophys.* **288**, 481 (1991).
8. F. J. Schopfer, P. R. Baker, B. A. Freeman, *Trends Biochem. Sci.* **28**, 646 (2003).
9. D. A. Wink *et al.*, *Science* **254**, 1001 (1991).
10. A. R. Richardson, P. M. Dunman, F. C. Fang, *Mol. Microbiol.* **61**, 927 (2006).
11. S. Fuchs, J. Pane-Farre, C. Kohler, M. Hecker, S. Engelmann, *J. Bacteriol.* **189**, 4275 (2007).
12. G. C. Brown, A. G. McBride, E. J. Fox, K. S. McNaught, V. Borutaite, *Biochem. Soc. Trans.* **25**, 901 (1997).
13. J. S. Stamler, S. Lamas, F. C. Fang, *Cell* **106**, 675 (2001).

14. R. N. Perham, L. C. Packman, S. E. Radford, *Biochem. Soc. Symp.* **54**, 67 (1987).
15. A. Becker *et al.*, *Nat. Struct. Biol.* **6**, 969 (1999).
16. J. B. Broderick *et al.*, *Biochem. Biophys. Res. Commun.* **269**, 451 (2000).
17. See supporting material on *Science* Online.
18. We thank C. Harwood and her laboratory for the use of their anaerobic chamber facilities; the University of Washington Department of Pathology for assistance with histological specimens; A. Robertson for her contribution to the statistical analyses described herein; and J. McKinlay for critically reading this manuscript. Supported by NIH grants AI039557 (F.C.F.) and AI055396 (A.R.R.). GenBank accession numbers for the Ldh proteins, by strain designation: *S. aureus* SACOL0222, Q5HJD7; *S. saprophyticus* SSP1001, Q49YJ3; *S. epidermidis* SERP2156, Q5HI31; *S. aureus* SACOL2618, AAW38617; *S. saprophyticus* SSP0249, BAE17394.

Supporting Online Material
www.sciencemag.org/cgi/content/full/319/5870/1672/DC1
Materials and Methods
Figs. S1 to S6
Table S1
References

14 January 2008; accepted 13 February 2008
10.1126/science.1155207

Oncogenic *CARD11* Mutations in Human Diffuse Large B Cell Lymphoma

Georg Lenz,[1,2]* R. Eric Davis,[1,3]* Vu N. Ngo,[1] Lloyd Lam,[1] Thaddeus C. George,[2] George W. Wright,[3] Sandeep S. Dave,[1] Hong Zhao,[1] Weihong Xu,[1] Andreas Rosenwald,[4] German Ott,[4,5] Hans Konrad Muller-Hermelink,[4] Randy D. Gascoyne,[6] Joseph M. Connors,[6] Lisa M. Rimsza,[7] Elias Campo,[8] Elaine S. Jaffe,[9] Jan Delabie,[10] Erlend B. Smeland,[11,12] Richard I. Fisher,[13,14] Wing C. Chan,[15] Louis M. Staudt[1]†

Diffuse large B cell lymphoma (DLBCL) is the most common form of non-Hodgkin's lymphoma. In the least curable (ABC) subtype of DLBCL, survival of the malignant cells is dependent on constitutive activation of the nuclear factor–κB (NF-κB) signaling pathway. In normal B cells, antigen receptor–induced NF-κB activation requires CARD11, a cytoplasmic scaffolding protein. To determine whether CARD11 contributes to tumorigenesis, we sequenced the *CARD11* gene in human DLBCL tumors. We detected missense mutations in 7 of 73 ABC DLBCL biopsies (9.6%), all within exons encoding the coiled-coil domain. Experimental introduction of CARD11 coiled-coil domain mutants into lymphoma cell lines resulted in constitutive NF-κB activation and enhanced NF-κB activity upon antigen receptor stimulation. These results demonstrate that *CARD11* is a bona fide oncogene in DLBCL, providing a genetic rationale for the development of pharmacological inhibitors of the CARD11 pathway for DLBCL therapy.

Diffuse large B cell lymphoma (DLBCL) is the most common type of non-Hodgkin's lymphoma, accounting for 30 to 40% of cases (*1*). DLBCL consists of three subtypes: germinal center B cell–like (GCB) DLBCL, activated B cell–like (ABC) DLBCL, and primary mediastinal B cell lymphoma (*2*, *3*). Although more than half of DLBCLs are curable (*4*), the ABC DLBCL subtype, which accounts for roughly one-third of the cases, has an inferior prognosis (*3*).

A characteristic feature of ABC DLBCLs is constitutive activation of the NF-κB pathway, which plays a pivotal role in proliferation, differentiation, and survival of normal lymphoid cells (*5*). It was previously shown that survival of ABC DLBCLs depends on NF-κB function; inhibition of the NF-κB pathway was toxic to ABC DLBCL but not to GCB DLBCL cell lines (*6*). In an RNA interference screen, small hairpin RNAs (shRNAs) targeting *CARD11* (also known as *CARMA1* or *Bimp3*) were toxic to ABC but not GCB DLBCL cell lines (*6*). During antigen stimulation of normal lymphocytes, CARD11 functions as a signaling scaffold protein to coordinate the activation of IκB kinase β (IKK), a positive regulator of the NF-κB pathway (*9*).

Although these studies showed that CARD11 is required for the constitutive activation of NF-κB in ABC DLBCL, they did not address the mechanism of CARD11 activation in these lymphomas. Normal B cells require "tonic" B cell receptor (BCR) signaling to the NF-κB pathway for survival (*10*, *11*), and CARD11 is required for the differentiation and/or survival of discrete B cell subpopulations (*12*, *13*). Thus, ABC DLBCLs might "inherit" their dependence on CARD11 from their normal cellular counterparts. Alternatively, addiction of ABC DLBCLs to CARD11 signaling might stem from oncogenic mutations in this pathway. To address this issue, we initially resequenced all coding exons of *CARD11* in 16 ABC DLBCL biopsies and four ABC DLBCL cell lines; we discovered missense base substitutions in three biopsies and one cell line. All substitutions affected the coiled-coil domain, which mediates CARD11 oligomerization and NF-κB pathway activation (*14*, *16*). We next resequenced the coiled-coil domain exons in 136 additional DLBCL biopsies. In all, we detected missense substitutions affecting amino acids in or immediately adjacent to the coiled-coil domain in 9.6% (7/73) of ABC DLBCL biopsies but in only 3.8% (3/79) of GCB DLBCL biopsies (Fig. 1A). As a control, we analyzed 19 mucosa-associated lymphoid tissue (MALT) lymphoma biopsies because MALT lymphomas can also have constitutive NF-κB activation; no coiled-coil domain substitutions were detected.

To test whether these base substitutions represent acquired tumor-specific mutations or rare *CARD11* polymorphisms, we sequenced the germline *CARD11* locus in the four cases for which constitutional DNA was available (cases 4, 5, 10, and 11). Each of these normal samples was wild type for the *CARD11* coiled-coil region, and thus the base substitutions in the tumors were somatic mutations. In a fifth case, some alleles cloned from the tumor DNA had two separate base substitutions (9a and 9b) but other alleles had only one of these (9a). We conclude that base substitution 9b occurred as a somatic mutation that was acquired by the tumor after 9a. Together, these data make it likely that all of the coiled-coil domain substitutions represent somatic mutations, a view supported by their functional activity, as detailed below.

A gene expression signature of NF-κB pathway activity was highly expressed in all ABC DLBCL biopsies, irrespective of *CARD11* mutational status, as expected (*7*) (Fig. 1B). Notably, this signature was higher in GCB DLBCLs with mutant *CARD11* than in those with wild-type *CARD11*, indicating activation of the NF-κB pathway by these mutations ($P = 0.046$).

To explore the functional consequences of the *CARD11* mutations, we expressed mutant or wild-type CARD11 proteins in a variant of the Jurkat human T cell line that lacks endogenous CARD11 expression and harbors an NF-κB–driven enhanced green fluorescent protein (EGFP) reporter (*17*). Six of 11 CARD11 mutants (numbers 2, 3, 5, 7, 9a, 9ab, and 10) produced strong NF-κB activity without any exogenous stimulation, which was not observed with wild-type CARD11 even though wild-type and mutant CARD11 proteins accumulated to comparable levels (Fig. 2A and fig. S1, A and B). The five remaining mutants (numbers 4, 6, 8, 9b, and 11) produced a more

[1]Metabolism Branch, Division of Cancer Treatment and Diagnosis, Center for Cancer Research, National Cancer Institute, Bethesda, MD 20892, USA. [2]Amnis Corporation, Seattle, WA 98121, USA. [3]Biometric Research Branch, Division of Cancer Treatment and Diagnosis, Center for Cancer Research, National Cancer Institute, Bethesda, MD 20892, USA. [4]Department of Pathology, University of Würzburg, 97080 Würzburg, Germany. [5]Department of Clinical Pathology, Robert-Bosch-Krankenhaus, 70376 Stuttgart, Germany. [6]British Columbia Cancer Agency, Vancouver, British Columbia V5Z 4E6, Canada. [7]Department of Pathology, University of Arizona, Tucson, AZ 85724, USA. [8]Hospital Clinic, University of Barcelona, 08036 Barcelona, Spain. [9]Laboratory of Pathology, Division of Cancer Treatment and Diagnosis, Center for Cancer Research, National Cancer Institute, Bethesda, MD 20892, USA. [10]Department of Immunology, Rikshospitalet-Radiumhospitalet Medical Center, N-0310 Oslo, Norway. [11]Institute for Cancer Research, Rikshospitalet University Hospital, N-0310 Oslo, Norway. [12]Centre for Cancer Biomedicine, Faculty Division, Norwegian Radium Hospital, University of Oslo, N-0310 Oslo, Norway. [13]Southwest Oncology Group, 24 Frank Lloyd Wright Drive, Ann Arbor, MI 48106, USA. [14]James P. Wilmot Cancer Center, University of Rochester School of Medicine, Rochester, NY 14642, USA. [15]Departments of Pathology and Microbiology, University of Nebraska Medical Center, Omaha, NE 68198, USA.

*These authors contributed equally to this work.
†To whom correspondence should be addressed. E-mail: staudt@mail.nih.gov

modest degree of constitutive NF-κB activation, which was nonetheless greater than that of wild-type CARD11. In response to T cell receptor activation, cells expressing wild-type CARD11 showed a moderate increase in NF-κB activity, but the induction was more pronounced in cells bearing the CARD11 mutants (Fig. 2A). In the BJAB human B cell line, these mutants induced expression of NF-κB target genes, including CD83, to a much greater degree than wild-type CARD11, both with or without BCR stimulation (fig. S1, C to E). We expressed the CARD11 isoforms as fusion proteins with EGFP and monitored CD83 expression as a function of CARD11 expression by flow cytometry. The CD83 response to increasing expression of the CARD11 mutants was much steeper than observed with wild-type CARD11 (Fig. 2B and fig. S1F). Thus, at comparable protein levels, the CARD11 mutants were consistently more effective than wild-type CARD11 in activating NF-κB.

To determine whether the CARD11 mutants functioned upstream of IKK in the NF-κB pathway, we measured IKK activity with the use of a B cell line expressing a fusion protein between *Photinus* luciferase and the IKK substrate IκBα, as described (*8*, *18*). Whereas wild-type CARD11 did not alter the IκBα-luciferase level, all CARD11 mutants produced a time-dependent decrease in the reporter, indicating IKK activation (Fig. 2C). Mutants 3, 9a, 9ab, and 10 produced the strongest IKK activation, in accord with their greater ability to induce NF-κB in other cell lines.

We next examined the subcellular localization patterns of the EGFP-CARD11 isoforms expressed in BJAB cells by fluorescence microscopy. In unstimulated cells, wild-type CARD11 was localized diffusely in the cytoplasm, whereas CARD11 mutants were concentrated in cytosolic aggregates (Fig. 2D). To quantify the aggregation of CARD11 mutants, we used a multispectral imaging flow cytometer that obtains a microscopic image of each flow-sorted cell (fig. S2, A and B) (*19*, *20*). Fewer than 5% of cells expressing wild-type CARD11 had aggregates, whereas 38 to 88% of the cells expressing CARD11 mutants showed aggregate formation (fig. S2C). The degree of aggregation by each mutant correlated with its ability to spontaneously activate the NF-κB pathway, as judged by degradation of the IκBα-luciferase reporter ($P = 0.0059$; Fig. 2E). The CARD11 mutant aggregates colocalized with total and phosphorylated IKK as well as MALT1, a signaling protein required for IKK activation by CARD11 (*20*), but in cells with wild-type CARD11, IKK and MALT1 were diffusely cytoplasmic (fig. S2D). We conclude that the CARD11 mutations confer a gain-of-function phenotype, which is characterized by constitutive IKK activity, enhanced NF-κB response to exogenous stimulation, and a propensity to form cytoplasmic structures that colocalize with NF-κB signaling components.

One ABC DLBCL cell line, OCI-Ly3, had a single mutated *CARD11* allele (fig. S3), but three others (HBL-1, U2932, and OCI-Ly10) had wild-type *CARD11* alleles, all of which nonetheless depend on CARD11 for survival (*8*). We devised a complementation experiment to test whether OCI-Ly3 cells require mutated CARD11 for survival, or whether wild-type CARD11 would suffice. OCI-Ly3 cells were first engineered to express the coding region for wild-type CARD11 or CARD11 mutant 2 (derived from OCI-Ly3). These cells were then transduced with a shRNA targeting the *CARD11* 3′-untranslated region to knock down the expression of the endogenous *CARD11* gene but spare the exogenously introduced *CARD11* coding regions. Exogenous CARD11 mutant 2 protected OCI-Ly3 cells from CARD11 shRNA toxicity, but exogenous wild-type CARD11 did not (Fig. 3A). Other CARD11 mutants that strongly activated NF-κB were able to rescue OCI-Ly3 from CARD11 shRNA toxicity, but mutants with moderate ability to constitutively activate NF-κB only partially rescued the cells. Conceivably, these less active CARD11 mutants may have been selected to enhance the NF-κB response of the malignant clone to stimuli from the microenvironment or to other endogenous stimuli. Unlike the results seen for OCI-Ly3 cells, wild-type CARD11 was able to rescue OCI-Ly10 cells from the toxicity of CARD11 shRNA, as could mutant CARD11 (Fig. 3B). These findings demonstrate that some ABC DLBCLs become addicted to the action of mutant CARD11, whereas others have alternative mechanisms to activate wild-type CARD11 that are not present (or needed) in ABC DLBCLs with mutated CARD11.

Our results firmly establish *CARD11* as a bona fide oncogene in DLBCL. Previous reports described the dependence of ABC DLBCLs on CARD11 signaling to NF-κB (*7*, *8*), but they did not address whether this represents tonic BCR signaling (*10*, *11*) or is a feature of the stage of B cell differentiation from which ABC DLBCLs derive. We have now shown that a subset of ABC DLBCLs acquire activating CARD11 mutations that induce NF-κB constitutively, providing genetic evidence that addiction to the CARD11

Fig. 1. CARD11 mutations in DLBCL. (**A**) General domain structure of CARD11 and a schematic of the coiled-coil domains, showing the amino acids mutationally altered in DBLCL. Mutations from ABC DLBCLs (blue) and GCB DLBCLs (orange) are shown. Mutants 7 and 9 both cause two amino acid substitutions. Abbreviations for amino acid residues: A, Ala; C, Cys; D, Asp; E, Glu; F, Phe; G, Gly; H, His; I, Ile; K, Lys; L, Leu; M, Met; N, Asn; P, Pro; Q, Gln; R, Arg; S, Ser; T, Thr; V, Val; W, Trp; Y, Tyr. (**B**) NF-κB target gene signature expression in ABC DLBCL and GCB DLBCL cases with either wild-type (WT) or mutant CARD11. Means and SEs are shown.

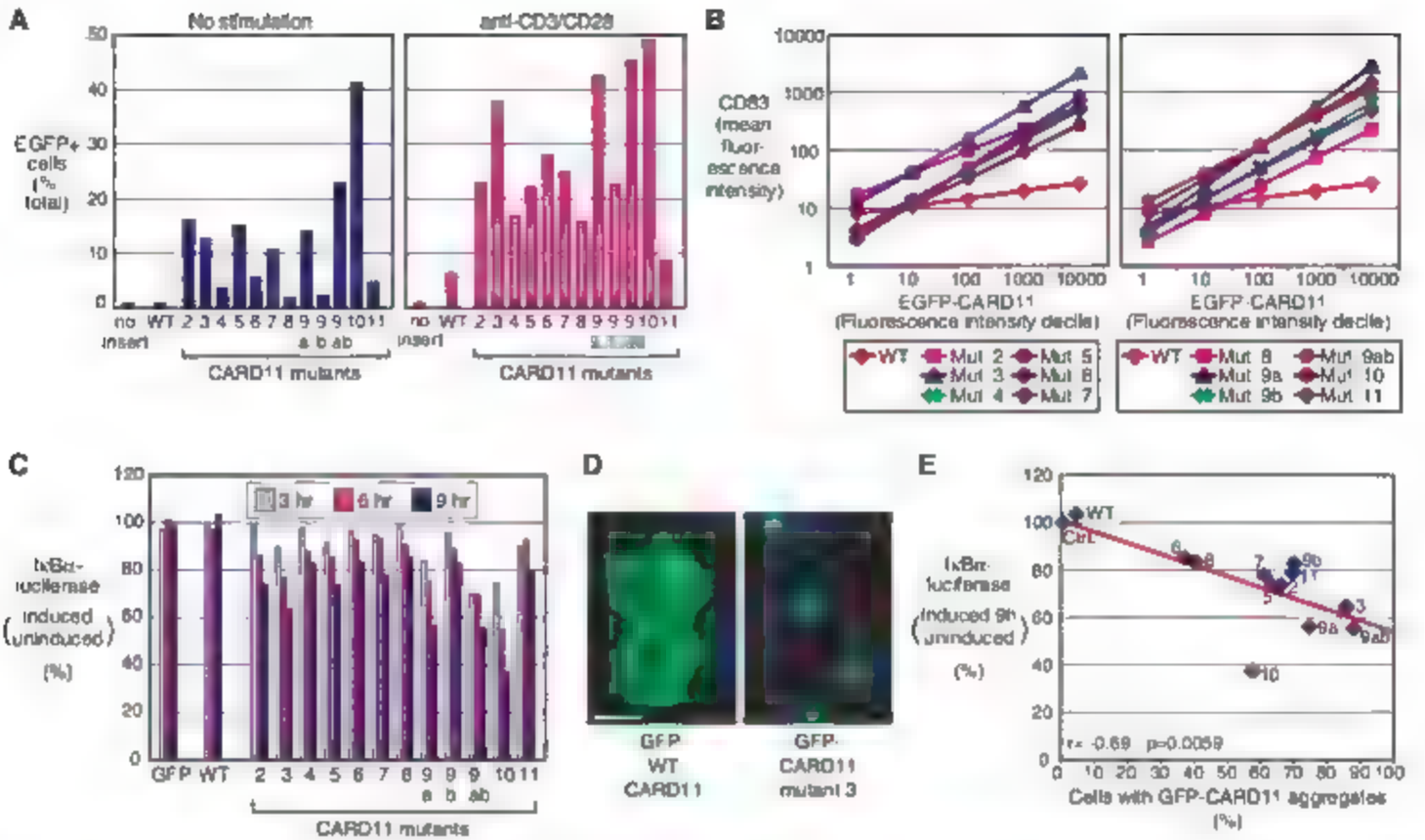

Fig. 2. CARD11 coiled-coil mutants constitutively activate the NF-κB pathway and enhance antigen receptor signaling to NF-κB. **(A)** Expression of wild-type CARD11 or CARD11 mutants in the Jurkat human T cell line JPM50.6, which lacks endogenous CARD11 and harbors an NF-κB–driven expression EGFP reporter. Shown are EGFP levels in unstimulated cells (left) or in cells stimulated by cross-linking with antibodies to CD3 and CD28 (right). **(B)** Linear regression analysis of EGFP-CARD11 levels (in decile bins) and CD83 expression in the GCB DLBCL cell line BJAB expressing either exogenous wild-type or mutant EGFP-CARD11 isoforms. **(C)** Cell-based assay of IKK activation by exogenous CARD11 isoforms. The GCB DLBCL cell line OCI-Ly19 was engineered to express an IκBα–*Photinus* luciferase fusion protein, a control *Renilla* luciferase, and doxycycline-inducible constructs for CARD11 isoforms. Values represent IκBα–*Photinus* luciferase/*Renilla* luciferase ratios in doxycycline induced cells, normalized to ratios in uninduced cells. A decrease in the ratio indicates increased degradation of the IκBα–*Photinus* luciferase reporter, attributable to increased IKK activity. **(D)** Aggregate formation by CARD11 coiled-coil domain mutants. Composite fluorescence photomicroscopy of BJAB cells expressing EGFP-tagged wild-type CARD11 or mutant 3, with 4′,6′-diamidino-2-phenylindole nuclear counterstain (blue); scale bar, 10 μm. **(E)** Correlation between CARD11 aggregate formation (as measured in (D)) and IKK activation, showing percent decrease in the IκBα-luciferase reporter in OCI-Ly19 cells after 9 hours of doxycycline induction of wild-type or mutant CARD11. A regression line representing the inverse correlation of the variables is shown (Pearson correlation coefficient = −0.694, $P = 0.0059$). Ctrl., EGFP control.

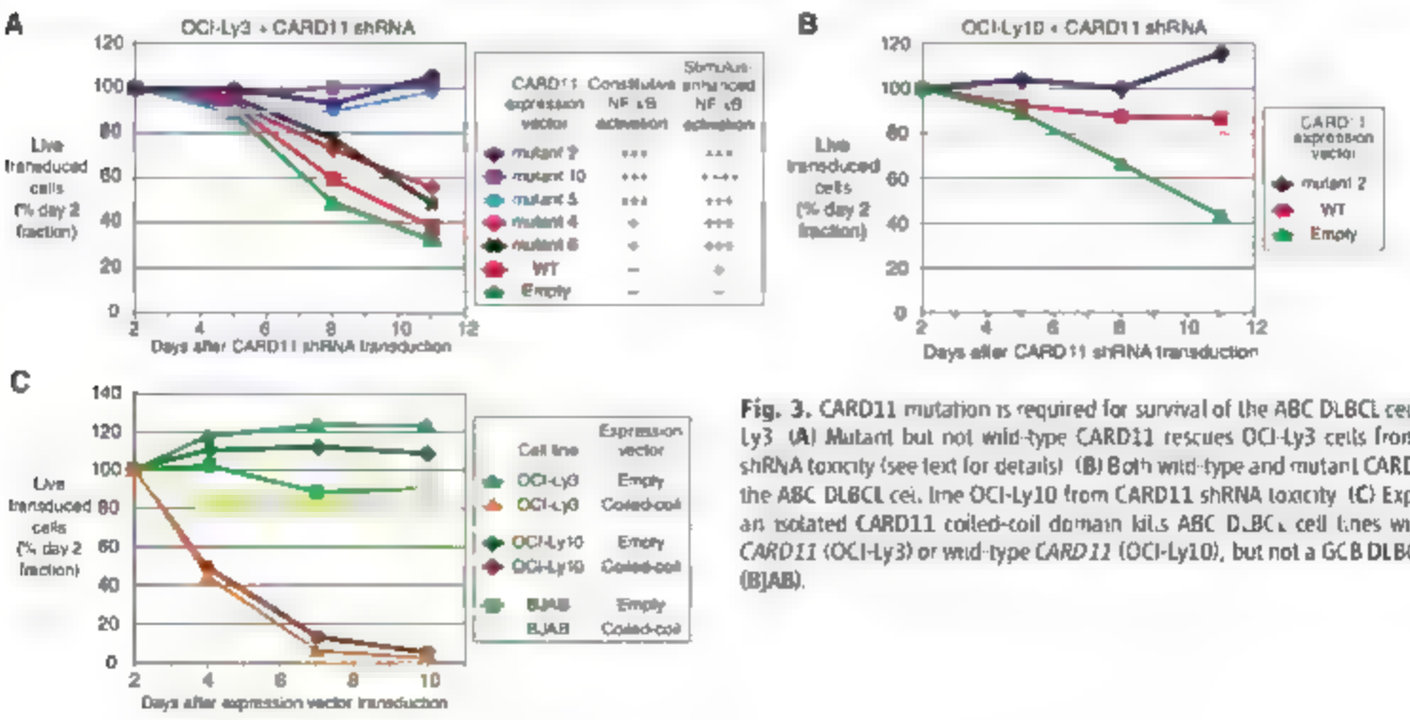

Fig. 3. CARD11 mutation is required for survival of the ABC DLBCL cell line OCI-Ly3. **(A)** Mutant but not wild-type CARD11 rescues OCI-Ly3 cells from CARD11 shRNA toxicity (see text for details). **(B)** Both wild-type and mutant CARD11 rescue the ABC DLBCL cell line OCI-Ly10 from CARD11 shRNA toxicity. **(C)** Expression of an isolated CARD11 coiled-coil domain kills ABC DLBCL cell lines with mutant *CARD11* (OCI-Ly3) or wild-type *CARD11* (OCI-Ly10), but not a GCB DLBCL cell line (BJAB).

pathway is a phenotype that is positively selected during evolution of these lymphomas. CARD11 mutations may allow the lymphoma cells to engage the NF-κB pathway in the absence of antigen receptor signals. In this regard, it is notable that CARD11 coiled-coil domain mutants were constitutively active in OCI-Ly19 and OCI-Ly3 cells, both of which lack detectable PKC-β protein (fig. S4) (*21*), which phosphorylates and activates CARD11 during normal BCR signaling (*22*, *23*).

The fact that the CARD11 mutations in ABC DLBCL are confined to the coiled-coil domain highlights the central importance of this domain in CARD11 function. That the mutations are activating suggests that the coiled-coil domain keeps CARD11 in a latent state, which can be disrupted physiologically by antigen receptor signaling or pathologically by mutation. Several of the CARD11 mutations that we uncovered introduce helix-breaking prolines, whereas others affect charged amino acids, which can regulate the oligomerization of coiled-coil domains as part of "trigger sites" and can contribute to the stability of coiled-coil interactions (*24*). These observations suggest that coiled-coil interactions may actually be a feature of inactive CARD11.

How might CARD11 be attacked therapeutically? Expression of the isolated CARD11 coiled-coil domain was toxic to both OCI-Ly3 and OCI-Ly10 cells, but not to the GCB DLBCL cell line BJAB (Fig. 3C). This result shows that DLBCLs with activating mutations in *CARD11* are just as vulnerable to interference with coiled-coil function as those with wild-type *CARD11*. Together, our results provide a compelling genetic and functional rationale for the development of molecular inhibitors aimed at the coiled-coil domain of CARD11, which could have activity in ABC DLBCL, the subtype of DLBCL that is least curable by our current therapies (*25*).

References and Notes

1. The Non-Hodgkin's Lymphoma Classification Project, *Blood* **89**, 3909 (1997).
2. A. A. Alizadeh *et al.*, *Nature* **403**, 503 (2000).
3. A. Rosenwald *et al.*, *N. Engl. J. Med.* **346**, 1937 (2002).
4. A. Rosenwald *et al.*, *J. Exp. Med.* **198**, 851 (2003).
5. K. J. Savage *et al.*, *Blood* **102**, 3871 (2003).
6. R. Colhan *et al.*, *N. Engl. J. Med.* **346**, 235 (2002).
7. R. E. Davis, K. D. Brown, U. Siebenlist, L. M. Staudt, *J. Exp. Med.* **194**, 1861 (2001).
8. V. N. Ngo *et al.*, *Nature* **441**, 106 (2006).
9. D. J. Rawlings, K. Sommer, M. E. Moreno-Garcia, *Nat. Rev. Immunol.* **6**, 799 (2006).
10. K. P. Lam, R. Kühn, K. Rajewsky, *Cell* **90**, 1073 (1997).
11. M. Pasparakis, M. Schmidt-Supprian, K. Rajewsky, *J. Exp. Med.* **196**, 743 (2002).
12. T. Egawa *et al.*, *Curr. Biol.* **13**, 1252 (2003).
13. H. Hara *et al.*, *Immunity* **18**, 763 (2003).
14. J. E. Jun *et al.*, *Immunity* **18**, 751 (2003).
15. K. Newton, V. M. Dixit, *Curr. Biol.* **13**, 1247 (2003).
16. M. J. Tanner, W. Hanel, S. E. Gallen, K. Lin, *J. Biol. Chem.* **282**, 17141 (2007).
17. D. Wang *et al.*, *Nat. Immunol.* **3**, 830 (2002).
18. See supporting material on *Science* Online.
19. T. C. George *et al.*, *J. Immunol. Methods* **311**, 117 (2006).
20. M. Thome, *Nat. Rev. Immunol.* **4**, 348 (2004).
21. T. T. Su *et al.*, *Nat. Immunol.* **3**, 780 (2002).
22. R. Matsumoto *et al.*, *Immunity* **23**, 575 (2005).
23. K. Sommer *et al.*, *Immunity* **23**, 561 (2005).
24. P. Burkhard, J. Stetefeld, S. V. Strelkov, *Trends Cell Biol.* **11**, 82 (2001).
25. L. M. Staudt, S. Dave, *Adv. Immunol.* **87**, 163 (2005).

26. We thank M. Thome for kindly providing the CARD11 cDNA, J. Cohen for use of an ImageStream cytometer, Y. Tagaya for assistance with microscopy, and U. Siebenlist for helpful comments. Supported by a Deutsche Forschungsgemeinschaft research grant (G.L.); by the Intramural Research Program of the NIH, National Cancer Institute, Center for Cancer Research; and by NCI Director's Challenge grant (OD1-CA84967). This project was performed under the auspices of the Lymphoma/Leukemia Molecular Profiling Project of the NCI.

Supporting Online Material

www.sciencemag.org/cgi/content/full/1153629/DC1
Materials and Methods
Figs. S1 to S4
Table S1
References

30 November 2007; accepted 5 February 2008
Published online 6 March 2008;
10.1126/science.1153629
Include this information when citing this paper.

Drosophila Egg-Laying Site Selection as a System to Study Simple Decision-Making Processes

Chung-hui Yang,[1] Priyanka Belawat,[2] Ernst Hafen,[2] Lily Y. Jan,[1] Yuh Nung Jan[1]*

The ability to select a better option from multiple acceptable ones is important for animals to optimize their resources. The mechanisms that underlie such decision-making processes are not well understood. We found that selection of egg-laying site in *Drosophila melanogaster* is a suitable system to probe the neural circuit that governs simple decision-making processes. First, *Drosophila* females pursue active probing of the environment before depositing each egg, apparently to evaluate site quality for every egg. Second, *Drosophila* females can either accept or reject a sucrose-containing medium, depending on the context. Last, communication of the "acceptability" of the sucrose-containing medium as an egg-laying option to the reproductive system depends on the function of a group of insulin-like peptide 7 (ILP7)–producing neurons. These findings suggest that selection of egg-laying site involves a simple decision-making process and provide an entry point toward a systematic dissection of this process.

Decision-making, in one view, is the process by which animals deliberate whether to invest in one action or not by taking into account the values and costs associated with available options. Selection of egg-laying site by *Drosophila* provides a plausible system to investigate such decision-making processes. Egg production is costly; thus, the ability to weigh egg-laying options might have been selected to ensure better survival of offspring in an uncertain environment. *Drosophila* females are known to be selective toward egg-laying sites and will withhold eggs when there are no appropriate sites (*1*–*6*). It is less clear, however, whether *Drosophila* females value a given egg-laying site differently according to the availability of other laying options. We examined the selection of an egg-laying site by individual *Drosophila* females, in an attempt to find a genetically tractable system to study the molecular and cellular basis of simple decision-making processes.

The first indications that egg-laying site selection may employ a simple decision-based process emerged from our observations of females as they lay eggs. For consistent viewing of egg-laying events, we deprived females of egg-laying for 24 hours before placing them in a chamber filled with grape agar, an attractive egg-laying substrate (Fig. 1, A and B). By reviewing hundreds of egg-laying events, we found that immediately before each physical egg expulsion, females stereotypically bend the abdomen downward until it is nearly perpendicular to the substrate surface to extrude and insert the ovipositor into the substrate (Fig. 1C) before initiating a series of back-and-forth movements to expel and insert a single egg into the substrate (Movie S1). This behavioral component always accompanies the physical deposition of an egg and typically lasts about 6 s (Fig. 1I) on grape agar. We called this behavioral component the "ovipositor motor program" because it is reminiscent of the "oviposition motor program" of grasshopper egg-laying (*7*). We next found two more behavioral components that regularly follow the ovipositor program: An animal always grooms its ovipositor with its hind legs (Fig. 1D and Movie S1) for a few seconds and then stays immobile for a while as though it is resting (Fig. 1E). After the "clean and rest program" and before the initiation of the next ovipositor program, the animals presumably have the opportunity to locate an appropriate site for the next egg (Fig. 1H). Indeed,

[1]Howard Hughes Medical Institute, Department of Physiology, Biochemistry, and Biophysics, University of California at San Francisco, San Francisco, CA 94143–0725, USA. [2]Institute for Molecular Systems Biology, Eidgenössische Technische Hochschule Zürich HPT E 72, Wolfgang-Pauli-Strasse 16, 8093 Zurich, Switzerland.

*To whom correspondence should be addressed. E-mail: yuhnung.jan@ucsf.edu

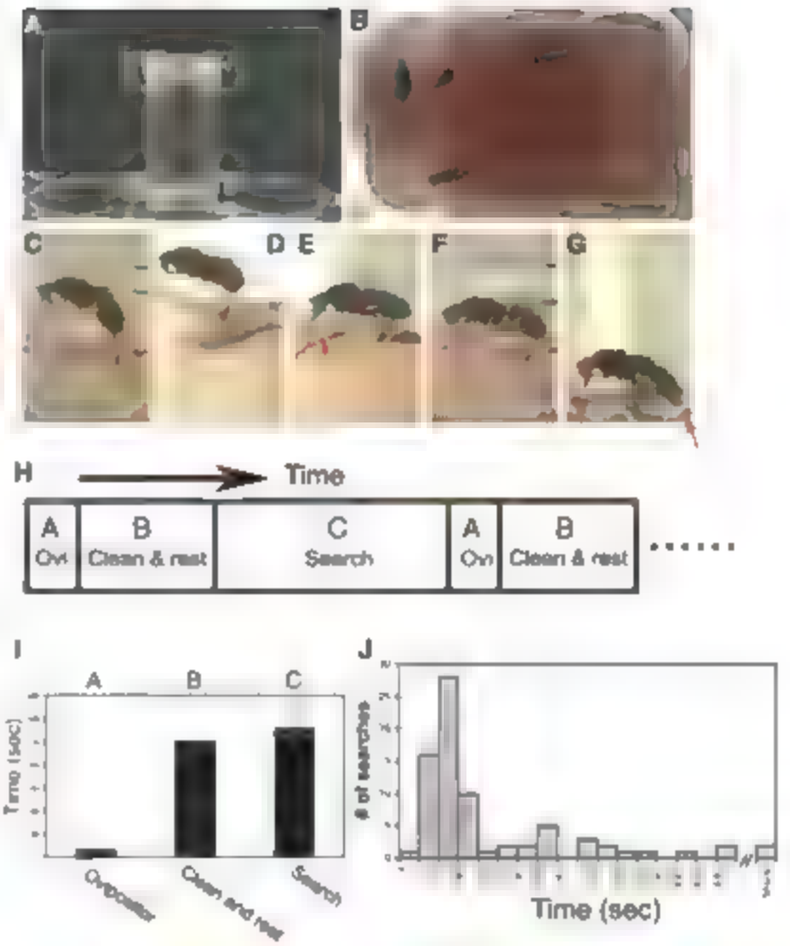

Fig. 1. The egg-laying behavioral sequence of *Drosophila* females. (**A**) The grape-agar chamber used for observing egg-laying behavior. (**B**) Top view of the chamber through the camcorder. (**C**) Animal performing the ovipositor motor program. Note the downward-bending of the abdomen. Red arrow, ovipositor. (**D**) Animal cleaning the ovipositor (red arrow) with its hind legs. (**E**) Animal probing the substrate with its proboscis (red arrow). (**F** and **G**) Animal probing the substrate with its ovipositor (red arrow). (**H**) Egg-laying temporal sequence. The physical deposition of an egg starts from "A" and continues to "B." Between the end of "B" and the beginning of the next "A" is period "C," in which animals are consistently seen displaying the probing actions described in (E), (F), and (G). Ovi, ovipositor motor program. (**I**) Time spent on each of the programs described above. "A" 6.7 ± 0.25 s; "B" 101 ± 4.7 s; "C": 113.2 ± 18.9 s. For programs "A" and "B," N = 50 egg-layings displayed by four animals from four chambers. For program "C," N = 77 egg-layings displayed by four animals from four chambers. Error bars indicate SEM. A comparison of behaviors between *CantonS* and *W1118* is shown in fig. S1. (**J**) Distribution of time spent on the searchlike program. N = 77 individual egg-layings displayed by four animals from four chambers. Unless otherwise mentioned, all quantifications in this work were conducted by using *CantonS* animals or transgenic animals in *CantonS* background.

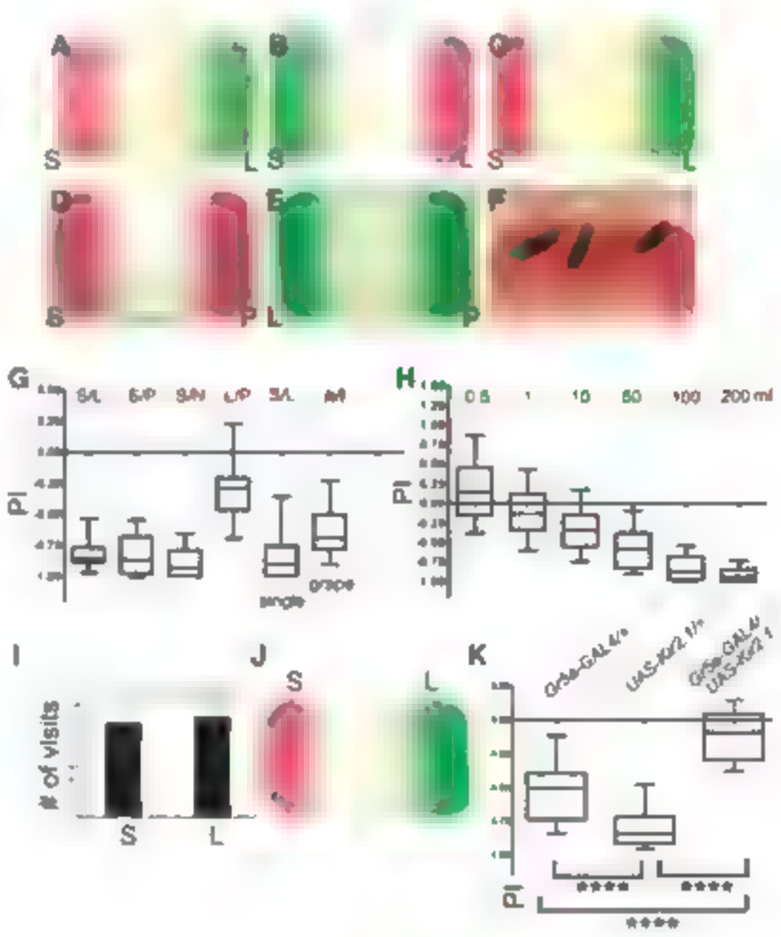

Fig. 2. *Drosophila* avoid laying eggs on media containing high levels of sucrose. (**A** to **E**) Representative outcomes of various two-choice tests. Single-female assay was used in (C), the rest were three-female assays. S, sucrose; L, lobeline; P, plain. The same designations will be used throughout the figure legend. (**F**) Animals extending their proboscis onto the sucrose medium (arrows) for foraging. (**G**) Preference index (PI) of various two-choice conditions (see supporting online material for derivation). N, NaCl; *l*, agar with 15% grape juice; *h*, agar with 45% grape juice. "Single" indicates that single animals were used in this assay; no difference was found between PI from single- versus three-female assay (P > 0.5, Mann-Whitney Test). Significant deviations from 0 were found for all conditions tested (P = 0.01 for L/P, P < 0.0001 for the rest, Wilcoxon Signed Rank Test). All box-whisker plots in this work display median, 25/75%, and 10/90% quartiles of each data set. The last entry shows that females prefer agar with less grape juice for egg-laying. The number of assays used and the mean PI are (29, −0.82), (26, −0.79), (10, −0.89), (34, −0.27), (50, −0.83), and (34, −0.62). (**H**) Females avoid sucrose medium less as its concentration drops in the sucrose versus plain two-choice assays and even showed a slight preference at the 0.5 mM setting (P = 0.0116, Wilcoxon Signed Rank Test). No significant avoidance can be found at 1 mM (P = 0.095, Wilcoxon Signed Rank Test). The rest of the entries all show significant avoidance of sucrose medium (P < 0.0001, Wilcoxon Signed Rank Test). The number of assays used and the mean PI are (49, 0.18), (34, −0.102), (36, −0.33), (34, −0.56), (34, −0.83), and (35, −0.90). (**I**) For each egg deposited on the lobeline medium in two-choice chambers, animals pay 1.51 ± 0.17 and 1.61 ± 0.15 respective previous visits to each substrate. N = 185 egg-depositions by eight females. (**J** and **K**) Hyperpolarizing *Gr5a* neurons decreases egg-laying bias against the sucrose-containing medium. The difference between animals carrying *Gr5a-GAL4* with or without *UAS-Kir2.1* is significant (Mann-Whitney Test). Number of assays used and mean PI are (38, −0.52), (40, −0.79), (41, −0.09). ****P < 0.001. The exact cause(s) for the reduction of PI of *Gr5a-GAL4/+* animals is unclear; however, these animals contain two insertions of *Gr5a-GAL4* transgenes, so an excess of GAL4 proteins in these neurons alone could potentially contribute somewhat to reduction of neuronal function.

despite being placed in a relatively attractive grape-agar environment. the animals in virtually all cases display a "searchlike" behavior by walking around and probing the substrates with their proboscis and ovipositor (Fig. 1, E to G, and Movie S1). Because the proboscis, legs, and ovipositor all contain sensory receptors (*16*), this searchlike program should aid the animals in identifying appropriate egg-laying sites. In 199 out of the 200 cases that we observed (20 egg-layings each by 10 animals), we detected the searchlike behavior preceding the ovipositor program (Fig. 1J), although its duration varied. Thus, *Drosophila* females deposit their eggs one at a time and nearly always follow the cycle of search, oviposit, and clean and rest, with the searchlike program lasting from a few seconds to several minutes (Fig. 1J), whereas the other programs remain relatively constant in duration (Fig. 1I and fig. S1).

We next examined what the females seek by presenting them with different egg-laying options in the behavioral chamber. We placed in the chamber a sweet (sucrose-containing) and a bitter (lobeline-containing) (*9*) soft agarose medium separated by a region of hard agarose that deters egg-laying and prevents simultaneous detection of the two soft media. Unexpectedly, animals consistently laid more eggs on the lobeline side of the chamber (Fig. 2, A to C, and G, and fig. S2). This bias against sucrose medium was not caused by intrinsic attraction to the lobeline medium for egg-laying, however, because animals tended to avoid lobeline when the other option was a plain medium (Fig. 2, E and G), consistent with previous findings on quinine avoidance in egg-laying (*10*). Furthermore, females avoided laying eggs on the sucrose-containing medium in our chambers no matter whether the alternative was lobeline-containing, plain, or a substrate containing sodium chloride at the same concentration as the sucrose (Fig. 2, A to D and G).

To determine whether females actually encountered both options before laying an egg on the lobeline medium, we next tracked individual animals for 2 hours and found that for each egg deposited on the lobeline side, the animals had paid an average of 1.5 previous visits to the sucrose option (Fig. 2I). Animals often probed the sucrose substrate actively but rarely activated the ovipositor program while they were still in contact with this medium (Movie S2); in contrast, activation of the ovipositor program was frequently seen when the animals were probing the lobeline medium (Movie S2). Thus, lack of substantial egg-laying on the sucrose medium is not due to animals' not making regular contacts with this medium. General repulsion to the sucrose-containing medium in our chamber is not the cause either—animals were often seen actively feeding on the sucrose medium by extending their proboscis onto it (Fig. 2F and Movie S3). Moreover, the avoidance of egg-laying on the sucrose medium (when it is paired with a plain one) is concentration dependent. It attenuates and can even turn into mild attraction as the concentration of sucrose decreases (Fig. 2H).

The reliance on neuronal activities of the sweet taste receptor (*Gr5a*) neurons (*11*) is evident in the experiments employing the *G H4-I 45* method to express in these *Gr5a*-expressing neurons a hyperpolarizing Kir2.1 potassium channel (*12*). This manipulation significantly increased egg-laying on the sucrose-containing medium (Fig. 2, J and K), which suggests that sucrose detection through the *Gr5a* neurons is important for the low egg-laying on this medium in the two-choice chamber.

To determine whether the desirability, or "value," of the sucrose-containing medium for egg-laying might change according to context,

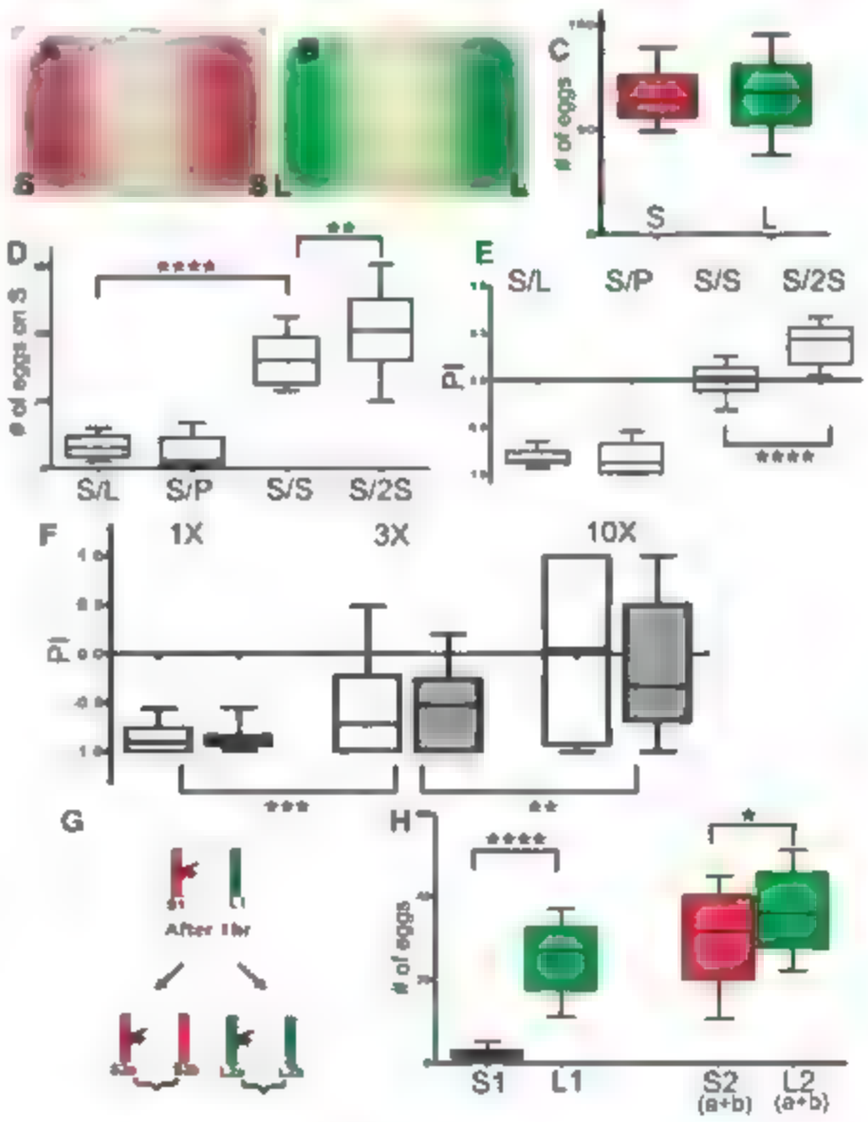

Fig. 3. Avoidance of sucrose-containing medium is context-dependent. (**A** to **C**) Comparable numbers of eggs were laid in the two single-choice (sucrose versus lobeline) chambers, $P > 0.5$, Mann-Whitney Test. Number of assays used and sample means are (39, 67.6) and (38, 67.6). (**D** and **E**) Pairing the same sucrose medium (100 mM, S) with different options alters the number of eggs deposited on (D) and the PI against this medium (E). 25, 200 mM sucrose. Assay number and sample mean for (D) are (29, 7.3), (35, 4.9), (39, 33.26), and (36, 40.89). For (E), (29, –0.82), (35, –0.82), (39, –0.01), (36, 0.37). $^{****}P < 0.0001$, $^{**}P < 0.005$, Mann-Whitney Test. (**F**) Comparison of the PI shows that animals avoided the sucrose-containing medium less when distance between the sucrose and lobeline media increased. Single females were used. White bars, without food deprivation; gray bars, 24-hour food deprivation before experiments. In both treatments, there were significant differences between 1X and 3X and between 3X and 10X. Food deprivation did not significantly impact PI for all three distances tested. Assay number and mean PI are: (52, –0.84), (23, –0.84), (47, –0.5), (55, –0.46), (31, –0.002), and (35, –0.08). $^{**}P < 0.005$, $^{***}P < 0.001$, Mann-Whitney Test. (**G**) Exposure assay set-up. Animals were placed in two-choice "exposure" chambers for 1 hour before being transferred into sucrose-only or lobeline-only single-choice chambers. (**H**) Despite robust preference for lobeline medium in the exposure chambers (S1 versus L1), the difference in egg numbers between the two single-choice chambers [S2(a+b) versus L2(a+b)] is less, although still significant. Number of assays used and the sample means are (69, 2.15), (69, 25.54), (34, 30.09), and (35, 36.16). $^{*}P = 0.05$, $^{****}P < 0.0001$, Mann-Whitney Test.

we examined egg-laying in single-choice chambers that contain either only the sucrose-containing medium or only the lobeline-containing medium. Interestingly, females lay comparable numbers of eggs in the two single-choice chambers (Fig. 3, A to C); thus, in the absence of other options, females readily accept the sucrose-containing medium for egg-laying. Furthermore, the same sucrose-containing medium can even become a preferred option for egg-laying if it is paired with a more repulsive medium that contains twice the amount of sucrose (Fig. 3, D and E).

To explore further how context affects the valuation of sucrose medium, we varied the physical separation between the sucrose- and lobeline-containing media in the two-choice chamber. We found that when the distance between the two choices was increased by a factor of 3 to 10, egg-laying on the sucrose medium progressively increased (Fig. 3F), and some of the individual animals tested actually laid more eggs on the sucrose-containing medium than on the lobeline medium (Fig. 3F). This result suggests that the preference of sucrose medium over lobeline is not absolute and that animals can weigh the "desirability" of egg-laying sites versus the "effort it takes to locate them" in making their decisions. Interestingly, this distance-dependent response to sucrose-containing medium was not altered by food deprivation before assays (Fig. 3F), suggesting that egg-laying and foraging are distinctive tasks with distinctive substrate preferences.

Sequential placement of the same animals first in a two-choice chamber and then in a sucrose medium only single-choice chamber (Fig. 3G) revealed speedy recovery of egg-laying interests on the sucrose-containing medium (Fig. 3H), suggesting that the substrate evaluation process is efficient and performed predominantly on an egg by egg (search by search) basis. However, compared with the number of eggs deposited in a lobeline medium only chamber, there were fewer eggs in the sucrose medium only chamber (S2 versus L2, Fig. 3H), whereas no difference was observed when naïve flies were introduced to the single-choice chambers (Fig. 3C); it thus appears that previous experience may exert some influence in egg-laying decisions. Taken together, our results suggest that *Drosophila* females possess some neural process that assigns "acceptability" or "value" to a given egg-laying substrate by taking readily into account the availability of other options. Such "value" can then be used by the motor output systems to decode whether a particular option is appropriate to trigger the physical egg-laying action in the given context.

To begin discerning the neural circuitry that underlies egg-laying site selection, we first sought to identify specific neurons that regulate the egg-laying rate as they might be engaged by the "value system" to control egg-laying on a given substrate. Neurons that express an insulin-like neuropeptide, ILP7, are of interest because ILP7 shares some homology with Relaxin, an important reproductive hormone in mammals (*13*, *14*). Our antibodies revealed that ILP7 is present in only very few cells in the larval and adult central nervous system (Fig. 4, A and B, and fig. S6), with some cells sending projections to the subesophageal ganglion (SOG) and distinct positions in the ventral nerve cord (Fig. 4A, B), which are all sites where gustatory information is thought to occur. Moreover, projection of ILP7 to the female internal reproductive tract can also be found (Fig. 4C), in support of the notion that ILP7 may be the *Drosophila* Relaxin. Interestingly, many of the *ILP7*-neurons are also positive for *fruitless* expression in adult males (fig. S7). This result suggests a potential role of these neurons in male reproductive behavior, because *fruitless* has been shown to be a master regulator of male courtship behavior in *Drosophila* (*15*).

We next created an *ILP7-GAL4* to specifically alter *ILP7*-neurons' function (Fig. 4, F to H, and

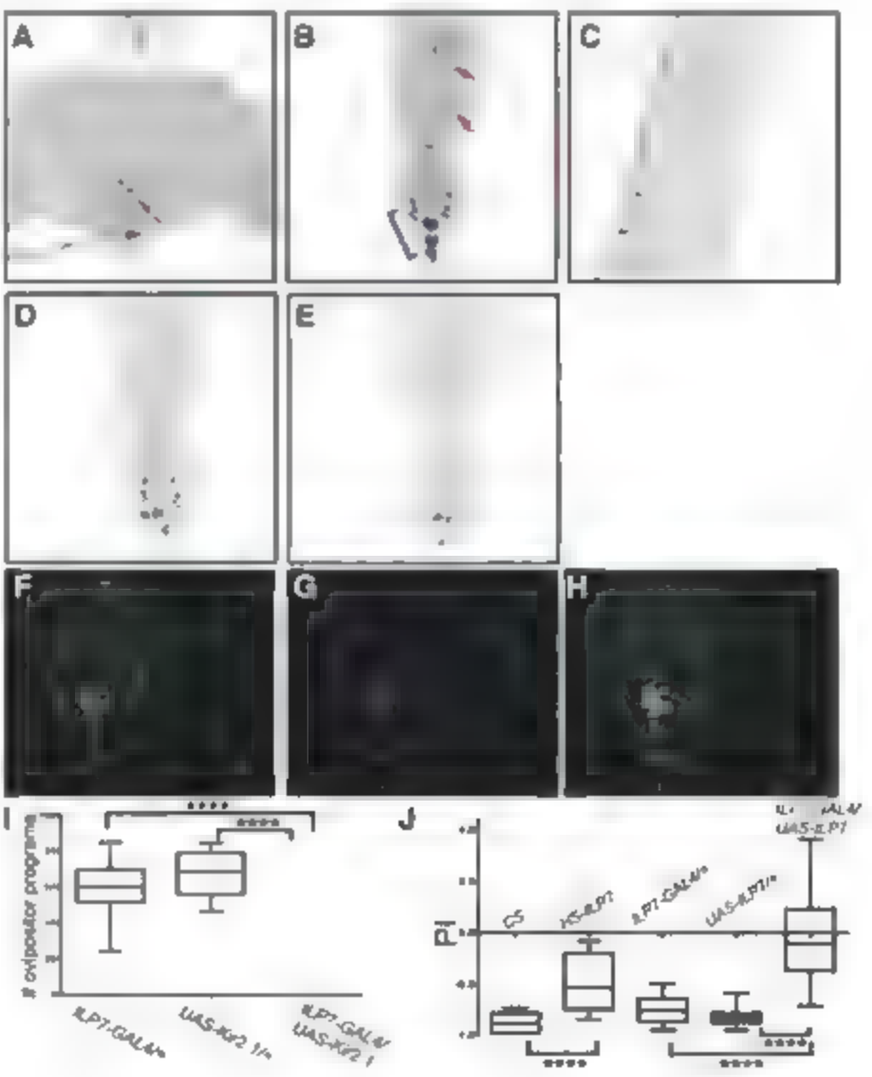

Fig. 4. Adequate level of ILP7 is important for normal egg-laying and proper bias in egg-laying site selection. (**A** to **C**) ILP7 antibody staining in adults. (A) *ILP7*-neurons send projection into SOG (red arrow) in the brain. (B) ILP7 is present in very few cells (blue bracket), with distinctive projection in the thoracic segments in ventral nerve cord (red arrow). (C) ILP7 is also present on the female internal reproductive tract. (**D** and **E**) Specificity of ILP7 antibodies was confirmed by the reduced signal in animals that overexpress an *ILP7 RNAi* construct (E) (D) Staining control. (**F** to **H**) *ILP7-GAL4* specificity was confirmed by the colocalization of signals from ILP7 staining (F) and *UAS-nuclear-RFP* expressed by *ILP7-GAL4* (G) in the same cells (H). (**I**) Reducing neuronal function of *ILP7*-neurons through *Kir2.1* overexpression causes a loss of ovipositor program. For the two control groups, number of eggs laid was used to substitute for the number of ovipositor program. The number of assays and the sample means are (20, 59.7), (20, 67.2), and (10, 0). ****$P < 0.0001$, Mann-Whitney Test. (**J**) Animals carrying an *HS-ILP7* construct or overexpressing *UAS-ILP7* by *ILP7-GAL4* avoided sucrose medium significantly less than control animals in sucrose versus lobeline two-choice assays. Number of assays used and sample means are (21, −0.87), (23, −0.51), (15, −0.73), (20, −0.86), and (20, −0.11). ****$P < 0.0001$, Mann-Whitney Test. *HS-ILP7* animals that were raised at 18°C show comparable sucrose avoidance to control animals in sucrose versus plain two-choice assays ($P > 0.5$, Mann-Whitney Test). Number of assays used and sample means are (14, −0.88) versus (34, −0.9).

fig. S4). Using the *GAL4-UAS* approach, we found that females with hyperpolarized *ILP7*-neurons showed no discernable developmental defects but displayed virtually no oviposition motor programs and are thus sterile (Fig. 4I). To distinguish between the possibility that *ILP7*-neurons are required merely for housekeeping processes to push the egg through the internal reproductive tract [which could account for the fully penetrant egg-jamming phenotype due to silencing *ILP7*-neurons (fig. S5)] and the possibility that *ILP7*-neurons also participate in conveying the "acceptability" of potential laying options to the reproductive system (e.g., the reproductive tract and the oviposition motor program), we examined the effect of elevated *ILP7* level in *ILP7*-neurons or ubiquitously on egg-laying choice (Fig. 4J and fig. S6). In both cases, the elevation of *ILP7* level caused the animals to be more receptive to laying eggs on the sucrose medium in the "regular" two-choice chambers (Fig. 4J). These results are consistent with the idea that ILP7 might participate in the relay of the appropriateness of a given option to the reproductive systems to execute egg-laying on that option.

Drosophila females can accept or avoid a given sucrose-containing medium for egg-laying depending on context. Whereas such context-dependent avoidance of high-sucrose medium shows little discernable advantage in the laboratory setting [embryo hatching rate on sucrose-containing and lobeline-containing media are comparable (fig. S3)], it could have been selected by virtue of predation avoidance and larval dietary balance (protein-carbohydrate ratio). Our finding that *Drosophila* employs a simple decision-making process in selecting egg-laying sites raises the possibility that the fruit fly has the capacity to compute and assess available options by performing integrations and amplifications in its nervous system. Dopamine and octopamine are both candidates for mediating such amplification integration processes: The former is important for decision-making in primates and flies (*16*–*18*) and is used to signal the unconditional stimulus of "punishment" during learning tasks in *Drosophila* (*19*, *20*); the latter is a reinforcing signal for appetitive conditioning in both *Drosophila* and honeybees (*19*–*21*) and an important regulator of egg-laying in *Drosophila* (*22*). In addition, our work suggests that the *ILP7*-expressing neurons are important for proper execution of egg-laying decisions, thus providing an additional anatomical and molecular entry point into dissecting the decision-making processes during egg-laying site selection.

References and Notes

1. W. van Delden, A. Kamping, *Behav. Genet.* **20**, 661 (1990).
2. T. Takamura, Y. Fuyama, *Behav. Genet.* **10**, 105 (1980).
3. R. Allemand, J. Bouletreau-Merle, *Experientia* **45**, 1147 (1989).
4. A. Spradling, in *The Development of Drosophila melanogaster*, M. Bate, A. Martinez Arias, Eds. (Cold Spring Harbor Laboratory Press, Woodbury, NY, 1993), pp. 1–70.
5. R. C. Richmond, J. L. Gerberg, *Behav. Genet.* **9**, 233 (1979).
6. K. T. Elvin, *Behav. Genet.* **27**, 171 (1997).
7. K. J. Thompson, *J. Exp. Biol.* **122**, 387 (1986).
8. E. A. Hallem, A. Dahanukar, J. R. Carlson, *Annu. Rev. Entomol.* **51**, 113 (2006).
9. S. Marella *et al.*, *Neuron* **49**, 285 (2006).
10. F. Mery, T. J. Kawecki, *Proc. Natl. Acad. Sci. U.S.A.* **99**, 14274 (2002).
11. S. Chyb, A. Dahanukar, A. Wickens, J. R. Carlson, *Proc. Natl. Acad. Sci. U.S.A.* **100** (suppl. 2), 14526 (2003).
12. R. A. Barnes, J. P. Uhler, A. Thompson, S. T. Sweeney, M. Bate, *J. Neurosci.* **21**, 1523 (2001).
13. W. Broglio *et al.*, *Curr. Biol.* **11**, 213 (2001).
14. P. Hodson, J. Haley, M. Cronk, J. Shine, H. Niall, *Nature* **291**, 127 (1981).
15. L. C. Ryner *et al.*, *Cell* **87**, 1079 (1996).
16. L. P. Sugrue, G. S. Corrado, W. T. Newsome, *Nat. Rev. Neurosci.* **6**, 363 (2005).
17. W. Schultz, P. Dayan, P. R. Montague, *Science* **275**, 1593 (1997).
18. K. Zhang, J. Z. Guo, Y. Peng, W. Xi, A. Guo, *Science* **316**, 1901 (2007).
19. M. Schwaerzel *et al.*, *J. Neurosci.* **23**, 10495 (2003).
20. C. Schroll *et al.*, *Curr. Biol.* **16**, 1741 (2006).
21. M. Hammer, R. Menzel, *Learn. Mem.* **5**, 146 (1998).
22. M. Monastirioti, C. E. Linn Jr., K. White, *J. Neurosci.* **16**, 3900 (1996).

23. We wish to dedicate this paper to Seymour Benzer who pioneered the field of *Drosophila* neurogenetics. We are very grateful to K. Scott, G. Davis, B. Baker, J. Carlson, B. Dickson, and the Bloomington Stock Center for reagents. We thank Q. Yuan and W. Song for suggestions on the behavioral set-up and experiments. This work is supported by an NIH grant (RO1 NS40929) to Y.-N. J. and a Swiss National Foundation grant to E. H. C.-H. Y. was supported by a Jane Coffin Childs fellowship. Y.-N. J. and L.Y.J. are investigators of the Howard Hughes Medical Institute.

Supporting Online Material

www.sciencemag.org/cgi/content/full/319/5870/1679/DC1
Materials and Methods
Figs. S1 to S7
Movies S1 to S3

17 October 2007; accepted 21 February 2008
10.1126/science.1151842

Protein Synthesis and Neurotrophin-Dependent Structural Plasticity of Single Dendritic Spines

Jun-ichi Tanaka,[1,2,3]* Yoshihiro Horiike,[1,2]* Masanori Matsuzaki,[1,2,3,4] Takashi Miyazaki,[1,2,3] Graham C. R. Ellis-Davies,[5] Haruo Kasai[1,2,3]†

Long-term potentiation (LTP) at glutamatergic synapses is considered to underlie learning and memory and is associated with the enlargement of dendritic spines. Because the consolidation of memory and LTP require protein synthesis, it is important to clarify how protein synthesis affects spine enlargement. In rat brain slices, the repetitive pairing of postsynaptic spikes and two-photon uncaging of glutamate at single spines (a spike-timing protocol) produced both immediate and gradual phases of spine enlargement in CA1 pyramidal neurons. The gradual enlargement was strongly dependent on protein synthesis and brain-derived neurotrophic factor (BDNF) action, often associated with spine twitching, and was induced specifically at the spines that were immediately enlarged by the synaptic stimulation. Thus, this spike-timing protocol is an efficient trigger for BDNF secretion and induces protein synthesis–dependent long-term enlargement at the level of single spines.

The consolidation of memory and long-term potentiation (LTP) require protein synthesis (*1*, *2*). Therefore, it is important to clarify whether protein synthesis can regulate synaptic plasticity at the level of a single synapse and how it affects synaptic structure. The spine enlargement associated with LTP can be immediately induced by intensive stimulation of postsynaptic *N*-methyl-D-aspartate (NMDA)–sensitive glutamate receptors (the conventional protocol) in CA1 pyramidal neurons (*3*–*5*). Thus, spine enlargement can be induced even in the absence of postsynaptic spikes (*3*), although if synaptic stimulation is closely followed in time by postsynaptic spikes (a spike-timing protocol), a more robust form of LTP is induced that plays an important role in the development and learning of neuronal networks (*6*). In rat brain slices, we examined the structural plasticity of dendritic spines induced by the stimulation of single spines, using two-photon uncaging of glutamate (*7*) in the absence or presence of postsynaptic spikes in CA1 pyramidal neurons (uncaging is photorelease from a biologically inert precursor).

CA1 pyramidal neurons in slice culture were subjected to whole-cell perfusion with a solution containing the fluorescent dye Alexa594 (50 μM) and β-actin (5 μM) (*8*). The latter protein was

[1]Laboratory of Structural Physiology, Center for Disease Biology and Integrative Medicine, Graduate School of Medicine, University of Tokyo, Tokyo 113-0033, Japan. [2]Center for NanoBio Integration, University of Tokyo, Tokyo 113-0033, Japan. [3]Department of Cell Physiology, National Institute for Physiological Sciences, and Graduate University of Advanced Studies (SOKENDAI), Myodaiji, Okazaki 444-8787, Japan. [4]PRESTO, Japan Science and Technology Agency, 4-1-8 Honcho, Kawaguchi, Saitama, Japan. [5]Department of Pharmacology and Physiology, Drexel University College of Medicine, Philadelphia, PA 19102, USA.

*These authors contributed equally to this work.
†To whom correspondence should be addressed. E-mail: hkasai@m.u-tokyo.ac.jp

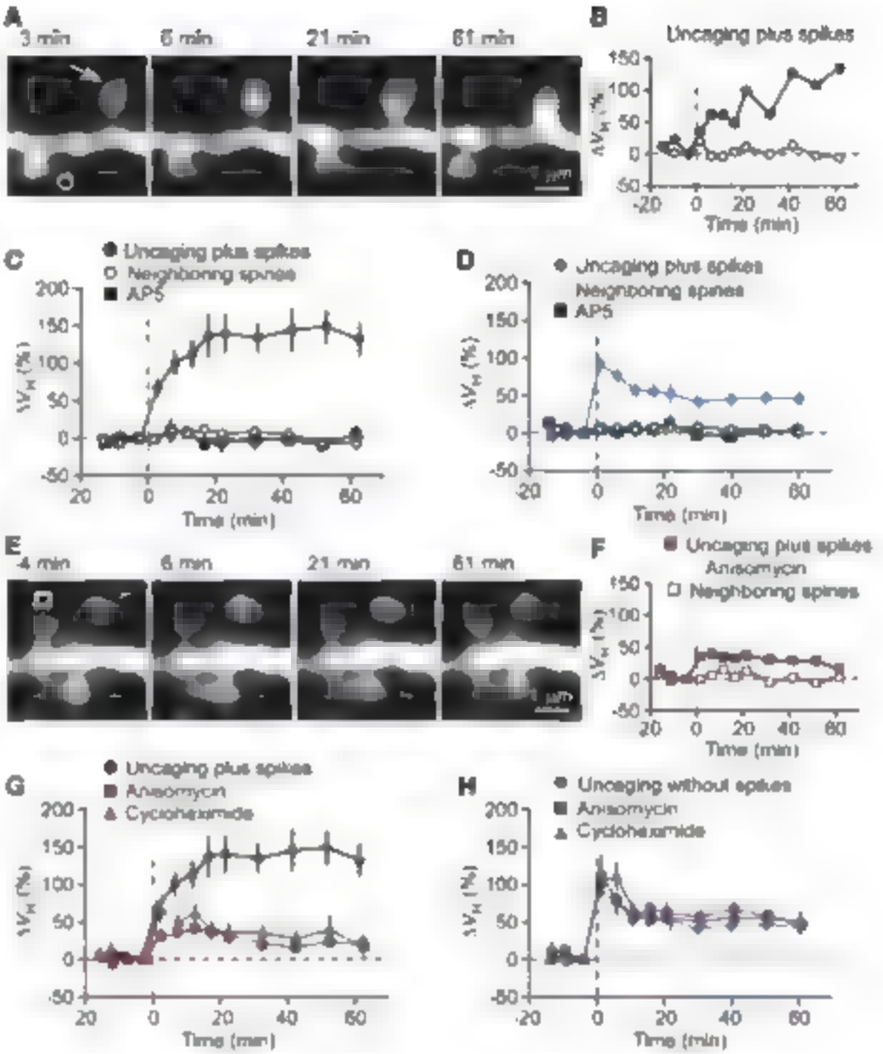

Fig. 1. Spine-head enlargement induced by uncaging of glutamate with or without the application of postsynaptic spikes for single identified spines of CA1 pyramidal neurons in hippocampal slice culture. (**A** and **E**) Time-lapse z-integrated (z-stack) images of spines stimulated at time 0 by uncaging plus spikes in the absence (A) or presence (E) of anisomycin. Arrows indicate spots of two-photon uncaging of MNI-glutamate; open symbols indicate neighboring spines. (**B** and **F**) Time courses of changes in ΔV_H for the stimulated (solid symbols) and neighboring (open symbols) spines shown in (A) and (E), respectively. (**C** and **D**) Averaged time courses of changes in ΔV_H for spines stimulated by uncaging plus (C) or without (D) spikes in the absence (solid circles) or presence (solid squares) of APS. Open circles represent data from neighboring spines in the absence of APS (open circles). Uncaging without spikes was performed in a Mg^{2+}-free solution. Data are means ± SEM (n = 10 to 27 spines). The control trace shown in (C) and (G) was the average of 27 experiments performed in the same batches of slice preparations used for the test experiments. (**G** and **H**) Averaged time courses of changes in spine-head volume for spines stimulated by uncaging plus (G) or without (H) spikes in the absence (circles) or presence of anisomycin (red squares) or cycloheximide (green triangles). Data are means ± SEM (n = 7 to 27 spines).

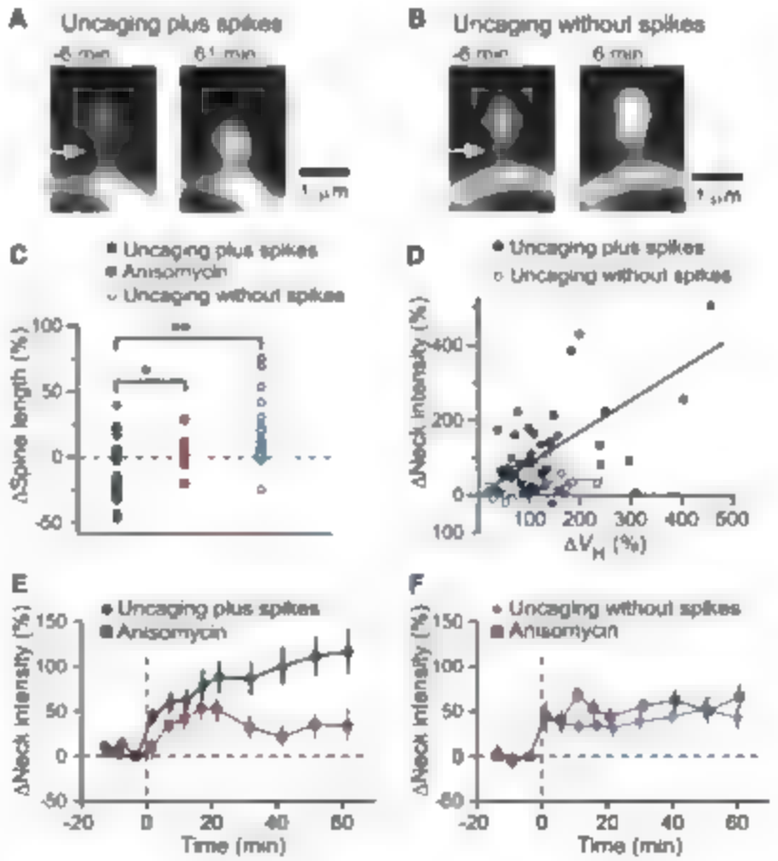

Fig. 2. Spine-neck plasticity induced by glutamate uncaging plus or without postsynaptic spikes. (**A** and **B**) Images of spines before (left) and after (right) uncaging of MNI-glutamate with (A) or without (B) spikes. Arrows indicate the spine necks. (**C**) Changes in spine length induced either by uncaging plus spikes in the absence (black circles) or presence (red squares) of anisomycin or by uncaging without spikes (blue circles). $^*P < 0.05$, $^{**}P < 0.01$ (Mann-Whitney U test). (**D**) Correlation between the increases in spine-neck fluorescence intensity and ΔV_H induced by uncaging plus (black circles; Spearman's correlation coefficient = 0.37, $P = 0.013$) or without (blue circles, $P = 0.16$) spikes. Data correspond to the increases observed at the time of maximal spine-head enlargement. (**E** and **F**) Time courses of changes in spine-neck fluorescence intensity for spines stimulated by uncaging plus (E) or without (F) spikes in the absence or presence of anisomycin. Data are means ± SEM (n = 10 to 41 spines).

included because we found that it delayed the washout of plasticity (*3*) (fig. S1 and supporting online text). We detected marked (>50%) increases in spine-head volume (ΔV_H) in most (37 of 41) small spines stimulated by repetitive (80 times at 1 Hz) uncaging of 4-methoxy-7-nitroindolinyl (MNI) glutamate paired with postsynaptic spikes within 20 ms (spike-timing protocol or uncaging plus spikes) (Fig. 1, A to C). Spine enlargement was not induced by repetitive glutamate uncaging (1.6 ± 6.6%, n = 9 spines, in the presence of Mg^{2+}) or spike application alone (−3.0 ± 2.6%, n = 54). It was also not induced when spikes were triggered ~50 ms after uncaging (3.9 ± 3.4%, n = 10). Spine enlargement was restricted to stimulated spines; it did not spread to neighboring spines (Fig. 1, A to C). The NMDA receptor blocker (*R*)-2-amino-5-phosphonopentanoic acid (AP5, 50 μM) prevented spine enlargement induced by uncaging plus spikes (n = 9) (Fig. 1C), as well as conventional enlargement (*3*) induced by uncaging without spikes in a Mg^{2+}-free solution (Fig. 1D) (*8*). Subsequent experiments were performed with small spines (V_H < 0.1 μm^3), most (95%) of which underwent enlargement in response to uncaging plus spikes (fig. S2). The enlargement was associated with an increase in postsynaptic glutamate sensitivity (fig. S3, A to D).

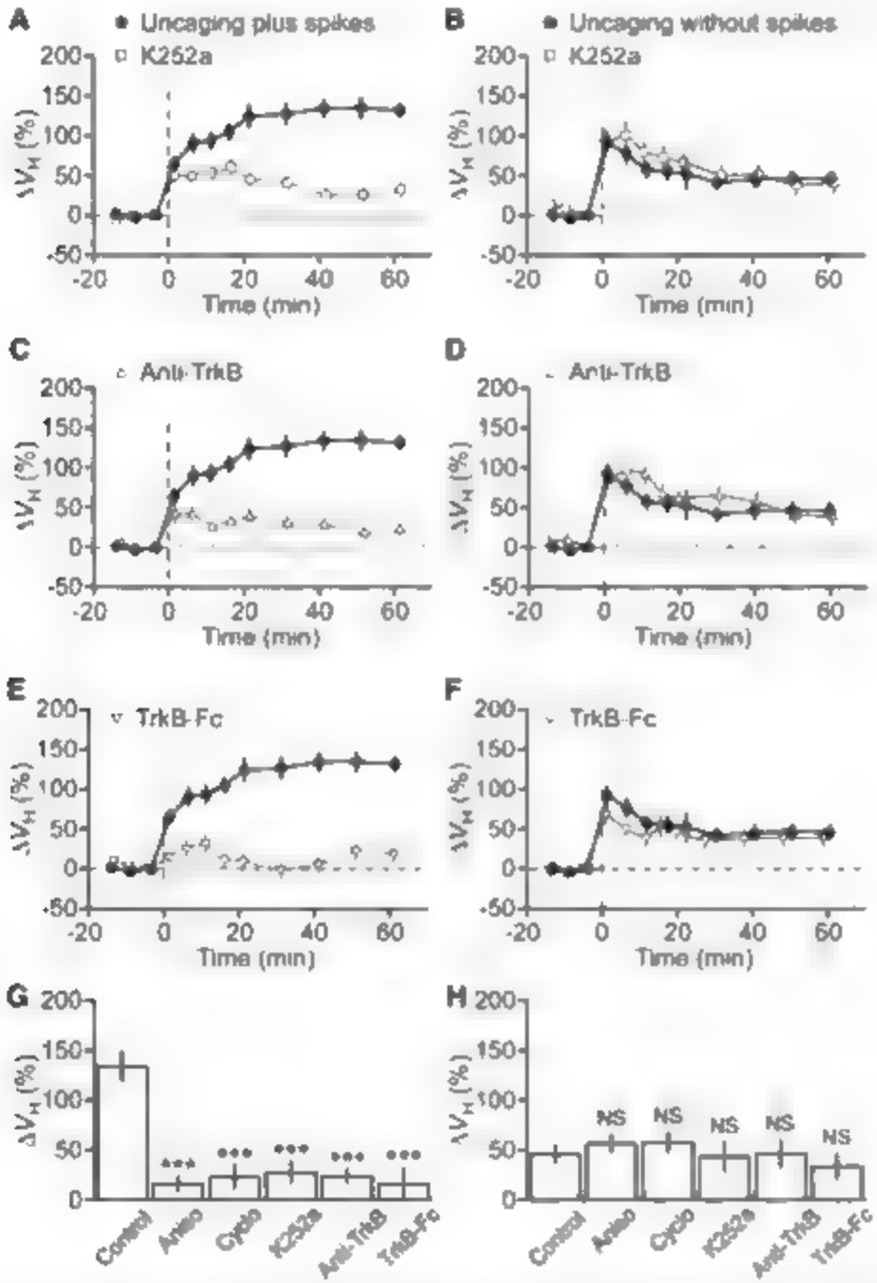

Fig. 3. Dependence of the gradual, long-term enlargement of spine heads on BDNF-TrkB signaling (**A** to **F**) Effects of inhibitors of BDNF-TrkB signaling, including K252a [(A) and (B)], an antibody to TrkB [(C) and (D)], and TrkB-Fc [(E) and (F)] on the time course of spine-head enlargement induced by glutamate uncaging plus [(A), (C), and (E), or without [(B), (D), and (F)] postsynaptic spikes. The control traces are the average of 14 and 20 experiments for uncaging plus and without spikes, respectively, performed in the same batches of slice preparations used for the test experiments. (**G** and **H**) Mean enlargement of spine heads measured 40 to 60 min after the onset of uncaging plus (G) or without (H) spikes in the absence (control) or presence of inhibitors of protein synthesis or BDNF-TrkB signaling. All data are means ± SEM (n = 8 to 20 spines). ***P < 0.001 versus corresponding control value (Mann-Whitney U test). NS, not significant.

We found critical differences between spine enlargement induced by uncaging plus spikes and that induced by uncaging without spikes (Figs. 1 to 3). First, the former protocol induced a secondary long-term phase (Fig. 1, B and C), unlike the latter one (Fig. 1D). The total ΔV_H apparent after a 60-min recording period was 132 ± 22% (n = 27) (Fig. 1C) for uncaging plus spikes as compared with only 45.7 ± 9.6% for uncaging without spikes (n = 20) (Fig. 1D). A similar difference was apparent in the increases in the amplitude of glutamate-induced currents evoked at the spines, which were 162 ± 38% (n = 12) (fig. S3B) and 36 ± 7% (n = 9) for uncaging plus or without (*3*) spikes, respectively. The larger long-term enlargement was not simply ascribed to the strength of stimulation, because the immediate enlargement produced by uncaging plus spikes (67.5 ± 11.2%, mean ± SEM) (Fig. 1C) was smaller than that induced by uncaging without spikes (*3*) (92.4 ± 10.7%, P = 0.01) (Fig. 1D).

The gradual long-term phase of spine-head enlargement was entirely dependent on protein synthesis. Pretreatment of hippocampal slices with the protein synthesis inhibitors anisomycin (n = 10 spines) or cycloheximide (n = 8) abolished this secondary phase (Fig. 1, E to G) without substantially affecting the immediate phase (Fig. 1, F and G). Anisomycin also blocked the gradual long-term increase in the size of glutamate-induced currents at the stimulated spines (fig. S3, E and F). In contrast, spine enlargement elicited by uncaging without spikes was unaffected by anisomycin (n = 11) (Fig. 1D and fig. S4, C and D) or cycloheximide (n = 7). This was the case even when the number of repetitive stimulation was further increased (up to 80 times, n = 18).

Uncaging plus spikes often induced shortening of the spine length, or spine twitching (Figs. 1A and 2A). Apparent shortening of spines was detected in 23 out of 41 spines (mean = 9.9 ± 2.2%) (Fig. 2C), and in the remaining spines, it appeared to be canceled out by the enlargement of the spine heads. In contrast, spine twitching was rarely (2 out of 20) induced by uncaging without spikes (Fig. 2B and fig. S4A); rather, such spines often elongated as a result of spine-head enlargement (6.7 ± 4.9%) (Fig. 2C). To examine the spine-neck plasticity and its time course, we measured the fluorescence intensity of the spine neck (*8*), because it was difficult to delineate the spine-neck unambiguously, particularly when spines twitched. We detected pronounced increases in spine-neck fluorescence produced by uncaging plus spikes (128 ± 19%, mean ± SEM, n = 41) (Fig. 2D), but far less fluorescence was produced by uncaging without

spikes (43 ± 12%, $n = 20$). The increase in spine-neck fluorescence was not correlated with that in ΔV_H in uncaging without spikes (Fig. 2D), indicating that the increase in spine-neck fluorescence did not simply represent spine-head enlargement. The increase in spine-neck fluorescence occurred gradually in parallel with spine-head enlargement (Figs. 1A and 2E) and was inhibited by anisomycin (Figs. 1F and 2E), as was spine twitching (2.0 ± 1.9%) (Fig. 2C). In contrast, the smaller increase in neck fluorescence induced by uncaging without spikes was unaffected by anisomycin (Fig. 2F). The spine twitching may involve the spine apparatus (9) and translation machinery in the spine necks (*10, 11*) for protein synthesis–dependent spine-head enlargement.

A late phase of LTP has been shown to require BDNF (*12–14*), although the nature of this requirement varies depending on the induction protocol (*15–18*). We therefore investigated whether BDNF might play a role in the gradual long-term spine enlargement induced by uncaging plus spikes. K252a (200 nM), a tyrosine kinase inhibitor that blocks BDNF-TrkB signaling, abolished long-term enlargement of spine heads ($n = 13$) (Fig. 3, A and G), whereas it had no effect on the immediate enlargement induced by uncaging plus spikes (Fig. 3A) or without spikes ($n = 15$) (Fig. 3, B and H). The long-term enlargement of spine heads was also blocked by an antibody to TrkB ($n = 9$) (Fig. 3, C and G), whereas the same antibody did not affect the immediate enlargement induced by uncaging plus spikes (Fig. 3C) or without spikes ($n = 8$) (Fig. 3, D and H). Activation of TrkB induced by uncaging plus spikes was dependent on the secretion of BDNF, given that the long-term enlargement of spine heads was also abolished by a TrkB-Fc fusion protein that acts as a scavenger of BDNF ($n = 10$) (Fig. 3, E and G). Again, the immediate spine-head enlargement induced by uncaging without spikes was largely unaffected by the scavenger ($n = 10$) (Fig. 3, F and H).

Moreover, the increase in spine-neck fluorescence induced by uncaging plus spikes was abolished by K252a, the antibody to TrkB, or TrkB-Fc (fig. S5). The gradual long-term plasticity of spine structures was thus strongly dependent on the endogenous secretion of BDNF and postsynaptic spikes were required for the secretion.

Finally, we examined whether exogenous BDNF might be able to replace postsynaptic spikes in the induction of protein synthesis–dependent spine-head enlargement. Bath application of a low concentration (20 ng/ml) of BDNF did not by itself induce spine-head enlargement ($n = 30$) (Fig. 4A) or inward currents (0.5 ± 1.2 pA, $n = 5$) (Fig. 4B) (*19, 20*). However, uncaging without spikes in the presence of BDNF (20 ng/ml) resulted in marked enhancement in the long-term phase of spine-head enlargement ($n = 16$) as compared with that observed in the absence of BDNF ($n = 20$) (Fig. 4, C and D, and supporting online text). BDNF also induced gradual increases in spine-neck fluorescence (110 ± 21%, $P < 0.05$) (Fig. 4C). The effect of BDNF was selective for stimulated spines, was not observed for neighboring spines ($n = 16$) (Fig. 4D), and was blocked by anisomycin ($n = 11$) (Fig. 4D). BDNF thus induced additional spine-head enlargement that was dependent on protein synthesis and specific to stimulated spines. BDNF could induce spine-head enlargement even when applied 0.5 min ($n = 17$) after the offset of stimulation, but it did not do so when applied 10 min after stimulation ($n = 10$) (Fig. 4E). Exogenous BDNF did not further augment the spine-head enlargement induced by uncaging plus spikes ($n = 6$) (Fig. 4F), suggesting that a sufficient amount of BDNF was released in response to synaptic stimulation paired with postsynaptic spikes. The spine-head enlargement induced by uncaging plus spikes was blocked by anisomycin even in the presence of BDNF ($n = 9$) (Fig. 4F), indicating that protein synthesis is required for the action of BDNF.

We have shown that synaptic stimulation paired with postsynaptic spikes induces a gradual long-term enlargement of spine heads that is mediated by BDNF and dependent on protein synthesis (fig. S7). In contrast, synaptic stimulation alone was not sufficient to trigger BDNF secretion (fig. S7), even though it induces a marked increase in the intracellular calcium concentration ($[Ca^{2+}]_i$ (>10 μM) of spines via NMDA receptors (*21*). Because BDNF secretion is not induced by a 1-Hz spike train alone (*22–24*), our data suggest that the secretion of this neurotrophin is responsive to the synchrony of synaptic input and postsynaptic spikes. Given that such synchronous events result in only a short-lasting influx of Ca^{2+} through NMDA receptors during each spike (<2 μM) (*24, 25*), postsynaptic spikes must play the key role in the exocytosis of BDNF, for example, involving $Ca^{2+}{}_i$ increases in the dendritic shaft via voltage-gated Ca^{2+} channels. Thus, BDNF secretion is

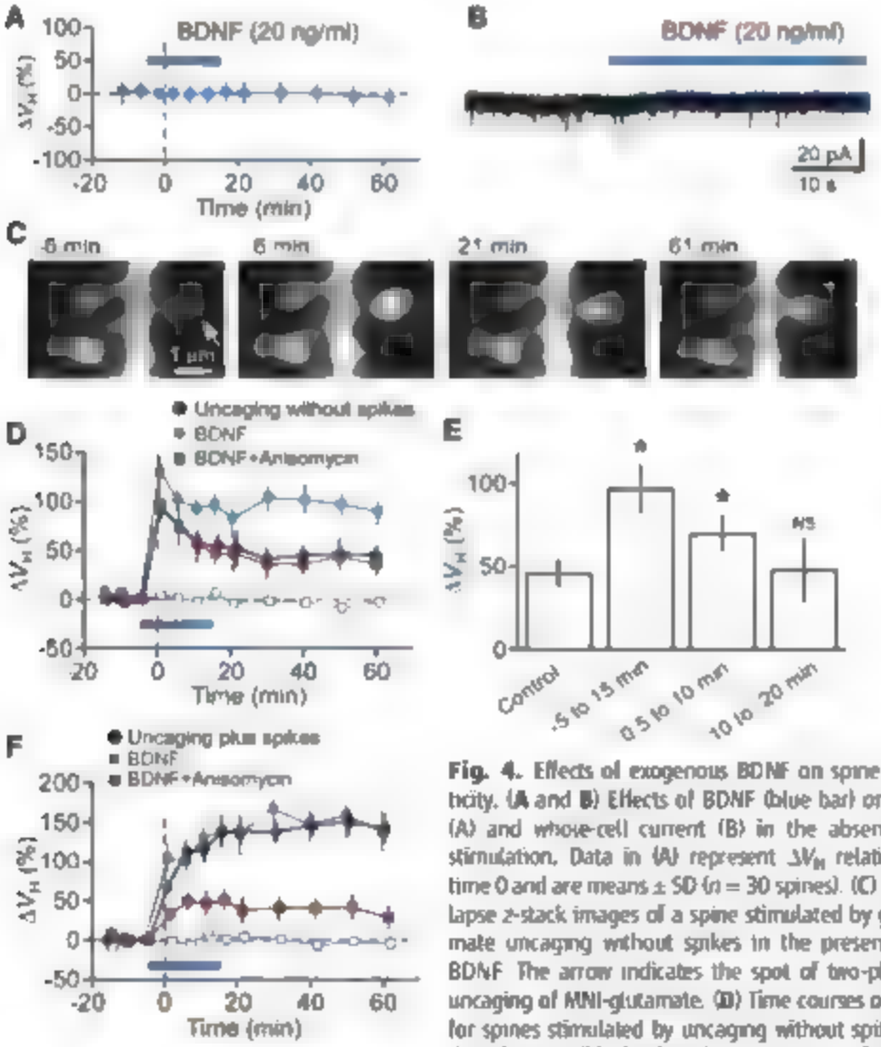

Fig. 4. Effects of exogenous BDNF on spine plasticity. (**A** and **B**) Effects of BDNF (blue bar) on ΔV_H (A) and whole-cell current (B) in the absence of stimulation. Data in (A) represent ΔV_H relative to time 0 and are means ± SD ($n = 30$ spines). (**C**) Time-lapse z-stack images of a spine stimulated by glutamate uncaging without spikes in the presence of BDNF. The arrow indicates the spot of two-photon uncaging of MNI-glutamate. (**D**) Time courses of ΔV_H for spines stimulated by uncaging without spikes in the absence (black circles) or presence of BDNF either alone (solid blue squares) or together with anisomycin (red squares). The effect of BDNF on neighboring spines (open blue squares) was also determined. Data are means ± SEM ($n = 11$ to 20 spines). (**E**) Spine-head enlargement induced by uncaging without spikes in the absence or presence of BDNF during the indicated time periods after the offset of synaptic stimulation (0 min). Data are means ± SEM ($n = 10$ to 20 spines). *$P < 0.05$ versus control value (Mann-Whitney *U* test). (**F**) Spine-head enlargement induced by uncaging plus spikes in the absence or presence of exogenous BDNF and anisomycin as in (D).

timely regulated by correlated activities in a neuronal network and may consolidate nearby stimulated synapses by autocrine or paracrine mechanisms. BDNF action was selective on the spines that showed immediate enlargement, which may act as the structural tag for selective trapping (*26*) of the protein-synthetic machinery (*11*, *27*) and the capture of plasticity proteins (*2*, *28*) for long-term spine-head enlargement. Thus, BDNF acts as an associative messenger for the consolidation of synaptic plasticity, and the protein-synthetic process can regulate dendritic structures at the level of single spines.

References and Notes

1. L. R. Squire, *Memory and Brain* (Oxford Univ. Press, New York, 1987).
2. R. J. Kelleher III, A. Govindarajan, S. Tonegawa, *Neuron* **44**, 59 (2004).
3. M. Matsuzaki, N. Honkura, G. C. Ellis-Davies, H. Kasai, *Nature* **429**, 761 (2004).
4. K. Okamoto, T. Nagai, A. Miyawaki, Y. Hayashi, *Nat. Neurosci.* **7**, 1104 (2004).
5. C. D. Kopec, B. Li, W. Wei, J. Boehm, R. Malinow, *J. Neurosci.* **26**, 2000 (2006).
6. Y. Dan, M. M. Poo, *Physiol. Rev.* **86**, 1033 (2006).
7. M. Matsuzaki *et al.*, *Nat. Neurosci.* **4**, 1086 (2001).
8. Materials and methods are available as supporting material on *Science* Online.
9. J. Spacek, K. M. Harris, *J. Neurosci.* **17**, 190 (1997).
10. O. Steward, W. B. Levy, *J. Neurosci.* **2**, 284 (1982).
11. C. Job, J. Eberwine, *Nat. Rev. Neurosci.* **2**, 889 (2001).
12. S. L. Patterson *et al.*, *Neuron* **16**, 1137 (1996).
13. L. Minichiello *et al.*, *Neuron* **24**, 401 (1999).
14. M. M. Poo, *Nat. Rev. Neurosci.* **2**, 24 (2001).
15. A. Figurov, L. D. Pozzo-Miller, P. Olafsson, T. Wang, B. Lu, *Nature* **381**, 706 (1996).
16. H. Kang, A. A. Welcher, D. Shelton, E. M. Schuman, *Neuron* **19**, 653 (1997).
17. S. L. Patterson *et al.*, *Neuron* **32**, 123 (2001).
18. Y. Ma, M. M. Poo, *Neuron* **50**, 115 (2006).
19. R. Blum, K. W. Kafitz, A. Konnerth, *Nature* **419**, 687 (2002).
20. H. S. Li, X. Z. Xie, C. Montell, *Neuron* **24**, 261 (1999).
21. J. Noguchi, M. Matsuzaki, G. C. R. Ellis-Davies, H. Kasai, *Neuron* **46**, 609 (2005).
22. A. Gartner, V. Stager, *Proc. Natl. Acad. Sci. U.S.A.* **99**, 6386 (2002).
23. G. Acardi *et al.*, *Proc. Natl. Acad. Sci. U.S.A.* **101**, 15788 (2004).
24. R. Yuste, W. Denk, *Nature* **375**, 682 (1995).
25. T. Nevian, B. Sakmann, *J. Neurosci.* **26**, 11001 (2006).
26. F. Santamaria, S. Wils, S. E. De, G. J. Augustine, *Neuron* **52**, 635 (2006).
27. L. E. Ostroff, J. C. Fiala, B. Allwardt, K. M. Harris, *Neuron* **35**, 535 (2002).
28. U. Frey, R. G. Morris, *Nature* **385**, 533 (1997).

29. This work was supported by grants-in-aid from MEXT of Japan (H.K. and M.M.), the Global COE Program (Integrative Life Science) of MEXT (H.K.), and NIH (G.C.R.E.-D. and H.K.).

Supporting Online Material

www.sciencemag.org/cgi/content/full/1152864/DC1
Materials and Methods
Text
Figs. S1 to S7
References

12 November 2007; accepted 21 January 2008
Published online 28 February 2008;
10.1126/science.1152864
Include this information when citing this paper.

Spending Money on Others Promotes Happiness

Elizabeth W. Dunn,[1]* Lara B. Aknin,[1] Michael I. Norton[2]

Although much research has examined the effect of income on happiness, we suggest that how people spend their money may be at least as important as how much money they earn. Specifically, we hypothesized that spending money on other people may have a more positive impact on happiness than spending money on oneself. Providing converging evidence for this hypothesis, we found that spending more of one's income on others predicted greater happiness both cross-sectionally (in a nationally representative survey study) and longitudinally (in a field study of windfall spending). Finally, participants who were randomly assigned to spend money on others experienced greater happiness than those assigned to spend money on themselves.

Can money buy happiness? A large body of cross-sectional survey research has demonstrated that income has a reliable but surprisingly weak effect on happiness within nations (*1*–*3*), particularly once basic needs are met (*4*). Indeed, although real incomes have surged dramatically in recent decades, happiness levels have remained largely flat within developed countries across time (*5*). One of the most intriguing explanations for this counterintuitive finding is that people often pour their increased wealth into pursuits that provide little in the way of lasting happiness, such as purchasing costly consumer goods (*6*). An emerging challenge, then, is to identify whether and how disposable income might be used to increase happiness.

Ironically, the potential for money to increase happiness may be subverted by the kinds of choices that thinking about money promotes; the more thought of having money makes people less likely to help acquaintances, to donate to charity, or to choose to spend time with others (*7*), precisely the kinds of behaviors that are strongly associated with happiness (*8*–*12*). At the same time, although thinking about money may drive people away from prosocial behavior, money can also provide a powerful vehicle for accomplishing such prosocial goals. We suggest that using money in this fashion—investing income in others rather than oneself—may have measurable benefits for one's own happiness.

As an initial test of the relation between spending choices and happiness, we asked a nationally representative sample of 632 Americans (55% female) to rate their general happiness, to report their annual income, and to estimate how much they spent in a typical month on (i) bills and expenses, (ii) gifts for themselves, (iii) gifts for others, and (iv) donations to charity (*13*). The first two categories were summed to create an index of personal spending [mean (M) = $1,713.91, SD = 1895.65], and the latter two categories were summed to create an index of prosocial spending (M = $145.96, SD = 306.06). Entering the personal and prosocial spending indices simultaneously into a regression predicting general happiness revealed that personal spending was unrelated to happiness (standardized regression coefficient β = 0.02, NS), but higher prosocial spending was associated with significantly greater happiness (β = 0.11, $P < 0.01$). When we included income in this regression, we found that the effects of income (β = 0.11, $P < 0.01$) and prosocial spending (β = 0.10, $P < 0.03$) were independent and similar in magnitude, whereas personal spending remained unrelated to happiness (β = 0.04, NS). Although the correlational nature of this design precludes causal inferences, this study provides initial evidence that how people spend their money may be as important for their happiness as how much money they earn—and that spending money on others might represent a more effective route to happiness than spending money on oneself (*13*).

If this interpretation is correct, then people who receive an economic windfall should experience greater happiness after receiving the windfall if they spend it on others rather than themselves, even controlling for happiness before the windfall. We tested this prediction by examining the happiness of 16 employees before and after they received a profit-sharing bonus from their company (*13*). One month before receiving this bonus (M = $4918.64, SD = 1816.98), the employees reported their general happiness as well as their annual income. Approximately 6 to 8 weeks after receiving the bonus, participants again reported their general happiness and then reported what percentage of their bonus they had spent on (i) bills and expenses, (ii) rent or mortgage, (iii) buying something for themselves, (iv) buying something for someone else, (v) donating to charity, and (vi) other. The first three categories were summed to create an index of personal spending

[1]Department of Psychology, 2136 West Mall, the University of British Columbia, Vancouver, BC V6T 1Z4, Canada. [2]Marketing Unit, 189 Morgan Hall, Harvard Business School, Soldiers Field Road, Boston, MA 02163, USA.

*To whom correspondence should be addressed. E-mail: edunn@psych.ubc.ca

(M = 63.44, SD = 38.20), and the fourth and fifth categories were summed to create an index of prosocial spending (M = 12.19, SD = 18.35).

Entering Time 1 happiness and our two spending indices into a regression predicting Time 2 happiness revealed that prosocial spending was the only significant predictor of happiness at Time 2 (β = 0.81, P < 0.02). With income included as an additional predictor in this regression (β = 0.03, NS), the effect of prosocial spending remained significant (β = 0.96, P < 0.02). Similarly, the prosocial spending effect was significant (β = 0.81, P < 0.03) when controlling for bonus amount (β = 0.00, NS). Thus, employees who devoted more of their bonus to prosocial spending experienced greater happiness after receiving the bonus, and the manner in which they spent that bonus was a more important predictor of their happiness than the size of the bonus itself (*13*).

Building on our correlational and longitudinal evidence that spending on others may promote happiness, we next demonstrated the causal impact of prosocial spending, using experimental methodology (*13*). Participants (N = 46) rated their happiness in the morning and then were given an envelope that contained either $5 or $20, which they were asked to spend by 5:00 p.m. that day. Participants randomly assigned to the personal spending condition were instructed to spend the money on a bill, an expense, or a gift for themselves, whereas participants assigned to the prosocial spending condition were instructed to spend the money on a gift for someone else or charitable donation. Participants were called after 5:00 p.m. that day and again reported their happiness. We submitted postwindfall happiness to a 2 (windfall size: $5 versus $20) × 2 (spending direction: personal versus prosocial) between-subjects analysis of covariance (ANCOVA), with prewindfall happiness included as a covariate. This analysis revealed a significant main effect of spending instructions ($F_{1,41}$ = 4.39, P < 0.04, effect size estimate (η_p^2) = 0.10), whereby participants in the prosocial spending condition (M = 0.18, SD = 0.62) reported greater postwindfall happiness than did participants in the personal spending condition (M = −0.19, SD = 0.66). Neither the main effect of windfall size ($F_{1,41}$ = 0.09, NS) nor the Windfall Size × Spending Direction interaction ($F_{1,41}$ = 0.12, NS) approached significance. These experimental results provide direct support for our causal argument that spending money on others promotes happiness more than spending money on oneself.

In moving away from the traditional focus on income toward an examination of spending choices, our perspective dovetails with recent theorizing by Lyubomirsky, Sheldon, and Schkade (*8*) on the architecture of sustainable changes in happiness. According to Lyubomirsky *et al.* (*8*), the historical focus on life circumstances (e.g., income, gender, and religious affiliation) as predictors of happiness may be somewhat misplaced: because people readily adapt to the stable circumstances of their lives, circumstantial factors tend to have rather limited long-term effects on happiness levels. Thus, intentional activities—practices in which people actively and effortfully choose to engage—may represent a more promising route to lasting happiness. Supporting this premise, our work demonstrates that how people choose to spend their money is at least as important as how much money they make.

Finally, despite the observable benefits of prosocial spending, our participants spent relatively little of their income on prosocial ends. Participants in our national survey, for example, reported devoting more than 10 times as much money for personal as for prosocial spending each month. Although personal spending is of necessity likely to exceed prosocial spending for most North Americans, our findings suggest that very minor alterations in spending allocations—as little as $5 in our final study—may be sufficient to produce nontrivial gains in happiness on a given day. Why, then, don't people make these small changes? When we provided descriptions of the four experimental conditions from our final study to a new set of students at the same university (N = 109) and asked them to select the condition that would make them happiest, Fisher's Exact Tests revealed that participants were doubly wrong about the impact of money on happiness: we found that a significant majority thought that personal spending (n = 69) would make them happier than prosocial spending (n = 40) (P < 0.01) and that $20 ($n$ = 94) would make them happier than $5 ($n$ = 15) (P < 0.0005). Given that people appear to overlook the benefits of prosocial spending, policy interventions that promote prosocial spending—encouraging people to invest income in others rather than in themselves—may be worthwhile in the service of translating increased national wealth into increased national happiness.

References and Notes

1. E. Diener, R. Biswas-Diener, *Soc. Indic. Res.* **57**, 119 (2002).
2. B. S. Frey, A. Stutzer, *Econ. J.* **110**, 918 (2000).
3. D. Kahneman, A. B. Krueger, D. Schkade, N. Schwarz, A. A. Stone, *Science* **312**, 1908 (2006).
4. E. Diener, E. Sandvik, L. Seidlitz, M. Diener, *Soc. Indic. Res.* **28**, 195 (1993).
5. R. A. Easterlin, *J. Econ. Behav. Organ.* **27**, 35 (1995).
6. R. H. Frank, *Daedalus* **133**, 69 (2004).
7. K. D. Vohs, N. L. Mead, M. R. Goode, *Science* **314**, 1154 (2006).
8. S. Lyubomirsky, K. M. Sheldon, D. Schkade, *Rev. Gen. Psychol.* **9**, 111 (2005).
9. E. Diener, M. E. P. Seligman, *Psychol. Sci.* **13**, 81 (2002).
10. P. A. Thoits, L. N. Hewitt, *J. Health Soc. Behav.* **42**, 115 (2001).
11. J. A. Piliavin, in *Flourishing: Positive Psychology and the Life Well-Lived*, C. L. M. Keyes, J. Haidt, Eds. (APA, Washington, DC, 2003), pp. 227–247.
12. T. Kasser, K. M. Sheldon, *J. Happiness Stud.* **3**, 313 (2002).
13. Materials and methods are available as supporting material on *Science* Online.

14. This work was funded by a Hampton Research Grant to the first author. We thank T. Rogers, S. Shababi and J. Beretta for data collection; J. Biesanz, I. Dar-Nimrod, D. Gilbert, S. Heine, J. Helliwell, S. Lyubomirsky, A. McConnell, V. Savalei, B. Simpson, and T. Wilson for helpful input; and J. Goldshine for his invaluable assistance.

Supporting Online Material

www.sciencemag.org/cgi/content/full/319/5870/1687/DC1
Materials and Methods
Figs. S1 to S6
Tables S1 and S2
References

25 September 2007; accepted 12 February 2008
10.1126/science.1150952

High Throughput Cellular Analysis

The Cell Lab Quanta SC MPL Flow Cytometer can be integrated into a cell culture system to provide data and cellular growth parameters for the evaluation of clone selection, cell expansion, and protein expression results. The Quanta SC MPL can be integrated online with other peripheral devices and a robotic arm that moves cell culture plates to the flow cytometer for analysis. Data from the analysis is automatically captured by the instrument's software for real-time and subsequent analysis and interpretation. The integration of this advanced flow cytometer provides an expanded range of measurements for high throughput, walkaway cell analyses, including cell count and viability, apoptosis, cell cycle, and cell surface marker. The Quanta SC features three-color fluorescence, side scatter, electronic volume, and absolute count measurements along with easy-to-use software, automated color compensation, and multiple excitation wavelengths, including ultraviolet. It can analyze a sample in as little as 30 seconds.

Beckman Coulter
For information 714-993-8955
www.beckmancoulter.com

Waterborne Contamination Prevention

The AquaTec water preservation cell is for prevention of waterborne contamination in carbon dioxide incubators and water baths. The AquaTec provides up to six months of protection from more than 600 types of bacteria, viruses, molds, and fungi without the use of harsh chemicals. It is designed for all types of laboratory water and is suitable for use in equipment from any manufacturer across a broad range of biological research temperature environments. One three-inch AquaTec cell placed into the water reservoir provides long-lasting disinfection without the need for mixing or measuring potentially hazardous materials. Self-regulation maintains the correct level of anti-microbial concentration regardless of water level, negating the need for constant monitoring and testing. The AquaTec has optional suction cups for fixation in the water bath or incubator reservoir.

ThermoFisher
For information 828-365-1205
www.thermofisher.com

PCR Competent Cells

The ExCyto PCR (polymerase chain reaction) Competent Cells express a thermostable DNA polymerase, offering a reliable, fast, and inexpensive way to screen transformed colonies. The user simply transforms ExCyto PCR Cells using any *E. coli* vector, plates and incubates overnight, picks colonies, adds them to the provided reaction mix with primers, and cycles. ExCyto PCR eliminates minipreps and the need for a purified, exogenous DNA polymerase for single colony PCR. Amplification is robust even with single-copy vectors. Amplicons up to 5 kb can be directly sequenced without purification.

Lucigen
For information 608-831-9011
www.lucigen.com

Nucleic Acid Purification Automation

The epMotion is an automated liquid handling system with ready-to-go methods for automated nucleic acid purification. The epMotion Plug'n'Prep technology offers pretested methods for walkaway DNA and RNA purification using a choice of more than 25 different protocols. The instrument gives researchers freedom to choose any purification technology: Invitrogen, Promega, Macherey-Nagel, Invitek, and 5 Prime have all developed epMotion methods. New users can simply select their preferred brand and type of extraction kit, download the method from epMotion.com, and transfer the method data file to the epMotion. No further adaptation is needed, and setup time is less than an hour. A wide range of applications is available, including genomic DNA extraction from blood, tissue cultured cells, and bacteria; isolation of total RNA, viral DNA, and RNA; plasmid purification; and polymerase chain reaction cleanup.

Eppendorf
For information +49 40 538 01 640
www.eppendorf.com

Thermocycler Workstation

The BLM-TC Planar Lipid Bilayer Thermocycler Workstation is a Peltier-driven platform that provides tight and reproducible temperature control to facilitate the measurement of single-channel events at temperatures between 5° and 50°C. This device heats and cools at an average rate of 3°C per minute and can maintain a temperature to within 0.2°C of the set temperature.

Warner Instruments
For information 800-599-4203
www.warnerinstruments.com

Thermostable Polymerase

The PyroPhage 3173 DNA Polymerase is cloned from thermophilic phage infecting boiling hot springs thermophiles. It is available as the Wild Type enzyme and as an Exonuclease Minus mutant. It is more effective than polymerase chain reaction (PCR) enzymes in amplifying certain templates. Its efficient reverse transcription activity enables single-tube, single-enzyme reverse-transcription PCR, and potent strand-displacing activity allows for isothermal DNA synthesis through double-stranded DNA. The enzyme initiates efficiently at nicks, therefore, DNA synthesis can be initiated either with primers or at a nick introduced by site-specific nicking enzymes.

Lucigen
For information 608-831-9011
www.lucigen.com

Electronically submit your new product description or product literature information! Go to www.sciencemag.org/products/newproducts.dtl for more information.

Newly offered instrumentation, apparatus, and laboratory materials of interest to researchers in all disciplines in academic, industrial, and governmental organizations are featured in this space. Emphasis is given to purpose, chief characteristics, and availability of products and materials. Endorsement by *Science* or AAAS of any products or materials mentioned is not implied. Additional information may be obtained from the manufacturer or supplier.

EXODUS TO ASIA:

RESEARCH OPPORTUNITIES ABOUND

Asia is enjoying enormous investment in science and technology, and is proving a major attraction in the scientific jobs market. **By Julie Clayton**

Science and technology is booming in Asia, and acting as a magnet for Asian scientists wishing to return home after training in the West—especially to China—attracted to full- or part-time positions in both academia and industry.

Promoting the eastward migration is a strong government push—particularly in China, Singapore, Korea, and Japan—to become global players in science and technology, and massive investment from the pharmaceutical industry. The result is a heady mix of new R&D opportunities.

Yet the "returnees" are only one side of the story. Also finding new opportunities are Western scientists wishing to work in Asia—including academics taking up professorships at Chinese universities. At the same time, scientific institutions in the West are keen to seize the new opportunities for research collaboration in Asia.

All of this means that Asia is now enjoying a significant brain gain.

The Road to China

Several major international pharmaceutical companies are expanding their research and development in China. The city of Shanghai, which has become a mecca for science generally, is now home to both a growing local pharmaceutical industry as well as international companies like Roche, Novartis, Novo Nordisk, GlaxoSmithKline, and AstraZeneca. Consequently, research opportunities go beyond the R&D pipeline to include drug manufacturing, clinical research, quality assessment, and quality control.

Roche was the first multinational pharmaceutical company to arrive at the Zhangjiang Hi-Tech Park in 1994. It opened a new research center in 2004 followed by a development center in 2007, and aims to bridge the gap between basic research and China's "huge resource in clinical research." The goal is to identify new disease diagnostic markers and develop new therapies, according to the company's head of R&D in China, **Andreas Tschirky**, and chief scientific officer **Li Chen**.

Chen, who returned to China after training in the United States, notes, "For many years there was a brain drain to the United States and Europe, but now there is a reversal because of the attractiveness of the job market for highly qualified people."

According to Tschirky, scientific enterprise in China is being actively welcomed by the Chinese government and local authorities, who are showing "strong leadership" and are "more proactive" than in the United States or Europe in listening to the views of scientists on the need for scientific innovation. To capture this momentum, Roche aims to provide a platform for local innovation to be transformed into marketable products.

Besides actively recruiting, the company is striving to team up more with Chinese academics, clinicians, and local biotech as well as providing basic research grants—no strings attached—to promote understanding of disease processes.

Novartis also has an existing research facility at the Zhangjiang Hi-Tech Park in Shanghai with approximately 100 scientists. This will be superceded by a new, larger facility on which construction begins this spring, with a capacity for around 400 scientists.

"Shanghai is clearly emerging as a new epicenter of global science,

> "Shanghai is clearly emerging as a new epicenter of global science, and is a magnet for top research scientists."

Upper: A*Star's diverse community
Lower: En Li, vice president and head of the new Novartis facility in Shanghai

[illegible]

Vaccine Research March 28
Translational Research (online only) April 18
Diversity 2: Affinity Groups (online only) May 9

CREDIT (ILLUSTRATION): ©ISTOCKPHOTO.COM, FILO; (TOP PHOTO): A*STAR; (BOTTOM) NOVARTIS

Focus on Asia

"In the last few years, our small institute [now with 17 principal investigators] is publishing at least one-third of all high-profile papers in the biological sciences from China."
—Mu-ming Poo

and is a magnet for top research scientists," says **En Li**, vice president and head of the new facility, which provides "a significant opportunity for Novartis to develop life-saving treatments," with particular regard to cancers that are endemic to the region.

Denmark-based Novo Nordisk, which focuses on diagnosis and treatment of diabetes and other conditions, is actively expanding its R&D base in Beijing. "China is a grossly underestimated scientific force," says chief scientific officer **Mads Krogsgaard**, pointing to China's current world ranking as fourth in publications output (according to National Science Foundation Science and Engineering Indicators 2008).

The company is recruiting graduates from local universities into scientific posts at its R&D center, while looking mainly to Chinese expatriates from Europe and the United States to fill managerial positions. The latter have the advantage of "an international mindset but are still culturally Chinese," says Krogsgaard, highlighting, in particular, analytical skills and the ability to collaborate with people of different backgrounds as particular strengths of Western trained scientists.

The Novo Nordisk R&D center was first established in 2002 to optimize recombinant protein production, but is now moving on to do "real project work and be more innovative," including developing new drug targets. To complement the R&D expansion, the company is also creating a new research foundation, in partnership with the Chinese Academy of Sciences (CAS), to fund new research projects, scholarships, and exchanges for scientists working in protein science, particularly diabetes—a condition affecting around 40 million Chinese.

In contrast, China's biotech industry is in a fairly fledgling stage, according to **Zailin Yu**, a Chinese biologist who has returned to China from California. He took up a position as an adjunct professor at Peking University College of Life Sciences, and set up two companies. Despite owning the patent to a new technology for the production of recombinant protein-based drugs, he has not found it easy to attract private investment within China, and has had to turn to Chinese government grants and venture capital from the US, to fund his startups.

"In China it's hard to find [a venture capitalist] who is patient enough to wait for animal testing, clinical trials, and then a product." But he expects this to change in future as the market for new drugs is rapidly growing.

Scientists returning to China are also finding attractive positions in academia. **Mu-ming Poo**, director of the Institute of Neuroscience (ION) in Shanghai, part of CAS, is actively recruiting from abroad to the institute. He knows well the experience and skills that such researchers can bring to China, having spent nearly 30 years working in the US when he took up the directorship in 1999.

When Poo was about to accept a professorship at the University of California, Berkeley, in 1998, he was asked by president Lu Yongxiang of CAS to help promote Chinese neuroscience. Poo felt that he would not have the right impact if his task were just to "renovate old institutes." Instead, he proposed a brand new Institute of Neuroscience with a modern infrastructure, "in other words merit-based rather than seniority-based promotion and resource allocation."

Poo, now director of ION, spends one week per month there, while at the same time maintaining his position as Paul Licht Distinguished Professor in Biology in the Department of Molecular and Cell Biology at Berkeley. He is proud that the institute has made its name with a high quality of scientific output. "In the last few years, our small institute [now with 17 principal investigators] is publishing at least one-third of all high profile papers in the biological sciences from China."

Most of the scientists moving to China are returning expatriates, as the culture and bureaucracy means that it is easier continued »

Agency for Science and Technology Research (A*STAR)
www.a-star.edu.sg/astar

Biomedical Research Council
www.a-star.edu.sg

Brain Science Institute of Riken
www.brain.riken.jp

Chinese Academy of Sciences
www.english.cas.ac.cn

Hong Kong University of Science and Technology
www.ust.hk

Institute for Bioengineering and Nanotechnology
www.ibn.a-star.edu.sg

Institute of Cell and Molecular Biology
www.imcb.a-star.edu.sg/php/main.php

Institute of Materials Research and Engineering
www.imre.a-star.edu.sg

Institute of Neuroscience
www.ion.ac.cn

Japan Society of Promotion of Science
www.jsps.go.jp/english

Nanyang Technological University
www.ntu.edu.sg/publicportal

National University of Singapore
www.nus.edu.sg

Novartis Integrated Biomedical Research Development Center
www.novartis.com/research/research-centers/nibr-shanghai.shtml

Novo Nordisk
www.novonordisk.com

Peking University
www.pku.edu.cn

Roche
www.roche.com

Science and Engineering Research Council
www.a-star.edu.sg

University of California, Berkeley
www.berkeley.edu

Zhangjiang Hi-Tech Park
www.zjpark.com/zjpark_en

"It's the easiest place to work I've ever been. Facilities, resources, and money are amazing. And the drive to accomplish something world class is breathtaking!"
—Victor Nurcombe

for Chinese speakers to gain positions in the country, according to Poo. All documentation regarding work permits, contracts, and grant applications, for example, are in Chinese.

He and others at ION are trying to make it easier for non-Chinese researchers by employing office staff who can speak and write in English, and by conducting seminars and lab meetings in English. "We now have a few non-Chinese students and postdocs. Our plan is that in a few years we are ready to accommodate non-Chinese principal investigators. Our goal is to be an international research institute, with a substantial fraction of non-Chinese PIs, similar to the Brain Science Institute of Riken in Tokyo, which now has 20 percent to 30 percent non-Japanese research staff."

Scientists returning to China are having a strong impact, comments **Nancy Ip**, director of the Biotechnology Research Institute (BRI) at Hong Kong University of Science and Technology (HKUST). "These returnees enhance the innovation capabilities of China as they bring back with them a wealth of overseas experience such as exposure to cutting-edge research, knowledge of international standards, and a broad international network," she says.

In Hong Kong, in contrast, the biopharmaceutical industry is more in its infancy, according to Ip. Most of the cutting-edge research is university based, and is thriving in all areas of life sciences and medicine as well as in the physical sciences, particularly analytical and synthetic chemistry.

Jobs Galore in Singapore

Meanwhile Singapore is attracting considerable attention with the establishment of two flagship R&D centers by the government Agency for Science and Technology Research (A*STAR). The first is Biopolis, opened in 2003 to develop biomedical sciences. The second is Fusionopolis, devoted to creating the next generation of technologies, materials, and devices and due to open later this year.

The two megacenters currently employ around 3,000 researchers across 14 separate research institutes and are overseen by the Biomedical Research Council (BMRC) and the Science and Engineering Research Council (SERC). They are intended to improve the visibility of Singapore's R&D, foster multidisciplinary research, create new commercial spinoffs, and partner with local industries. They are attracting local and returning Singaporeans and scientists from other countries.

Agency for Science and Technology Research (A*STAR), Fusionopolis

"It is a truly international research community, embracing all nationalities, all faiths, and all ethnic groups," says **Andre Wan** of BMRC.

"A lot of things are happening at a very fast pace," says **Jackie Ying**, who was a professor for 11 years at MIT in Cambridge, Massachusetts, before moving to Singapore in 2003 as executive director of the Institute for Bioengineering and Nanotechnology, "and Singapore has tremendous research opportunities, especially in the biomedical areas."

Around 80 percent of the institute's scientists are either returning Singaporeans or foreign-born—mostly from the United States, Europe, Australia, and Asia—and include chemists, biologists, computer scientists, electrical and mechanical engineers, and medical doctors. "They come over because they are excited about the research," says Ying.

In comparison to when she was in the US, Ying feels she has more funding options and more flexibility about research directions in Singapore. However, she still maintains an adjunct position at MIT.

Singapore's legacy as a former British colony means that English is the official working language, making the recruitment of scientists, for example, from North America, Europe, and Australia relatively easy compared to elsewhere in Asia.

For **Victor Nurcombe**, coming to Singapore after working in Europe, the United States, and Australia was "a revelation." He arrived four years ago from the University of Queensland to work at the Institute of Cell and Molecular Biology. "It's the easiest place to work I've ever been. Facilities, resources, and money are amazing. continued »

CREDIT (RIGHT PHOTO): A*STAR

"Don't flock with your own kind too much. Although you may be tempted to work preferentially with fellow countrymen, especially if you feel yourself in a strange land, it will inevitably limit your horizons."
—Jonathan Hobley

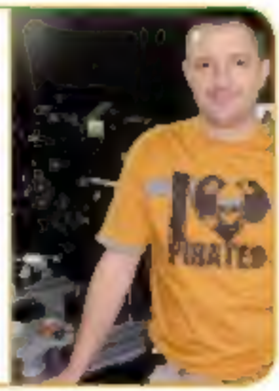

And the drive to accomplish something world class is breathtaking!" he enthuses. "To be relieved of all the burdensome administration, to be just left alone to do the best science, not constrained by endless grant writing or budgets—what's not to like?"

Certainly, if the investment is anything to go by, then Singapore is well on the way to its aim of becoming a major scientific hub in Asia. A*STAR gets a five-year budget of US$3.6 billion, and this for a population of only 4 million people.

The multiethnic makeup of Singapore (particularly Chinese, Indian, and Malay communities) together with good health care infrastructure is attracting pharmaceutical companies wishing to do clinical trials—for example GlaxoSmithKline, Novartis, Eli Lilly and Company, Pfizer, Merck, and Schering-Plough.

Elsewhere in Singapore existing links with the West are already strong, and getting stronger. For example at the Nanyang Technological University (NTU), recruitment of international faculty is occurring across a wide range of subject areas, including engineering and science, with special emphasis on its Nanyang Assistant Professorship scheme, awarding 10 to 12 distinguished young faculty each year with a competitive salary and up to $1 million startup funds over the first three years. And at the postdoctoral level, NTU is working through the SINGA Scheme with A*STAR to recruit candidates from Eastern Europe, Russia and Ukraine, and the Middle East as well as to bring in Singaporean students.

Similarly, the National University of Singapore (NUS) is thriving in many areas. "We recruit both locally and overseas, and particularly like to 'attract back' overseas Singaporeans who have distinguished themselves in research," says **Barry Halliwell**, deputy president (research and technology). NUS also has links with leading overseas partners and international education alliances.

East Meets West

Meanwhile, scientific institutions in Europe and North America are forging international partnerships spanning East and West. The German Research Foundation (DFG) is encouraging links between its scientists and collaborators in China, Korea, and Japan. This is most advanced in China, where the Sino-German Center for Research Promotion in Beijing, funded jointly with the National Natural Science Foundation of China, supports cooperation between Chinese and German scientists doing basic research in the natural, life, engineering, and management sciences.

"We would warmly encourage scientists to [come to China], because China's science system is becoming increasingly interesting and offers a growing number of opportunities," says the center's German director **Armin Krawisch.**

At a more preliminary stage, but also promising, is the promotion of new ties between DFG and the Japan Society for the Promotion of Science (JSPS), illustrated by a joint symposium in Hamburg in January 2008 for young researchers on global climate change science.

Along similar lines, the umbrella organization for the UK's research councils—RCUK—opened an office in Beijing in October 2007, with a view to enabling the research councils to offer UK-China funding opportunities (ideally in conjunction with Chinese funding agencies) and make it easier for individual researchers to develop contacts with key partners in other countries, according to the office director, **Chris Godwin.**

Current plans include several small schemes for facilitating research and travel, while four major projects are also under way involving different UK academic institutions, to promote research into urban sustainability.

Other links between Europe and Asia include plans by the European Science Foundation and the Korea Research Foundation to create new exchange and research initiatives. The Korean government has invested heavily in R&D, for example, in both the private and academic sectors, having increased spending between 2000 and 2004 from 2.4 percent to 2.9 percent, and is looking to forge links with other countries. But Korea has yet to see the influx of trained scientists that China is enjoying, and increasing numbers of students are opting to study abroad, particularly in the US, and may not return to Korea.

Tips for Travelers

So what tips are there for all the foreign scientists in the West who are considering packing their bags for Asia?

Scientists heading for China should "be willing to adapt to, or at least accept, the different conditions in work life, habits, salaries, structures and hierarchies, decision making, equipment, and so on," says Krawisch. He adds that "cultural training on Chinese characteristics and—for those who stay longer—some Chinese language skills are highly recommended."

In Singapore, Nurcombe advises, "Use the opportunities given to you as best you can. The island is developing its research foci and its research style so, because it's very compact, you can have a major effect on how things happen."

British researcher **Jonathan Hobley** at the Institute of Materials Research and Engineering recommends that foreign scientists begin networking as soon as they arrive—taking advantage of the high density of labs. "It is valuable and pays rapid dividends if you let people know what you are doing and where you can work with them." But, he warns, "Don't flock with your own kind too much. Although you may be tempted to work preferentially with fellow countrymen, especially if you feel yourself in a strange land, it will inevitably limit your horizons."

Julie Clayton, a freelance science writer and journalist, works out of Bristol, UK.

DOI: 10.1126/science.opms.r0800050


X-ray


Unmixed Fluorescent Signals


Reflectance


4 Layer Composite

New!

Multiple ways to look at a mouse

KODAK In-Vivo Multispectral Imaging System FX: Enables advanced ***unmixing of multiple fluorochromes.***

- Automated protocols for precise identification, unmixing and analysis of fluorescent signals
- Sophisticated software algorithms remove autofluorescence for improved signal-to-noise and detection sensitivity
- 29-position excitation filters ranging from 380-780 nm
- Multimodal capabilities include white light, multiwavelength fluorescence, UV fluorescence, luminescence, radioisotopic and x-ray imaging
- Automated digital system with 4MP CCD and 10x optical zoom lens deliver powerful imaging results

Learn more. Call **1-877-747-4357**, exp. code 7. Outside the U.S. call **+1-203-786-5657**.

With the Kodak In-Vivo Multispectral Imaging System FX can be used for in vivo and in vitro molecular imaging of materials, researchers should be aware that the methods of preparing and viewing the materials for molecular imaging may be subject to various patent rights. All images were captured using Kodak Molecular Imaging Products.

www.carestreamhealth.com/go/invivo5

Kodak
Licensed Product

Carestream Molecular Imaging

A division of Carestream Health

The Innovation Powering KODAK Molecular Imaging Products

Carestream Health, Inc.
4 Science Park • New Haven, CT 06511